BULLETIN

OF THE KARAGANDA UNIVERSITY

CHEMISTRY

Series

ҚАРАҒАНДЫ УНИВЕРСИТЕТІНІҢ ХАБАРШЫСЫ

ВЕСТНИК
КАРАГАНДИНСКОГО УНИВЕРСИТЕТА

BULLETIN
OF THE KARAGANDA UNIVERSITY

ХИМИЯ сериясы

Серия ХИМИЯ

CHEMISTRY Series

№ 2(106)/2022

CONTENTS

ORGANIC CHEMISTRY

PHYSICAL AND ANALYTICAL CHEMISTRY

INORGANIC CHEMISTRY

CHEMICAL TECHNOLOGY

ORGANIC CHEMISTRY

G.K. Kudaibergen[*], M.S. Zhunussova

National Center for Biotechnology, Nur-Sultan, Kazakhstan
([*]Corresponding author's e-mail: kudaibergen@biocenter.kz)

Study of the Effect of Temperature on the Properties of Gelatin-Chitosan Cryogels

Cryopolymers are a class of 3D structural polymers, which are widely used in tissue engineering. Using cryopolymerization technology, physical cross-linked macroporous cryogels based on gelatin and chitosan were synthesized at –12 ºC, –30 ºC and –70 ºC for application as carriers for cell cultures. The presence of functional groups was investigated by IR spectroscopy. The effect of temperature on physicochemical properties, such as pore volume, density, gel fraction and biodegradation of cryogels, was studied. The obtained results showed that the pore volume (up to 87.6 %) and the gel fraction (up to 80 %) increased, and the density (0.078 %) and pore sizes of cryogels decreased as the temperature decreased from –12 ºC to –70 ºC. The study of biodegradation showed that polymers had a more degradable property in relation to saline solution with an increase in the cryopolymerization temperature. The results of electron microscopy showed the porous morphology of the surfaces of the synthesized cryogels. The average pore size varied from 150 to 300 μm. The toxicity test showed that aqueous extracts from cryogels did not have a highly toxic effect on mesenchymal stem cells in the adipose rats tissue, since the cell viability was 55–75 %.

Keywords: cryogel, gelatin, chitosan, biopolymer, non-toxic, biocompatible, porosity, tissue engineering.

Introduction

Cryogels obtained by the cryotropic gelation process/cryopolymerization are macroporous hydrogels with a well-developed system of interconnected pores, high swelling capacities, and large surface areas [1–5]. Professor V.I. Lozinsky made a huge contribution to the development of the cryopolymerization concept [6–10]. Cryogels can be used in controlled drug delivery, carriers for cell immobilization, sensors, bioseparation, purification, and tissue engineering [11, 12]. Common cryogel compositions include natural polymers, such as gelatin, chitosan, alginate, hyaluronic acid and synthetic acrylamide-based polymers and poly (lactic acid) (PLA), poly (lactic-co-glycolide) (PLGA), poly(ε-caprolactone) (PCL) [13, 14].

There are chemical and physical cross-linked cryogels. Crosslinkers, such as glutaraldehyde, N-(3-dimethylaminopropyl)-N-ethylcarbodiimide hydrochloride and N-hydroxysuccinimide are often used in the creation of chemically cross-linked cryogels. Physically cross-linked cryogels are formed through the interaction of intermolecular sub-chains in macromolecules [15–17].

To date, there are many studies on the synthesis of polymers based on gelatin and/or chitosan using chemical cross-linking agents [18–25]. There are also studies on the synthesis of polyelectrolyte polymers of gelatin and chitosan [26–30]. However, there is no data on the synthesis of physical cross-linked Gel:Ch scaffolds by cryopolymerization without the participation of cross-linking agents. The synthesis of such polymers is advantageous since no chemical cross-linking agents are used that can be toxic to cells or tissues.

Pinto Ramos et al. derived biopolymer films from chitosan, gelatin and Ch/Gel mixture in salt solutions (NaCl, CaCl₂ and Na₂SO₄) with varying concentrations and ion charges. The authors investigated the polyelectrolyte and polyampholytic properties of the films so that in the future it would be possible to create biopolymer films using them in ionic media [31]. A team of scientists synthesized 3D chitosan scaffolds that,

in combination with bFGF, facilitated the neural differentiation of dental pulp stem cells (DPSCs). As shown by the results, DPSCs adhered successfully and grew well on the surface of chitosan scaffolds. According to the authors, the transplantation of DPSCs/chitosan-scaffold+bFGF might be a secure and effective method of treating spinal cord injury and other neuronal diseases [32, 33].

The main goal of this work is to obtain macroporous scaffolds as a base and carrier for mesenchymal stem cells (MSC). To achieve this goal, we first synthesized and characterized novel physical cross-linked scaffolds based on gelatin (Gel) and chitosan (Ch) by cryopolymerization. This research is of great importance in tissue engineering, as it provides a new understanding of new effective ways of obtaining biopolymers without the use of chemicals that are toxic to cells and tissues. Thus, the obtained cryogels can be used as carriers of stem cells and can be used in the treatment of bone damage.

Experimental

Preparation and characterization of cryogels

The GelCh cryogels were prepared by dissolving a gelatin (0.4 % w/v) and a chitosan (0.2 % w/v) in 1 % acetic acid solution. The acidity of the solution was then adjusted using 1 M of NaOH to pH = 5 to protonate amine groups of Ch. After the solution was transferred in syringes and incubated for –12 ºC (GelCh12), –30 ºC (GelCh30) and –70 ºC (GelCh70) for 24 h. After thawing at room temperature, the thus formed physically cross-linked polymers were washed with Milli-Q water and PBS (pH = 7.4) and lyophilized using Martin Christ Beta 2-8 LDplus freeze dryer. GelCh cryogels were stored in a dark place at room temperature for further use.

Gel fractions, the degree of degradation, and the density of cryogels were determined according to a well-known method [15].

The gel percent was calculated by the formula [34]:

$$Gel\,(\%) = \frac{W_w}{W_i} \times 100 , \tag{1}$$

where W_w and W_i are weight of the swollen dry gel and a sample, which was not immersed in water but directly freeze-dried.

Cryogels were weighed (W_1) and transferred to 50 ml tubes filled with sterile 0.1M PBS (pH 7.4). The tubes were incubated at 37 °C for 8 weeks, during which the solution was refreshed twice in a week. At predetermined times, cryogel samples were taken from the solution and washed with deionized water. After freeze-drying overnight and weighing (W_2) the degree of degradation was determined by the following formula [15, 18]:

$$DD\,(\%) = \frac{W_1 - W_2}{W_1} \times 100 . \tag{2}$$

The density of cryogels was evaluated from the mass-to-volume ratio of dry cryogels. The apparent density (ρ) was obtained from the equation [15, 35]:

$$\rho = \frac{W}{\pi \times (D/2)^2 \times H} , \tag{3}$$

where W is the weight of the cryogel, D is the diameter, and H is the thickness of polymers.

The pore volume of the cryogels was estimated from the uptake of ethanol into the pores. Ethanol is a non-solvent for the cryogels and it easily penetrates into the pores. The measurements were carried out by immersing dry cryogel specimens with a mass of W_D into absolute ethanol for 1 h and then recording their final mass W_S. The pore volume (PV) was calculated by applying the following formula [15, 36]:

$$PV\,(\%) = \frac{(W_S - W_D)}{W_S} \times 100 . \tag{4}$$

The measurements were performed in triplicate and the average value was found.

The cryogels were lyophilized and the Fourier-transform infrared spectra (FTIR) (Nicolet iS 10, Thermo Fisher Scientific) of these lyophilized samples were recorded in the wavelength range of 4000–400 cm^{-1}.

The morphology of dried cryogels was observed using a scanning electron microscope (SEM, Auriga Crossbeam 540, Carl Zeiss) after coating with gold 5 nm.

MTT assay

The cultivation of rat adipose-derived MSC (ADMSC) and MTT assay were obtained as previously described [15]. In this study outbred male Wistar rats weighing 280–330 grams were used. The study was car-

ried out according to the guidelines of the Declaration of Helsinki and approved by the Local Ethics Committee of the National Center for Biotechnology (number NCB-04-2020).

For the statistical analysis, all the physical, chemical, and biological experiments on cryogel samples were performed in triplicate. All the experimental values were expressed in the form of mean ± standard error and the limit of experimental error of each test was ± 5 %, which had been considered as statistically significant.

Results and Discussion

Ch contains amine groups and exhibits the properties of polyelectrolytes [37]. Gel, consisting of negative carboxyl and positive amine groups, shows the properties of polyampholytes [38]. The formation of the 3D macroporous structure of GelCh cryogels occurs due to the interaction of negatively charged carboxyl groups (–COOH) of gelatin and positively charged amino groups (–NH$_2$) of chitosan, which form a polyelectrolyte interaction between the macromolecules chains (Fig. 1).
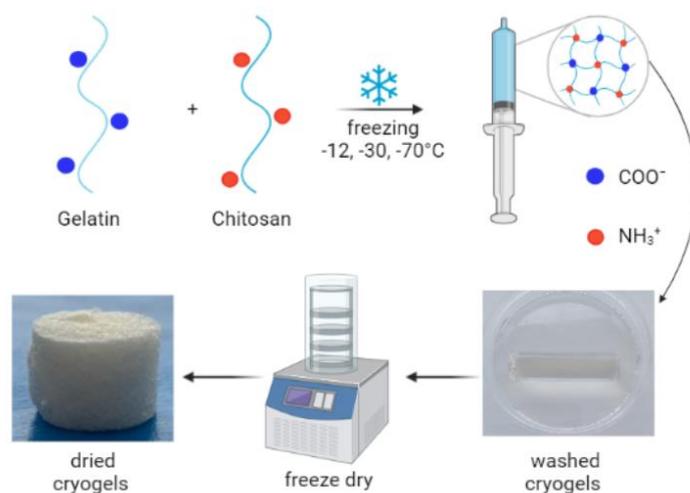
Figure 1. Scheme of the cryogels formation
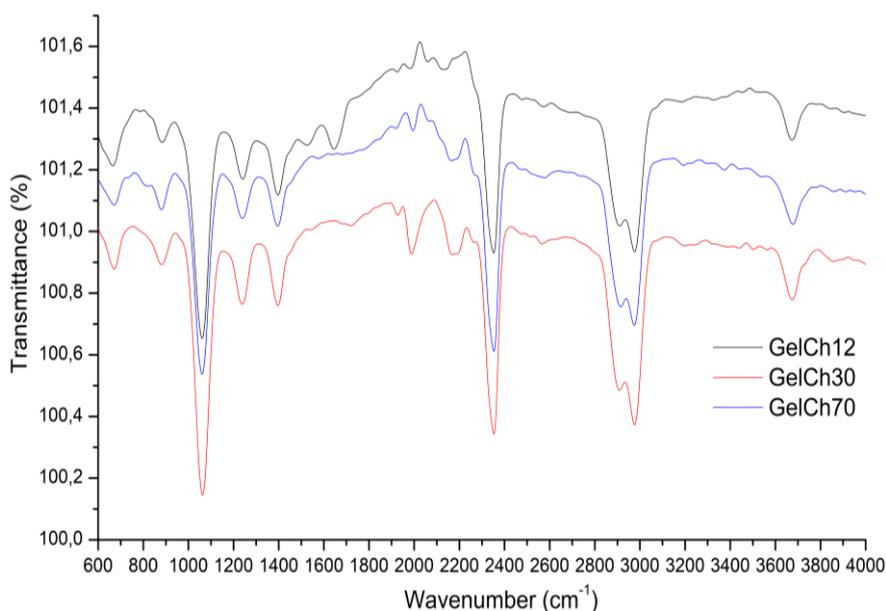
Figure 2. FTIR spectra of GelChCS cryogels

The spectrum of cryogels illustrates a band in the range of 3000–3600 cm^{-1}, which belongs to the stretching vibrations of the O–H and N–H functional group (amide A) that is involved in the intramolecular

hydrogen bond between chitosan and gelatin molecules. The bands at 2800–2900 cm^{-1} are due to several symmetric and asymmetric stretching vibrations of C–H. The bands at 1650 cm^{-1} refer to CO and CN amide I. The spectra at 1535 cm^{-1} refer to bending vibrations of NH groups and stretching vibrations of CN groups (amide II). The absorption of the spectrum in the 1243 cm^{-1} range belongs to stretching vibrations of CN-groups (amide III). The troughs at 1065 cm^{-1} are due to stretching vibrations of C–O groups. The bands at 887 and 675 cm^{-1} are related to the vibrations of C–H and N–H groups (Fig. 2).

GelCh cryogels were synthesized by dissolving gelatin and chitosan in acetic acid using cryogelation technology at –12 °C, –30 °C and –70 °C without using any chemical crosslinkers (Table 1).

T a b l e 1

Summary properties of GelCh cryogels

Samples	T, °C	Gel percent (%)	Density (g/ml)	Pore volume (%)
GelCh12	–12	73±1	0.095±0.005	84.6±3
GelCh30	–30	79±3	0.085±0.006	86.5±4
GelCh70	–70	80±1	0.078±0.005	87.6±2

According to Table 1, the yield of the gel fraction for cryogels is the maximum one with decreasing temperature. This is because that, at a lower temperature, tightly cross-linked polymer networks are formed, in which the sol (soluble part) fraction is present to a lesser extent. Compared to the GelCh70 sample in the GelCh12 sample, the yield of the gel and sol fractions is 80 and 73 %, respectively. This may also be due to the hydrophilic properties of gelatin and the looser structure of the polymer. As the results show, the porosity of scaffolds decreases with an increase in their density. The synthesized cryogels have a high pore volume of 85–88 %. The more porous the polymer, the better it is for the penetration of fluids and cells. Biodegradation in PBS solution over 8 weeks was studied to confirm the cryogels biocompatibility (Fig. 3).
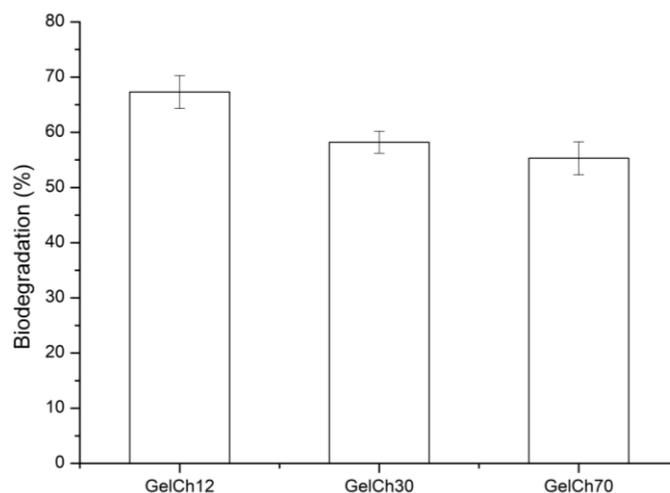
Figure 3. Biodegradation behavior of the cryogels in PBS at 37 °C for 8 weeks

The *in vitro* decomposition rate of cryogels was 67 % (GelCh12), 58 % (GelCh30) and 55 % (GelCh70). Compared to covalently bonded cryogels, the synthesized cryogels demonstrated a high percentage of degradation of the polymer matrix. Upon biodegradation, cryogel macromolecules (long polymer chains) break down into low molecules (oligomeric units), which dissolve in the solvent and lead to weight loss. The presence of water-soluble gelatin gives additional hydrophilicity to polymers, in which monomer chains are rapidly hydrolyzed. The degree of biodegradation decreases with decreasing temperature, since cryogels are not linked by a covalent bond. All cryogels exhibit a high degree of decomposition. The degradation of cryogels is influenced by its surface morphology and pore size (Fig. 4).
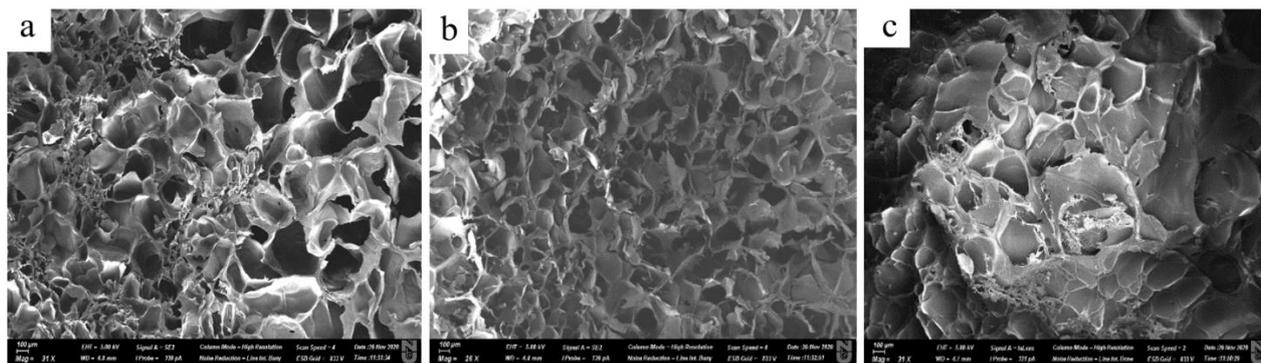
a — GelCh12; *b* — GelCh30; *c* — GelCh70

Figure 4. SEM of cryogels

The surface morphology of the synthesized polymers was investigated by the SEM method. As can be seen from Figure 4, the surface of the synthesized cryogels is changed significantly under the influence of temperature. The surface of cryogels has a porous structure with unevenly distributed pores. As the temperature decreases, the formation of more closed pores is observed. The pore size of cryogels varies from 150 to 300 μm. Comparing cryogels, one can notice a tendency that GelCh30 has a more uniform pore distribution, while GelCh12 has a random distribution. This is possibly due to self-assembly between gelatin and chitosan. The resulting pore sizes can be sufficient for cell cultivation, since the biggest pore size accommodates more cells that can agglomerate. Thus, the pores provide intercellular contact between cells, showing higher markers of chondrogenesis, and can be used for the treatment of bone regeneration and in tissue engineering in general.

To determine the cytotoxicity of cryogels, an MTT assay was conducted using primary culture of rat ADMSC (Fig. 5).
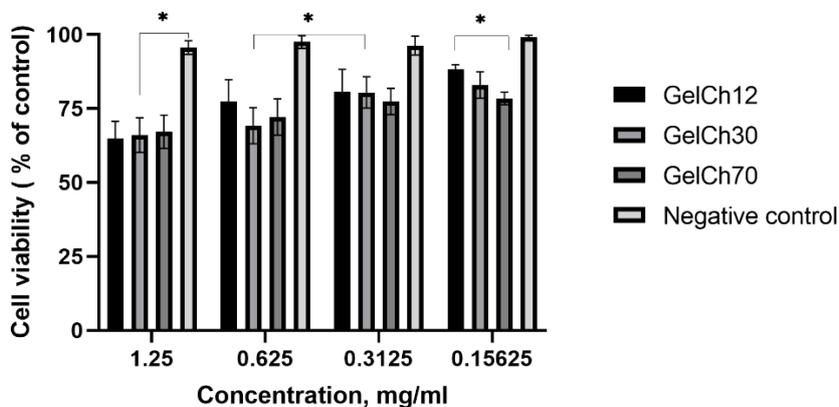
Figure 5. Effects of extracts of cryogels on cell viability of rat ADMSC
presented as percentage of cell viability versus concentration of the extracts (*p value ≤ 0.05)

The extracts from cryogels exhibit a weak toxic effect on rat ADMSC and display more than 55 % of cell viability after treatment with concentration of 1.25 mg/ml. The viability of rat ADMSC cells at a concentration of 0.156 mg/ml with cryogel extracts showed the highest cell viability (up to 75 %). Thus, MTT assay revealed that GelCh12, GelCh30 and GelCh70 cryogels are biocompatible and suitable for further applications in *in vivo* studies.

Conclusions

Macroporous cryogels based on gelatin and chitosan were synthesized using the cryopolymerization method at various temperatures (–12, –30 and –70 °C) without chemical cross-linking agents. The formation of the 3D macroporous structure of GelCh cryogels occurs due to the interaction of negatively charged carboxyl groups (–COOH) of gelatin and positively charged amino groups (–NH$_2$) of chitosan, which form a polyelectrolyte interaction between the macromolecules chains. The functional groups of cryogels were iden-

tified by IR spectroscopy. The effect of temperature on physicochemical properties of cryogels, namely GelCh12, GelCh30 and GelCh70, was studied. Thus, the pore volume (up to 87.6 %) and the gel fraction (up to 80 %) increase and the density (0.078 %) and the pore size of cryogels decrease with decreasing temperature. SEM results showed a macroporous surface of the cryogels. Comparing cryogels, one can notice a tendency that GelCh30 has a more uniform pore distribution, while GelCh12 has a random distribution. Since cryogels are composed of natural polymers and obtained without the use of chemical cross-linking agents, degradation products are expected not to cause immune rejection problems during implantation, which makes such materials potentially useful for tissue engineering.

References

1   Savina, I.N., Zoughaib, M., & Yergeshov, A.A. (2021). Design and Assessment of Biodegradable Macroporous Cryogels as Advanced Tissue Engineering and Drug Carrying Materials. *Gels*, *7*(3), 79. https://doi.org/10.3390/gels5020027

2   Jones, L.O., Williams, L., Boam, T., Kalmet, M., Oguike, C., & Hatton, F.L. (2021). Cryogels: Recent applications in 3D-bioprinting, injectable cryogels, drug delivery, and wound healing. *Beilstein Journal of Organic Chemistry, 17*, 2553–2569. https://doi.org/10.3762/bjoc.17.171

3   Lozinsky, V.I. (2020). Cryostructuring of Polymeric Systems. 55. Retrospective View on the More than 40 Years of Studies Performed in the A.N. Nesmeyanov Institute of Organoelement Compounds with Respect of the Cryostructuring Processes in Polymeric Systems. *Gels, 6*(3), 29. https://doi.org/10.3390/gels6030029

4   Razavi, M., Qiao, Y., & Thakor, A.S. (2019). Three-dimensional cryogels for biomedical applications. *Journal of Biomedical Materials Research Part A, 107*(12), 2736–2755. https://doi.org/10.1002/jbm.a.36777

5   Klivenko, A., Mussabayeva, B., Gaisina, B., & Sabitova, A. (2021). Biocompatible cryogels: Preparation and application. *Bulletin of the University of Karaganda — Chemistry, 103*(3), 4–20. https:// doi:10.31489/2021ch3/4-20

6   Rodionov, I.A., Grinberg, N.V., Burova, T.V., Grinberg, V.Y., & Lozinsky, V.I. (2015). Cryostructuring of polymer systems. Proteinaceous wide-pore cryogels generated by the action of denaturant/reductant mixtures on bovine serum albumin in moderately frozen aqueous media. *Soft Matter, 11*(24), 4921–4931. https://doi.org/10.1039/C4SM02814G

7   Podorozhko, E.A., Ul'yabaeva, G.R., Kil'deeva, N. R., Tikhonov, V.E., Antonov, Y.A., Zhuravleva, I.L., & Lozinsky, V.I. (2016). A Study of cryostructuring of polymer systems. 41. Complex and composite poly(vinyl alcohol) cryogels containing soluble and insoluble forms of chitosan, respectively. *Colloid Journal, 78*(1), 90–101. https:// doi:10.1134/s1061933x16010130

8   Lozinsky, V. (2018). Cryostructuring of Polymeric Systems. 50. Cryogels and Cryotropic Gel-Formation: Terms and Definitions. *Gels, 4*(3), 77. https://doi.org/10.3390/gels4030077

9   Podorozhko, E.A., Vasil'ev, V.G., Vasiliev, N.K., & Lozinsky, V.I. (2019). A Study of Cryostructuring of Polymer Systems. 51. The Combined Influence of Porous Cellulose-Containing Dispersed Fillers and Salting-Out Electrolytes on the Physicochemical Properties of Composite Poly(vinyl alcohol) Cryogels. *Colloid Journal, 81*(3), 261–271. http://link.springer.com/article/10.1134/S1061933X19020121

10   Podorozhko, E.A., Buzin, M.I., Golubev, E.K., Shcherbina, M.A., & Lozinsky, V.I. (2021). A Study of Cryostructuring of Polymer Systems. 59. Effect of Cryogenic Treatment of Preliminarily Deformed Poly(vinyl alcohol) Cryogels on Their Physicochemical Properties. *Colloid Journal, 83*(5), 634–641. https://doi.org/10.1134/S1061933X21050112

11   Memic, A., Colombani, T., Eggermont, L.J., Rezaeeyazdi, M., Steingold, J., Rogers, Z.J., & Bencherif, S.A. (2019). Latest Advances in Cryogel Technology for Biomedical Applications. *Advanced Therapeutics, 2*(4), 1800114. https://doi.org/10.1002/adtp.201800114

12   Shiekh, P.A., Andrabi, S.M., Singh, A., Majumder, S., & Kumar, A. (2021). Designing cryogels through cryostructuring of polymeric matrices for biomedical applications. *European Polymer Journal, 144*, 110234. https://doi.org/10.1016/j.eurpolymj.2020.110234

13   Bharadwaz, A., & Jayasuriya, A.C. (2020). Recent trends in the application of widely used natural and synthetic polymer nanocomposites in bone tissue regeneration. *Materials Science and Engineering: C, 110*, 110698. https://doi.org/10.1016/j.msec.2020.110698

14   Asghari, F., Samiei, M., Adibkia, K., Akbarzadeh, A., & Davaran, S. (2016). Biodegradable and biocompatible polymers for tissue engineering application: A review. *Artificial Cells, Nanomedicine, and Biotechnology, 45*(2), 185–192. https://doi.org/10.3109/21691401.2016.1146731

15   Kudaibergen, G., Zhunussova, M., Mun, E.A., Arinova, A., & Ogay, V. (2021). Studying the Effect of Chondroitin Sulfate on the Physicochemical Properties of Novel Gelatin/Chitosan Biopolymer-Based Cryogels. *Applied Sciences, 11*(21), 10056. https://doi.org/10.3390/app112110056

16   Wang, J., & Yang, H. (2018). Superelastic and pH-Responsive Degradable Dendrimer Cryogels Prepared by Cryo-aza-Michael Addition Reaction. *Scientific Reports, 8*(1), 1–10. https://doi.org/10.1038/s41598-018-25456-y

17 Kumar, N., Desagani, D., Chandran, G., Ghosh, N.N., Karthikeyan, G., Waigaonkar, S., & Ganguly, A. (2017). Biocompatible agarose-chitosan coated silver nanoparticle composite for soft tissue engineering applications. *Artificial Cells, Nanomedicine, and Biotechnology, 46*(3), 637–649. https://doi.org/10.1080/21691401.2017.1337021

18 Kathuria, N., Tripathi, A., Kar, K., & Kumar, A. (2009). Synthesis and characterization of elastic and macroporous chitosan–gelatin cryogels for tissue engineering. *Acta Biomaterialia, 5*(1), 406–418. https://doi.org/10.1016/j.actbio.2008.07.009

19 Inci, I., Kirsebom, H., Galaev, I.Y., Mattiasson, B., & Piskin, E. (2012). Gelatin cryogels crosslinked with oxidized dextran and containing freshly formed hydroxyapatite as potential bone tissue-engineering scaffolds. *Journal of Tissue Engineering and Regenerative Medicine, 7*(7), 584–588. https://doi.org/10.1002/term.1464

20 Vishnoi, T., & Kumar, A. (2013). Comparative Study of Various Delivery Methods for the Supply of Alpha-Ketoglutarate to the Neural Cells for Tissue Engineering. *BioMed Research International, ID 294679,* 1–11. https://doi.org/10.1155/2013/294679

21 Jurga, M., Dainiak, M. B., Sarnowska, A., Jablonska, A., Tripathi, A., Plieva, F.M., & Kumar, A. (2011). The performance of laminin-containing cryogel scaffolds in neural tissue regeneration. *Biomaterials, 32*(13), 3423–3434. https://doi.org/10.1016/j.biomaterials.2011.01.049

22 Berillo, D., Elowsson, L., & Kirsebom, H. (2012). Oxidized Dextran as Crosslinker for Chitosan Cryogel Scaffolds and Formation of Polyelectrolyte Complexes between Chitosan and Gelatin. *Macromolecular Bioscience, 12*(8), 1090–1099. https://doi.org/10.1002/mabi.201200023

23 Sarnowska, A., Jablonska, A., Jurga, M., Dainiak, M., Strojek, L., Drela, K., & Domanska-Janik, K. (2013). Encapsulation of Mesenchymal Stem Cells by Bioscaffolds Protects Cell Survival and Attenuates Neuroinflammatory Reaction in Injured Brain Tissue after Transplantation. *Cell Transplantation, 22*(1), 67–82. https://doi.org/10.3727/096368913X672172

24 Nieto-Suárez, M., López-Quintela, M.A., & Lazzari, M. (2016). Preparation and characterization of crosslinked chitosan/gelatin scaffolds by ice segregation induced self-assembly. *Carbohydrate Polymers, 141*, 175–183. https://doi.org/10.1016/j.carbpol.2015.12.064

25 Fischetti, T., Celikkin, N., Negrini, N.C., Farè, S., & Swieszkowski, W. (2020). Tripolyphosphate-Crosslinked Chitosan/Gelatin Biocomposite Ink for 3D Printing of Uniaxial Scaffolds. *Frontiers in Bioengineering and Biotechnology, 8*. https://doi.org/10.3389/fbioe.2020.00400

26 Derkach, S.R., Kuchina, Y.A., Kolotova, D.S., & Voron'ko, N.G. (2020). Polyelectrolyte Polysaccharide–Gelatin Complexes: Rheology and Structure. *Polymers, 12*(2), 266. https://doi.org/10.3390/polym12020266

27 Derkach, S.R., Voron'ko, N.G., & Sokolan, N.I. (2016). The rheology of hydrogels based on chitosan–gelatin (bio)polyelectrolyte complexes. *Journal of Dispersion Science and Technology, 38*(10), 1427–1434. https://doi.org/10.1080/01932691.2016.1250218

28 Voron'ko, N.G., Derkach, S.R., Kuchina, Y.A., & Sokolan, N.I. (2016). The chitosan–gelatin (bio)polyelectrolyte complexes formation in an acidic medium. *Carbohydrate Polymers, 138*, 265–272. https://doi.org/10.1016/j.carbpol.2015.11.059

29 Podorozhko, E. A., Ul'yabaeva, G. R., Tikhonov, V. E., Kil'deeva, N. R., & Lozinsky, V. I. (2020). A Study of Cryostructuring of Polymer Systems. 53. The "Abnormal" Character of Variations in the Properties of Chitosan-Containing Composite Poly(vinyl alcohol) Cryogels upon Repeated Freezing-Defrosting. *Colloid Journal*, *82*(1), 36-48. https://doi.org/10.1134/s1061933x2001010x

30 Insua, I., Wilkinson, A., & Fernandez-Trillo, F. (2016). Polyion complex (PIC) particles: Preparation and biomedical applications. *European Polymer Journal, 81*, 198–215. https://doi.org/10.1016/j.eurpolymj.2016.06.003

31 Ramos, D.P., Sarjinsky, S., Alizadehgiashi, M., Möbus, J., & Kumacheva, E. (2019). Polyelectrolyte vs Polyampholyte Behavior of Composite Chitosan/Gelatin Films. *ACS Omega, 4*(5), 8795–8803. https://doi.org/10.1021/acsomega.9b00251

32 Feng, X., Lu, X., Huang, D., Xing, J., Feng, G., Jin, G., & Zhang, X. (2014). 3D Porous Chitosan Scaffolds Suit Survival and Neural Differentiation of Dental Pulp Stem Cells. *Cellular and Molecular Neurobiology, 34*(6), 859–870. https://doi.org/10.1007/s10571-014-0063-8

33 Zheng, K., Feng, G., Zhang, J., Xing, J., Huang, D., Lian, M., & Feng, X. (2020). Basic fibroblast growth factor promotes human dental pulp stem cells cultured in 3D porous chitosan scaffolds to neural differentiation. *International Journal of Neuroscience, 131*(7), 625–633. https://doi.org/10.1080/00207454.2020.1744592

34 Caló, E., Barros, J., Ballamy, L., & Khutoryanskiy, V.V. (2016). Poly(vinyl alcohol)–Gantrez® AN cryogels for wound care applications. *RSC Advances, 6*(107), 105487–105494. https://doi.org/10.1039/C6RA24573K

35 Tripathi, A., Vishnoi, T., Singh, D., & Kumar, A. (2013). Modulated Crosslinking of Macroporous Polymeric Cryogel Affects In Vitro Cell Adhesion and Growth. *Macromolecular Bioscience, 13*(7), 838–850. https://doi.org/10.1002/mabi.201200398

36 Plieva, F.M., Karlsson, M., Aguilar, M., Gomez, D., Mikhalovsky, S., & Galaev', I.Y. (2005). Pore structure in supermacroporous polyacrylamide based cryogels. *Soft Matter, 1*(4), 303. https://doi.org/10.1039/B510010K

37 Rinaudo, M. (2006). Chitin and chitosan: Properties and applications. *Progress in Polymer Science, 31*(7), 603–632. https://doi.org/10.1016/j.progpolymsci.2006.06.001

38 Gómez-Guillén, M., Giménez, B., López-Caballero, M., & Montero, M. (2011). Functional and bioactive properties of collagen and gelatin from alternative sources: A review. *Food Hydrocolloids, 25*(8), 1813–1827. https://doi.org/10.1016/j.foodhyd.2011.02.007

Г.Қ. Құдайберген, М.С. Жунусова

Криогельдердің қасиеттеріне температураның әсерін зерттеу

Криополимерлер дегеніміз — тіндік инженерияда кеңінен қолданылатын 3D құрылымдық полимерлер класы. Криополимерлену технологиясының көмегімен жасуша дақылдарының негізі ретінде пайдалану үшін –12 ºС, –30 ºС және –70 ºС температурада желатин мен хитозан негізіндегі физикалық тігілген макрокеуекті криогельдер синтезделді. Функционалдық топтардың болуы ИҚ-спектроскопия әдісі арқылы анықталды. Температураның криогельдердің физика-химиялық қасиеттеріне әсері зерттелді, мысалы, кеуектер көлемі, тығыздығы, гель фракциясы және биодеградациясы. Алынған нәтижелер температура –12 ºС-тан –70 ºС-қа дейін төмендеген сайын кеуектердің көлемі (87,6 %-ға дейін) және гельдік фракцияның (80 %-ға дейін) артатынын, ал криогельдер кеуектерінің өлшемі және тығыздығы (0,078 %-ге дейін) кішірейетінін көрсетті. Биодеградацияны зерттеу криополимерлену температурасының жоғарылауымен полимерлердің тұз ерітіндісіне қатысты ыдырайтын қасиеті бар екенін көрсетті. Электрондық микроскопияның нәтижелері синтезделген криогельдердің беттерінің кеуекті морфологиясын көрсетті. Кеуектің орташа мөлшері 150-ден 300 мкм-ге дейін өзгерді. Уыттылық сынағы криогельдерден алынған сулы сығындылардың егеуқұйрықтардың майлы тіндеріндегі МДЖ-ге жоғары уытты әсер етпейтінін көрсетті, өйткені жасуша өміршеңдігі 55–75 % құрады.

Кілт сөздер: криогель, желатин, хитозан, биополимер, уытты емес, биоүйлесімді, кеуекті, тін инженериясы.

Г.Қ. Құдайберген, М.С. Жунусова

Исследование влияния температуры на свойства криогелей

Криополимеры — это класс 3D структурных полимеров, которые широко используются в тканевой инженерии. С помощью технологии криополимеризации синтезированы физически сшитые макропористые криогели на основе желатина и хитозана при –12 ºС, –30 ºС и –70 ºС для применения в качестве основы клеточных культур. Наличие функциональных групп исследовано методом ИК-спектроскопии. Изучено влияние температуры на физико-химические свойства, такие как объем пор, плотность, гелевая фракция и биодеградация криогелей. Полученные результаты показывают, что при понижении температуры от –12 ºС до –70 ºС увеличиваются объемы пор (до 87,6 %) и гелевой фракции (до 80 %) и уменьшаются плотность (0,078 %) и размер пор криогелей. Исследование биодеградации показал, что при повышении температуры криополимеризации полимеры обладают более деградируемым свойством по отношению к солевому раствору. Результаты электронной микроскопии показали пористую морфологию поверхностей синтезированных криогелей. Средний размер пор варьировался от 150 до 300 мкм. Тест на токсичность показал, что водные вытяжки из криогелей не оказывают высокотоксического действия на МСК жировой ткани крыс, поскольку жизнеспособность клеток составляла 55–75 %.

Ключевые слова: криогель, желатин, хитозан, биополимер, нетоксичный, биосовместимый, пористость, тканевая инженерия.

Information about authors*

Kudaibergen, Gulshakhar Kudaibergenkyzy (*corresponding author*) — PhD of Chemistry, Senior Researcher, National Center for Biotechnology, Korgalzhyn highway 13/5, 100000, Nur-Sultan, Kazakhstan; e-mail: kudaibergen@biocenter.kz; https://orcid.org/0000-0002-0779-4099;

Zhunussova, Madina — Master of Natural Sciences, Junior Researcher, National Center for Biotechnology, Korgalzhyn highway 13/5, 100000, Nur-Sultan, Kazakhstan; e-mail: zhunussova@biocenter.kz; https://orcid.org/0000-0003-2486-093X

*The author's name is presented in the order: *Last Name, First and Middle Names*

Zh.S. Nurmaganbetov[1, 2*], S.D. Fazylov[1, 3], K.M. Turdybekov[3], O.A. Nurkenov[1, 4], D.M. Turdybekov[4], G.K. Mukusheva[3], Ye.V. Minayeva[3], G. Khabdolda[2]

[1]Institute of Organic Synthesis and Coal Chemistry of the Republic of Kazakhstan, Karaganda, Kazakhstan;
[2]Karaganda Medical University, Karaganda, Kazakhstan;
[3]Karagandy University of the name of academician E.A. Buketov, Kazakhstan;
[4]Karaganda Technical University, Karaganda, Kazakhstan
(*Corresponding author's e-mail: nzhangeldy@yandex.ru)

Synthesis and Structure of 4-Substituted (1*S*,9a*R*)-1-[(1,2,3-triazol-1-yl)methyl]octahydro-1*H*-quinolysines of Lupinine

The article presents results on the synthesis and investigation of the structural features of a number of 1,4-disubstituted 1*H*-1,2,3-triazole derivatives of the alkaloid lupinine. Lupinine modification reactions have been carried out at the hydroxymethylene group in the C-1 position of the quinolysine backbone. It has been shown that (octahydro-2*H*-quinolysine-1-ylmethyl)methanesulfonate in high yield (93%) is formed by the interaction of lupinine with methanesulfonyl chloride in methylene chloride. Subsequent treatment of this compound with sodium azide in dimethylformamide on heating leads to the formation of 1-(azidomethyl)octahydro-2*H*-quinolysine in 61% yield. It has been found that the reaction of a new azide with terminal alkynes of various nature in the presence of aqueous CuSO$_4$ and sodium ascorbate in dimethylformamide can form the corresponding 4-substituted (1*S*,9a*R*)-1-[(1,2,3-triazol-1-yl)methyl]octahydro-1*H*-quinolysines. New 1,2,3-triazole derivatives of lupinine containing various aryl substituents at the C-4 position of the triazole ring have been obtained. The high selectivity of the reaction is explained by the action mechanism of the Sharpless catalyst. The spatial structure of the molecules of lupinine methanesulfonate, 4-aryltriazolylmethyl-octahydroquinolysines has been established by X-ray diffraction analysis. X-ray structural analysis data of new compounds have been deposited in the form of CIF files at the Cambridge Crystallographic Data Center.

Keywords: quinolysine alkaloids, lupinine, azides, triazoles, methanesulfonyl chloride, terminal alkynes, 1,3-dipolar cycloaddition reaction, X-ray structural analysis.

Introduction

The products of secondary plant metabolism, namely alkaloids are promising models for studying the relationship patterns "structure-biological activity". A wide range of biological properties of their derivatives allows accumulating factual material for a databank of their structural derivatives and using them in the search for new drugs. The development of methods for the chemical modification of alkaloid compounds opens up new possibilities for the creation of original agents with specific biological activity. The alkaloid lupinine obtained from plants of the genera *Lupinus* and *Anabasis* is one of these important compounds in terms of the search for new bioactive substances [1–3]. The presence of a primary alcohol group makes it possible to obtain various modifications of lupinine derivatives [4]. Also, lupinine, having a transquinolizidine ring with an axial oxymethyl group, is able to change its configuration from trans- to cis-junction of the quinolizidine ring upon the nitrogen atom protonation [5, 6]. This leads to the transition of the axial oxymethyl group to the equatorial position with a change in the sign of the angle of rotation, which can lead to the manifestation of new types of activities.

In terms of pharmacological action, lupinine has a bactericidal, sedative effect, and short-term anthelmintic, as well as hypotensive properties [3, 4, 6]. The presence of an active hydroxyl function in the lupinine molecule makes it possible to synthesize a variety of derivatives on its basis. In [4, 5], pharmacological studies of the compound [(4-nitrobenzylidene)-imino]lupinine and [(2,4-dihydroxybenzylidene)-imino]lupinine were carried out, which showed high antibiotic activity against plague and cholera microbes. A number of lupinine esters have shown a local anesthetic effect, as well as anti-tuberculosis and anticholinesterase activity [6]. Compound 11-[(gossypolydene)-imino]lupinine has been shown to have high anti-AIDS activity [7]. Esters of lupinine [8], which have pronounced antiviral, antitumor and hepatoprotective activity,

are the most studied ones among the known lupinine derivatives [9]. Therefore, the interest in lupinine and its new derivatives continues unabated.

The synthesis and investigation of lupinine triazole derivatives is one of the poorly studied and promising directions for modifying the lupinine structure. Compounds with triazole moieties have a wide range of applications in the production of pharmaceuticals, photoactive chemicals dyes, and agricultural chemicals [10, 11]. Recently, the search for compounds with antiviral activity is an extremely urgent task due to the global COVID–19 pandemic. Particular importance is attached to the search for broad-spectrum antiviral agents capable of suppressing the replication of various viruses. Compounds with anti-HIV, anti-antiviral, and antihistaminic activity have been identified among 1,2,3-triazole derivatives; it should be noted that they also inhibit β3-adrenergic receptors selectively [12–14]. The creation of medicines on their basis that will be used in the treatment of socially significant infectious diseases of viral etiology is one of paramount tasks of modern pharmaceutical chemistry.

This work aims to synthesize 4-substituted (1*S*,9a*R*)-1-[(1,2,3-triazol-1-yl)methyl]octahydro-1*H*-quinolysines of lupinine alkaloid using the "click"-reaction technology and study the structure of new synthesized compounds by ^{1}H-, ^{13}C- and two-dimensional NMR spectra, namely COSY (^{1}H-^{1}H) and HMQC (^{1}H-^{13}C), as well as X-ray analysis.

Experimental

IR spectra were recorded on a Vector-22 Fourier spectrometer in KBr pellets. ^{1}H and ^{13}C NMR spectra were recorded on a Bruker AV-400 (400 and 101 MHz, respectively) and Bruker DRX-500 (500 and 125 MHz, respectively) spectrometers. The compounds spectra were recorded in CDCl$_3$, the signal of which (δ_C=76.9 ppm) and the residual signal of CHCl$_3$ (δ_H=7.24 ppm) were used as an internal standard.

The structure of the obtained compounds was established by analyzing the ^{1}H and ^{13}C NMR spectra, the signal multiplicity in the ^{13}C NMR spectra was determined from the spectra recorded in the J-modulation mode (JMOD). The signals assignment in the spectra was carried out applying various correlation spectroscopy ^{1}H-^{1}H (COSY), and ^{1}H-^{13}C (HMBC, HSQC) using literature data for the quinolysine backbone. When describing the spectra, we used the numbering of the core atoms given in structure (**1**). Specific rotation values were measured on a PolAAr 3005 polarimeter. High-resolution mass spectra were recorded on a DFS Thermo Scientific mass spectrometer (evaporator temperature 200–250 °C, EI ionization, 70 eV). Melting points were determined on a Mettler Toledo FP900 thermosystem. X-ray structural analysis of compounds (**2**, **5a**, **5b**) was carried out on an Xcalibur, Ruby diffractometer with a CCD detector (CuKα radiation, graphite monochromator, λ 1.54184 Å, ω-scanning). Processing of the initial array of measured intensities and the absorption was carried out using the CrysAlisPro software (multi-scan) [15].

The structure was solved by a direct method. The positions of non-hydrogen atoms were refined in the anisotropic approximation using full-matrix least squares. Hydrogen atoms were placed in geometrically calculated positions and their positions were refined in the isotropic approximation with fixed positional and thermal parameters ("rider" model). The structures were determined by a direct method and refined using the SHELXS-2014 and SHELXL-2014 software packages [16]. Spectral-analytical studies were carried out at the Chemical Service Center for Collective Use of the Siberian Branch of the Russian Academy of Sciences.

The reaction progress was monitored by TLC on Sorbfil UV-254 plates using chloroform, chloroform – ethanol, 10:1 systems. Detection was carried out in an iodine chamber and in UV light. The reaction products were isolated by recrystallization or using column chromatography on Acros silicagel (0.035–0.240 mm), eluents CHCl$_3$; CHCl$_3$ – EtOH, 100:1 → 10:1).

The reagents used in the work were sodium azide, 4-methoxyphenylacetylene (**4a**), *m*-tolylacetylene (**4b**). They were purchased from Alfa Aesar. Solvents (chloroform, DMF) and Et$_3$N were purified according to standard methods; DMF was additionally distilled in a stream of argon immediately before carrying out the reactions.

(Octahydro-2H-quinolysine-1-ylmethyl)methanesulfonate (**2**). A solution of methanesulfonyl chloride (4.8 g, 42 mmol) in 20 ml of CH$_2$Cl$_2$ was added dropwise to an ice bath-cooled solution of lupinine (**1**) (3.54 g, 21 mmol) and triethylamine (6.36 g, 63 mmol) in CH$_2$Cl$_2$ (200 ml). The reaction mixture was stirred for 30 min while cooling to 0°C and for 6 h at room temperature, then washed with saturated sodium chloride solution (2×20 ml), dried over anhydrous MgSO$_4$, the drying agent was filtered off; the solvent was distilled off in a vacuum. The residue was chromatographed on a silicagel column (chloroform, chloroform-ethanol, 50:1). Yield was 4.84 g (93%). Cream crystals are obtained; m.p. is 57–58 °C (from ether). [α]$_D^{25}$ –21.6 (c 1.4, CHCl$_3$). IR spectrum (KBr), ν, cm^{-1}: 1184, 1336 (OSO$_2$), 2740, 2757, 2798 (quinolizidine).

^{1}H NMR spectrum (400 MHz, CDCl$_3$), δ, ppm (J, Hz): 1.12–1.26 (1H, m, H-2a); 1.28-1.51 (5H, m, H-2e, 8a, 8e, 3a, 7a); 1.54 (1H, m, H-9a); 1.59-1.77 (2H, m, H-3e, 7e); 1.84-2.02 (5H, m, H-1.4a, 6a, 9e, 9a); 2.73-2.80 (2H, m, H-4e, 6e); 2.97 (3H, s, CH$_3$); 4.37 (1H, dd, J = 10.6, J = 9.8, H-10); 4.47 (1H, dd, J = 10.6, J = 5.3, H-10). ^{13}C NMR spectrum (101 MHz, CDCl$_3$), δ, ppm: 20.6 (C-3); 24.7; 25.4 C-7.8); 26.3 (C-2); 29.8 (C-9); 37.0 (CH$_3$); 38.0 (C-1); 56.8; 57.1 (C-4.6); 64.0 (C-9a); 69.5 (C-10). Mass spectrum, m/z (I, %): 248 (1), 247 (7), 153 (10), 152 (100), 150 (3), 98 (6). Found, m/z: 247.1238 [M]$^+$. C$_{11}$H$_{21}$NO$_3$S. Calculated, m/z: 247.1237.

X-ray structural study of compound (**2**). Table 1 presents the main crystallographic data and characteristics of the X-ray diffraction experiment. The XRD data in the form of a CIF file were deposited at the Cambridge Crystallographic Data Center (deposit CCDC 2087144).

1-(Azidomethyl)octahydro-2H-quinolysine (**3**). A mixture of compound (**2**) (4.84 g, 20 mmol) and sodium azide 3.44 g (53 mmol) in DMF (50 ml) was stirred at 70 °C for 5 h (TLC control). After the end of the reaction, the solvent was removed from the reaction mixture, the residue was dissolved in CH$_2$Cl$_2$, washed with a saturated sodium chloride solution, dried over anhydrous MgSO$_4$, the desiccant was filtered, the solvent was distilled in vacuum, the residue was chromatographed on a column with silicagel (chloroform-ethanol, 50:1). Yield was 2.33 g (60%). Light yellow mobile liquid was obtained. [α]$_D^{26}$ –29.85 (s 2.4, chloroform). IR spectrum, ν, cm^{-1}: 1269, 2096 (N≡N), 2744, 2762, 2804 (quinolizidine). ^{1}H NMR spectrum (400 MHz, CDCl$_3$), δ, ppm (J, Hz): 1.12–1.26 (1H, m, H-2a); 1.30-1.57 (6H, m, H-8a, 8e, 9a, 9e, 3a, 7a); 1.58-1.76 (3H, m, H-2e, 3e, 7e); 1.80-1.99 (4H, m, H-1.4a, 6a, 9a); 2.72-2.82 (2H, m, H-4e, 6e); 3.42 (1H, dd, J = 12.6, J = 9.6, CH$_2$-10); 3.54 (1H, dd, J = 12.6, J = 5.3, CH$_2$-10). ^{13}C NMR spectrum (125 MHz, CDCl$_3$), δ, ppm: 20.7 (C-3); 24.9 (C-8); 25.4 (C-7); 27.3 (C-2); 29.6 (C-9); 38.2 (C-1); 50.4 (C-10); 56.8; 57.2 (C-4.6); 64.3 (C-9a). Mass spectrum, m/z (I, %): 194 (2), 153 (10), 152 (100), 137 (7), 136 (5), 98 (12), 84 (7), 83 (9), 82 (6), 55 (10), 41 (14). Found, m/z: 194.1528 [M]$^+$. C$_{10}$H$_{18}$N$_4$. Calculated, m/z: 194.1526.

Synthesis of compounds (**5a,b**) *(General method).* A mixture of azide (**3**) (0.29 g, 1.5 mmol), substituted acetylene (**4a,b**) (1.35 mmol), CuSO$_4$×5H$_2$O (0.017 g, 0.0675 mmol) and sodium ascorbate (0.013 g, 0.0675 mmol) in DMF (4 ml) was stirred at 75°C for 4-6 h (TLC control). The precipitate formed upon cooling was filtered off, washed with hexane, and dried to obtain triazoles (**5a,b**). The solvent was distilled off in vacuum to isolate triazoles (**5a,b**); the residue was chromatographed on a silicagel column (eluent chloroform, mixture of chloroform with ethanol, 100:1 → 10:1).

(1S,9aR)-1-{[4-(4-Methoxyphenyl)-1H-1,2,3-triazole-1-yl]methyl}octahydro-1H-quinolysine (**5a**). Yield was 0.35 g (83 %). There are obtained white crystals; m.p. was 177–178 °C (from ethyl acetate). [α]$_D^{26}$ –16.9 (c 0.8, chloroform). IR spectrum, ν, cm^{-1}: 829, 920, 1443, 1458, 1498, 1560, 1618, 3097 (C=C, C=N); 1008, 1132, 1246 (C–O); 2761, 2804 (quinolizidine). ^{1}H NMR spectrum (400 MHz, CDCl$_3$), δ, ppm (J, Hz): 1.17–1.40 (3H, m, H-2a, 2e, 8a); 1.40–1.64 (5H, m, H-8e, 9a, 9e, 3a, 7a); 1.73–1.90 (2H, m, H-3e, 7e); 1.92–2.05 (2H, m, H-4a, 6a); 2.06-2.10 (1H, m, H-9a), 2.22–2.26 (1H, m, H-1); 2.83–2.88 (2H, m, H-4e, 6e); 3.81 (3H, s, OCH$_3$); 4.54 (1H, dd, J = 13.8, J = 5.5, H-10); 4.60 (1H, dd, J = 13.8, J = 12.5, H-10); 6.92 (2H, d, J = 8.6, H-3″, 5″); 7.61 (1H, s, H-5′); 7.73 (2H, d, J = 8.6, H-2″, 6″). ^{13}C NMR spectrum (101 MHz, CDCl$_3$), δ, ppm: 20.5 (C-3); 24.7; 25.4 (C-7.8); 26.1 (C-2); 29.5 (C-9); 39.1 (C-1); 48.4 (C-10); 55.2 OCH$_3$); 56.9; 57.2 (C-4.6); 64.3 (C-9a); 114.1 (C-3″, 5″); 119.3 (C-5′); 123.3 (C-1″); 126.8 (C-2″, 6″); 147.2 (C-4′); 159.4 (C-4″). Mass spectrum, m/z (I, %): 328 (1), 327 (12), 226 (49), 152 (42), 151 (100), 150 (66), 138 (18), 137 (14), 136 (33), 111 (18), 96 (17), 83 (25), 41 (150). Found, m/z: 326.2100 [M]$^+$. C$_{19}$H$_{26}$N$_4$O. Calculated, m/z: 326.2101.

X-ray structural study of compound (**5a**). The main crystallographic data and characteristics of the X-ray diffraction experiment are presented in Table 1. The XRD data in the form of a CIF file were deposited at the Cambridge Crystallographic Data Center (deposit CCDC 2087145).

(1S,9aR)-1-{[4-(m-Tolyl)-1H-1,2,3-triazole-1-yl]methyl}octahydro-1H-quinolysine (**5b**). Yield was 0.52 g (80 %). There were obtained white crystals; m.p. was 141–142 °C (from ethyl acetate). [α]$_D^{26}$ –13.8 (c 1.0, chloroform). IR spectrum, ν, cm^{-1}: 694, 791, 846, 1443, 1464, 1487, 1614, 3122 (C=C, C=N); 2763, 2804 (quinolizidine). ^{1}H NMR spectrum (500 MHz, CDCl$_3$), δ, ppm (J, Hz): 1.20–1.40 (3H, m, H-2a, e, 8a); 1.41–1.63 (5H, m, H-8 e, 9a, 9e, 3a, 7a); 1.74–1.91 (2H, m, H-3e, 7e); 1.94–2.02 (2H, m, H-4a, 6a); 2.06–2.09 (1H, m, H-9a), 2.22–2.26 (1H, m, H-1); 2.37 (3H, s, CH$_3$); 2.83–2.88 (2H, m, H-4e, 6e); 4.56 (1H, dd, J = 13.8, J = 5.8, H-10); 4.61 (1H, dd, J = 13.8, J = 11.2, H-10); 7.11 (1H, d, J = 7.5, H-4″); 7.27 (1H, t, J = 7.5, H-5″); 7.58 (1H, dd, J = 7.5, J = 1.6, H-6″); 7.66 (1H, s, H-5′); 7.72 (1H, d, J = 1.6, H-2″). ^{13}C NMR spectrum (125 MHz, CDCl$_3$), δ, ppm: 20.5 (C-3); 21.3 (CH$_3$); 24.7; 25.4 (C-7.8); 26.2 (C-2); 29.6 (C-9); 39.1 (C-1); 48.5 (C-10); 56.91; 57.2 (C-4.6); 64.3 (C-9a); 120.0 (C-5′); 122.7; 126.2; 128.5; 128.6 (C-2″, 4″, 5″,

6″); 130.5 (C-1″); 138.3 (C-3″); 147.5 (C-4′). Mass spectrum, m/z (I, %): 312 (1), 311 (9), 310 (42), 152 (28), 151 (100), 150 (52), 138 (15), 136 (35), 83 (20). Found, m/z: 310.2155 [M]$^+$. $C_{19}H_{26}N_4$. Calculated, m/z: 310.2152.

Results and Discussion

In this work, we describe the synthesis of lupinyl azide (**3**) and an unknown group of quinolysine alkaloids derivatives containing a 1,2,3-triazole substituent. The synthesis of triazoles (**5a**) and (**5b**) was carried out by the reaction of 1,3-dipolar addition according to Huesgen in the presence of a Sharpless catalyst, which is a sodium ascorbate – copper (II) sulfate system. This method is convenient because the addition of acetylene to an azide leads to the formation of 1,4-substituted triazoles, while a mixture of 1,4- and 1,5-isomers is formed during thermal cyclization [17].

When lupinine (**1**) interacts with methanesulfonyl chloride in the presence of triethylamine in methylene chloride, (octahydro-2*H*-quinolysine-1-ylmethyl)methanesulfonate (**2**) is formed smoothly upon cooling (yield is 93 %). Treatment of compound (**2**) with NaN$_3$ in DMF medium upon heating led to the formation of 1-(azidomethyl)octahydro-2*H*-quinolysine (**3**), which was isolated in 61 % yield as a result of column chromatography in silicagel.
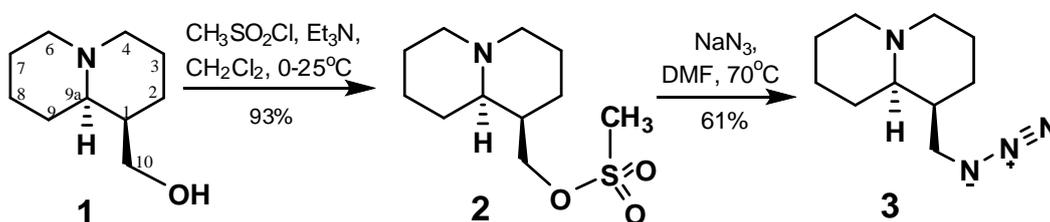
The reaction of lupinylazide (**3**) with arylalkynes [4-methoxyphenylacetylene (**4a**), *m*-tolylacetylene (**4b**)] proceeded smoothly in DMF in the presence of copper sulfate CuSO$_4$×5H$_2$O and sodium ascorbate (NaAsc) upon heating to 75 °C (TLC control). (1*S*,9a*R*)-1-[(1,2,3-triazole-1-yl)methyl]octahydro-2*H*-quinolysines (**5a, b**), containing aryl substituents at C-4 position of 1,2,3-triazole ring, were isolated by the column chromatography on silicagel.

4a, **5a**: R^1 = R^3 = H, R^2 = OCH$_3$;

4b, **5b**: R^1 = CH$_3$, R^2 = R^3 = H
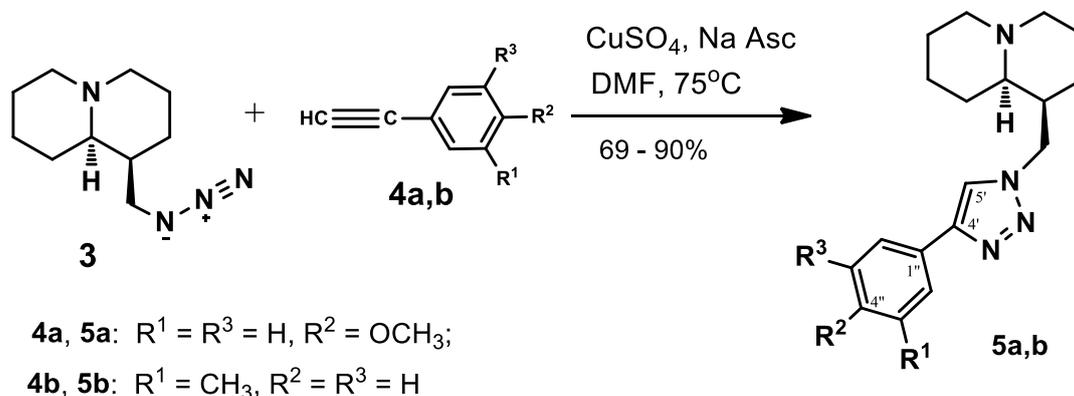
The high selectivity can be explained by the mechanism of this addition. The principle of the Sharpless catalyst operation is that the resulting monovalent copper, when reacted with acidic terminal acetylene, gives acetylene, which selectively coordinates with azides to form 1,4-substituted triazole ("click" reaction technology) [17, 18].

The composition and structure of the synthesized compounds were confirmed by IR, ^{1}H and ^{13}C NMR spectroscopy, mass spectrometry, and X-ray diffraction data. The presence of an azide substituent in structure (**3**) was confirmed by the IR spectrum data (an intense absorption band at 2096 cm^{-1}, corresponding to the stretching vibrations of the azide group).

The ^{1}H and ^{13}C NMR spectra of the synthesized quinolysine 1,2,3-triazoles contain a characteristic set of signals from the quinolysine backbone and the corresponding substituent. In the high-field region (δ 1.17–

1.70 ppm), there are broad multiplet signals with an integrated intensity of 8H, which include protons of the lupinine core of both axial and equatorial orientations (H-2*a,e*, 8*a,e*, 9*a,e*, 3*a*, 7*a*).

The multiplet signal (δ 1.70–1.92 ppm) belongs to the equatorially oriented protons H-3,7. Then the axial protons 4, 6 (δ 1.88–2.08 ppm), the nodal proton 9a (δ 2.05–2.18 ppm), and the C-1 proton (δ 2.18–2.30 ppm) resonate. Equatorial protons 4, 6 are represented by a narrow multiplet in the range of δ 2.80–2.88 ppm. The protons of the H-10 methylene group resonate in the form of two doublets in the range of δ 4.51–4.65 ppm. The proton of 1,2,3-triazole rings in the ^{1}H NMR spectra of compounds (**5a,b**) corresponds to a singlet signal located in the range of δ 7.37–7.71 ppm. The carbon atoms of the triazole ring in the ^{13}C NMR spectra correspond to signals at 119.3–122.4 (C-5) and 146.2–156.8 ppm (C-4) doublet and singlet, respectively (recording of the spectra in the JMOD mode). These data confirm the formation of 1,4-disubstituted 1*H*-1,2,3-triazoles as a result of the CuAAC reaction.

The mass spectra of all compounds contain peaks of molecular ions of various intensities. In the spectra of all synthesized quinolizidinotriazoles (**5a,b**), there is a peak of the fragmentary $C_{10}H_{17}N$ ion (150–151 a.u.), corresponding to the cleavage of the molecule at the C-10 atom of the quinolizidine backbone.

The spatial structure of (octahydro-2*H*-quinolysine-1-ylmethyl)methanesulfonate (**2**) and 1-[(4-aryl-1,2,3-triazol-1-yl)methyl]octahydro-1*H*-quinolysines (**5a**) and (**5b**) established by the X-ray diffraction method is shown in Fig. 1–3, respectively.
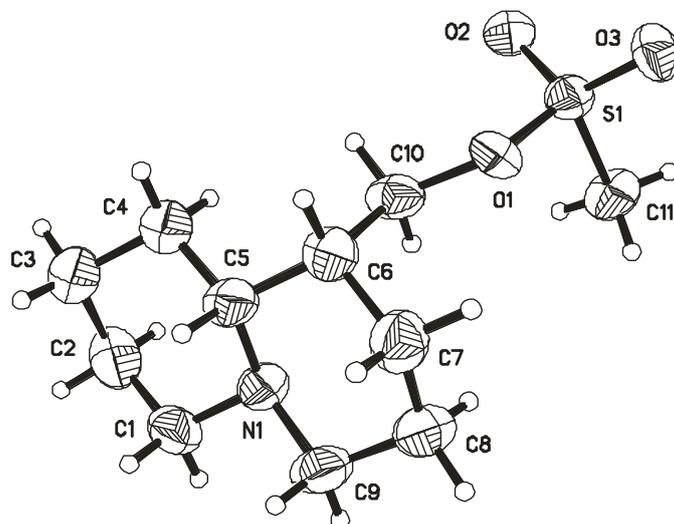
Figure 1. Structure of (octahydro-2*H*-quinolysine-1-ylmethyl)methanesulfonate (**2**)
(thermal vibration ellipsoids are shown with a probability of 30%)
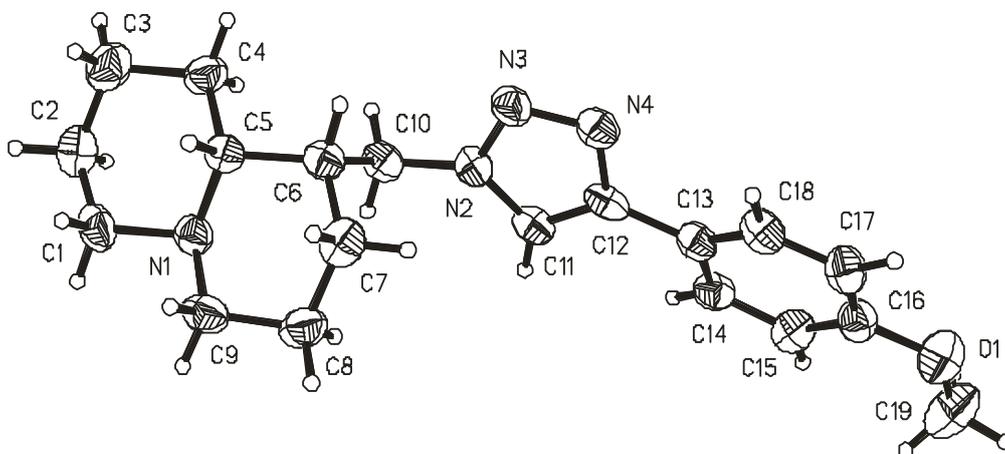
Figure 2. The structure of (1*S*,9a*R*)-1-{[4-(4-methoxyphenyl)-1*H*-1,2,3-triazol-1-yl]methyl}octahydro-2*H*-quinolysine (**5a**) (thermal vibration ellipsoids are shown with a probability of 30%)
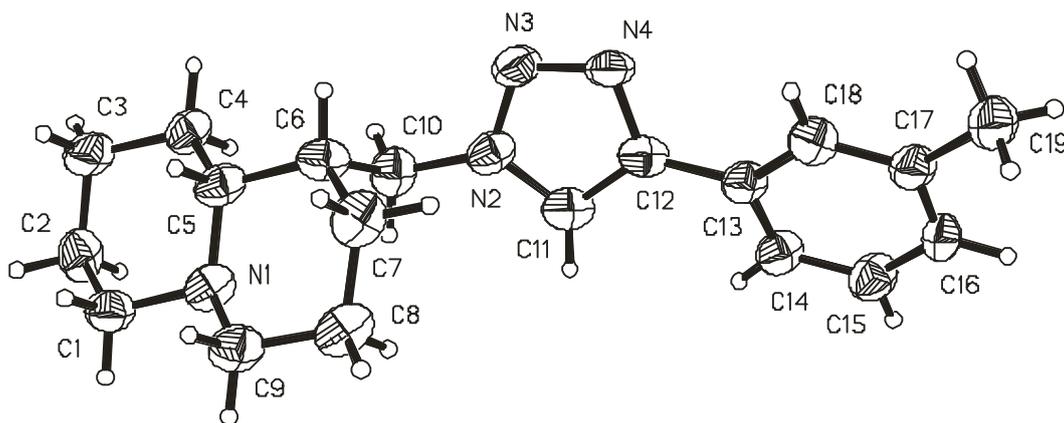
Figure 3. The structure of (1*S*,9a*R*)-1-{[4-(*m*-tolyl)-1*H*-1,2,3-triazole-1-yl]methyl}octahydro-1*H*-quinolysine (**5b**) (thermal vibration ellipsoids are shown with a probability of 30%)

The configurations of the C5 and C6 chiral centers are correlated with the absolute one in the crystal structure of lupinine chloride [19]. It follows from the obtained data that the bond lengths and bond angles in compounds (**2**), (**5a**), and (**5b**) are close to the usual ones [20]. The conformations of the six-membered rings N1, C1… C5 (A) and N1, C5… C9 (B) in the quinolizidine framework in compounds (**2**), (**5a**), and (**5b**) are close to those in the crystal structure of lupinine [19, 20]. Data on intracyclic torsion angles and parameters of asymmetry of cycles [19] are given in Table 1. Cycles A and B in two crystallographically independent molecules (**2-1**) and (**2-2**) of compound (**2**) as well as (**5a-1**) and (**5a-2**) of compound (**5a**), are in a conformation close to a somewhat distorted chair as in molecule (**5b**).

In crystal (**2**), molecules (**2-1**) and (**2-2**) have different orientations of the sulfonyl group, namely the C5-C6-C10-O1 torsion angles are 177 and 76°, respectively. In two independent crystal molecules (**5a**) and in crystal (**5b**), the orientation of the 1,2,3-triazole ring is the same, namely the C6-C10-N2-N3 torsion angles are 53, 63, and 58°, respectively. The 1,2,3-triazole and phenyl rings in the molecules of compounds (**5a**) and (**5b**) are planar with an accuracy of no more than ± 0.013 Å. The angles between the planes of the triazole and aryl substituents are 23 and 21° in crystal (**5a**) and 27° in crystal (**5b**).

T a b l e 1

Intracyclic torsion angles (τ, deg.) in compounds (2), (5a) and (5b)

Compound	(2-1)	(2-2)	(5a-1)	(5a-2)	(5b)	Lupinine
Angle				τ		
Cycle N1-C1-C2-C3-C4-C5 (A)						
N1-C1-C2-C3	−58(2)	−59(2)	−57(1)	−58(1)	−58(2)	−56.2
C1-C2-C3-C4	55(2)	58(2)	56(1)	55(1)	56(2)	52.9
C2-C3-C4-C5	−55(2)	−57(2)	−57(1)	−57(1)	−57(2)	−54.3
C3-C4-C5-N1	56(2)	54(1)	59(1)	60(1)	58(2)	56.7
C4-C5-N1-C1	−54(2)	−52(1)	−58(1)	−60(1)	−59(1)	−57.8
C5-N1-C1-C2	57(2)	55(2)	58(1)	60(1)	60(1)	58.9
Asymmetry parameter (ΔC_{min}, deg.)	ΔC_s^1=1.0 $\Delta C_2^{1,2}$=1.5	ΔC_s^2=1.7 $\Delta C_2^{2,3}$=1.6	ΔC_s^2=1.0 $\Delta C_2^{2,3}$=0.7	ΔC_s^3=1.6 $\Delta C_2^{2,3}$=0.7	ΔC_s^3=0.8 $\Delta C_2^{3,4}$=1.6	ΔC_s^3=1.1 $\Delta C_2^{2,3}$=2.1
Cycle N1-C5-C6-C7-C8-C9 (B)						
C9-N1-C5-C6	55(2)	58(1)	57(1)	60(1)	59(1)	56.5
N1-C5-C6-C7	−54(2)	−59(1)	−55(1)	−56(1)	−57(1)	−54.5
C5-C6-C7-C8	54(2)	57(2)	54(1)	55(1)	54(2)	53.6
C6-C7-C8-C9	−55(2)	−53(2)	−57(1)	−57(1)	−53(2)	−54.9
C7-C8-C9-N1	58(2)	55(2)	59(1)	61(1)	56(2)	58.1
C5-N1-C9-C8	−58(2)	−59(2)	−60(1)	−62(1)	−59(2)	−58.9
Asymmetry parameter (ΔC_{min})	ΔC_s^6=0.0 $\Delta C_2^{5,6}$=2.2	ΔC_s^5=1.7 $\Delta C_2^{7,8}$=1.4	ΔC_s^6=0.8 $\Delta C_2^{6,7}$=2.0	ΔC_s^6=1.9 $\Delta C_2^{6,7}$=1.0	ΔC_s^7=0.8 $\Delta C_2^{7,8}$=2.0	ΔC_s^6=1.2 $\Delta C_2^{6,7}$=1.2

Table 2 presents the main crystallographic data and characteristics of the X-ray diffraction experiment of compounds (**2**), (**5a**) and (**5b**) . The X-ray structural analysis data were deposited in the form of a CIF file at the Cambridge Crystallographic Data Center (deposit CCDC 2087146).

T a b l e   2

Crystallographic data and characteristics of an X-ray diffraction experiment for compounds (2), (5a) and (5b)

Compound	(**2**)	(**5a**)	(**5b**)
Molecular formula	$C_{11}H_{21}NO_3S$	$C_{38}H_{52}N_8O_2$	$C_{19}H_{26}N_4$
M	247.35	652.87	309.43
Syngonia	Triclinic	Monoclinic	Monoclinic
T, K	293	293	293
a, Å	5.435(3)	5.5545(5)	19.692(4)
b, Å	8.766(3)	17.804(2)	5.6186(9)
c, Å	14.395(5)	17.840(2)	16.185(3)
α, degrees	97.90(3)	90	90
β, degrees	98.95(4)	98.95(4)	104.80(2)
γ, degrees	103.60(4)	90	90
V, Å^3; Z	647.6(5); 2	1762.6(3); 2	1731.4(6); 4
Space group	P1	P2$_1$	I2
$D_{calc.}$, g/cm^3	1.268	1.230	1.191
μ, mm^{-1}	2.180	0.618	0.558
Number of measured reflections	3594	7368	7134
Number of independent reflections	2746 R(int) = 0.0826)	5281 (R(int) = 0.0939)	3358 (R(int) = 0.0203)
Reflections observed (I≥2σ(I))	1493	3088	1225
Number of refined parameters	292	436	210
T_{min}, T_{max} (multiscan)	0.38568, 1.00000	0.92224, 1.00000	0.37817, 1.00000
F(000)	268	704	284
Area θ, degrees	$5.279 \leq \theta \leq 76.035$	$3.509 \leq \theta \leq 76.092$	$2.916 \leq \theta \leq 27.934$
R_1, $_wR_2$ ($I \geq 2\sigma(I)$)	0.0826, 0.1956	0.0935, 0.2264	0.1080, 0.2861
R_1, $_wR_2$ (whole array)	0.1269, 0.2444	0.1333, 0.2786	0.1968, 0.3817
GooF	0.963	1.057	0.983
$\Delta\rho_{max}$, $\Delta\rho_{min}$, e/Å^3	0.298, -0.624	0.411, -0.209	0.261, -0.226

Conclusions

In this work, the optimal conditions for the modification of the structure of the alkaloid lupinine at the hydroxymethylene group C-1 of the quinolizidine backbone have been proposed and developed. As a result of these studies, potentially bioactive 1,2,3-triazole derivatives of lupinine have been obtained for the first time in high yields. The application of the "click"-reaction technique allowed the synthesis of lupinine azide and its 1,3-dipolar [3+2]-cycloaddition to various alkynes.

The reactions were carried out in the presence of an aqueous solution of $CuSO_4$ and sodium ascorbate in DMF. The developed conditions allowed the corresponding 4-substituted (1*S*,9a*R*)-1-[(1,2,3-triazol-1-yl)methyl]octahydro-2*H*-quinolysines to be synthesized in good yields. New synthesized lupinine derivatives with a 1,2,3-triazole fragment can provide additional ligand-receptor interactions of a biologically active substrate and thereby change the selectivity of the substrate biological action. The complex use of modern physicochemical methods, namely one-dimensional ^{1}H-, ^{13}C- NMR spectra and two-dimensional COSY (^{1}H-^{1}H) and HMQC (^{1}H-^{13}C) spectra, as well as XRD analysis made it possible to unambiguously establish the structure of the new 4-substituted (1*S*,9a*R*)-1-[(1,2,3-triazol-1-yl)methyl]octahydro-1*H*-quinolysines of lupinine. X-ray structural analysis data for synthesized compounds were deposited as CIF files at the Cambridge Crystallographic Data Center (CCDC deposit for **2** is 2087144, for **5a** is 2087145, for **5b** is 2087146).

Acknowledgments

References

1 Michael J.P. Indolizidine and quinolizidine alkaloids / J.P. Michael // Nat. Prod. Rep. — 2008. — Vol. 25. — P. 139–165. https://doi.org/10.1039/b612166g

2 Romeo F.V. Characterization and Antimicrobial Activity of Alkaloid Extracts from Seeds of Different Genotypes of Lupinus spp. / F.V. Romeo, S. Fabroni, G. Ballistreri, S. Muccilli, A. Spina, P. Rapisarda // Sustainability. — 2018. — Vol. 10, No. 3. — P. 788–799. https://doi.org/10.3390/su10030788

3 Tuzimski T. Application of HPLC-DAD for In Vitro Investigation of Acetylcholinesterase Inhibition Activity of Selected Isoquinoline Alkaloids from Sanguinaria Canadensis Extracts / T. Tuzimski, A. Petruczynik // Molecules. — 2021. — Vol. 26. — P. 1–13. https://doi.org/10.3390/molecules26010230

4 Газалиев А.М. Новые биоактивные производные алкалоидов / А.М. Газалиев, М.Ж. Журинов, С.Д. Фазылов. — Алма-Ата: Ғылым, 1992. — 208 с.

5 Тлегенов Р.Т. Синтез 8-бензодиоксановых азометинов алкалоида лупинина / Р.Т. Тлегенов // Химия природных соединений. — 2007. — № 4. — С. 407, 408. https://doi.org/10.1007/s10600-007-0176-0

6 Абдувахабов А.А. Лупинин / А.А. Абдувахабов, Д.Н. Далимов, К.У. Утениязов, Х.А. Асланов. — Нукус, 1993. — 198 с.

7 Нуркенов О.А. Синтез, строение и свойства новых O-ацилпроизводных алкалоида лупинина / О.А. Нуркенов, Ж.С. Нурмаганбетов, С.Д. Фазылов, Ж.Б. Сатпаева, К.М. Турдыбеков, Т.М. Сейлханов, С.А. Талипов // Химия природных соединений. — 2019. — № 3. — С. 434–436. https://doi.org/10.1007/s10600-019-02726-3

8 Тлегенов Р.Т. Синтез новых диалкиламиноуксусных эфиров алкалоида лупинина / Р.Т. Тлегенов // Химия и химическая технология. — 2007. — Т. 50, № 12. — С. 125–127.

9 Тилябаев З. Синтез фосфорилированных производных алкалоидов, их структура, биологическая активность и перспективы практического использования / З. Тилябаев, М.Б. Гафуров, Д.Н. Далимов, А.А. Абдувахабов. — Ташкент: ФАН, 2017. — 185 с.

10 Nurkenov O.A. Study of supramolecular inclusion complexes of pseudoephedrine, lupinine, anabasine and cytisine with beta-cyclodextrin by NMR spectroscopy / O.A. Nurkenov, T.M. Seilkhanov, S.D. Fazylov, A.Z. Issayeva, O.T. Seilkhanov, L.M. Vlasova // Bulletin of the University of Karaganda – Chemistry. — 2019. — Vol. 94. — P. 19–28. https://doi.org/10.31489/2019Ch2/19-28

11 Криволапов В.П. 1,2,3-Триазол и его производные. Развитие методов формирования триазольного кольца / В.П. Криволапов, О.П. Шкурко // Успехи химии. — 2005. — Т. 74, № 4. — С. 369–410. https://doi.org/10.1070/RC2005v074n04ABEH000893

12 Косенко И.Д. Синтез 1,4-дизамещенных 1,2,3-триазолов на основе бис(1,2-дикарболлид)кобальта // И.Д. Косенко, И.А. Лобанова, Л.А. Чекулаева, И.А. Годовиков, В.И. Брегадзе // Изв. АН. Сер. хим. — 2013. — № 2. — С. 497–503. https://doi.org/10.1007/s11172-013-0069-2

13 Katritzky A.R. 1,2,3-Triazole formation under mild conditions via 1,3-dipolar cycloaddition of acetylenes with azides / A.R. Katritzky, Y. Zhang, S.K. Singh // Heterocycles. — 2003. — Vol. 60, No. 5. — P. 1225–1239. https://doi.org/10.3987/REV-02-562

14 Tornoe C.W. Peptidotriazoles on solid phase: 1,2,3-triazoles by regiospecific copper (I)-catalyzed 1,3-dipolar cycloadditions of terminal alkynes to azides / C.W. Tornoe, C. Christensen, M. Mendal // J. Org. Chem. — 2002. — 67. — P. 3057–3064. https://doi.org/10.1021/jo011148j

15 Koziol A.E. Structure of the alkaloid lupinine / A.E. Koziol, Z. Kosturkiewicz, H. Podkowinska // Acta crystallogr. — 1978. — Vol. 34. — P. 3491–3494.

16 Duax W.L. Atlas of Steroid Structure / W.L. Duax, D.A. Norton. — New-York: IFI/Plenum, 1975. — P. 18.

17 Каторов Д.В. Синтез энергоемких производных 1,2,3-триазолов из α-нитроазидов / Д.В. Каторов, А.В. Якушков, Г.Ф. Рудаков, В.Ф. Жилин // Успехи в химии и химической технологии. — 2007. — Т. 21, № 5. — С. 20–23.

18 Бакулев В.А. NH-1,2,3-триазолы: синтез и реакции с электрофильными реагентами / В.А. Бакулев, Т.В. Березкина // Химия гетероциклических соединений. — 2016. — Т. 52, № 1. — С. 4–6. https://doi.org/10.1007/s10593-016-1821-y

19 Koziol A.E. Structure of (-)-lupinine / A.E. Koziol, M. Gdaniec, Z. Kosturkiewicz // Acta Crystallogr. — 1980. — Vol. 36. — P. 980–981.

20 Allen F.H. Tables of bond lengths determined by X-ray and neutron diffraction / F.H. Allen, O. Kennard, D.G. Watson, L. Brammer, A.G. Orpen, R. Taylor // J. Chem. Soc. Perkin Trans. — 1987. — Vol. 2. — P. 1–19.

Ж.С. Нұрмағанбетов, С.Д. Фазылов, Қ.М. Тұрдыбеков, О.А. Нүркенов,
Д.М. Тұрдыбеков, Г.К. Мұқышева, Е.В. Минаева, Г. Хабдолда

Лупининнің 4-орынбасылған (1*S*,9*a*R)-1-[(1,2,3-триазол-1-ил)метил]-октагидро-1*H*-хинолизиндерінің синтезі және құрылысы

Мақалада лупинин алкалоидының 1,4-алмастырылған 1*H*-1,2,3-триазол туындылары қатарының синтездеу және рентгендік құрылымдық ерекшеліктерін зерттеу нәтижелері келтірілген. Лупинин алкалоидының химиялық модификациясы хинолизин қаңқасының С-1 орналасқан гидроксиметилен тобы бойынша жүзеге асырылды. Реакциялар бірнеше кезеңде жүргізілді. Лупининнің метансульфохлоридпен хлорлы метиленде триэтиламин қатысуымен өзара әрекеттесуі кезінде жоғары шығымдылығы бар (93 %) (октагидро-2*H*-хинолизин-1-илметил)метансульфонат оңай түзілетіні көрсетілген. Осы қосылысты диметилформамид ерітіндісінде натрий азидімен ары қарай қыздырып өңдеу нәтижесінде 61% шығыммен 1-(азидометр)октагидро-2*H*-хинолизиннің түзілуі жүреді. Жаңа азидтің сулы CuSO$_4$ және натрий аскорбаты қатысуымен диметилформамид ерітіндісінде әртүрлі сипаттағы терминалдық алкиндермен өзара әрекеттесуі кезінде сәйкес 4-алмастырылған (1*S*,9*aR*)-1-[(1,2,3-триазол-1-ил)метил]октагидро-1*H*-хинолизиндер түзілуі мүмкін екендігі анықталды. Триазол циклінің С-4 жағдайында әртүрлі арил алмастырғыштары бар лупининнің жаңа 1,2,3-триазол туындылары алынды. Реакцияның жоғары селективтілігі Шарплес катализаторының әсер ету механизмімен түсіндіріледі. Рентгенқұрылымдық талдау әдісімен лупинин метансульфонаты, 4-арилтриазолилметил-октагидрохинолизиндер молекулаларының кеңістіктік құрылымы анықталды. CIF файлдары түріндегі жаңа қосылыстарды рентгенқұрылымдық талдау деректері Кембридждегі кристаллқұрылымдық деректер орталығында сақталған.

Кілт сөздер: хинолизинді алкалоидтар, лупинин, азидтер, триазолдар, метансульфонил хлориді, терминалды алкиндер, 1,3-диполярлы циклоқосылу реакциясы, РҚА.

Ж.С. Нурмаганбетов, С.Д. Фазылов, К.М. Турдыбеков, О.А. Нуркенов,
Д.М. Турдыбеков, Г.К. Мукушева, Е.В. Минаева, Г. Хабдолда

Синтез и строение 4-замещенных (1*S*,9a*R*)-1-[(1,2,3-триазол-1-ил)метил]октагидро-1*H*-хинолизинов лупинина

В статье приведены результаты исследований по синтезу и рентгеноструктурному исследованию особенностей строения ряда 1,4-дизамещенных 1*H*-1,2,3-триазоловых производных алкалоида лупинина. Химическая модификация алкалоида лупинина осуществлялась по гидроксиметиленовой группе в положении С-1 хинолизинового остова. Реакции проводились в несколько стадий. Показано, что при взаимодействии лупинина с метансульфохлоридом в присутствии триэтиламина в хлористом метилене гладко образуется (октагидро-2*H*-хинолизин-1-илметил)метансульфонат с высоким выходом (93 %). Последующая обработка данного соединения действием азида натрия в среде диметилформамида при нагревании проводит к образованию 1-(азидометил)октагидро-2*H*-хинолизина с выходом 61 %. Установлено, что при взаимодействии нового азида с терминальными алкинами различной природы в присутствии водного CuSO$_4$ и аскорбата натрия в диметилформамиде могут быть образованы соответствующие 4-замещенные (1*S*,9a*R*)-1-[(1,2,3-триазол-1-ил)метил]октагидро-1*H*-хинолизины. Получены новые 1,2,3-триазоловые производных лупинина, содержащие различные арильные заместители в положении С-4 триазольного цикла. Высокая селективность реакции объяснена механизмом действия катализатора Шарплеса. Методом рентгеноструктурного анализа установлено пространственное строение молекул метансульфоната лупинина, 4-арилтриазолилметил-октагидрохинолизинов. Данные рентгеноструктурного анализа новых соединений в виде CIF файлов депонированы в Кембриджском центре кристаллоструктурных данных.

Ключевые слова: хинолизиновые алкалоиды, лупинин, азиды, триазолы, метансульфонил хлорид, терминальные алкины, реакция 1,3-диполярного циклоприсоединения, РСА.

References

1 Michael, J.P. (2008). Indolizidine and quinolizidine alkaloids. *Nat. Prod. Rep.*, 25, 139–165. https://doi.org/10.1039/b612166g

2 Romeo, F.V., Fabroni, S., Ballistreri, G., Muccilli, S., Spina, A., & Rapisarda, P. (2018). Characterization and Antimicrobial Activity of Alkaloid Extracts from Seeds of Different Genotypes of Lupinus spp. *Sustainability*, 10(3), 788–799. https://doi.org/10.3390/su10030788

3 Tuzimski, T., & Petruczynik, A. (2021). Application of HPLC-DAD for In Vitro Investigation of Acetylcholinesterase Inhibition Activity of Selected Isoquinoline Alkaloids from *Sanguinaria canadensis* Extracts. *Molecules*, 26, 1–13. https://doi.org/10.3390/molecules26010230

4 Gazaliev, A.M., Zhurinov, M.Zh., & Fazylov, S.D. (1992). *Novye bioaktivnye proizvodnye alkaloidov [New bioactive derivatives of alkaloids]*. Alma-Ata: Gylym [in Russian].

5 Tlegenov, R.T. (2007). Sintez 8-benzodioksanovykh azometinov alkaloida lupinina [Synthesis of 8-benzodioxane azomethines of the alkaloid lupinine]. *Chemistry of Natural Compounds*, 43(4), 499–500 [in Russian]. https://doi.org/10.1007/s10600-007-0176-0.

6 Abduvakhabov, A.A., Dalimov, D.N., Uteniyasov, K.U., & Aslanov, H.A. (1993). *Lupinin [Lupinine]*. Nukus [in Russian].

7 Nurkenov, O.A., Nurmaganbetov, Zh.S., Fazylov, S.D., Satpaeva, Zh.B., Turdybekov, K.M., Seilkhanov, T.M., & Talipov, S.A. (2019). Sintez, stroenie i svoistva novykh *O*-atsilproizvodnykh alkaloida lupinina [Synthesis, structure, and properties of new lupinine O-acyl derivatives]. *Chemistry of Natural Compounds*, 55(3), 506–508 [in Russian]. https://doi.org/10.1007/s10600-019-02726-3

8 Tlegenov, R.T. (2007). Sintez novykh dialkilaminouksusnykh efirov alkaloida lupinina [Synthesis of new dialkylamineacetic esters of lupinine alkaloid]. *Khimiia i khimicheskaia tekhnologiia – Chemistry and Chemical Technology*, 50(12), 125–127 [in Russian].

9 Tilyabaev, Z., Gafurov, M.B., Dalimov, D.N., & Abduvakhabov, A.A. (2017). Sintez fosforilirovannykh proizvodnykh alkaloidov, ikh struktura, biologicheskaia aktivnost i perspektivy prakticheskogo ispolzovaniia [Synthesis of phosphorylated alkaloid derivatives, their structure, biological activity, and prospects for practical use]. Tashkent: FAN [in Russian].

10 Nurkenov, O.A., Seilkhanov, T.M., Fazylov, S.D., Issayeva, A.Z., Seilkhanov, O.T., & Vlasova, L.M. (2019). Study of supramolecular inclusion complexes of pseudoephedrine, lupinine, anabasine and cytisine with beta-cyclodextrin by NMR spectroscopy. *Bulletin of the University of Karaganda – Chemistry,* 94, 19–28. https://doi.org/10.31489/2019Ch2/19-28

11 Krivolapov, V.P., & Shkurko, O.P. (2005). 1,2,3-Triazol i ego proizvodnye. Razvitie metodov formirovaniia triazolnogo koltsa [1,2,3-Triazole and its derivatives. Development of methods for forming a triazole ring]. *Uspekhi khimii – Advances in Chemistry*, 74(4), 369–410 [in Russian]. https://doi.org/10.1070/RC2005v074n04ABEH000893

12 Kosenko, I.D., Lobanova, I.A., Chekulaeva, L.A., Godovikov, I.A., & Bregadze, V.I. (2013). Sintez 1,4-dizameshchennykh 1,2,3-triazolov na osnove bis(1,2-dikarbollid) kobalta [Synthesis of 1,4-disubstituted 1,2,3-triazoles based on cobalt bis(1,2-dicarbollide]. *Russian Chemical Bulletin*, 62(2), 497–503 [in Russian]. https://doi.org/10.1007/s11172-013-0069-2

13 Katritzky, A.R., Zhang, Y., & Singh, S.K. (2003). 1,2,3-Triazole formation under mild conditions via 1,3-dipolar cycloaddition of acetylenes with azides. *Heterocycles,* 60(5), 1225–1239. https://doi.org/10.3987/REV-02-562

14 Tornoe, C.W., Christensen, C., & Mendal, M. (2002). Peptidotriazoles on solid phase: 1,2,3-triazoles by regiospecific copper (I)-catalyzed 1,3-dipolar cycloadditions of terminal alkynes to azides. *J. Org. Chem.*, 67, 3057–3064. https://doi.org/10.1021/jo011148j

15 Koziol, A.E., Kosturkiewicz, Z., & Podkowinska, H. (1978). Structure of the alkaloid lupinine. *Acta crystallogr.*, 34, 3491–3494.

16 Duax, W.L., & Norton, D.A. (1975). Atlas of Steroid Structure. New-York: IFI/Plenum.

17 Katorov, D.V., Yakushkov, A.V., Rudakov, G.F., & Zhilin, V.F. (2007). Sintez energoemkikh proizvodnykh 1,2,3-triazolov iz α-nitroazidov [Synthesis of energy-intensive derivatives of 1,2,3-triazoles from α-nitroazides]. *Uspekhi v khimii i khimicheskoi tekhnologii – Achievements of Chemistry and Chemical Technology*, 21(5), 20–23 [in Russian].

18 Bakulev, V.A., & Beryozkina, T.A. (2016). NH-1,2,3-triazoly: sintez i reaktsii s elektrofilnymi reagentami [NH-1,2,3-triazoles: synthesis and reactions with electrophilic agents]. *Chemistry of Heterocyclic Compounds*, 52(4), 4–6 [in Russian]. https://doi.org/10.1007/s10593-016-1821-y

19 Koziol, A.E., Gdaniec, M., & Kosturkiewicz, Z. (1980). Structure of (-)-lupinine. *Acta Crystallogr.*, 36, 980–981.

20 Allen, F.H., Kennard, O., Watson, D.G., Brammer, L., Orpen, A.G., & Taylor, R. (1987). Tables of bond lengths determined by X-ray and neutron diffraction. *J. Chem. Soc. Perkin Trans.*, 2, 1–19.

Information about authors*

Nurmaganbetov, Zhangeldy Seitovich — Candidate of Chemical Sciences, Associate Professor, Institute of Organic Synthesis and Coal Chemistry, Alikhanov str. 1, 100008; Karaganda Medical University, Gogol str., 40, 100012, Karaganda, Kazakhstan; e-mail: nzhangeldy@yandex.ru; https://orcid.org/0000-0002-0978-5663;

Fazylov, Serik Drakhmetovich — Doctor of Chemical Sciences, Professor, Institute of Organic Synthesis and Coal Chemistry, Alikhanov str. 1, 100008, Karaganda, Kazakhstan; Karagandy University of the name of academician E.A. Buketov, Universitetskaya street, 28, 100024, Karaganda, Kazakhstan; e-mail: iosu8990@mail.ru; https://orcid.org/0000-0002-4240-6450;

Turdybekov, Koblandy Muboryakovich — Doctor of Chemical sciences, Professor, Karagandy University of the name of academician E.A. Buketov, Universitetskaya street, 28, 100024, Karaganda, Kazakhstan; e-mail: xray-phyto@yandex.kz; https://orcid.org/0000-0001-9625-0060;

Nurkenov, Oralgazy Aktayevich — Doctor of Chemical Sciences, Professor, Institute of Organic Synthesis and Coal Chemistry, Alikhanov str. 1, 100008, Karaganda, Kazakhstan; Karaganda Technical University, Ave. Nursultan Nazarbayev 56, 100027, Karaganda, Kazakhstan; e-mail: nurkenov_oral@mail.ru; https://orcid.org/0000-0003-1878-2787;

Turdybekov, Dastan Mukhtarovich — Candidate of Chemical Sciences, Karaganda Technical University, Ave. Nursultan Nazarbayev 56, 100027, Karaganda, Kazakhstan; e-mail: turdas@mail.ru; https://orcid.org/0000-0002-0245-022X;

Mukusheva, Gulim Kenesbekovna — Candidate of Chemical Sciences, Associate Professor, Karagandy University of the name of academician E.A. Buketov, Universitetskaya street, 28, 100024, Karaganda, Kazakhstan; e-mail: mukusheva1977@list.ru; https://orcid.org/0000-0001-6706-4816;

Minayeva, Yelena Viktorovna — Candidate of Chemical Sciences, Karagandy University of the name of academician E.A. Buketov, Universitetskaya street, 28, 100024, Karaganda, Kazakhstan; e-mail yelenaminayeva@yandex.ru; https://orcid.org/0000-0001-9382-5965;

Khabdolda, Gaukhar — Candidate of Chemical Sciences, Associate Professor, Karaganda Medical University, Gogol str., 40, 100012, Karaganda, Kazakhstan; e-mail: khabdoldag@mail.ru; https://orcid.org/0000-0002-8152-1136

_____

*The author's name is presented in the order: *Last Name, First and Middle Names*

G.K. Burkeyeva, Ye.M. Tazhbayev, D.M. Muslimova[*], G.D. Nurseiit, L.Zh. Zhaparova

Karagandy University of the name of academician E.A. Buketov, Kazakhstan
(*Corresponding author's e-mail: m.dana_777@mail.ru)

"Cold Curing" of Polyethylene Glycol Maleate with Acrylic Acid and Some Physicochemical Properties of Their Solutions

The possibility of using the copolymers based on unsaturated polyesters with acrylic acid (AA) as the main component (polymeric basis) for the creation of novel highly effective sealants and glues of domestic production was demonstrated. Polyethylene glycol maleate (p-EGM) was synthesized by step-growth polymerization of maleic anhydride with ethylene glycol using the catalyst, which shortened the process duration. A number of solutions of p-EGM with AA were obtained. Physicochemical characteristics of initial solutions were determined. Some rheological properties of the solutions of p-EGM in unsaturated carboxylic acid were studied. Radical polymerization — the process of "cold curing" of the solutions of p-EGM with AA at room temperature was carried out. The combination of initiating a system of cold curing consisting of initiator (benzoyl peroxide) and promoter (dimethylaniline) was selected and their optimal content in the initial monomer mixture was established. The main parameters of curing, namely gelation time and curing time, were determined. Identification of the copolymers was performed using IR-spectroscopy. The morphology of the surfaces of cured samples of p-EGM with AA was studied using SEM. The optimal composition requiring further studies as highly filled compositional polymeric materials for using as sealants and glue basis was established.

Keywords: sealant, glue, unsaturated polyester, polyethylene glycol maleate, unsaturated carboxylic acid, acrylic acid, radical copolymerization, cold curing.

Introduction

At present, the volume of house-building and reconstruction of buildings is consistently being increased in Kazakhstan. Modern building technologies require the use of high-quality products of construction chemicals. These are sealants, glues, mastics, which allow the construction to bond firmly and reliably. Polymeric materials are more commonly used nowadays as sealants and glues [1–3]. Glues and sealants based on polymers have a wide field of application and universal properties starting with the use at home, as well as in professional, repairing and mechanical installation, aircraft-, and automobile as well as shipbuilding industries. As it is known [4–8], among the wide assortment of glues and sealants, silicon-, polyurethane, acrylic, polysulfide, and others are the most widely spread ones. Advantage of such sealing and gluing materials is an opportunity for reliable surfaces pressurization of any kind of shapes directly on the objects being built almost without the evolution of solvents. Sealants and glues based on polymers possess high exploitation characteristics under any climatic conditions. High elastic properties allow using them for sealing various interfaces including the spaces between panels in house buildings, glass units, etc. [4–8]. The sealants and glues of curing types including those hardened with air oxygen are the most widely used. In this regard, it is more desired rather fast curing the sealing composition at rather low or room temperatures. It is necessary to note that along with general advantages one can accentuate the shortcomings, which are peculiar for curing sealants and glues depending on polymer basis.

So, the main drawback of Thiokol sealants is a high volume of production wastes, drain water, and salts. In turn, polyurethane sealants are known for their highest deformation-strength properties. However, the necessity of curing on ending isocyanate groups requires considerable preparation of the components (drying) before the introduction to the product composition, which limits the storage period before use, worsens the monolithicity of the hardened product and finally its quality [4–8].

The diversity of sealants and glues is confirmed by their variety in the market of building materials and the patents on their recipes. This, in turn, emphasizes a high interest of researchers in the search and development of new recipes for the above-said materials. Formulation of sealing and gluing systems includes a base, a filler, an accelerating system and an initiator. In a number of cases a stabilizing system, a plasticizer,

a dye and a photoinitiating system, which provides the curing of the sealing agent by the exposure to UV radiation, are also included in the recipe. Examples can be acrylic sealants of the trade "ACH", "Anatherm-50U", "Anatherm-50UV". The shortcomings of the above-mentioned trademarks are the followings: In the first case, it is a low-reliability index, which is less than 85 %, whereas in the case of using the trade "Anatherm" in spite of 100 % encapsulation there is a necessity of using additional equipment as UV-radiator, carrying out additional acts of controller and huge manufacturing areas. Also, there are other main drawbacks, including low water-proof ability, high sensitivity to UV-light and decrease of the firmness at high temperatures, application limitations (restoration inside the buildings) and the high price [4]. These shortcomings reduce essentially the quality indexes and rentability of production in general [1]. In this regard, modern technologies of obtaining the sealants are directed to the search for new raw materials, fillers and additives with the aim of improving the adhesion properties, time of curing, working life, optimal meanings of firmness and elasticity, and so on.

Promising compounds for the creation of this kind of materials are the solutions of unsaturated polyesters in vinyl monomers, which save necessary consistency in a wide range of concentrations [9–11]. Unsaturated polyesters are the main representatives of oligomers, which are capable of polymerization. They belong to thermoreactive materials with rather a useful complex of properties such as rather low viscosity, capability to harden not only at high but also at room temperature. Owing to the reactive double bond, the unsaturated polyesters can enter the copolymerization reaction with a lot of monomers obtaining the hardened products. Obtained hardened unsaturated polyester resins are materials with high durability, attrition hardness, very good dielectric properties, high chemical stability to various mediums, environmental safety during exploitation period and so on. In this case, there is a possibility of varying properties of the final product due to the variety of unsaturated polyester compositions.

Most part of the investigations in the field of unsaturated polyesters is devoted to the synthesis and study of their properties hardened with styrene [9–11]. The main drawback of these polymers is the limitations in application because of toxicity and flammability of styrene. At the same time, questions about modifying unsaturated polyesters by functional monomers aimed at improving their exploiting characteristics and technological properties of compositional materials in the processing stage have not been studied enough.

Considering the above-listed advantages of unsaturated polyesters, their use as an agent when obtaining adhesive materials of hardened type seems to be perspective. Therefore, the goal of this work is a study of the main physicochemical characteristics of glues and sealants based on polyethylene glycol maleate with acrylic acid, the establishment of kinetics parameters of cold curing (the lifetime and the curing) by selection and varying the initial composition of comonomers and the initiating system.

Experimental

The following reagents, namely ethylene glycol, acrylic acid, benzoyl peroxide, dimethylaniline ("Sigma-Aldrich"), maleic anhydride ("Vekon"), aluminum chloride ("Reachem"), were used in the work. All chemicals were used without additional purification.

Polyethylene glycol maleate (p-EGM) was obtained by the polycondensation reaction of ethylene glycol with maleic anhydride at a temperature of 423–433 K in a four-neck flask, which was equipped with a reflux condenser, a stirrer (was set from a top of a flask), a thermometer, a Dean-Stark apparatus, and a feeding tube (nitrogen). Step-growth polymerization was carried out according to the procedure given in [12] at a constant stirring in the presence of a catalyst (zinc chloride) in a nitrogen atmosphere to avoid the gelatinization process.

Molecular weight of p-EGM was determined using gel permeation chromatography (Agilent 1100 Ser) where polystyrene was chosen as a standard substance and dioxane was chosen as a solvent. The value of molecular weight was approximately M_w ~2358 Da.

Radical copolymerization of p-EGM with acrylic acid (AA) was carried out in bulk at various initial mass ratios of comonomers at a temperature of 293 K, where benzoyl peroxide (BP) was used as an initiator and dimethylaniline (DMA) served as an accelerating agent.

The dynamic viscosity of the initial solutions of p-EGM-AA was measured at 293 K on a vibrational viscosimeter SV-10 provided with a liquid thermostat BT3 for sustaining a given temperature [13].

The density of the initial solutions and the p-EGM-AA copolymers was measured using a pycnometer and hydrostatic methods correspondingly [14].

The gelation time was determined automatically on a Gel Timer Gelnorm GT-S. The curing time of p-EGM-AA was determined according to the procedure described in [15].

The samples IR-spectra were recorded in KBr tablets on an FSM 1201 spectrometer [16].

Electron microscopic pictures were made on a scanning electron microscope MIRA 3 (TESCAN) at an accelerating voltage of 20 kW.

Results and Discussion

Glue bonds are becoming an alternative to mechanical compounds in engineering applications and they provide a number of advantages in comparison to usual mechanical fixing parts. This kind of bond provides a more uniform distribution of tension on the binding area. As it is known from [17], the sealing materials have to meet the following requirements: they must totally prevent the juncture from moisture; do not allow filtering the air (exceeding the amount which is prescribed in the documents); to be capable of saving the sealing properties not depending on atmospheric influences; do not undergo aging for a long period of time; to have rather low price and to be produced from acceptable raw materials [18]. For the formation of glue sews, the following conditions are demanded. In the beginning, the sealant/glue should be in a liquid form; it should easily flow on the surface and wet properly the elements, which are to be glued; then a liquidlike sealant/glue should harden (either by drying, or by polymerization; either by curing with the help of a curing agent, or by cooling for the glue-alloy).

Thus, our studies should be divided into several stages for the goal accomplishment and obtaining polymers with adhesive properties of the hardened type, namely:
− obtaining the solutions of p-EGM in acrylic acid of various compositions and investigation of their rheological properties;
− selection of the initiating system, i.e. the curing additives;
− curing the initial solutions of p-EGM-AA at room temperature by radical copolymerization — "cold curing".

Table 1 presents the data on the composition of initial solutions of p-EGM in acrylic acid and their properties. According to this data the content of unsaturated polyester (p-EGM) in initial compositions of the solutions varies within the interval 30-45 mass.%.

Table 1

Rheological properties of the initial solution of p-EGM-AA, T = 293К

Composition of the initial solution, mass.%		Dynamic Viscosity (η), mPa·s	Density of Solution (ρ), g/cm³
p-EGM	AA		
31.21	68.79	25.6 ± 0.2	1.1428 ± 0.063
35.43	64.57	36.9 ± 0.2	1.1489 ± 0.084
40.59	59.41	83.4 ± 0.2	1.1687 ± 0.094
46.04	53.96	181.0 ± 0.2	1.1934 ± 0.058

Physical and rheological properties of polymers at different states not only predetermine the possibilities of their rational application in a certain field but also, determine the selection of investigation methods. In this regard, there was a necessity to study the dynamic viscosity and density of initial (liquid) solutions of p-EGM in AA at various mass ratios of co-reagents. As it is seen from the obtained results, the dynamic viscosity and the solution's density increase with increasing the content of p-EGM. The results of dynamic viscosity and the solution's density have a good correlation with each other. So, the solution with the composition of 31.21:68.79 mass.% is characterized by rather low viscosity values, namely 25.6 mPa·s and the density value is equal to 1.1428 g/cm³, whereas these indicators are equal to 181.0 mPa·s and 1.1934 g/cm³, respectively, for the solution of p-EGM-AA of the 46.04:53.96 mass.% composition. The increase in the viscosity (Fig. 1) and the solutions density is due to the increase in the content of p-EGM indices in the studied samples, which is characterized by the high viscosity of the latter.

As it has been noted before, the sealants/glues of curing type are the highly-demanded adhesives in the market. In this regard, fast curing of the sealing composition at rather low temperatures is preferred. It is necessary to note that the time and temperature of curing must be optimal depending on the exploitation field of the product. Controlling the parameters of curing process (time and temperature) in case of unsaturated polyesters and obtaining the copolymers with optimal properties is possible by introduction of special additives, namely inhibitors, initiators, and promoters.
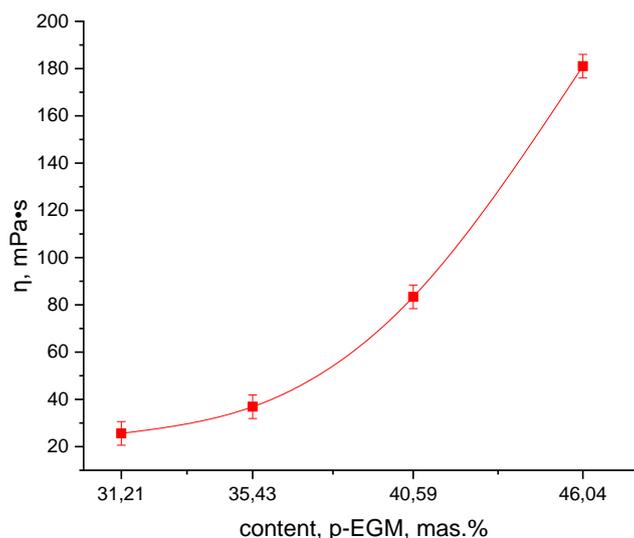
Figure 1. Dependence of a dynamic viscosity on a content of p-EGM in the initial solutions

In connection with this, the main task of controlling the curing process is the right choice of combination of the initiating system. Therefore, in the next stage of work, the selection of curing additives, which are introduced in different quantities, has been done. According to [10], the curing of unsaturated polyesters is carried out in the presence of the radical polymerization initiators, mainly, peroxides are used. As a rule, the use of such initiators requires high curing temperatures and long-term curing, which is not cost efficient, as well as uncomfortable during exploitation. Therefore, promoters play a significant role in initiating systems of cold curing of unsaturated polyesters, as they decompose the peroxides by forming free radicals at room temperature.

The double-component initial system of cold curing was used for curing the p-EGM at a temperature of the environment and lower. It comprised a BP as an initiator and DMA as a promoter (Table 2).

T a b l e 2

**Dependence of the promoter influence on a time of gelation
and curing the solution of p-EGM-AA (BP+DMA, T=273 K)**

Amount, %		Gelation time ($\tau_{gel.}$), min.	Curing time ($\tau_{curing.}$), min.
BP	DMA		
1	0.06	90.10 ± 1.66	150.18 ± 5.58
1	0.1	59.63 ± 1.30	101.06 ± 4.43
1	0.15	43.30 ± 1.08	72.49 ± 3.52
1	0.2	7.11 ± 0.47	13.51 ± 1.14

Figure 2 illustrates the mechanism of interaction between BP and DMA. According to this scheme, in the beginning, a formation of complex takes place, and as a result of electron transfer from DMA to BP, an ionic pair and benzoic radical appear [10]. In this case, DMA activates a high-temperature peroxide BP initiator and promotes generating free radicals during the cold curing process.
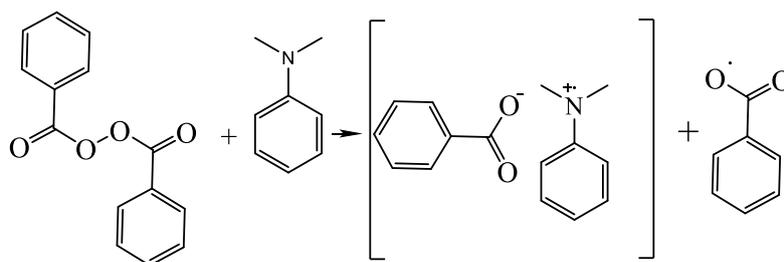
Figure 2. The reaction scheme of BP with DMA

According to Table 2, curing of the system is possible at a temperature range from 18 to 30 °C, when using a pair of initiating system BP+DMA. The correct selection of the quantity of the initiator and promoter allows for reaching the optimal time of curing (τ_{curing}) and gelation ($\tau_{gelation}$). Figure 3 demonstrates the dependence of curing time on the composition of initiating system, in particular, the content of the promoter DMA. It is necessary to note that the quantity of radical-forming peroxide initiator is constant and equal to 1 %. The practicability of the chosen BP concentration is based on the analysis of the works carried out before [11] and literature data [9–11]. It is known [10] that the curing systems/additives have a considerable influence on the properties of unsaturated polyesters. In particular, the quantity of BP affects extensible-structural characteristics and elasticity. Also, it should be pointed out that in case of the systems based on unsaturated polyesters, the gelation process is characterized by the term "adhesive working life" [10, 11]. Thus, one of the main technological properties of adhesives is adhesive working life, — the time within which a sealant or a glue is capable of used in a viscous-flow state after introduction of compounds that cause the curing (Table 2). The studies were carried out and the curing parameters were determined when the content of DMA was 0.01–0.2 %. However, when using DMA in a quantity within the interval of 0.01–0.05 % (from initial mass of the solution) the process of "cold curing" was lengthy and characterized by high values of curing time (t_{curing}) ~ 750.00–250.00 min. As it is seen from the table and graphical data, the time of gelation/working life and curing was decreased with increasing the DMA content. So, the introduction of 0.06 % of DMA to the initial solution of p-EGM-AA was characterized by rather high values of curing time, namely τ_{curing} =150.18 min and at 0.2 % the value was minimum and equal to τ_{curing} =13.51 min, which was not acceptable in exploitation.

In this regard, according to the purpose of the work the most optimal result was observed when using DMA as a promoter in a quantity of 0.15 %, at which the gelation time ($\tau_{gel.}$) and curing time (τ_{curing}) were equal to 43.30 and 72.49 min, respectively.
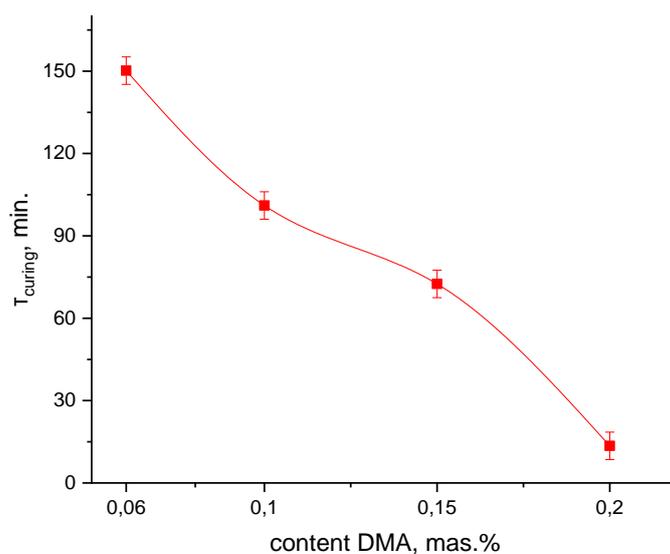
Figure 3. The influence of DMA promoter content on curing time
of p-EGM-AA in the presence of BP at 20°C

In continuation of the studies the radical copolymerization, i.e., the process of "cold curing" of the solution of p-EGM-AA, was carried out at 293 K. PB was used as an initiator and DMA was a promoter in the quantities of 1.0 % and 0.15 %, respectively (calculated from the initial mass of the solution). The curing was carried out in the following way: 0.15 % of DMA was introduced to the initial solution of unsaturated polyester resin (p-EGM-AA), then after thorough stirring, the BP was added and the mixture was extensively stirred within 1 min. After that, the gelation time (adhesive working life) and the curing time were determined according to standard procedures [15]. Identification of the cured products of p-EGM-AA was performed by analyzing IR-spectroscopy data [16]. Thus, all IR spectra of p-EGM-AA contain stretching vibrations of C–O–C ether groups (1090 cm^{-1}), C–H groups (2940 cm^{-1}), and carboxyl groups–COOH (range 650–1000 cm^{-1}).

Figure 4 demonstrates the copolymerization process schematically. During radical copolymerization of p-EGM with unsaturated carboxylic acids the three-dimensional cross-linked polymers of non-solving nature are formed [11, 18].

where R_I — is the initiator radical
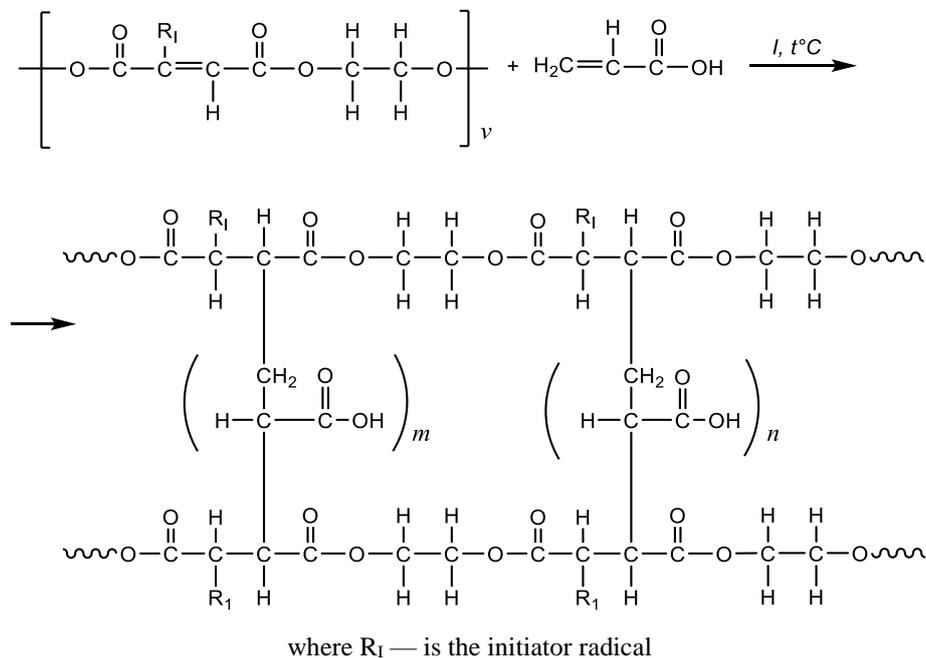
Figure 4. The p-EGM-AA synthesis scheme

Parameters of the curing kinetics and copolymers properties depending on the composition of the initial mixture p-EGM-AA, BP+DMA (1.0 %+0.15 %), T = 293 К

Monomers initial ratio, mol.%		Density (ρ), g/cm^3	Gelation time ($\tau_{gel.}$), min.	Curing time (τ_{curing}), min.
31.21	68.79	1.2635± 0.023	43.30± 1.18	72.49± 2.10
35.43	64.57	1.2695±0.046	50.27± 1.92	83.45± 2.66
40.59	59.41	1.2961± 0.041	57.04± 2.42	94.15± 3.46
46.04	53.96	1.3347± 0.088	64.24± 2.94	107.19± 4.69
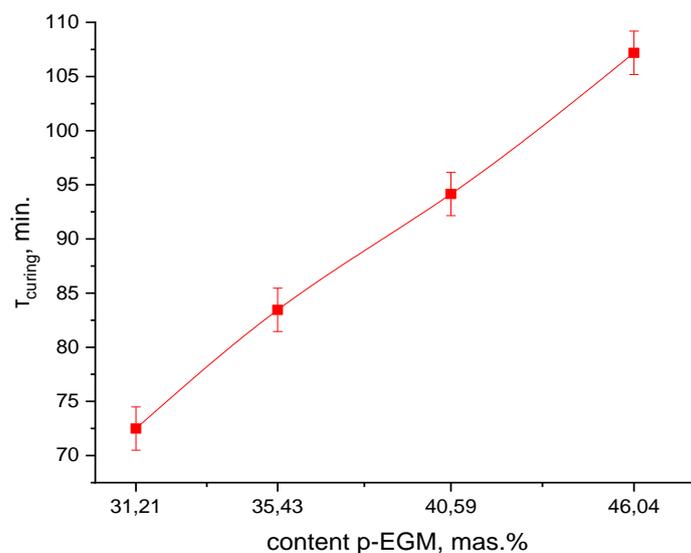
Figure 5. Dependence of the curing time on the content of p-EGM-AA

Thus, the investigation of the p-EGM-AA gelation time points to an increase in adhesive working life (τ_{gelation} = 43–64 min.) with the increasing the p-EGM content. The same dependence is observed when determining the curing time. This phenomenon can be explained by comparing the activity indexes of p-EGM and AA, where this parameter for the last one (r_2 1,22) is higher than the corresponding value for p-EGM (r_1 0,89). It is seen from the previously carried out investigations on studying the kinetic parameters of p-EGM-AA radical copolymerization that the reaction rate increases with the increasing AA content in the monomer mixture [19]. It is also necessary to note that the difference between the values of curing time is insignificant and it varies within the interval of 10–20 min. According to Table 1, with increasing the content of unsaturated polyester, the densities of the initial solutions of p-EGM and AA are increased, which has a good correlation with the data of dynamic viscosity. So, the solution of p-EGM-AA of 46.04:53.96 mass.% is characterized by the high value of dynamic viscosity (181 mPa·s) because of higher content of p-EGM and minimum rate of curing.

Surface morphology of the cured samples was studied using scanning electron microscopy (Fig. 6).
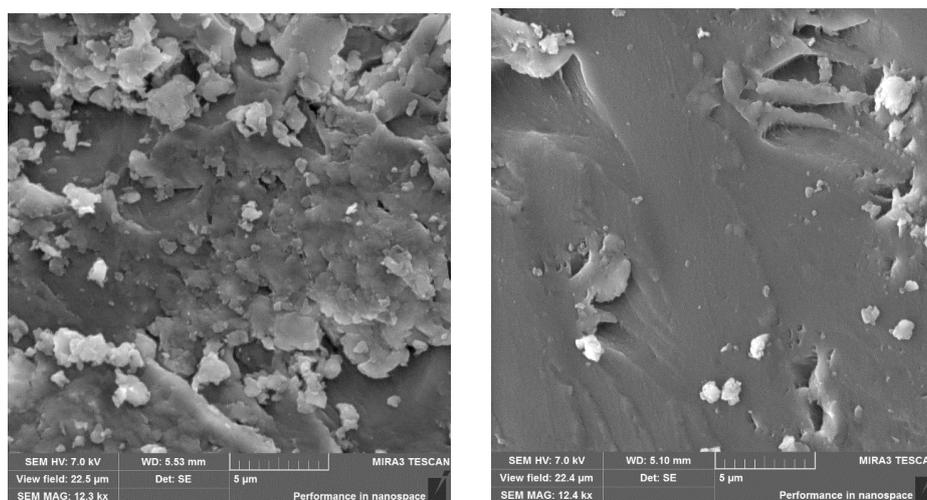
Figure 6. SEM pictures of the surfaces of p-EGM-AA cured samples
with the content of monomers 31.21:68.79 mass.% (in the left) and 46.04:53.96 mass.% (in the right)

According to the obtained pictures, there are some differences in morphological surfaces of the samples (Fig. 6). From the presented pictures, it is seen that the copolymers with higher content of p-EGM 46.04:53.96 mass.% (in the right) is characterized by a dense structure, which is also in good accordance with the results of dynamic viscosity and density of cured samples.

Conclusions

Thus, the investigation of physicochemical properties of the initial solutions of p-EGM-AA in different ratios points to promising prospective of using them as the basis for the sealing and glue composition. The solutions of polyethylene glycol maleate in acrylic acid are characterized by optimal values of viscosity, density, and water absorption. So, in all cases, the change of dynamic viscosity is correlated with the change of density of initial solutions samples. It is also established that the rheological properties of the solutions depend on the content of initial reagents, in particular, the increase of the p-EGM content within the interval of 31.21–46.04 mass.% increases the viscosity from 25.6 to 181.0 mPa·s. The results obtained by SEM point to non-uniformity of the surface with decreasing the unsaturated polyester content. So, monolithicity of the surface is observed in the cured samples with the exceeding p-EGM content. During the work presented the optimal combination of initial system of cold curing has been found. So, the curing system consisting of BP and DMA (1.0 % and 0.15 %, respectively) can be used in the composition of polymeric basis of p-EGM-AA and it is characterized by energy-effective temperature-time regimen of curing without using additional devices, such as UV-lamps. The introduction of the "cold curing" method excludes the stage of exposure to UV light from the production loop. It is also should be noted that varying the composition of the initial polymer-monomer mixture and initiating system allows operating not only physicochemical properties (viscosity, density and water-absorbance) of obtained products, but also to control the conditions of curing (time, working life in viscous-flow state, volume contraction), which is an important characteristic of sealing and glue

systems depending on the application field. In this regard, it can be concluded from the results obtained that the composition of p-EGM-AA 46.04:53.96 mass.% is optimal for further investigations as highly-filled compositional polymer materials for use as sealing and glue basis.

References

1 Comyn, J. Adhesives and sealants: general knowledge, application techniques, new curing techniques / J. Comyn // Handbook of Adhesives and Sealants. — 2006. — Vol. 2. — P. 1–50. https://www.webofscience.com/wos/woscc/full-record/WOS:000311042700002

2 Sancaktar E. Classification of Adhesive and Sealant Materials / E. Sancaktar // Handbook of adhesion technology. — 2011. — Vol. 1 and 2. — P. 261–290. https://doi:10.1007/978-3-642-01169-6_12

3 Cognard, Ph. Technical Characteristics and Testing Methods for Adhesives and Sealants / Ph. Cognard // Netherland: Elsiever. — 2005. WOS:000311048300002

4 ГОСТ 27952-2017. Смолы полиэфирные ненасыщенные. — Дата введения: 2018-05-01. — МКС 83.080.20 — https://docs.cntd.ru/document/1200157967

5 Wolf, A.T. Efficient Materials Silicone-based Sealants and Adhesives Part I: Solidification Mechanisms / A.T. Wolf. — Chemie in unserer zeit, — 2020. — Vol. 54, No. 5. — P. 284–295. https://doi.org/10.1002/ciuz.201900062

6 Wolf, A.T. Efficient Materials Silicone-based Sealants and Adhesives Part II: Structure-Property Relationships and Applications / A.T. Wolf // Chemie in unserer zeit. — 2020. — Vol. 54, No. 6. — P. 386–396. https://doi.org/10.1002/ciuz.201900063

7 Буренин В.В. Герметики для стыков наружных стен зданий и сооружений / В.В. Буренин // Строительные материалы. — 2000. — № 11. — С. 11–13.

8 Sancaktar, E. Constitutive Adhesive and Sealant Models / E. Sancaktar // Handbook of adhesion technology. — 2011. — Vol. 1 and 2. — P. 553–595. https://doi:10.1007/978-3-642-01169-6_23

9 Burkeev, M.Zh. Research of the influence of external factors on copolymers based on unsaturated polyester resins / M.Zh. Burkeev, G.M. Zhumanazarova, G.K. Kudaibergen, E.M. Tazhbayev, G.A. Turlybek // Bulletin of the University of Karaganda — Chemistry. — 2018. — Vol. 98, No. 2. — P. 51–57. https://doi.10.31489/2020Ch2/51-57

10 Burkeyev M. Zh. Synthesis and Properties of Poly(Propylene Glycol Maleate Phthalate)-Styrene Copolymers as a Base of Composite Materials / M.Zh. Burkeyev, J. Plocek, E.M. Tazhbayev, G.K. Burkeyeva, A.N. Bolatbai, S.Zh. Davrenbekov // Russian Journal of Applied Chemistry. — 2018. — Vol. 91, No. 11. — P. 1742–1749. https://doi.10.1134/S1070427218110022

11 Sarsenbekova A.Zh. Comparative Analysis of the Thermal Decomposition Kinetics of Polyethylene Glycol Fumarate-Acrylic Acid Copolymers / A.Zh. Sarsenbekova, G.K. Kudaibergen, M.Zh. Burkeev, G.K. Burkeyeva // Russian Journal Of Physical Chemistry A. — Vol. 93, No. 7. — P. 1252–1257. https://doi.10.1134/S0036024419060281

12 Sharma A.K. Biocatalytic synthesis and characterization of copolymers based on poly(ethylene glycol) and unsaturated methyl esters / A.K. Sharma, R. Kumar, T.C. Canteenwala, V.S. Parmar, S. Patkar, J. Kumar, A.C. Watterson // Journal of Macromolecular Science-Pure and Applied Chemistry. — 2005. — Vol. A42, No. 11. — P. 1515–1521. https://doi.org/10.1080/10601320500229061

13 Вибровискозиметр серии SV: Руководство по эксплуатации и технический паспорт. — Р. 61. сайт: http://and.nt-rt.ru/ https://and.nt-rt.ru/images/manuals/SV-10_100_vaszimetri.pdf

14 ГОСТ 18329-2014. Смолы и пластификаторы жидкие. Методы определения плотности. — Дата введения: 2016-03-01. — МКС 83.080.01. https://docs.cntd.ru/document/1200121303

15 ГОСТ 18329-2014(ISO 1675:1985). Смолы и пластификаторы жидкие. Методы определения плотности. — Дата введения: 2016-03-01–МКС 83.140. https://docs.cntd.ru/document/1200127491

16 Eichhoff U. Dynamic infrared spectroscopy with a step-scan FT-IR for the characterization of polymers / U. Eichhoff, A. Simon // XVI International Conference on Spectroscopy of Molecules and Crystals. — 2004. — Vol. 5507 — P. 396–402. https://doi.org/10.1117/12.570020

17 Burkeev M.Zh. Effect of external factors on the swelling of hydrogels based on poly(ethylene glycol) maleate with some vinyl monomers / M.Zh. Burkeev, A.K. Magzumovaa, E.M. Tazhbaeva, G.K. Burkeevaa, A.K. Kovalevaa, T.O. Khamitovaa, M.M. Mataev // Russian Journal of Applied Chemistry. — 2013. — Vol. 86, No. 1. — P. 63–68. https://doi.org/10.1134/s1070427213010114

18 Патент № 28334. Гидрогели на основе полиэтиленгликольмалеината, обладающие высокими влагосорбирующими свойствами / Е.М. Тажбаев, Т.О. Хамитова, Т.С. Жумагалиева, А.К. Магзумова, Р.З. Касенов, М.Ж. Буркеев, А.Т. Кажмуратова, Ж.Ж. Турганбаева // МПК: C08F 220/18

19 Буркеев М.Ж. Ненасыщенные полиэфирные смолы в реакциях радикальной сополимеризации: моногр. / М.Ж. Буркеев, Е.М. Тажбаев, Г.К. Буркеева. — Караганда: НОИЦ «Parasat– М», 2016. — 96 с.

Г.К. Бүркеева, Е.М. Тажбаев, Д.М. Мүслімова, Г.Д. Нұрсейіт, Л.Ж. Жапарова

Полиэтиленгликоль малеатын акрил қышқылымен «суық» қатайту және олардың ерітінділерінің кейбір физика-химиялық қасиеттері

Отандық өндірістің жаңа тығыздағыштар мен желімдер үшін негіздік компонент (полимер негізі) ретінде акрил қышқылымен (АҚ) қанықпаған полиэфирлер негізіндегі сополимерлерді пайдалану мүмкіндігі көрсетілген. Процесс ұзақтығын азайтатын катализаторды қолдану арқылы малеин ангидриді мен этиленгликольді поликонденсациялау әдісімен полиэтиленгликоль малеинаты (п-ЭГМ) синтезделді. АҚ-дағы п-ЭГМ бірқатар ерітінділер алынды. Бастапқы ерітінділердің физика-химиялық сипаттамалары анықталды. Осылайша, қанықпаған карбон қышқылындағы п-ЭГМ ерітінділерінің кейбір реологиялық қасиеттері зерттелді. Радикалды сополимерлеу — бөлме температурасында п-ЭГМ-АК ерітінділері «суық» қатайту процесінде жүргізілді. Зерттеу барысында суық қатайтудың бастамашы жүйесінің (бастамашы мен промотордың) үйлесімі таңдалды, олардың бастапқы мономерлі қоспасындағы оңтайлы құрамы анықталған. Қатайтудың негізгі параметрлері табылған: желатиндеу уақыты (өміршеңдігі), қатайту уақыты. Сополимерлерді анықтау ИҚ-спектроскопиялық талдау арқылы жүзеге асырылды. п-ЭГМ-АҚ өңделген үлгілерінің беткі морфологиясы сканерлеуші электронды микроскоп арқылы зерттелді. Оңтайлы құрамы (бастапқы реагенттердің қатынасы) анықталды, ол тығыздауыш және жабысқақ негіз ретінде пайдалану үшін жоғары толтырылған композиттік полимерлі материалдар ретінде әрі қарай зерттеуді қажет етеді.

Кілт сөздер: герметик, желім, қанықпаған полиэфир, полиэтиленгликоль малеинаты, қанықпаған карбон қышқылы, акрил қышқылы, радикалды сополимерлеу, суық қатайту.

Г.К. Буркеева, Е.М. Тажбаев, Д.М. Муслимова, Г.Д. Нұрсейіт, Л.Ж. Жапарова

«Холодное» отверждение полиэтиленгликольмалеината с акриловой кислотой и некоторые физико-химические свойства их растворов

Показана возможность применения сополимеров на основе ненасыщенных полиэфиров с акриловой кислотой (АК) в качестве базового компонента (полимерной основы) для новых герметиков и клеев отечественного производства. Методом поликонденсации малеинового ангидрида и этиленгликоля с применением катализатора, сокращающего длительность процесса, синтезирован полиэтиленгликоль-малеинат (п-ЭГМ). Получен ряд растворов п-ЭГМ в АК. Определены физико-химические характеристики исходных растворов. Так, изучены некоторые реологические свойства растворов п-ЭГМ в ненасыщенной карбоновой кислоте. Проведена радикальная сополимеризация — процесс «холодного отверждения» растворов п-ЭГМ-АК при комнатной температуре. В ходе исследований подобрано сочетание инициирующей системы холодного отверждения (инициатора и промотора), выявлено их оптимальное содержание в исходной мономерной смеси. Определены основные параметры отверждения: время желатинизации (жизнеспособность), время отверждения. Идентификацию сополимеров осуществляли методом ИК-спектроскопии. Методом сканирующей электронной микроскопии исследована морфология поверхности отвержденных образцов п-ЭГМ-АК. Выявлен оптимальный состав (соотношение исходных реагентов), требующий дальнейших исследований в качестве высоконаполненных композиционных полимерных материалов для применения в качестве герметизирующей и клеевой основы.

Ключевые слова: герметик, клей, ненасыщенный полиэфир, полиэтиленгликольмалеинат, ненасыщенная карбоновая кислота, акриловая кислота, радикальная сополимеризация, холодное отверждение.

References

1   Comyn, J. (2006). Adhesives and sealants: general knowledge, application techniques, new curing techniques. *Handbook of Adhesives and Sealants, 2,* 1–50. https://www.webofscience.com/wos/woscc/full-record/WOS:000311042700002

2   Sancaktar, E. (2011). Classification of Adhesive and Sealant Materials. *Handbook of adhesion technology*, 1–2, 261–290. https://doi:10.1007/978-3-642-01169-6_12

3   Cognard, Ph. (2005).Technical Characteristics and Testing Methods for Adhesives and Sealants. *Netherland: Elsiever*.

4   Smoly poliefirnye nenasyshchennye [Unsaturated polyester resins]. (2018). HOST R ISO 27952-2017 from 1st May 2018 [in Russian].

5   Wolf, A.T. (2020). Efficient Materials Silicone-based Sealants and Adhesives Part I: Solidification Mechanisms. *Chemie in unserer zeit, 54,* 5, 284–295. https://doi.org/10.1002/ciuz.201900062

6   Wolf, A.T. (2020). Efficient Materials Silicone-based Sealants and Adhesives Part II: Structure-Property Relationships and Applications. *Chemie in unserer zeit, 54,* 6, 386–396. https://doi.org/10.1002/ciuz.201900063

7 Burenin, V.V. (2000). Germetiki dlia stykov naruzhnykh sten zdanii i sooruzhenii [Sealants for joints of external walls of buildings and structures]. *Stroitelnye materialy — Construction materials, 11,* 11–13 [in Russian].

8 Sancaktar, E. (2011). Constitutive Adhesive and Sealant Models. *Handbook of adhesion technology, 1–2,* 553–595. https://doi:10.1007/978-3-642-01169-6_23

9 Burkeev, M.Zh., Zhumanazarova, G.M, Kudaibergan, G.K, Tazhbayev, E.M., & Turlybek, G.A. (2018). Research of the influence of external factors on copolymers based on unsaturated polyester resins. *Bulletin of the University of Karaganda — Chemistry, 98,* 2, 51–57. https://doi.10.31489/2020Ch2/51-57

10 Burkeyev, M. Zh., Plocek, J., Tazhbayev, E.M., Burkeyeva, G. K., Bolatbai, A.N., & Davrenbekov, S.Zh. (2018). Synthesis and Properties of Poly(Propylene Glycol Maleate Phthalate)-Styrene Copolymers as a Base of Composite Materials. *Russian Journal of Applied Chemistry, 91,* 11, 1742–1749. https://doi.10.1134/S1070427218110022

11 Sarsenbekova, A.Zh., Kudaibergen, G.K., Burkeev, M.Zh., & Burkeeva, G.K. (2019). Comparative Analysis of the Thermal Decomposition Kinetics of Polyethylene Glycol Fumarate-Acrylic Acid Copolymers. *Russian Journal Of Physical Chemistry A, 93,* 7, 1252–1257. https://doi.10.1134/S0036024419060281

12 Sharma, A.K., Kumar, R., Canteenwala, T.C., Parmar, V.S., Patkar, S., Kumar, J., & Watterson, A.C. (2005). Biocatalytic synthesis and characterization of copolymers based on poly(ethylene glycol) and unsaturated methyl esters. *Journal of Macromolecular Science-Pure and Applied Chemistry, A42,* 11, 1515–1521. https://doi.org/10.1080/10601320500229061

13 Vibroviskozimetr serii SV: Rukovodstvo po ekspluatatsii i tekhnicheskii pasport [Vibro viscosimeter of SV series: Operating manual technical data sheet] [in Russian]. Retrieved from https://and.nt-rt.ru/images/manuals/SV-10_100_vaszimetri.pdf

14 Smoly i plastifikatory zhidkie. Metody opredeleniia plotnosti [Resins and plasticizers are liquid. Density determination methods]. (2016). HOST RISO 1675-1985 from 1st March 2016. *Moscow: Standartin form Rossiskoi Federatsii* [in Russian]. https://docs.cntd.ru/document/1200121303

15 Smoly poliefirnye nenasyshchennye. Metody opredeleniia vremeni otverzhdeniia [Unsaturated polyester resins. Methods for determining the curing time]. (2017). HOST R ISO ISO 2535-2001 from 1st January 2017 [in Russian]. https://docs.cntd.ru/document/1200127491

16 Eichhoff, U., & Simon, A. (2004). Dynamic infrared spectroscopy with a step-scan FT-IR for the characterization of polymers. *XVI international conference on spectroscopy of molecules and crystals,* 5507, 396–402. https://doi.org/10.1117/12.570020

17 Burkeev, M.Zh., Magzumovaa, A.K., Tazhbaeva, E.M., Burkeevaa, G.K., Kovalevaa, A.K., Khamitovaa, T.O., & Mataev, M.M. (2013). Effect of external factors on the swelling of hydrogels based on poly(ethylene glycol) maleate with some vinyl monomers. *Russian Journal of Applied Chemistry, 86,* 1, 63–68. https://doi.org/10.1134/s1070427213010114

18 Tazhbaev, E.M., Hamitova, T.O., Zhumagalieva, T.S., Magzumova, A.K., Kasenov, R.Z., Burkeev, M.Zh., Kazhmuratova, A.T., & Turganbaeva, Zh.Zh. (2014). Patent № 28334. Gidrogeli na osnove polietilenglikolmaleinata, obladaiushchie vysokimi vlagosorbiruiushchimi svoistvami [Patent No. 28334 KZ.MPK: C08F 220/18. Hydrogels based on polyethylene glycolmaleinate with high moisture adsorbing properties] [in Russian].

19 Burkeev, M.Zh., Tazhbaev, E.M., & Burkeeva, G.K. (2016). Nenasyshchennye poliefirnye smoly v reaktsiiakh radikalnoi sopolimerizatsii [Unsaturated polyester resins in radical copolymerization reactions]. Karaganda: NOIC «Parasat– M» [in Russian].

Information about authors*

Burkeyeva, Gulsym Kabaevna — PhD, Associate Professor of Chemical Sciences, Karagandy University of the name of academician E.A. Buketov, Universitetskaya street, 28, 100024, Karaganda, Kazakhstan; e-mail: guls_b@mail.ru; https://orcid.org/0000-0003-1993-7648;

Tazhbayev, Yerkeblan Muratovich — Doctor of Chemical Sciences, Professor, Karagandy University of the name of academician E.A. Buketov, Universitetskaya street, 28, 100024, Karaganda, Kazakhstan; e-mail: tazhbaev@mail.ru; https://orcid.org/0000-0003-4828-2521;

Muslimova, Danagul Magazovna (corresponding author) — 1st year PhD student, Karagandy University of the name of Academician E.A. Buketov, Universitetskaya street, 28, 100024, Karaganda, Kazakhstan; e-mail: m.dana_777@mail.ru; https://orcid.org/0000-0002-3041-7072;

Nurseiit, Gulim Dauletkyzy — Master student, Karagandy University of the name of academician E.A. Buketov, Universitetskaya street, 28, 100024, Karaganda, Kazakhstan; e-mail: guli.rts@mail.ru; https://orcid.org/0000-0002-0819-1441;

Zhaparova, Lyazzat Zhanybekovna — PhD, Associate Professor, Karagandy University of the name of academician E.A. Buketov, Universitetskaya street, 28, 100024, Karaganda, Kazakhstan; e-mail: lyazzh@mail.ru; https://orcid.org/0000-0003-1894-0255

_____
*The author's name is presented in the order: *Last Name, First and Middle Names*

PHYSICAL AND ANALYTICAL CHEMISTRY

S.S. Chitlange, S.R. Chandani[*], S.P. Gandhi, P.A. Thorat, H.B. Lad

Dr. D.Y. Patil Institute of Pharmaceutical Sciences and Research, Pimpri, Pune, Maharashtra, India
([*]Corresponding author's e-mail: sneharchandani@gmail.com)

Development and Validation of HPTLC Method for Simultaneous Estimation of Berberine, Gallic Acid and Ursolic Acid in a Polyherbal Blend

A sensitive high-performance thin-layer chromatography method was developed for simultaneous estimation of berberine, gallic acid and ursolic acid in a polyherbal blend and validated as per ICH guidelines. Polyherbal blend was prepared using widely recommended herbal plants for platelet augmentation activity viz. Carica papaya, Berberis aristata, Ocimum Sanctum, and Tinospora Cordifolia. The optimized separation was obtained with TLC aluminum plates pre-coated with silica gel G60 F254 as a stationary phase and a solvent system containing Toluene : Ethyl acetate : Methanol : Formic acid (3:3:0.2:0.1 v/v/v/v). Berberine and gallic acid were found to demonstrate linearity in the range of 1µg/band – 6µg/band and ursolic acid in the range of 20 µg/band – 100 µg/band with the regression coefficient in acceptable limits. The method was also found to be specific and precise one. The accuracy of the developed method at 80 %, 100 % and 120 % levels was found to be within limits and % RSD was found to be less than 2. LOD and LOQ of all three standards were also determined. Blend was also quantified for the amount of berberine, gallic acid and ursolic acid presence and was found to be 37.8 µg, 46.1 µg and 108 µg per mg, respectively.

Keywords: HPTLC, polyherbal, gallic acid, berberine, ursolic acid, method development, validation.

Introduction

Polyherbal formulations are common in traditional system of medicine. The standardization of these polyherbal formulations with complex chemical composition is a major challenge faced by analysts. High-performance thin-layer chromatography (HPTLC) can be a useful tool for analysis and standardization with the use of markers/biomarkers due to a number of advantages, such as analysis speed, sensitivity, and low operational cost.

In the current study, an analytical method was developed for in-house platelet booster polyherbal formulation comprising of *Carica papaya*, *Berberis aristata*, *Ocimum Sanctum* and *Tinospora Cordifolia*. The selected plants have reported platelet augmentation [1, 2] and anti-dengue activities [3–6].

The markers viz. gallic acid, ursolic acid and berberine (Fig. 1) used for the standardization of the polyherbal formulation are widely found in many herbal drugs. Gallic acid or 3,4,5-trihydroxybenzoic acid with anti-dengue, astringent, cyclooxygenase-2 (COX-2) inhibitory, antioxidant and anti-neoplastic activity [7, 8] is a constituent found in *Carica papaya* [9]. Ursolic acid, a pentacyclic triterpenoid, 3β-hydroxyurs-12-en-28-oic acid present in *Ocimum sanctum* [10] is reported to have activities like anti-inflammatory, antioxidant, antiviral, serum lipid-lowering, and antineoplastic activities [11, 12]. The phytoconstituent of *Berberis aristata and Tinospora cordifolia,* berberine, [13] an isoquinoline alkaloid, with diverse biological activity including antiviral, anti-diabetic, anti-neoplastic, anti-inflammatory and anti-lipidemic activities [14] was also used as a biomarker in the current study.

Several studies employing high-performance thin-layer chromatography (HPTLC) [15–19] and high-performance liquid chromatography (HPLC) [20–23] to estimate these markers alone or in combination have been published. However, a thorough review of the literature found that no validated HPTLC approach for simultaneously estimating all three markers has been published.

Thus, this study aims to establish a simple, reliable, precise, and validated HPTLC approach for estimating these markers simultaneously in a polyherbal preparation.
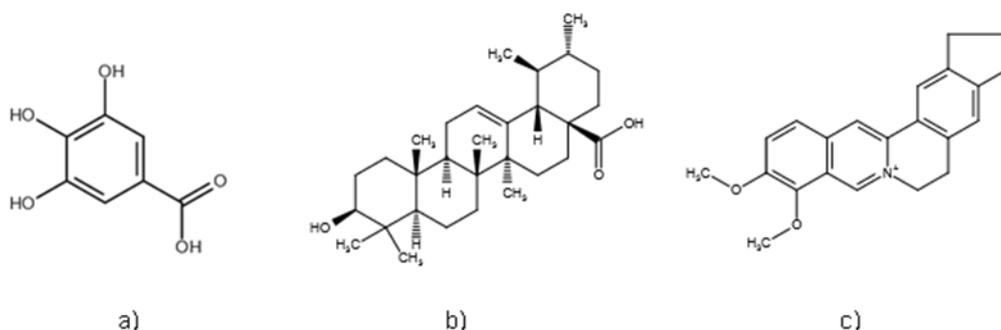
Figure 1: Structure of a) gallic acid, b) ursolic acid, c) berberine

Experimental

Chemicals and reagents: All chemicals and reagents used for the study were AR Grade. The herbal extracts used in the study and the marker ursolic acid was procured from Phyto Life Sciences P. Ltd, Gujarat, India. The markers, namely gallic acid and berberine, were procured from Natural Remedies Bangalore, India and Cayman Chemical Company, USA, respectively.

Preparation of polyherbal blends: The herbal blends were prepared by mixing *Carica papaya* leaf extract *(200 mg)*, *Berberis aristata* root extract (120 mg), *Tinospora cordifolia* stem extract (150 mg) and *Ocimum sanctum* leaf extract (120 mg). Blend was prepared by mixing extracts in increasing concentration.

Standardisation of blend by high-performance thin-layer chromatography

1) HPTLC method development

a. Preparation of standard solutions and a test solution: For a standard solution, 1mg of berberine was dissolved in 1ml of methanol to obtain a solution of 1000 µg/ml concentration, which was used further for spotting on TLC plate. Similarly, stock solutions for gallic acid (1000 µg/ml) and ursolic acid (1000 µg/ml) were prepared in methanol.

For a test solution, 200 mg of polyherbal blend was dissolved in 10 ml methanol by sonicating for 10 minutes followed by filtration through filter paper (Whatman No. 42). Filtrate was further used for spotting on TLC plates.

b. Selection of the mobile phase: A standard stock solution (4 µl) and a test solution (10 µl) were applied on a pre-coated TLC plate as a band (the band size was 6 mm). Different solvents and solvents combinations with varying polarity were used to obtain well-separated sharp bands.

c. Methodology: The Camag Linomat-V sample applicator, semi-automatic equipment was used to apply standard stock solutions of berberine, gallic acid and ursolic acid on pre-coated TLC plates. The development of plate was performed in a twin trough chamber saturated with the mobile phase for 20 minutes. After development, the air-dried material was scanned at 280 nm for densitometric evaluation.

2) The method validation: The developed methodology was validated using Methodological Validation Criteria of the International Conference on Harmonization's (ICH) Q2 (R1) [24–27].

a. Linearity: Linearity for standard berberine and gallic acid was obtained in the range of 1 µg/band – 6 µg/band and that of ursolic acid was found to be 20 µg/band – 100 µg/band by spotting them separately on TLC plates. For each concentration, the peak area was measured, and the calibration curve graph was plotted as concentration versus peak area.

b. Specificity: The determination of the method specificity was carried out by application of methanol as blank, berberine, gallic acid, and ursolic acid as a standard solution, and a polyherbal blend as a test solution into the HPTLC system.

c. Accuracy: Accuracy of the developed method was estimated at levels 80 %, 100 % and 120 % separately for the standards (with 4µl berberine, gallic acid, ursolic acid considered as 100 %, 10 µl blend con-

centration was taken as 100 %). The blend was spiked with standard of known concentration, and the calculation for percent recovery (recovered and expected concentrations) was performed as per ICH guidelines.

d. Precision

System precision: Six replicate bands of standard as 4µl of berberine, gallic acid, ursolic acid separately at 6 tracks were applied to determine system precision. Standard deviation and % relative standard deviation were calculated.

Method precision: The method precision was carried out for blend from six replicate applications (10 µl extract application at 6 tracks) and % relative standard deviation was calculated.

e. Robustness: Robustness was checked by making small deliberate alterations in the method. The standard deviations of peak areas were computed for two parameters as variation in the mobile phase volume (±1 ml) and saturation time of a chamber (± 5 min)

f. Limit of detection (LOD) and limit of quantitation (LOQ): Limit of detection and limit of quantitation were calculated using the standard calibration curve method for berberine, gallic acid, and ursolic acid.

3) Quantification of markers by the developed method

For quantification of markers, 10 mg of extract/blend was dissolved in 1ml of methanol (100µg/ml) by sonication for 10 minutes and finally filtered using Whatman filter paper No. 42. A total of 10µl of stock solution was applied, developed and scanned using the optimized chromatographic conditions. Concentration of berberine, gallic acid, ursolic acid in methanol extract/blend was calculated using linearity equation.

Results and Discussion

HPTLC Method Development: The solvent system containing Toluene : Ethyl acetate : Methanol : Formic acid (3:3:0.2:0.1 v/v/v/v) gave good resolution for berberine, gallic acid and ursolic acid. R_f value for standards berberine, ursolic acid and gallic acid were found to be 0.31, 0.53 and 0.65, respectively at 280 nm with optimized chromatographic conditions (Table 1, Fig. 2). At a wavelength of 280 nm, the densitometric evaluation of separated bands was performed. The polyherbal blend was subjected to similar chromatographic conditions to obtain well-separated peaks (Fig. 3).
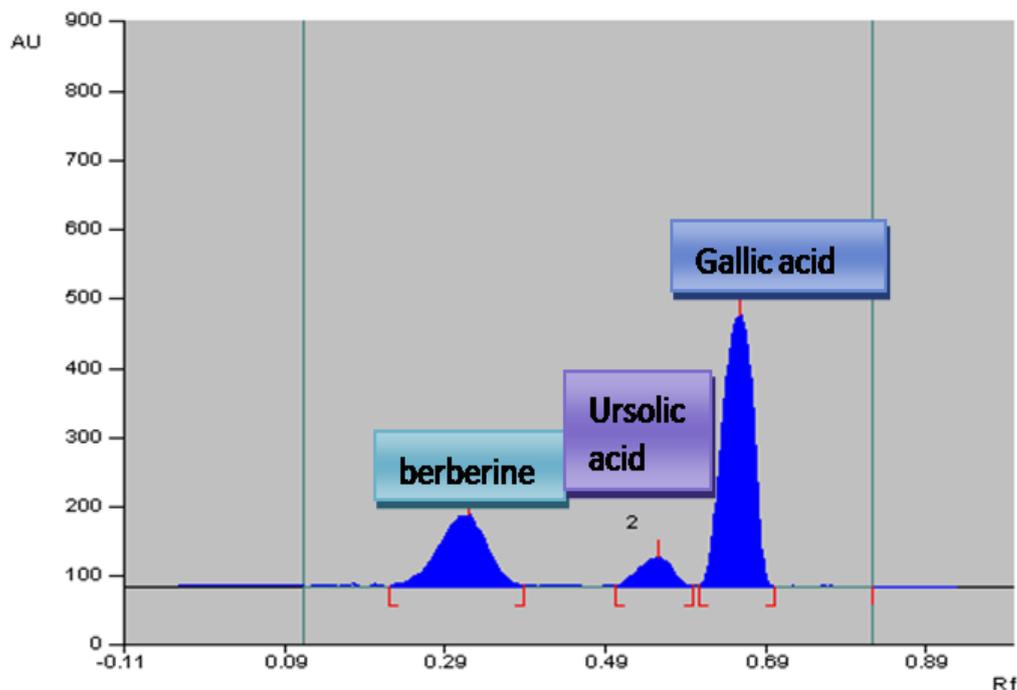
Figure 2. Densitogram of berberine (Rf is 0.31), ursolic acid (Rf is 0.53) and gallic acid (Rf is 0.65)
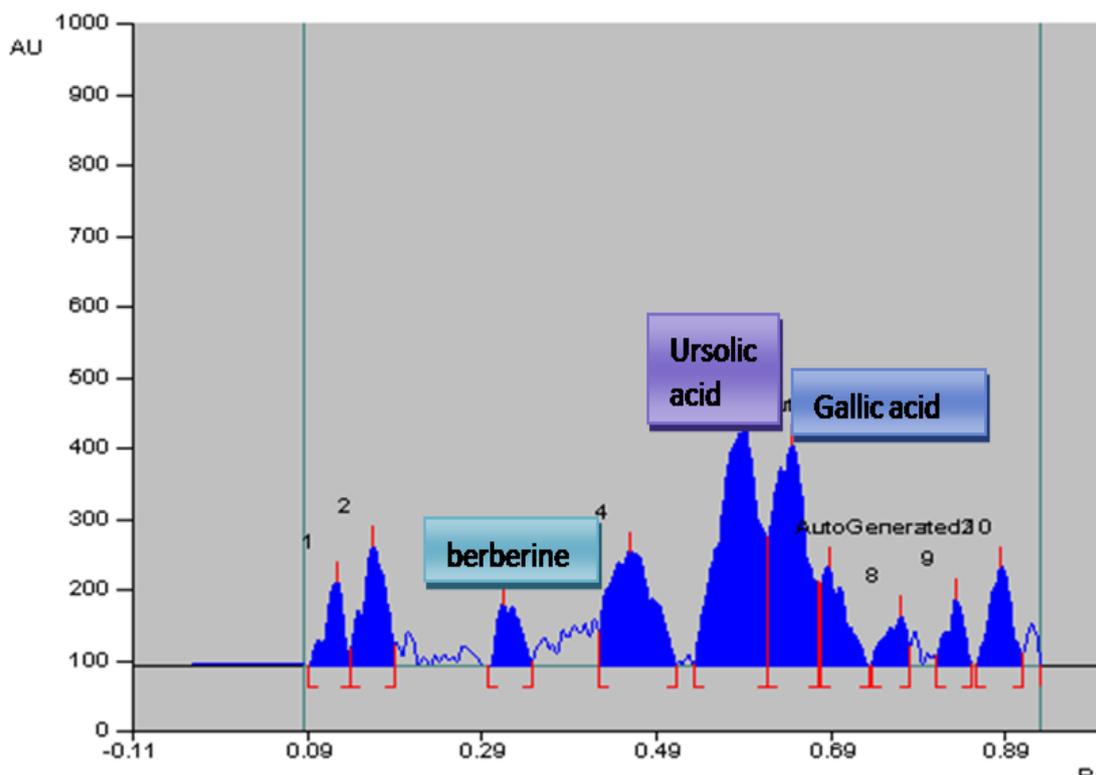
Figure 3. Densitogram of blend with berberine, ursolic acid and gallic acid

T a b l e   1

Optimized chromatographic conditions

Parameters	Specifications
Stationary phase	Aluminium plates pre-coated with silica gel 60 F_{254} (Merck)
Mobile phase	Toluene : Ethyl acetate : Methanol : Formic Acid (3:3:0.2:0.1 v/v/v/v)
Plate size	10 cm × 10 cm
Application mode	Band
Band size	6mm (Distance between two bands: 14mm)
Sample volume	4 µl
Development chamber	Twin-trough glass chamber, 10 cm × 10 cm with stainless steel lid
Saturation time	20 minutes.
Separation technique	Ascending
Migration distance	≈ 80 mm
Scanning mode	Absorbance/Reflectance
Slit dimensions	5 × 0.45 mm
Scanning wavelength	280nm

HPTLC Method Validation:

a. Linearity: Standards berberine and gallic acid were found to be linear in the range of 1µg/band – 6 µg/band. The linearity range for ursolic acid was found to be 20 µg/band – 100 µg/band. Regression coefficients for all the standards were in the acceptable limit according to the ICH guidelines.
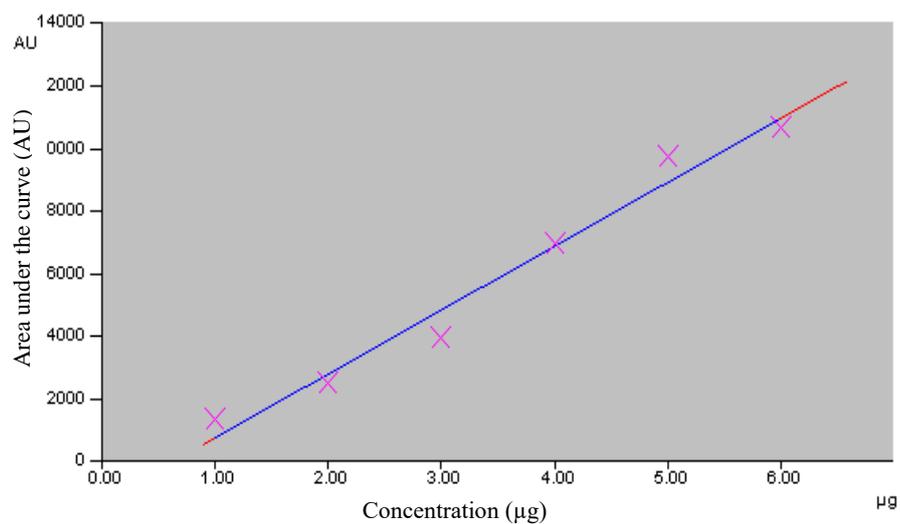
Figure 4. Linearity of berberine standard (1 µg/band – 6 µg/band)
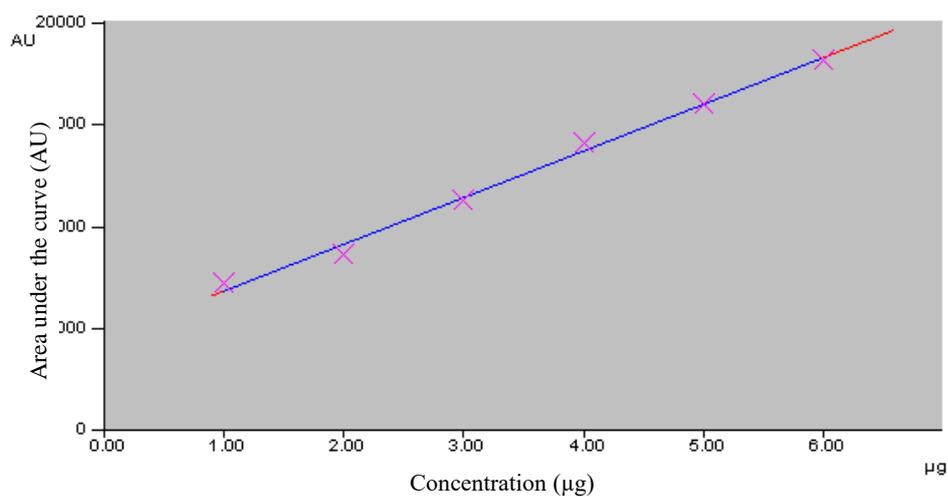
Figure 5. Linearity of gallic acid standard (1 µg/band – 6 µg/band)
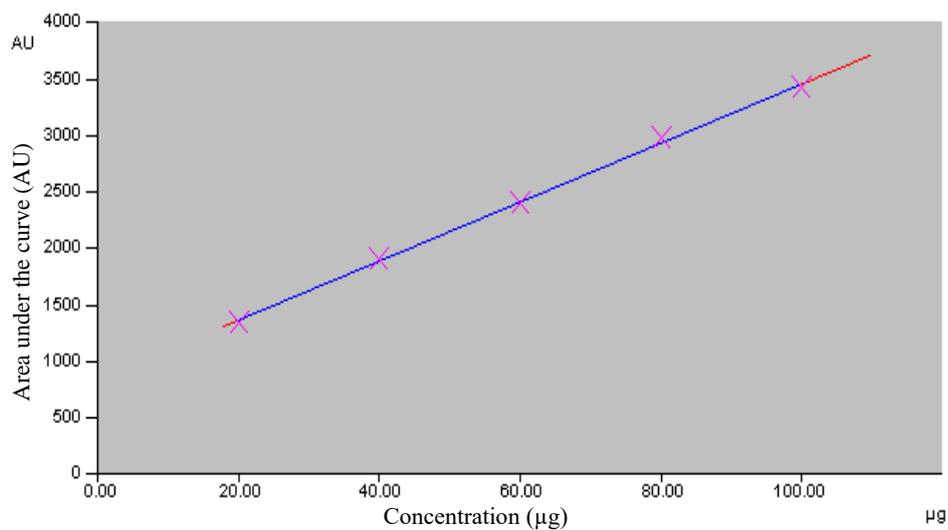
Figure 6. Linearity of ursolic acid standard (20 µg/band – 100 µg/band)

Linearity result of standards

Standard	Equation	Regression Co-efficient
Berberine	$Y = -1298 + 2039x$	0.987
Gallic Acid	$Y = 4529 + 2283x$	0.997
Ursolic Acid	$Y = 837 + 26.14x$	0.999

Specificity: Good correlation values and satisfactory peak purity were obtained with no interference in the quantification of ursolic acid, gallic acid, berberine, which proves that the method is specific.

Accuracy: Results from accuracy studies were reported as percentage recoveries calculated against respective levels (Table 3). The average % recovery of berberine, gallic acid, ursolic acid was found to be within the acceptance limit (98–102 %). The accuracy of the developed method was good as indicated by the low % RSD values.

Result of accuracy study

Analyte	Recovery Level	Average % Recovery (%)	S.D	% R.S.D
Berberine	80 %	101.06	0.013	0.012
	100 %	100.89	0.011	0.010
	120 %	100.71	0.017	0.016
Gallic acid	80 %	100.87	0.003	0.0029
	100 %	101.25	0.005	0.0030
	120 %	101.28	0.005	0.0032
Ursolic acid	80 %	101.7	0.011	0.010
	100 %	100.94	0.010	0.09
	120 %	102.11	0.013	0.012

d. Precision: Method and system precision was carried out using berberine, gallic acid and ursolic acid; % relative standard deviation was calculated. The % RSD is in the acceptable limit, that is, less than 2.0, which indicates that the method has an acceptable level of precision.

Results of precision studies

Analyte	Method Precision		System Precision	
	SD	% RSD	SD	% RSD
Berberine	0.32	0.02	0.82	0.011
Gallic cid	0.65	0.03	0.34	0.002
Ursolic acid	0.78	0.09	0.26	0.08

e. Robustness: The optimized parameters were intentionally varied depending on the chamber saturation time (±5 min) and the mobile phase volume (±1 ml). The unaffected R_f values and low values of the % RSD (less than 2) of peak areas indicate the method's robustness (Table 5).

Results of the Robustness study

Factor	Level	Ursolic acid (Rf)	Berberine (Rf)	Gallic acid (Rf)
1	2	3	4	5
Saturation time				
15 min	−5	0.53	0.32	0.66
20min	0	0.53	0.31	0.65
25 min	+5	0.52	0.31	0.67
SD ± RSD		0.006±1.09	0.006±1.84	0.01±1.5

1	2	3	4	5
Mobile phase volume				
6 ml	−1	0.51	0.31	0.63
7 ml	0	0.53	0.31	0.65
8 ml	+1	0.52	0.32	0.64
SD ± RSD		0.01±1.9	0.006±1.84	0.01±1.56

f. Limit of detection and limit of quantitation: The LOD and LOQ values for berberine, gallic acid, ursolic acid were calculated, which showed the adequate sensitivity of the developed method (Table 6).

T a b l e 6

Limit of detection and limit of quantitation

Compound	LOD (µg/band)	LOQ (µg/band)
Berberine	0.031	0.10
Gallic acid	0.020	0.07
Ursolic acid	0.080	0.010

3.4 Quantification of marker compounds in the polyherbal formulation by the developed method
The biomarkers were quantified in the in-house blend using the developed method (Table 7). The calculations were done using linearity curve of markers. The blend was found to contain 37.8 µg, 46.1 µg and 108 µg per mg of berberine, gallic acid and ursolic acid, respectively.

T a b l e 7

Quantification of markers

Sr. No.	Marker	Area (AU)	Percentage in blend (%, Calculated from linearity curve)
1	Berberine	6427.49	3.78 ± 0.02
2		6450.56	
3		6370.4	
4	Gallic acid	14717.39	4.61 ± 0.137
5		15091.32	
6		15337.19	
7	Ursolic acid	1119.44	10.80 ± 1.197
8		1087.98	
9		1150.56	

Conclusions

The HPTLC method was developed for the determination of berberine, gallic acid, and ursolic acid in the polyherbal blend and validated as per ICH guidelines. The study illustrates that the HPTLC method is simple, accurate and precise for the simultaneous estimation. The method is found to be specific and robust for the analysis. The method resulted in well-resolved sharp peaks. The recovery for all the biomarkers was close to 100 %, which confirmed no interference of other phytoconstituents of the extracts. The present method can be used for quantification of these biomarkers in the blend. Also, it was found that ursolic acid was present in the highest concentration in the formulated blend.

In summary, the developed method can be used for the routine standardization and quality control of herbal formulations containing the above mentioned markers, which are common ingredients of many polyherbal formulations. The method can also be used for quantification of the selected markers.

References

1 Subenthiran, S., Choon, T.C., Cheong, K.C., Thayan, R., Teck, M.B., Muniandy, P.K., Afzan, A., Abdullah, N.R., & Ismail, Z. (2013). Carica papaya leaves juice significantly accelerates the rate of increase in platelet count among patients with dengue fever and dengue haemorrhagic fever. *Evidence-Based Complementary and Alternative Medicine*, *2013*. https://doi.org/10.1155/2013/616737

2 Babu, R., Kubavat, S., Poulose, K., Kumar, K., Handae, S., Satyanarayana, Dhamodaran, V., & Elangovan, B. (2017). A randomized, double-blind, placebo-controlled, proof of concept study to assess the safety and efficacy of Carica papaya and Tinospora cordifolia leaf extract (Thrombobliss) in subjects undergoing chemotherapy treatment and subjects with systemic microbi. *International Journal of Clinical Trials*, *4*(3), 116. https://doi.org/10.18203/2349-3259.ijct20173088

3 Ahmad, N., Fazal, H., Ayaz, M., Abbasi, B.H., Mohammad, I., & Fazal, L. (2011). Dengue fever treatment with Carica papaya leaves extracts. *Asian Pacific journal of tropical biomedicine*, 1(4): 330–333. https://doi.org/10.1016/S2221-1691(11)60055-5. PMID: 23569787; PMCID: PMC3614241.

4 Pick, A., Ling, K., Khoo, B.F., Seah, C.H., Foo, K.Y., & Cheah, R.K. (2014). Inhibitory Activities of Methanol Extracts of Andrographis Paniculata and Ocimum Sanctum against Dengue-1 Virus, 47–52. https://doi.org/10.15242/iicbe.c814013

5 Abd Kadir, S.L., Yaakob, H., & Mohamed Zulkifli, R. (2013). Potential anti-dengue medicinal plants: a review. *Journal of Natural Medicines*, *67*(4), 677–689. https://doi.org/10.1007/s11418-013-0767-y

6 Ratanakomol, T., Roytrakul, S., Wikan, N., & Smith, D.R. (2021). Berberine inhibits dengue virus through dual mechanisms. *Molecules*, *26*(18). https://doi.org/10.3390/molecules26185501

7 Nowak, R., Olech, M., & Nowacka, N. (2014). Plant Polyphenols as Chemopreventive Agents. *Polyphenols in Human Health and Disease*, *2*, 1289–1307. https://doi.org/10.1016/B978-0-12-398456-2.00086-4

8 Kahkeshani, N., Farzaei, F., Fotouhi, M., Alavi, S., Bahramsoltani, R., Naseri, R., Momtaz, S., Abbasabadi, Z., Rahimi, R., Farzaei, M., & Bishayee, A. (2019). Pharmacological effects of gallic acid in health and diseases: A mechanistic review. *Iranian Journal of Basic Medical Sciences*, *22*(3), 225–237. https://doi.org/10.22038/ijbms.2019.32806.7897

9 Rk, S., Soundarya, R., Sudhakaran, T., & Tk, R. (2020). Estimation of Tannic Acid by RP-HPLC and Gallic Acid by HPTLC Method in the Methanolic Extract of Carica papaya Linn. Leaves and its Formulation Estimation of Tannic Acid Bb RP-HPLC and Gallic Acid by HPTLC Method in the Methanolic Extract of Carica papaya Linn. Leaves and its Formulation, (September).

10 Singh, D., & Chaudhuri, P.K. (2018). A review on phytochemical and pharmacological properties of Holy basil (Ocimum sanctum L.). *Industrial Crops and Products*. DOI:10.1016/j.indcrop.2018.03.048

11 Trujillo-Correa, A. I., Quintero-Gil, D. C., Diaz-Castillo, F., Quiñones, W., Robledo, S. M., & Martinez-Gutierrez, M. (2019). In vitro and in silico anti-dengue activity of compounds obtained from Psidium guajava through bioprospecting. *BMC complementary and alternative medicine*, *19*(1), 298. https://doi.org/10.1186/s12906-019-2695-1. PMID: 31694638; PMCID: PMC6836419.

12 Sun, Q., He, M., Zhang, M., Zeng, S., Chen, L., Zhou, L., & Xu, H. (2020). Ursolic acid: A systematic review of its pharmacology, toxicity and rethink on its pharmacokinetics based on PK-PD model. *Fitoterapia*, *147*. https://doi.org/10.1016/J.FITOTE.2020.104735

13 Malhotra, B., Kulkarni, G.T., Dhiman, N., Joshi, D.D., Chander, S., Kharkwal, A.C., Sharma, A.K., & Kharkwal, H. (2021). Recent advances on Berberis aristata emphasizing berberine alkaloid including phytochemistry, pharmacology and drug delivery system. *Journal of Herbal Medicine, 27*, 100433.

14 Och, A., Podgorski, R., & Nowak, R. (2020). Biological Activity of Berberine-A Summary Update. *Toxins*, *12*(11). https://doi.org/10.3390/TOXINS12110713

15 Sheikh, Z., Shakeel, S., Gul, S., Zahoor, A., Khan, S., Zaidi, F., & Usmanghani, K. (2015). A novel HPTLC method for quantitative estimation of biomarkers in polyherbal formulation. *Asian Pacific Journal of Tropical Biomedicine*, 5 (11). doi: 10.1016/j.apjtb.2015.06.016

16 Patel, D.K., Patel, K., & Dhanabal, S. (2012). Phytochemical standardization of Aloe vera extract by HPTLC techniques. *Journal of Acute Disease*, *1*(1), 47–50. https://doi.org/10.1016/S2221-6189(13)60011-6

17 Kumar, A., Lakshman, K., Jayaveera, K.N., Tripathi, S.N.M., & Satish, K.V. (2010). Estimation of gallic acid, rutin and quercetin in terminalia chebula by hptlc. *Jordan Journal of Pharmaceutical Sciences*, *3*(1), 63–68.

18 Srivastava, M. (2011). *High-performance thin-layer chromatography (HPTLC)*. https://doi.org/10.1007/978-3-642-14025-9

19 Kaur, P., Gupta, R.C., Dey, A., Malik, T., & Pandey, D.K. (2020). Validation and quantification of major biomarkers in 'Mahasudarshan Churna'- an ayurvedic polyherbal formulation through high-performance thin-layer chromatography. *BMC Complementary Medicine and Therapies*, *20*(1), 184. https://doi.org/10.1186/s12906-020-02970-z

20 Srinivasan, G.V., Unnikrishnan, K.P., Rema Shree, A.B., & Balachandran, I. (2008). HPLC Estimation of berberine in Tinospora cordifolia and Tinospora sinensis. *Indian journal of pharmaceutical sciences*, *70*(1), 96–99. https://doi.org/10.4103/0250-474X.40341

21 Fernandes, F.H., & Salgado, H.R. (2016). Gallic Acid: Review of the Methods of Determination and Quantification. *Critical reviews in analytical chemistry*, *46*(3), 257–265. https://doi.org/10.1080/10408347.2015.1095064. PMID: 26440222.

22 Wu, W., Wang, L., & Tian, S. (2021). Simultaneous qualitative and quantitative analyses of ursolic acid and oleanolic acid in Punica granatum L.(Pomegranate) flowers by high-performance thin-layer chromatography. JPC–Journal of Planar Chromatography–Modern TLC, 34(2), 165–172. DOI:10.1007/s00764-021-00092-x

23 Meena, A. K., Rekha, P., Perumal, A., Ilavarasan, R., Singh, R., Srikant, N., & Dhiman, K. S. (2021). Identification and estimation of bioactive constituents Negundoside, Berberine chloride, and Marmelosin by HPLC and HPTLC for development of quality control protocols for Ayurvedic medicated oil formulation. *Future journal of pharmaceutical sciences*, *7*(1), 171. https://doi.org/10.1186/s43094-021-00322-3

24 ICH. (2003). Ich Q1a (R2). *Stability Testing of New Drug Substances and Products*, *4* (February), 24.

25 Chitlange, S.S., Rawat, D.G. & Gandhi, S.P. (2017). Estimation of Anti Diabetic Teneligliptin in Bulk and Formulation by Densitometric and Spectrophotometric Method, Analytical Chemistry Letters, 7 (4), 556–566. https://doi.org/10.1080/22297928.2017.1364664

26 Thomas, A., Kanakdhar, A., Shirsat, A., Deshkar, S., & Kothapalli, L. (2020). A High Performance Thin Layer Chromatographic Method Using a Design of Experiment Approach for Estimation of Phytochemicals in Extracts of Moringa Oleifera Leaves, Turkish Journal of Pharmaceutical Sciences, 17(2), 148–158. https://doi.org/10.4274/tjps.galenos.2018.80958

27 Bhole, R.P., Jagtap, S.R., Bonde, C.G., & Zambare, Y.B. (2020). Development and validation of stability indicating HPTLC method for estimation of pirfenidone and characterization of degradation product by using mass spectroscopy. *Bulletin of the University of Karaganda – Chemistry, 99*, 99(3), 51–60. https://doi.org/10.31489/2020CH3/51-60

С.С. Читланж, С.Р. Чандани, С.П. Ганди, П.А. Торат, Х.Б. Лэд

Полишөпті қоспадағы берберинді, галл қышқылын және урсол қышқылын бір мезгілде анықтауға арналған ЖТЖҚХ әдісін жасау және валидациялау

Полишөпті қоспадағы берберинді, галл қышқылын және урзол қышқылын бір мезгілде анықтауға арналған сезімталдығы жоғары, тиімді жұқа қабатты хроматография әдісі ICH ұсыныстарына сәйкес әзірленді және валидацияланды. Шөп қоспасы тромбоциттердің белсенділігін арттыру үшін ұсынылатын белгілі шөптерді, атап айтқанда *Carica papaya, Berberis aristata, Ocimum Sanctum* және *Tinospora Cordifolia* өсімдіктерін пайдалана отырып дайындалды. Оңтайландырылған бөлуге стационарлық фаза ретінде G60 F254 силикагелімен алдын ала қапталған алюминий TLC пластиналарын және құрамында толуол : этилацетаты : метанол : құмырсқа қышқылы (3:3:0,2:0,1 көлемі) бар еріткіш жүйесі арқылы қол жеткізілді. Берберин мен галл қышқылы 1 мкг/жолақ – 6 мкг/жолақ, урзол қышқылы — 20 мкг/жолақ – 100 мкг/жолақ диапазонында регрессия коэффициентімен рұқсат етілген шектерде сызықтылықты көрсететіні анықталды. Сондай-ақ әдіс нақты және дәл болып шықты. Жасалған әдістің дәлдігі 80 %, 100 % және 120 % деңгейінде рұқсат етілген шектерде, ал % RSD екіден аз екені анықталды. LOD және LOQ барлық үш стандарт үшін де анықталды. Қоспа сонымен бірге құрамында берберин, галл қышқылы және урзол қышқылының бар екендігіне тексерілген, олар бір мг үшін сәйкесінше 37,8 мкг, 46,1 мкг және 108 мкг құрады.

Кілт сөздер: ЖТЖҚХ, полигравикалық қоспа, галл қышқылы, берберин, урсол қышқылы, әдісті жасау, валидация.

С.С. Читланж, С.Р. Чандани, С.П. Ганди, П.А. Торат, Х.Б. Лэд

Разработка и валидация метода высокоэффективнойтонкослойной хроматографии для одновременного определения берберина, галловой кислоты и урсоловой кислоты в политравной смеси

Был разработан чувствительный метод высокоэффективной тонкослойной хроматографии (ВЭТСХ) для одновременного определения содержания берберина, галловой кислоты и урсоловой кислоты в политравной смеси и утвержден в соответствии с рекомендациями ICH. Политравная смесь была приготовлена с использованием широко известных травяных растений, рекомендуемых для увеличения активности тромбоцитов, а именно *Carica papaya, Berberis aristata, Ocimum Sanctum* и *Tinospora Cordifolia*. Оптимизированное разделение было достигнуто с помощью алюминиевых пластин для ТСХ, предварительно покрытых силикагелем G60 F254 в качестве стационарной фазы, и системой растворителей, содержащей толуол : этилацетат : метанол : муравьиная кислота (3:3:0,2:0,1 об./об./об./об.). Установлено, что берберин и галловая кислота демонстрируют линейность в диапазоне 1 мкг/полоса — 6 мкг/полоса, урсоловая кислота — в диапазоне 20 мкг/полоса — 100 мкг/полоса с коэффициентом регрессии в допустимых пределах. Метод также оказался специфичным и точным. Было обнаружено, что точность разработанного метода на уровнях 80 %, 100 и 120 % находится в допустимых пределах, а % RSD меньше двух. Также были определены LOD и LOQ для всех трех стандартов. Смесь также была исследована на содержание берберина, галловой кислоты и урсоловой кислоты, которое составило 37,8 мкг, 46,1 мкг и 108 мкг на мг соответственно.

Ключевые слова: ВЭТСХ, политравная смесь, галловая кислота, берберин, урсоловая кислота, разработка метода, валидация.

Information about authors*

Chitlange, Sohan Satyanarayan — Principal, Department of Pharmaceutical Chemistry, Dr. D.Y. Patil Institute of Pharmaceutical Sciences and Research, Pimpri, Pune, 411018, Maharashtra, India; e-mail: sohanchitlange@rediffmail.com; https://orcid.org/0000-0002-9355-3303;

Chandani, Sneha Ramchandra (corresponding author) — Assistant Professor, Department of Pharmaceutical Chemistry, Dr. D.Y. Patil Institute of Pharmaceutical Sciences and Research, Pimpri, Pune, Maharashtra,411018, India; e-mail: sneharchandani@gmail.com; https://orcid.org/0000-0003-3891-2841;

Gandhi, Sejal Prakash — Assistant Professor, Department of Pharmaceutical Chemistry, Dr. D.Y. Patil Institute of Pharmaceutical Sciences and Research, Pimpri, Pune, Maharashtra,411018, India; e-mail: sejal.gandhi@dypvp.edu.in; https://orcid.org/0000-0002-7079-1886;

Thorat, Poonam Ashok — M. Pharm Student, Department of Pharmaceutical Chemistry, Dr. D.Y. Patil Institute of Pharmaceutical Sciences and Research, Pimpri, Pune, Maharashtra,411018, India. e-mail: poonam123thorat@gmail.com;

Lad, Himani Bhalchandra — M. Pharm Student, Department of Pharmaceutical Quality Assurance, Dr. D.Y. Patil Institute of Pharmaceutical Sciences and Research, Pimpri, Pune, Maharashtra,411018, India. e-mail: himanilads1598@gmail.com

_____

*The author's name is presented in the order: *Last Name, First and Middle Names*

A.F. Kurmanova[*], F.Zh. Abilkanova, A.S. Rakhimzhanova, I.A. Pustolaikina

Karagandy University of the name of academician E.A. Buketov, Karaganda, Kazakhstan
(*Corresponding author`s e-mail: alfiya_kurmanova@mail.ru)

DFT Study of Complexation Reactions Involving Dicarboxylic Acids: Hydrogen Bonds, Influence of Solvent Nature

Quantum chemical studies of the protolytic ability of some dicarboxylic acids are carried out. The geometric and kinetic parameters of the dimeric molecules of maleic, succinic, tartaric, oxalic, and adipic acids are investigated. The dimerization energies of these substances are determined by considering the basis set superposition error (BSSE). The effect of the presence of a carbon skeleton, unsaturated bonds, and hydroxy substituents on the dicarboxylic acids kinetic parameters is confirmed. The frontier molecular orbitals of the studied dimeric acids molecules are considered and the HOMO-LUMO energy gap is determined. The obtained values of the energy gaps show an increase in the stability of a number of cyclic compounds formed by the participation of two hydrogen bonds. The ability of the acids to form complexes with the 3,6-di-tert-butyl-2-hydroxyphenoxyl semiquinone radical is studied. The effect of the nature of the solvent on the activation barrier of the complexation reaction of the semiquinone radical — dicarboxylic acid system is analyzed using the CPCM and IEFPCM models. The dependence of the energy parameter on the solvent polarity is established using the examples of toluene, tetrahydrofuran, and nitrobenzene. The DFT method at the B3LYP level, together with the 6-31+G (d, p) basis set, is used to optimize molecular structures. The calculations are carried out using the Gaussian 16 Revision A.03 WIN64.

Keywords: quantum chemical calculations, density functional theory, hydrogen bond, intermolecular hydrogen bonds, transient formation; complex compounds, frontier molecular orbitals, dimerization energy, complexation energy, effect of the nature of the solvent.

Introduction

Hydrogen bonds and proton transfer reactions are of great importance and the subject of discussion, both in chemistry and other sciences such as biology, physics, and material science. At the same time, the mechanism of such interactions is complex and not fully understood. Experimental methods, such as NMR, IR, and ESR spectroscopy, are widely used to study hydrogen bonds. These methods make it possible to determine the initial and final structures of hydrogen-bonded complexes. The same methods are used in dynamic mode to determine the kinetic characteristics of these processes. However, the detailed mechanism of the proton transfer and exchange processes remains not fully elucidated. Today, it would be interesting to use computational modeling in the study, and in particular DFT calculations, since they are relevant for comparing experimental results with theory [1, 2].

Previously obtained ESR spectroscopy data suggest the ability of carboxylic acids to form dimer associates in nonpolar solvents. The authors of [3–7] showed that the proton exchange between the semiquinone radical and formic acid in toluene occurs predominantly with the dimeric form of the acid. Dicarboxylic acids containing two carboxyl groups are of greater interest compared to monosubstituted analogues since they have more pronounced electron acceptor properties [8]. An analysis of the obtained rate constants of the proton exchange reaction between molecules in combination with an ortho-substituted semiquinone radical in the dioxane showed that an increase in the degrees of freedom in acids leads to the raise of their reactivity. In addition, it is assumed that intermolecular proton exchange is facilitated by the formation of a complex transition intermediate of the reaction due to the coordination of both carbonyl groups. Furthermore, the presence of different functional groups affects the coordination of the four-center cyclic complex due to steric hindrances when approaching the reaction centers [3–8]. However, modern physical methods that make it possible to determine the kinetic parameters of reactions, such as the rate constant or the activation energy of the process, are not suitable for detecting the formation of intermediate particles in the composition of hydrogen-bonded complexes. The structure of the transition state itself remains unstudied since the lifetime of such complexes is much shorter than the characteristic frequencies of physical methods.

In this regard, there is the task of determining the structure of the intermediate complex by the density functional theory method, in which the corresponding processes with the participation of hydrogen bonds take place. Also, the purpose of this study is to establish the dependence of the stability of molecular complexes with the participation of dicarboxylic acids on the length of their structural skeleton and the nature of the solvent.

Experimental

Modern instrumental methods enable the researchers to study the kinetics of elementary chemical processes occurring in nano- or femtosecond modes. However, it is not always possible to register each individual stage of fast reactions by experimental methods. This also applies to proton transfer and exchange processes. Therefore, computer technologies and computational modelling are widely used to predict the electronic structure and physicochemical properties of various molecules.

Many methods have been developed to describe accurately weak interactions, including dispersion interactions. Thus, many authors prove by comparison that the B3LYP method generally gives good results in calculation of the length of hydrogen bonds and the binding energy of dimers [9]. To optimize the geometric structures of a number of dicarboxylic acids and to establish the activation characteristics of protolytic processes, the DFT B3LYP method with the 6-31+G(d, p) basis set was used. This method was chosen because it contains both polarization and diffusion functions, which are important in the study of systems containing intramolecular hydrogen bonds and radical particles. The 6-31+G(d, p) basis includes one set of d-functions for non-hydrogen atoms (such as C, O and N), one set of p-functions for the hydrogen atom, and diffuse functions for heavy atoms.

All calculations were carried out using Gaussian 16.

Results and Discussion

The objects of study were the most abundant dicarboxylic aliphatic acids, such as oxalic, succinic, adipic, as well as maleic and tartaric unsaturated acids. It was interesting how the structural features of molecules affect their protolytic ability.

Different conformers of carboxylic acids are described in the literature [9–15]. We chose the most kinetically stable conformations for study. Carboxylic acids form strong dimeric hydrogen-bonded complexes, which are stable even in the gas phase. Bonds between atoms in the reaction center can form linear (LHBC) or cyclic (CHBC) hydrogen-bonded complexes. These are especially interesting for the study by the methods of quantum mechanics since they allow us to consider them as a model in the study of protolytic processes involving semiquinone radicals.

The structure of a cyclic complex of two molecules of dicarboxylic acids in a dimer can be represented by the scheme:
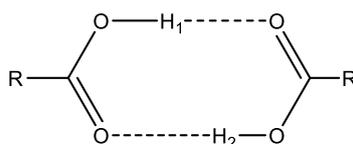
where R — the radical of a dicarboxylic acid.

It can be assumed that a hydrogen bond is formed between the acidic hydrogen of one carboxylic acid molecule and the carbonyl oxygen of the second molecule. Thus, two pairs of intermolecular hydrogen bonds between the carboxyl groups of two distinct molecules can be observed in a cyclic complex. Wang Xu and co-authors [16] determine the strength of the intermolecular hydrogen bond by the O-H elongation in O–H....O fragment and the reduction in the H…O distance. A shorter H…O distance corresponds to a stronger hydrogen bond.

In our studies, theoretical calculations were carried out in the gas phase without taking into account the influence of the medium. An analysis of bond lengths showed that O–H bond elongation is observed in a number of dimers: oxalic acid (1.0055 Å) < adipic acid (1.0057 Å) < maleic acid (1.0069 Å) < tartaric acid (1.0094Å) < succinic acid (1.012Å). At the same time, the strength of the hydrogen bond decreases from succinic acid to oxalic acid, respectively. The geometric parameters of the cyclic complex, such as the bond length R(H..O), R(OO), R(CO) and the valence angles formed by the H–O–C and O–C–O atoms, can also be used to describe the hydrogen bond (Table 1). Isomers molecules with the lowest energy were selected for the study of monomers and dimers.

Geometric parameters of dicarboxylic acid dimers obtained using DFT B3LYP/6-31G+(d, p) calculations

No.	Compound	$R_{(OH)}$, Å	$R_{(OO)}$, Å	$R_{(O\_\_H)}$, Å	$\angle$HOC, deg	$\angle$OCO, deg
1	Oxalic HOOC-COOH	1.0055	2.6500	1.6448	110.1	126.8
2	Maleic HOOCCH=CHCOOH	1.0069	2.6362	1.6293	110.3	124.6
3	Succinic HOOC-(CH$_2$)$_2$-COOH	1.0120	2.6171	1.6051	110.6	124.3
4	Tartaric HOOC-(CH-OH)$_2$-COOH	1.0094	2.6580	1.6159	110.9	125.6
5	Adipic HOOC-(CH$_2$)$_4$-COOH	1.0057	2.6456	1.6401	110.4	124.1

As can be seen from Table 1, there is no explicit dependence on the hydrogen bond strength in the dimers of the considered dicarboxylic acids. Perhaps this is due to the fact that the number of possible conformers increases significantly with the carbon skeleton growth, and we were not able to identify more stable possible structures. Also, it can be seen that DFT methods are sensitive to changes in the geometric structure of molecules, the presence of multiple bonds, and the presence of substituents.

The dimerization energy can be another parameter that makes it possible to judge the stability of hydrogen-bonded complexes [17–19]. Table 2 illustrates the energies of individual molecules (E_{acid}) and the energies of dimers (E_{dimer}), which were calculated considering the BSSE (Basis Set Superposition Error) correction for the imperfection of the basis set. To calculate the dimerization energy ($\Delta E(d)$), the following formula was used:

$$\Delta E(d) = 2E_{acid} - E_d \qquad (1)$$

where E_{acid} — the calculated energy values of the acid molecule; E_d — the calculated energy values of the dimer molecule.

Dimerization energies of a number of dicarboxylic acids obtained by the DFT B3LYP/6-31G+(d, p) calculations

No.	Acid	E_{acid}, a.u.*	E_{dimer}, a.u.*	ΔE_{d}, kJ/mol
1	Oxalic	–378.324383	–756.67244	62.15
2	Maleic	–455.740552	–911.493814	33.37
3	Succinic	–456.974237	–913.975589	71.19
4	Tartaric	–607.403223	–1214.82758	55.48
5	Adipic	–535.610467	–1071. 249247	74.34
Note: *1 a.u. = 2625.5 kJ·mol^{-1}				

As can be seen from Table 2, the dimerization energies depend on the length of the carbon skeleton of dicarboxylic acid molecules. The values of ΔE_{d} in the considered series from oxalic (62.1 kJ/mol) to succinic (71.2 kJ/mol) and adipic (74.3 kJ/mol) acids increase, which can be interpreted in favor of the strength of the resulting intermolecular hydrogen-bonded complexes. The presence of an unsaturated bond destabilizes the dimer molecule in the case of maleic acid ($\Delta E_{\text{d}} = 33.4$ kJ/mol). A similar effect is produced by the influence of steric factors, particularly in hydroxy-substituted tartaric acid. Theoretical calculations show lower dimerization energy for tartaric acid ($\Delta E_{\text{d}} = 55.5$ kJ/mol) compared to the unsubstituted analogue ($\Delta E_{\text{d}} = 71.19$ kJ/mol, succinic acid).

The analysis of frontier molecular orbitals allows us to study such an important parameter of quantum chemistry as a population. The highest occupied molecular orbitals (HOMO) are outer orbitals that tend to donate the electrons they contain, thereby being electron donors. The next orbital is the lowest unoccupied molecular orbital (LUMO) capable of receiving electrons. The energy difference between the described levels allows for measuring the HOMO-LUMO gap and can be used to characterize the stability of the molecule under study: If the energy gap is smaller, then the chemical reactivity is higher and the kinetic stability of the molecule is lower.

Table 3 demonstrates the HOMO and LUMO energies of dicarboxylic acid dimers. These data ensure the determination of the values of the HOMO-LUMO gap.

Theoretical levels of the HOMO-LUMO transition calculated by the DFT B3LYP/6-31G+(d, p) method

No.	Dimeric compounds of carboxylic acids	$E_{(LUMO)}$, a.u.	$E_{(HOMO)}$, a.u.	ΔE, a.u.
1	Oxalic	-0.08232	-0.28977	0.20745
2	Maleic	-0.07292	-0.28046	0.20754
3	Succinic	-0.01101	-0.27518	0.26417
4	Tartaric	-0.03833	-0.2669	0.22857
5	Adipic	-0.00101	-0.27756	0.27655
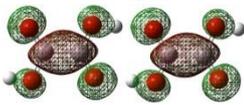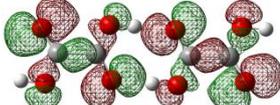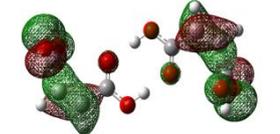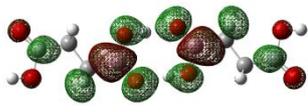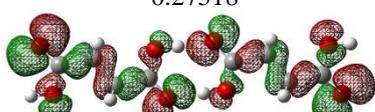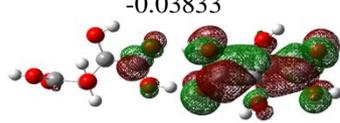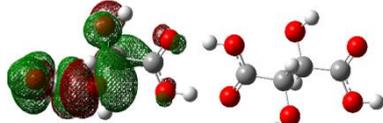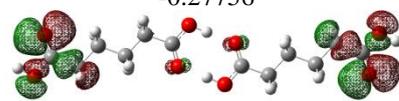
The data presented in Table 3 are ordered by increasing carbon skeleton of dicarboxylic acid molecules. The value of the energy gap rises from 0.20745 a.u. for oxalic acid to 0.26417 a.u. for succinic acid, and to 0.27655 a.u. for adipic acid. Comparison of dimers of acids with the same carbon skeleton showed that stability increases in the presence of multiple bonds (ΔE for maleic acid is 0.20754 a.u.), and reactivity increases with the introduction of hydroxy substituents (ΔE for tartaric acid is 0.22857 a.u.).

Another method for studying the strength of H-bonds is the analysis of natural bond orbitals (NBO). NBO analysis shows the role of intermolecular orbital interaction in the dimer due to charge transfer. Thus, knowing the charges on the O1–H....O2 atoms of the cycles formed because of hydrogen bonds in dicarboxylic acid dimers, it is possible to estimate the electrostatic forces affecting the strength of the hydrogen bond. According to our calculated data, the charge on the O1 atom of carboxyl groups increases in the series: oxalic acid (–0.624) < succinic acid (–0.663) < adipic acid (–0.670). The charge on the H atom decreases in the same sequence of acids: oxalic acid (0.525) > succinic acid (0.523) > adipic acid (0.521). This pattern indicates an increase in the electron density and, accordingly, shows an increase in the strength of the hydrogen bond with an increase in the length of the carbon chain of the aliphatic acid.

Based on the results of numerous studies on the proton exchange between semiquinone radicals and H-acids, there were ideas about the formation of a hydrogen-bonded complex (HBC), which has a cyclic structure. Figure 1 shows the spatial structure of the intermolecular complex of the studied dicarboxylic acids with 3,6-ditert.butyl-2-oxyphenoxyl, calculated with full optimization of all geometric parameters by the DFT method.
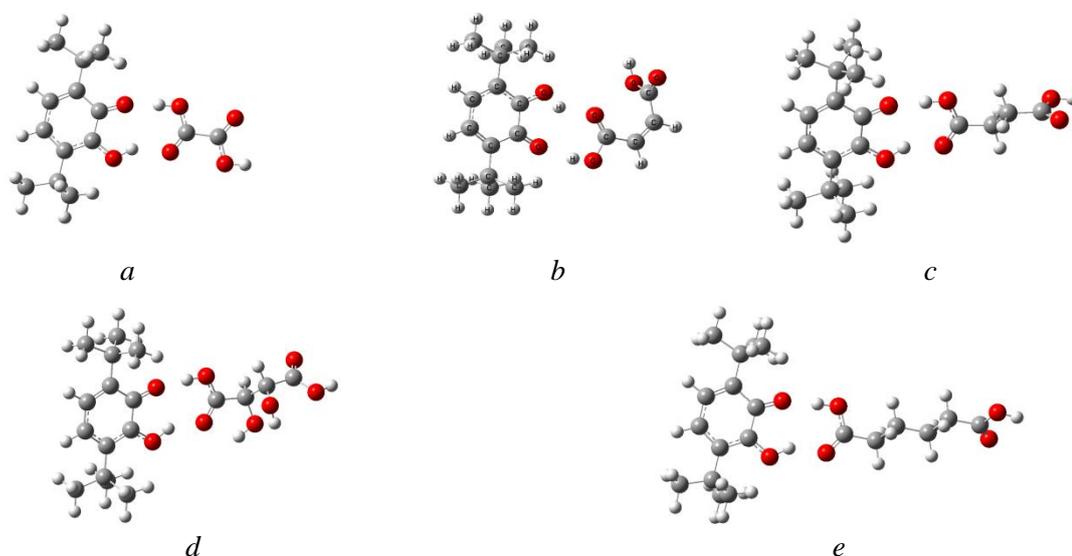
Figure 1. Spatial structures of HBC between 3,6-ditert.butyl-2-oxyphenoxyl and
a) oxalic acid; *b*) maleic acid; *c*) succinic acid; *d*) tartaric acid; *e*) adipic acid

The strength of the hydrogen bond increases correspondingly in a number of complexes with oxalic acid (1.84 Å) < succinic acid (1.78Å) < adipic acid (1.67 Å), thereby showing the possibility of faster proton transfer or exchange over a shorter intermolecular O–H...O bridge.

The presence of multiple bonds in molecules (maleic acid, R(O–H...O) = 1.89 Å) and hydroxo substituents (tartaric acid, R(O–H...O) = 1.85 Å) reduces the stability of hydrogen bonds, compared with similar molecules.

To predict the ability to complex formation, we analyzed the energy of complex formation ($\Delta E_{c.f.}$) in the studied acids with an ortho-substituted semiquinone radical (Table 4). The parameter was calculated according to the following equation:

$$\Delta E_{c.f.} = (E_{acid} + E_{radical}) - E_{complex} \tag{2}$$

where E_{acid} — the calculated energy values of the acid molecule; $E_{radical}$ — the calculated energy values of the 3,6-ditert-butyl-2-hydroxyphenoxyl molecule; $E_{complex}$ — the calculated values of the energy of a molecule of an acid complex with a semiquinone radical.

Table 4

The energies of complex formation of some dicarboxylic acids with 3,6-di-tert-butyl-2-hydroxyphenoxyl calculated by the DFT UB3LYP/6-31G+(d, p) method

Dicarboxylic acids	E_{acid}, a.u.*	$E_{radical}$, a.u.*	$E_{complex}$, a.u.*	$\Delta E_{c.f.}$, kJ/mol
Oxalic	–378.3243833	–696.6086038	–1074.954094	55.42
Maleic	–455.7405525	–696.6086038	–1152.370308	55.53
Succinic	–456.9742366	–696.6086038	–1153.604634	57.22
Tartaric	–607.4032232	–696.6086038	–1304.033289	56.35
Adipic	–535.6104668	–696.6086038	–1232.240235	55.57
Octanedioic	–614.2422408	–696.6086038	–1310.871977	55.48
Note: *1 a.u. = 2625.5 kJ·mol⁻¹				

The results of computational modelling show that the energy of complex formation with an increase in the number of –(CH₂)– chain links in the series of succinic ($\Delta E_{c.f.} = 57.22$ kJ/mol) > adipic ($\Delta E_{c.f.} = 55.57$ kJ/mol) > octanedioic ($\Delta E_{c.f.} = 55.48$ kJ/mol) acids decreases. Oxalic acid, which does not contain a methylene group, has the lowest energy parameter value ($\Delta E_{c.f.} = 55.42$ kJ/mol). It can be seen that the presence of a multiple bond in maleic acid ($\Delta E_{c.f.} = 55.53$ kJ/mol) or hydroxy substituents in tartaric acid ($\Delta E_{c.f.} = 56.35$ kJ/mol) also results in a decrease in the complex formation energy, in comparison with succinic acid.

In accordance with the experiment [8], the values of the HOMO-LUMO gap between the frontier orbitals in the molecules of the complexes were found (Table 5).

SOMO-LUMO gap in a complex of dicarboxylic acids with 3,6-ditert.butyl-2-oxyphenoxyl calculated by the DFT UB3LYP/6-31G+(d, p) method

No.	Dicarboxylic acids	$E_{(LUMO)}$, a.u.	$E_{(SOMO)}$, a.u.	ΔE, a.u.
1	Oxalic acid	−0.13290	−0.21364	0.08074
2	Maleic acid	−0.14055	−0.22124	0.08069
3	Succinic acid	−0.12874	−0.20945	0.08071
4	Tartaric acid	−0.13542	−0.21622	0.0808
5	Adipic acid	−0.12616	−0.20686	0.0807

It can be seen from Table 5 that the SOMO-LUMO gap decreases in the range from 0.08074 to 0.0807 a.u. for a number of complexes with acids from oxalic to succinic and adipic. Thus, an increase in the carbon skeleton of dicarboxylic acid increases the ability to form a stronger hydrogen-bonded complex. It should be noted that the double bond in maleic acid contributes to a lower value of the SOMO-LUMO gap, compared with oxalic acid. The presence of hydroxy substituents in tartaric acid, on the contrary, increases the energy difference between the frontier orbitals to 0.0808 a.u.

To establish the effect of the solvent nature on the kinetics of the proton exchange process in a cyclic type model complex between maleic acid and 3,6-di-tert-butyl-2-hydroxyphenoxyl, the activation characteristics were analyzed using a Conductor-like Polarizable Continuum Model (CPCM) and an Integral Equation Formalism Polarizable Continuum Model (IEFPCM) (Table 6). The synchronous transit method (TS) was used to find the transition states of the complexes. The values of activation barriers were determined as the difference between the energy obtained during the complete optimization of the complex (E_1) and the energy of the transition state (E_{TS}):

$$\Delta E = E_1 - E_{TS}. \tag{3}$$

Activation characteristics of the proton exchange process in a model complex of the cyclic type of maleic acid with 3,6-di-tert-butyl-2-hydroxyphenoxyl in various solvents

Solvents	Model of a polarizable medium	E_1, a.u.*	E_{TS}, a.u.*	ΔE, a.u.*	ΔE, kJ/mol
Vacuum	–	−1152.363912	−1152.351546	0.0123653	32.465
Dioxane	CPCM	−1152.369499	−1152.357417	0.0120821	31.722
	IEFPCM	−1152.368304	−1152.356311	0.01199307	31.488
Toluene	CPCM	−1152.369878	−1152.357614	0.012264	32.199
	IEFPCM	−1152.36867	−1152.356662	0.01200827	31.528
Tetrahydrofuran	CPCM	−1152.373574	−1152.361337	0.012237	32.128
	IEFPCM	−1152.372796	−1152.360529	0.01226661	32.206
Nitrobenzene	CPCM	−1152.37506	−1152.362794	0.012266	32.204
	IEFPCM	−1152.374846	−1152.362501	0.012345	32.412

Note: *1 a.u.=2625.5 kJ·mol^{-1}

As can be seen from Table 6, there is a decrease in the activation barrier regardless of the solvents nature and the chosen solvation model. An increase in the polarity of the solvent leads to stabilization of the complex in comparison with the data obtained for the gas phase. In the absence of a solvation medium, the calculated value of the activation barrier of the process is 32.47 kJ/mol. In the 1,4 dioxane aprotic solvent ($\varepsilon = 2.21$) the value of ΔE is lower than in vacuum. It is 31.722 kJ/mol according to CPCM and 31.49 kJ/mol according to IEFPCM model. In toluene indifferent solvent, ($\varepsilon = 2.379$) the barrier value decreases to 32.19 kJ/mol (CPCM) and 31.52 kJ/mol (IEFPCM), in the case of a tetrahydrofuran solvating solvent ($\varepsilon = 7.58$) this value is 32.13 kJ/mol (CPCM) and 32.20 kJ/mol (IEFPCM). A relatively high activation energy value of 32.2 kJ/mol (CPCM) and 32.41 kJ/mol (IEFPCM) is predicted for the nitrobenzene polar solvent ($\varepsilon = 35.72$).

Conclusions

Quantum-chemical studies using the DFT B3LYP method made it possible to establish a correlation between the activation energy obtained from the experimental kinetic parameters of protolytic processes involving dicarboxylic acids and the energies of formation of cyclic-type complexes in dimeric molecules. It was shown that an increase in the number of methylene groups in a molecule leads to a rise in dimerization energies. At the same time, the appearance of multiple bonds or substituents in acid molecules allows for detecting the opposite effect. The energy gap between the frontier molecular orbitals of the studied dimer molecules increases with the length of the carbon skeleton and decreases in unsaturated and substituted analogs. However, the observed dependencies require further confirmation.

The weakening of hydrogen bonds in the homologous series of acids, as well as in a molecule containing hydroxy substituents or multiple bonds was revealed during the study of the structure of complex formed by the semiquinone radical with dicarboxylic aliphatic acids. In addition, using the example of maleic acid and the semiquinone radical, it was found that with an increase in the polarity of the solvent, the activation characteristics of the complex formation process decrease.

Based on the availability of experimental ESR spectroscopy data on the kinetics of protolytic reactions involving dicarboxylic acids, it is possible to continue theoretical studies of the mechanism of the reactions described above.

References

1   Limbach, H.H., Baumgartner, S., Franke, R., Mannle, F., Scherer, G., & Denisov, G.S. (2021). Double Proton Tautomerism via Intra- or Intermolecular Pathways? The Case of Tetramethyl Reductic Acid Studied by Dynamic NMR: Hydrogen Bond Association, Solvent and Kinetic H/D Isotope Effects. *Molecules*, *26*(14), Article 4373. https://doi.org/10.3390/molecules26144373

2   Macchi, P., Casati, N., Marshall, W.G., & Sironi, A. (2010). The alpha and beta forms of oxalic acid di-hydrate at high pressure: a theoretical simulation and a neutron diffraction study. *Crystengcomm*, *12*(9), 2596–2603. https://doi.org/10.1039/c002471f

3   Nikolskiy, S.N., Abilkanova, F.Z., Golovenko, A.S., Pustolaikina, I.A., & Masalimov, A.S. (2020). Investigation of intermolecular proton exchange of 3,6-di-tert.butyl-2-oxyphenoxyl with N-phenylanthranilic acid by ESR spectroscopy method. *Bulletin of the University of Karaganda – Chemistry* (98), 35–41. https://doi.org/10.31489/2020Ch2/35-41

4   Kutzhanova, K. Z., Kurmanova, A.F., Pustolaikina, I.A., & Ismagulov, B.M. (2018). Nonempirical modeling of protolytic processes in dimeric molecules of amino acids. *Bulletin of the University of Karaganda – Chemistry, 2*(90), 58–63. https://doi.org/10.31489/2018ch2/58-63

5   Pustolaikina, I.A., Kutzhanova, K.Z., Pushchina, A.V., & Kurmanova, A.F. (2018). Proton exchange in ammonia, water and formic acid dimers: quantum-chemical calculation. *Bulletin of the University of Karaganda – Chemistry, 2*(90), 64–70. https://doi.org/10.31489/2018ch2/64-70

6   Pustolaikina, I.A., Kurmanova, A.F., & Embergenova, A.K. (2011). Evaluation of protolytic ability for the series of OH-acids by the semiempirical methods of quantum chemistry. *Bulletin of the University of Karaganda – Chemistry* (61), 4–9.

7   Masalimov, A.S., Kurmanova, A.F., Nikolskiy, S.N., Ospanov, A.U., & Tur, A.A. (2014). ESR-spectroscopy of the fast proton exchange reactions in solutions. *Bulletin of the University of Karaganda – Chemistry, 1*(73), 30–35.

8   Masalimov, A.S., Bocharova, A.V., Kurmanova, A.F., Khasanova, E.R., & Nikolsky, S.N. (2009). ESR spectroscopy of the protolytic ability of carboxylic acids. *Bulletin of the University of Karaganda – Chemistry,* (55), 4–10.

9   Wang, C.H., Zhang, R.Q., & Lin, Z.J. (2012). A comparative study on intermolecular hydrogen bond interactions in molecular dimers using different levels of computational methods. *Journal of Theoretical & Computational Chemistry*, *11*(6), 1237–1259. https://doi.org/10.1142/s0219633612500836

10 Thangarasu, S., Siva, V., Athimoolam, S., & Bahadur, S. A. (2018). Molecular structure, spectroscopic and quantum chemical studies on benzoic acid and succinic acid co-crystals of 2-aminopyrimidine. *Journal of Theoretical & Computational Chemistry*, *17*(4), Article 1850021. https://doi.org/10.1142/s0219633618500219

11 Mroz, D., Wang, R.M., Englert, U., & Dronskowski, R. (2021). Displacement parameters from density-functional theory and their validation in the experimental charge density of tartaric acid. *Crystengcomm, 23*(4), 1052–1058. https://doi.org/10.1039/d0ce01425g

12 Esrafili, M.D., & Behzadi, H. (2012). A theoretical study on H-bonding interactions in maleic acid: calculated O-17, H-1 NMR parameters and QTAIM analysis. *Molecular Simulation, 38*(11), 896–905. https://doi.org/10.1080/08927022.2012.669477

13 Ganesan, M., Vedamanickam, N., & Paranthaman, S. (2018). Studies of intramolecular H-bond interactions and solvent effects in the conformers of glycolic acid — A quantum chemical study. *Journal of Theoretical & Computational Chemistry, 17*(1). https://doi.org/10.1142/s0219633618500098

14 Malloum, A., & Conradie, J. (2021). Proton transfer free energy and enthalpy from water to methanol. *Computational and Theoretical Chemistry, 1199*. https://doi.org/10.1016/j.comptc.2021.113189

15 Bureiko, S.F. (2003, May 25–Jun 01). *The kinetic spectroscopy of hydrogen exchange processes in systems with hydrogen bond.* Paper presented at the 16th International Conference on Spectroscopy of Molecules and Crystals, Sevastopol, Ukraine.

16 Xu, W., & Zhang, R.Y. (2012). Theoretical Investigation of Interaction of Dicarboxylic Acids with Common Aerosol Nucleation Precursors. *Journal of Physical Chemistry A, 116*(18), 4539–4550. https://doi.org/10.1021/jp301964u

17 Otukile, K.P., & Kabanda, M.M. (2019). A DFT mechanistic, thermodynamic and kinetic study on the reaction of 1,3,5-trihydroxybenzene and 2, 4, 6-trihydroxyacetophenone with (OOH)-O-center dot in different media. *Journal of Theoretical & Computational Chemistry, 18*(4). https://doi.org/10.1142/s0219633619500238

18 Terent'ev, A.O., Borisova, N.S., Khamitov, E.M., Zimin, Y.S., & Mustafin, A.G. (2014). Experimental and Quantum-Chemical Studies of the Reactions of 6-Methyluracil with Succinic and Fumaric Acids. *Russian Journal of Physical Chemistry A, 88*(12), 2068–2072. https://doi.org/10.1134/s003602441412036x

19 Macoas, E.M.S., Fausto, R., Lundell, J., Pettersson, M., Khriachtchev, L., & Rasanen, M. (2001). A matrix isolation spectroscopic and quantum chemical study of fumaric and maleic acid. *Journal of Physical Chemistry A*, *105*(15), 3922–3933. https://doi.org/10.1021/jp003802p

А.Ф. Курманова, Ф.Ж. Абилканова, А.С. Рахимжанова, И.А. Пустолайкина

Дикарбон қышқылдары қатысатын комплекс түзілу реакцияларын DFT зерттеу: сутектік байланыс, еріткіш табиғатының әсері

Мақалада кейбір дикарбон қышқылдарының протолиттік қабілетіне кванттық-химиялық зерттеулер жүргізілген. Малеин, янтарь, шарап, қымыздық және адипин қышқылдарының димерлі молекулаларының геометриялық және кинетикалық параметрлері зерттелді. Олардың димерлену энергиясы базалық жиынтық суперпозиция қатесін (BSSE) ескере отырып анықталды. Дикарбон қышқылдарының кинетикалық параметрлерінің көміртек қаңқасы, қанықпаған байланыстар және гидроксил алмастырғыштары болған кездегі тәуелділігі дәлелденді. Зерттелетін димер қышқылы молекулаларының шекаралық молекулалық орбитальдары қарастырылды. ЖТМО және ТБМО деңгейлері арасындағы энергия параметрлерінің айырмашылығы анықталды. Энергиялық аралықтардың алынған мәндері екі сутектік байланыстың қатысуымен түзілетін циклдік қосылыстар қатарындағы тұрақтылықтың жоғарылауын көрсетеді. Қышқылдардың 3,6-ди-трет-бутил-2-оксифеноксил семихинон радикалымен комплекс түзу қабілеті зерттелді. СРСМ және IEFPCM үлгілерін пайдалана отырып, семихинон радикалы — дикарбон қышқылы жүйесінің күрделі түзілу реакциясының активтену тосқауылына еріткіш табиғатының әсерін талдау қарастырылған. Энергетикалық параметрдің еріткіштің полярлығына тәуелділігі толуол, тетрагидрофуран және нитробензол мысалында анықталды. Молекулалық құрылымдарды оңтайландыру үшін DFT әдісі 6-31+G (d, p) негізіндегі B3LYP жуықтауында қолданылды. Есептеулер Gaussian 16 Revision A.03 WIN64 бағдарламасы арқылы жүргізілді.

Кілт сөздер: кванттық химиялық есептеулер, тығыздықтың функционалдық теориясы, сутектік байланыс, молекулааралық сутектік байланыстар, өтпелі қалыптасу, комплекстер, шекаралық молекулалық орбитальдар, димерлену энергиясы, күрделі түзілу энергиясы, еріткіш табиғатының әсері.

А.Ф. Курманова, Ф.Ж. Абилканова, А.С. Рахимжанова, И.А. Пустолайкина

ДФТ изучение реакций комплексообразования с участием дикарбоновых кислот: водородные связи, влияние природы растворителя

В статье проведены квантово-химические исследования протолитической способности некоторых дикарбоновых кислот. Исследованы геометрические и кинетические параметры димерных молекул малеиновой, янтарной, винной, щавелевой и адипиновой кислот. Их энергии димеризации были определены с учетом ошибки суперпозиции базисного набора (BSSE). Подтверждена зависимость кинетических параметров дикарбоновых кислот от наличия углеродного скелета, ненасыщенных связей и гидроксильных заместителей. Были рассмотрены граничные молекулярные орбитали исследуемых молекул димерных кислот, и определена разница энергетических параметров между уровнями ВЗМО и НСМО. Полученные значения энергетических щелей свидетельствуют об увеличении устойчивости в ряду циклических соединений, образованных с участием двух водородных связей. Изучена способность кислот к комплексообразованию с радикалом семихинона 3,6-ди-трет.бутил-2-гидроксифеноксилом. Выполнен анализ влияния природы растворителя на активационный барьер реакции комплексообразования системы семихиноновый радикал–дикарбоновая кислота с использованием моделей СРСМ и IEFPCM. На примерах толуола, тетрагидрофурана и нитробензола установлена зависимость энергетического параметра от полярности растворителя. Для оптимизации молекулярных

структур использовали метод DFT в приближении B3LYP с базисным набором 6-31+G (d, p). Расчеты проводились с использованием программы Gaussian 16 Revision A.03 WIN64.

Ключевые слова: квантово-химические расчеты, теория функционала плотности, водородная связь, межмолекулярные водородные связи, переходное образование, комплексы, пограничные молекулярные орбитали, энергия димеризации, энергия комплексообразования, влияние природы растворителя.

Information about authors*

Kurmanova, Alfiya Faridovna — Candidate of Chemical Sciences, Professor, Karagandy University of the name of academician E.A. Buketov, Universitetskaya street, 28, 100024, Karaganda, Kazakhstan; e-mail: alfiya_kurmanova@mail.ru, https://orcid.org/0000-0003-4548-8145;

Abilkanova, Farida Zhumageldyevna — PhD student, Karagandy University of the name of academician E.A. Buketov, Universitetskaya street, 28, 100024, Karaganda, Kazakhstan; e-mail: Farida_b88@mail.ru, https://orcid.org/0000-0002-6894-5276;

Rakhimzhanova, Aida Sabitovna — PhD student, Karagandy University of the name of academician E.A. Buketov, Universitetskaya street, 28, 100024, Karaganda, Kazakhstan; e-mail: aida_ekb@mail.ru, https://orcid.org/0000-0002-4984-623X;

Pustolaikina, Irina Anatolevna — Candidate of Chemical Sciences, Associate Professor, Karagandy University of the name of academician E.A. Buketov, Universitetskaya street, 28, 100024, Karaganda, Kazakhstan; e-mail: ipustolaikina@gmail.com, https://orcid.org/0000-0001-6319-666X

_____

*The author's name is presented in the order: *Last Name, First and Middle Names*

K.M. Turdybekov[1*], S.A. Ivasenko[2], D.M. Turdybekov[3], A.S. Makhmutova[2], Yu.V. Gatilov[4], S.M. Adekenov[5]

[1]*Karagandy University of the name of academician E.A. Buketov, Kazakhstan;*
[2]*Karaganda Medical University, Kazakhstan;*
[3]*Karaganda Technical University, Kazakhstan;*
[4]*N.N. Vorozhtsov Novosibirsk Institute of Organic Chemistry, Russia;*
[5]*International Research and Production Holding "Phytochemistry", Karaganda, Kazakhstan*
*(*Corresponding author's e-mail: xray-phyto@yandex.kz)*

Isolation and Structure of the New Sesquiterpene Lactone 3-oxo-10β-hydroxy-5,7α(H),4,6β(H)-guai-1,11(13)-diene-6,12-olide

The article presents the results of a chemical study of *Tanacetopsis pjataevae*, which is an endemic plant in Kazakhstan. The number of extractive substances was obtained by extraction with chloroform from the air-dry crushed above-ground part of the plant collected in the flowering phase. Isolation of compounds was carried out by column chromatography on a column of silica gel brand KSK at a ratio of sum - carrier = 1:20. A colorless crystalline substance of the composition $C_{15}H_{18}O_4$ with m.p. 189–191°C (recrystallized from diethyl ether) was found when the column was eluted with a mixture of petroleum ether-ethyl acetate (87.5:12.5). The structure of the obtained new compound (3-oxo-10β-hydroxy-5,7α(H),6β(H)-guai-1,11(13)-diene-6,12-olide) was established based on IR, NMR analysis and mass spectra. The spatial structure was determined by the X-ray diffraction method. It was established that the 3-oxo-10β-hydroxy-5,7α(H),6β(H)-guai-1,11(13)-diene-6,12-olide molecule in the crystal is disordered over two conformational states in the 6:4 ratio. The stability of these conformers was confirmed by semi-empirical quantum-chemical calculations. It was established that the difference in the heat of formation of two conformers was 6.3 kJ/mol for a free molecule.

Keywords: NMR spectroscopy, IR spectroscopy, mass spectrometry, X-ray analysis, *Tanacetopsis pjataevae*, endemic, 3-oxo-10β-hydroxy-5,7α(H),6β(H)-guai-1,11(13)-diene-6,12-olide, sesquiterpene lactones.

Introduction

Natural sesquiterpene γ-lactones (STL) are potentially biologically active substances. The structure of STL includes such pharmacophore groups as α-methylene-γ-lactone ring and α,β-unsaturated enone system. Some STL have an epoxy ring, a hydroxyl group, and chlorine atoms. A study of the chemical composition of endemic plants is being actively carried out to search for new bioactive compounds in Kazakhstan. For the first time, over 30 STL were isolated and identified from endemic plants. A total of 11 of these compounds are new ones, namely raposerine, racerolide, 15-deacetylraposerine, racerin, anolide, achymicrin, gracilin and argracin, 1β-acetoxy-7α,6,11β(H)-eudesm-4(5)-en-6,12-olide, 1β-acetoxy-3β-hydroxy-eudesm-4(5)-en-6,12-olide, and artesin [1, 2].

In continuation of these works, it has been studied the chemical composition of the aboveground part of the *Tanacetopsis pjataevae* (Kovalevsk.) Karmyscheva, which is an endemic species of Kazakhstan, growing in the Karatau mountains [3]. The literature sources [4–8] describe the results of a chemical study of *Tanacetopsis mucronata* Rgl. et Schmalh. growing in Tajikistan. The sesquiterpene lactones, namely deacetyl laurenobiolide, dihydrodeacetyl laurenobiolide, mucrine, tavulin, tanakhine, tamirin, 13α-hydroxymethylene deacetyl laurenbiolide were isolated from Tanacetopsis spiky. Later, the chemical composition of another member of the *Tanacetopsis* genus was investigated. Sesquiterpene lactones 1R,10S,3S,4R-diepoxyguai-5S,6S,7S-11(13)-en-6,12-olide and hanfillin were isolated from the aboveground part of *Tanacetopsis karataviensis* (Kovalevsk.) [9]. The previously known sesquiterpene lactones arglabin and isoepoxyestafiatin were isolated from *Tanacetopsis pjataevae* (Kovalevsk.) Karmyscheva [2].

Experimental

IR spectra were obtained on a spectrometer "Thermo Nicolet Avatar-360" (USA) in potassium bromide tablets in the range from 4000 to 600 cm^{-1}. NMR spectra were recorded on a Bruker DRX-600 spectrometer

using standard Bruker software. The Finnigan DMS-8200 high-resolution mass spectrometer with an ionizing voltage of 70 eV (evaporator temperature was 220 °C) was used to record mass spectra, as well as determine the molecular weight and elemental composition. Melting point was determined on an SMF-38 heating table. The reaction progress was monitored by TLC. Sorbfil plates were used for TLC, which were developed by spraying with a 2% aqueous $KMnO_4$ solution. KSK silica gel was used for column chromatography.

Isolation of 3-oxo-10β-hydroxy-5,7α(H),6β(H)-guai-1,11(13)-diene-6,12-olide (**1**). Air-dry crushed raw materials of *Tanacetopsis pjataevae* (0.7 kg, leaves, flower baskets, buds) collected in the flowering phase in the Arpaozen Gorge, Karatau, South Kazakhstan region were extracted with chloroform 3 times. Then the solvent was evaporated. Next, the number of extractives (44 g) was chromatographed on a column of silica gel grade KSK at a ratio of sum – carrier = 1:20. When the column was eluted with a mixture of petroleum ether-ethyl acetate (87.5:12.5), substance **1** was isolated with a yield of 0.200 g (0.029% based on air-dry raw materials). The colorless crystalline substance of the $C_{15}H_{18}O_4$ composition with m.p. 189–191 °C was obtained by recrystallization from diethyl ether.

IR spectrum (KBr, ν, cm^{-1}): 3463 (OH group), 2935, 2872, 1750 (C=O γ-lactone), 1707 (C=O), 1608 (C=C), 1456, 1410, 1371, 1356, 1325, 1261, 1173, 1154, 1081, 1064, 989, 971, 957, 883, 819, 758, 728, 666, 640, 558, 501, 425.

^1H NMR spectrum (600 MHz, $CDCl_3$, δ, ppm, J/Hz): 6.33 (1H, s, H2), 2.57 (1H, d, J=6.0, overlapping with OH-10, H4), 2.69 (1H, d, J=11.0, H5), 3.95 (1H, t, J=10.0, H6), 2.93 (1H, m, H7), 1.75 (1H, m, H8a), 2.23 (1H, dd, J1=7.0, J2=7.0, H8b), 1.99 (2H, m, H9), 5.49 (1H, s, H13a), 6.18 (1H, s, H13b), 1.27 (3H, br.d, J=6.0, CH3-14), 1.54 (3H, s, CH₃-15). 2.57 d (1H, d, J=6.0, overlap with H-4, OH-10).

^{13}C NMR spectrum (150.96 MHz, $CDCl_3$ δ, ppm): 169.12 (s, C1), 129.78 (d, C2), 209.23 (s, C3), 46.52 (d, C4), 55.24 (d, C5), 82.89 (d, C6), 46.42 (d, C7), 21.49 (t, C8), 37.60 (t, C9), 73.42 (s, C10), 139.73 (s, C11), 181.07 (s, C12), 119.90 (t, C13), 27.83 (q, C14), 15.58 (q, C15).

Mass spectrum (70 eV, m/z, Irel. (%)): 262.1 [M]+. Calculated: m/z 262.1200. Found: m/z 262.1196.

Quantum-chemical calculations were carried out using the MOPAC software package version 9.0. Optimization of the molecule geometrical data was carried out by the PM6 method [10].

X-ray analysis of compound **1**. The cell parameters and the intensity of 15346 reflections (3216 independent, R_{int}=0.0491) were measured on a diffractometer "Bruker Kappa APEX2 CCD" ($MoK_α$, graphite monochromator, ω-scan, 2.667 ≤ θ ≤ 27.653) at 296 K. The crystals are orthorhombic, a=7.7072(3), b=11.8416(5), c=15.2767(6) Å, V=1394.2(1) Å^3, Z=4 ($C_{15}H_{18}O_4$), the space group $P2_12_12_1$, d_{calc}=1.250 g/cm^3, μ=0.090 mm^{-1}. The initial array of the measured intensities was processed and absorption was taken into account using the SAINT [11] and SADABS [12] programs (multi-scan, $T_{min.}$ 0.957, $T_{max.}$ 0.981).

The structure was solved via a direct method. The positions of nonhydrogen atoms were refined under anisotropic approximation by full-matrix least-squares method. All hydrogen atoms were put in the geometric positions and refined under isotropic approximation with constant position and heat parameters (*rider* model). The structure was determined and refined using the SHELXS [13] and SHELXL-2018/3 [14] software. A total of 2788 independent reflections with I ≥ 2σ(I) were used in the calculations and the number of refined parameters was 257.

The final divergence factors were R_1=0.0408, $_wR_2$=0.1068 (for reflections with $I ≥ 2σ(I)$), R_1 = 0.0495, $_wR_2$ = 0.1145 (for all reflections), *GooF* = 1.032. Peaks of residual density were Δρ = 0.156 and –0.128 e/Å^3. The CIF file containing the complete information on the structure examined was deposited in the Cambridge Center for Crystal Structural Data (CCDC) under number 2006552. The atomic coordinates are shown in Table 1.

T a b l e   1

The coordinates of the atoms in the cell fractions (×10⁴)
and isotropic thermal parameters (Å², ×10³) in the structure 1

Atom	x	y	z	$U_{eq.}$
1	2	3	4	5
O1	2036(2)	–776(1)	–151(1)	53(1)
O2A	260(30)	–2216(13)	–487(9)	86(4)
O2B	–100(40)	–1910(20)	–457(17)	91(6)
O3	4808(4)	2953(2)	–612(2)	113(1)
O4A	4186(16)	2035(8)	2583(6)	79(3)

1	2	3	4	5
O4B	4680(20)	2013(10)	2656(10)	81(5)
C1	4636(3)	1242(2)	1227(1)	47(1)
C2	4828(3)	2253(2)	863(2)	62(1)
C3	4755(4)	2177(2)	−87(2)	70(1)
C4	4627(4)	949(2)	−334(1)	65(1)
C5	4338(3)	327(2)	542(1)	46(1)
C6	2514(2)	−122(2)	630(1)	43(1)
C7	2233(3)	−948(2)	1382(1)	51(1)
C8A	2266(14)	−292(9)	2274(7)	80(3)
C8B	1867(19)	−541(10)	2289(11)	54(2)
C9A	4134(8)	−17(3)	2539(2)	70(2)
C9B	2465(8)	661(5)	2470(3)	54(2)
C10A	4902(12)	1073(8)	2150(6)	54(2)
C10B	4382(16)	957(12)	2275(8)	50(3)
C11A	610(20)	−1552(14)	988(9)	85(4)
C11B	920(30)	−1660(20)	1126(13)	69(4)
C12A	860(20)	−1507(17)	33(9)	72(4)
C12B	870(30)	−1640(30)	152(13)	64(5)
C13A	−717(14)	−1917(9)	1459(6)	114(4)
C13B	−178(19)	−2477(9)	1407(8)	83(3)
C14A	6907(7)	1086(6)	2354(4)	99(2)
C14B	5673(10)	98(6)	2536(4)	73(2)
C15	6255(6)	571(4)	−800(2)	118(2)

Results and Discussions

A colorless substance **1** of the $C_{15}H_{18}O_4$ composition was obtained from the extract of the aerial part of *Tanacetopsis pjataevae* when the column was eluted with a mixture of petroleum ether-ethyl acetate (87.5:12.5).

The IR spectrum of compound **1** contains absorption bands characteristic of the OH group at 3463 cm^{-1}, the carbonyl of the γ-lactone ring at 1750 cm^{-1}, and the C=O bonds at 1707 cm^{-1}, C=C at 1608 cm^{-1}. In the mass spectrum of **1** there is a peak of the molecular ion m/z 262.1 [M]$^+$, which corresponds to the molecular weight.

In the ^1H NMR spectrum of molecule **1**, signals of the protons of the methyl group at the C4 atom are observed as a doublet at 2.57 ppm with SSIC 6.0 Hz, protons of the methyl group at the hydroxyl group as a singlet at 1.54 ppm, proton H5 as a doublet at 2.69 ppm with SSIC 11 Hz. Two symmetrical singlets at 5.49 ppm and 6.18 ppm belong to the protons of the exomethylene group (C11=C13H$_2$). The H7 methine proton appears as a multiplet centered at 2.93 ppm, while the H6 lactone proton appears as a triplet at 3.95 ppm with SSIC 10.0 Hz. The vinyl H2 proton appears as a singlet at 6.33 ppm, the hydroxyl proton appears as a doublet at 2.57 ppm with SSIC 6.0 Hz. The nature of the splitting of the signal of the lactone proton indicates that the lactone ring in compound **1** is located at C6-C7 of the main skeleton, and the spin-spin coupling constant indicates its trans junction.

The ^{13}C NMR spectrum of the molecule **1** shows the presence of 5 singlets, 5 doublets, 3 triplets, and 2 quartets. This corresponds to the structural formula of compound **1**.

Based on spectral data, compound **1** was identified as 3-oxo-10β-hydroxy-5,7α(H),6β (H)-guai-1,11(13)-diene-6,12-olide, a new STL of guaiane type (Fig. 1).

An X-ray analysis was performed to finally establish the structure of compound **1**. From the obtained data it follows that there is one molecule **1**, half of whose atoms are statically disordered in two positions, in the independent part of the unitary crystalline cell. The bond lengths (Table 2) and bond angles (Table 3) in compounds **1**

Figure 1. Structural formula of molecule 3-oxo-10β-hydroxy-5,7α(H),6β(H)-guai-1,11(13)-diene-6,12-olide **(1)**

somewhat differ from the usual ones [15]. This is related to the disorder of a number of atoms of structure **1** in the crystalline state.

Bond lengths (*d*, Å) in conformers 1a and 1b of the structure 1

Bond	*d*		Bond	*d*	
	1a	**1b**		**1a**	**1b**
O1-C12	1.283(14)	1.44(2)	C4-C15	1.510(3)	1.510(3)
O1-C6	1.470(2)	1.470(2)	C5-C6	1.509(2)	1.509(2)
O2-C12	1.245(11)	1.236(16)	C6-C7	1.523(2)	1.523(2)
O3-C3	1.219(2)	1.219(2)	C7-C8	1.570(8)	1.494(12)
O4-C10	1.429(8)	1.398(12)	C7-C11	1.561(9)	1.372(15)
C1-C2	1.328(2)	1.328(2)	C8-C9	1.531(8)	1.522(9)
C1-C10	1.439(7)	1.648(9)	C9-C10	1.540(6)	1.547(9)
C1-C5	1.523(29)	1.523(29)	C10-14	1.576(8)	1.477(11)
C2-C3	1.455(3)	1.455(3)	C11-12	1.473(10)	1.489(14)
C3-C4	1.506(3)	1.506(3)	C11-13	1.323(10)	1.357(14)
C4-C5	1.544(2)	1.544(2)			

Valent angles (ω, deg.) in conformers 1a and 1b of the structure 1

Angle	ω		Angle	ω	
	1a	**1b**		**1a**	**1b**
C12-O1-C6	110.8(4)	105.7(6)	C6-C7-C11	96.7(4)	106.5(6)
C2-C1-C5	111.7(1)	111.7(1)	C6-C7-C8	109.5(3)	121.2(4)
C2-C1-C10	121.3(3)	127.2(4)	C11-C7-C8	125.0(6)	108.8(7)
C10-C1-C5	126.6(3)	120.2(4)	C9-C8-C7	110.4(5)	114.4(7)
C1-C2-C3	110.9(2)	110.9(2)	C8-C9-C10	115.9(5)	117.7(6)
O3-C3-C2	127.4(2)	127.4(2)	O4-C10-C1	106.8(5)	101.6(7)
O3-C3-C4	124.4(2)	124.4(2)	O4-C10-C9	110.0(5)	106.3(8)
C2-C3-C4	108.2(2)	108.2(2)	C1-C10-C9	116.1(5)	110.3(6)
C3-C4-C5	104.7(1)	104.7(1)	O4-C10-C14	106.3(6)	113.0(9)
C3-C4-C15	110.5(2)	110.5(2)	C1-C10-C14	109.3(4)	108.9(6)
C15-C4-C5	112.8(2)	112.8(2)	C9-C10-C14	108.0(5)	115.8(6)
C6-C5-C1	109.2(1)	109.2(1)	C13-C11-C12	130.7(9)	107.9(14)
C6-C5-C4	112.4(1)	112.4(1)	C13-C11-C7	124.0(8)	143.9(11)
C1-C5-C4	103.6(1)	103.6(1)	C12-C11-C7	105.1(7)	107.3(11)
O1-C6-C5	110.3(1)	110.3(1)	O2-C12-O1	125.3(11)	108.8(17)
O1-C6-C7	103.8(1)	103.8(1)	O2-C12-C11	123.9(13)	139.9(18)
C5-C6-C7	115.2(1)	115.2(1)	O1-C12-C11	109.5(8)	108.2(12)

It should be noted that in some STL crystalline structures, disordering of atoms is observed. Usually, some substituents are disordered in the main framework. For example, the phenyl group is disordered in eupatocunin-*o*-bromobenzoate [16], and the isobutyl group is disordered in 8α-isobutyryloxy-9-oxo-germacr-4E,1(10) Z-dien-6β,12-olide [17].

In compounds **1**, an unusual disorder of a part of the atoms of the main framework was observed. An analysis of the data showed that the positions of the atoms in the crystal structure **1** corresponded to two conformers **1a** and **1b** (Fig. 2).

1a   **1b**
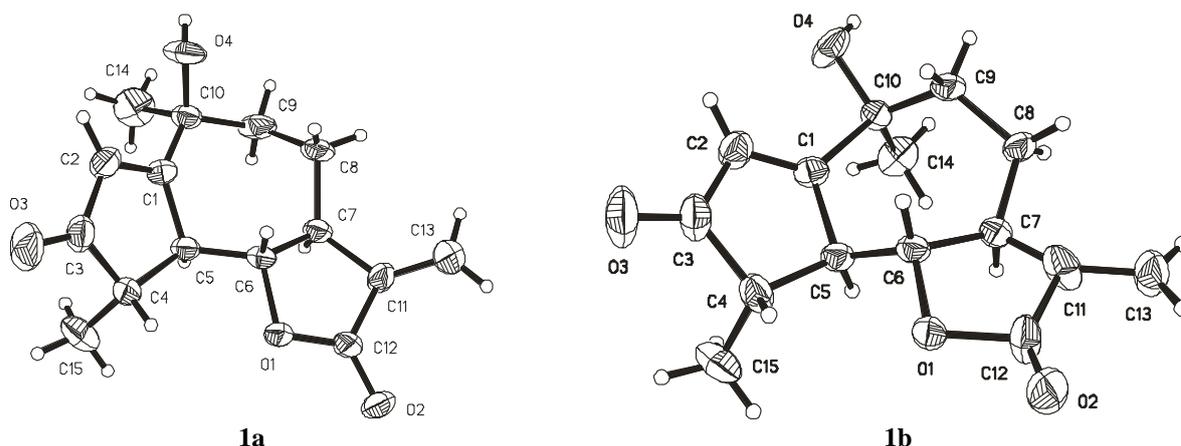
Figure 2. Conformers **1a** and **1b** of disordered molecule 3-oxo-10β-hydroxy-5,7α(H),6β (H)-guai-
1,11(13)-diene-6,12-olide **(1)** (thermal vibration ellipsoids are shown with a probability of 30%)

The conformation of the five-membered carbocycle (A) in both conformers is a strongly flattened, distorted 4α-envelope ((ΔC_S^4=2.0°). The seven-membered cycle (B) in conformer **1a** accepts the intermediate conformation between the 7α,1,10β- chair (ΔC_S^7=17.1°) и 5,6α,7,8β- twist-chair (ΔC_2^{10}=13.7°), in the conformer, **1b** accepts the intermediate conformation between 7.8α,1β-chair ((ΔC_S^1=18.5°) and 1.10α, 5,6β-twist-chair (ΔC_2^8=19.7°). The conformation of lactone cycle in both conformers is a distorted 6β,7α-half-chair (($\Delta C_2^{6,7}$=4.8° and 2.4° for **1a** and **1b**, respectively). Intracyclic torsion angles are illustrated in Table 4.

In the crystal, the ratio of conformers 1a and **1b** is 60:40, and the conformations of the seven-membered cycle in them are significantly distorted relative to the ideal chair and the twist chair. To optimize the geometry of conformers **1a** and **1b**, a quantum chemical calculation was performed using the MOPAC program in the PM6 [10] parameterization. As follows from the obtained calculations, the five-membered carbocycle is slightly flattened in comparison with the X-ray diffraction data and takes in **1a** and **1b** the conformation intermediate between the 4α-envelope and 4α,5β- half-chair (ΔC_S^4=2.0°, $\Delta C_2^{4,5}$=1.7°) for **1a** and (ΔC_S^4=1.9°, $\Delta C_2^{4,5}$=0.5° for **1b**. The seven-cycle conformation in **1a** and **1b** undergoes the greatest changes. In conformer **1a**, it changes from that observed in the crystal to the intermediate between the 7α,1,10β-chair (ΔC_S^7=19.8°) and 8.9α,6,7β-twist-chair (ΔC_2^8=8.8°). In conformer **1b**, the conformation of cycle B is generally preserved, leaning toward a highly distorted 1,10α, 5,6β-twist-chair (ΔC_2^8=8.8°). The lactone cycle is also somewhat flattened, but remains in the conformation of the somewhat distorted 6β,7α-half-chair (3.8° for **1a** and 3.1° for **1b**).

T a b l e 4

Intracyclic torsion angles (τ, degr.) in n conformers 1a and 1b

Angle	τ			
	1a (X-ray)	**1a** (PM6)	**1b** (X-ray)	**1b** (PM6)
1	2	3	4	5
Cycle A				
C5-C1-C2-C3	–2.0(3)	–1.8	–2.0(3)	–1.7
C1-C2-C3-C4	–4.5(3)	–4.0	–4.5(3)	–2.4
C2-C3-C4-C5	8.7(3)	7.7	8.7(3)	5.2
C3-C4-C5-C1	–9.3(2)	–8.5	–9.3(2)	–5.9
C2-C1-C5-C4	7.3(2)	6.7	7.3(2)	5.0
Cycle B				
C10-C1-C5-C6	74.6(5)	47.6	57.6(6)	52.1
C1-C5-C6-C7	–77.8(2)	–90.1	–77.8(2)	–72.5
C5-C6-C7-C8	72.7(5)	84.2	84.4(7)	95.9
C6-C7-C8-C	–77.7(7)	–67.8	–22.2(13)	–43.9
C7-C8-C9-C10	85.4(8)	79.6	–53.5(13)	–36.5
C8-C9-C10-C1	–46.5(9)	–75.5	82.2(11)	83.3
C5-C1-C10-C9	–25.4(9)	20.5	–64.6(10)	–68.0

1	2	3	4	5
Cycle C				
O1-C6-C7-C11	−35.7(6)	−28.4	−30.1(12)	−20.0
C12-O1-C6-C7	30.6(8)	22.4	24.3(11)	15.7
C6-O1-C12-C11	−8.9(13)	−6.9	−11.0(20)	−4.7
C7-C11-C12-O1	−15.7(15)	−11.9	−8.0(30)	−8.7
C6-C7-C11-C12	31.4(10)	24.3	23.0(20)	17.4

It should be noted that for a free molecule, the heat of formation of conformer **1a** is lower than that of **1b** (ΔH_f = 6.3 kJ/mol. Such a conformation of cycle B (ΔC_2^1=7.8°), as in **1a**, was observed in the structure of hypochaerin [18], which was the only studied by the X-ray diffraction method with the sp^2-hybridized C(1) atom of the seven-membered ring, being consistent with the theory of the implementation of the most stable conformer in the crystal [19].

Conclusions

As a result of the *Tanacetopsis pjataevae* chemical study, an endemic plant of Kazakhstan, a colorless crystalline substance of the $C_{15}H_{18}O_4$ composition with m.p. 189–191°C was isolated. The structure of the obtained new compound according to IR, NMR and mass spectra was determined as 3-oxo-10β-hydroxy-5,7α(H),6β(H)-guai-1,11(13)-diene-6,12-olide. From the data of X-ray diffraction analysis, it was established that the molecule of 3-oxo-10β-hydroxy-5,7α(H),6β(H)-guai-1(2),11(13)-diene-6,12-olide in the crystal was disordered in two conformational states in a ratio of 6:4. Quantum-chemical semi-empirical calculations established that for a free molecule the difference in the heats of formation of conformers was 6.3 kJ/mol.

References

1 Adekenov S.M. Sesquiterpene lactones from endemic species of the family Asteraceae / S.M. Adekenov // Chem. Natur. Comp. — 2013. — Vol. 49, No 1. — P. 158–162. https://doi:10.1007/s10600-013-0543-y

2 Адекенов С.М. Растения — источники новых лекарственных веществ / С.М. Адекенов, Е.М. Габдуллин, А.Н. Куприянов // Фармацевт. бюл. — 2015. — № 1, 2. — С. 9–16.

3 Павлов Н.Б. Флора Казахстана / Н.Б. Павлов. — Алма-Ата: Наука, 1966. — 639 с.

4 Abduazimov B.C. Components of Tanacetopsis mucronata / B.C. Abduazimov, A.I. Yunusov, G.P. Sidyakin // Chem. Natur. Comp. — 1983. — Vol. 19, No. 6. — P. 764, 765. https://doi.org/10.1007/BF00575207

5 Makhmudov M.K. Crystal and molecular structure of the sesquiterpene lactone mucrin / M.K. Makhmudov, B.K. Abduazimov, B. Tashkhodzhaev, B.T. Ibragimov, M.R. Yagudaev // Chem. Natur. Comp. — 1988, — Vol. 24, No. 1. — P. 49–53. https://doi.org/10.1007/BF00597573

6 Abduazimov B.C. Structure of macrolide / B.C. Abduazimov, B. Tashkhodzhaev, S. Nasirov, I.D. Sham'yanov, M.R. Yagudaev, V.M. Malikov //Chem. Natur. Comp. — 1991. — Vol. 27, No. 1. — P. 15–19. https://doi.org/10.1007/BF00629823

7 Izbosarov M.B. Structure of mucroflavone B / M.B. Izbosarov, B.R. Abduazimov, A. Vdovin, E.L. Kristallovich, M.P. Yuldashev // Chem. Natur. Comp. — 1999. — Vol. 35, No. 6. — P. 625–627. https://doi.org/10.1007/BF02236287

8 Tashkhodzhaev B. 13α-Hydroxymethylenedeacetyllaurenobiolide, a New Germacranolide from Tanacetopsis mucronata / B. Tashkhodzhaev, B.K. Abduazimov, M.B. Izbosarov, I.D. Sham'yanov, M.Y. Antipin // Chem. Natur. Comp. — 2002. — Vol. 38, No. 6. — P. 557–560. https://doi.org/10.1023/A:1022682620162

9 Dusmatova D.E. Isolation of cytotoxic sesquiterpene lactones from the Tanacetopsis karataviensis (Kovalevsk.) Kovalevsk / D.E. Dusmatova, K.M. Bobakulov, R.F. Mukhamatkhanova, K.K. Turgunov, E.O. Terenteva, E.A. Tsay, I.D. Sham'yanov, B. Tashkhodzhaev, S.S. Azimova, N.D. Abdullaev / Natur. Prod. Research. — 2021. — Vol. 35, No. 12. — P. 1939–1948. https://doi.org/10.1080/14786419.2019.1647423

10 Stewart J.J.P. Optimization of parameters for semiempirical methods V: modification of NDDO approximations and application to 70 elements / J.J.P. Stewart // J. Mol. Modeling. — 2007. — Vol. 13. — P. 1173–1213. https://doi:10.1007/s00894-007-0233-4

11 Bruker. SAINT. Bruker AXS Inc., Madison, Wisconsin, USA. 2015.

12 Bruker. SADABS. Bruker AXS Inc., Madison, Wisconsin, USA. 2015.

13 Sheldrick G.M. Crystal structure solution with SHELXS / G.M. Sheldrick // Acta Crystaollogr., Sect. A. — 2008. — Vol. 64, — P. 112–122. https://doi.org/10.1107/S0108767307043930

14 Sheldrick G.M. Crystal structure refinement with SHELXL / G.M. Sheldrick // Acta Crystaollogr., Sect. C. — 2015. — Vol. 71, — P. 20153–8. https://doi.org/10.1107/S2053229614024218

15 Allen F.H. Tables of bond lengths determined by x-ray and neutron diffraction / F.H. Allen, O. Kennard, D.G. Watson, L. Brammer, A.G. Orpen, R. Taylor //J. Chem. Soc., Perkin Trans. 2. — 1987. — P. S1–S19. https://doi.org/10.1039/A701672G

16 Cox P.J. X-ray and molecular mechanics studies on the sesquiterpene lactone eupatocunin-o-bromobenzoate — An unusual case of disorder involving atropisomerism / P.J. Cox // J. Crystallogr. Spectrosc. Res. — 1993. — Vol. 23, No. 3. — P. 203–208. https://doi.org/doi:10.1007/bf01190048

17 Quijano L. Structures of 8α-(2′-methylbutyryloxy)-9α-hydroxymontahibisciolide, a new skeletal type of sesquiterpene lactone, and of its precursor 8α-isobutyryloxy-9-oxo-germacra-4E, 1(10)Z-dien-6β,12-olide / L. Quijano, T. Rios, R.A. Toscano, F.R. Fronczek // J. Chem. Cryst. — 1996. — Vol. 26, No. 11. — P. 753–757. https://doi.org/10.1007/BF01664652

18 Gonzalez A.G. Hypochaerin: a new sesquiterpene lactone from Hypochaeris setosus / A.G. Gonzalez, J. Bermejo, G.M. Massanet, J.M. Amaro, B. Dominguez, J. Fayos // Cryst. Struct. Commun. — 1977. — Vol. 6. — P. 373–376.

19 Китайгородский А.И. Молекулярные кристаллы / А.И. Китайгородский. — М.: Наука, 1971. — 424 с.

Қ.М. Тұрдыбеков, С.А. Ивасенко, Д.М. Тұрдыбеков,
А.С. Махмұтова, Ю.В. Гатилов, С.М. Әдекенов

Жаңа сесквитерпендік лактон 3-оксо-10β-гидрокси-5,7α(Н),4,6β(Н)-гвай-1,11(13)-диен-6,12-олидтың оқшаулануы және құрылымы

Мақалада Қазақстанның эндемикалық Пятаева танацетопсисі (*Tanacetopsis Pyataeva*) өсімдігінің химиялық зерттеу нәтижелері келтірілген. Экстрактивті заттардың қосындысы гүлдену кезеңінде жиналған өсімдіктің ауада құрғақ ұсақталған жерүсті бөлігінен хлороформмен экстракцияланды. Қосылыстардың индивидуалды түрде бөлінуі КСК маркалы силикагель бағанасында қосындыны – тасымалдаушы = 1:20 қатынасында хроматография әдісімен жүргізілді. Бағананы петролейн эфир-этилацетат (87.5:12.5) қоспасымен элюирлегенде құрамы C$_{15}$H$_{18}$O$_4$ болатын, балқу температурасы 189-191°С құрайтын түссіз кристалды зат (диэтилді эфирімен қайта кристаллдандыру) бөлініп алынды. Бөлініп алынған жаңа қосылыстың құрылысы (3-оксо-10β-гидрокси-5,7α(Н),6β(Н)-гвай-1,11(13)-диен-6,12-олид) ИҚ-, ЯМР- және масс-спектрлердің талдау негізінде дәлелденген. Кеңістіктік құрылымы рентген құрылымдық әдіспен анықталған. Кристаллдағы 3-оксо-10β-гидрокси-5,7α(Н),6β(Н)-гвай-1,11(13)-диен-6,12-олид молекуласы 6:4 қатынасында екі конформациялық күйге бөлінгені анықталды. Бұл конформерлердің тұрақтылығы кванты-химиялық жартылай эмпирикалық есептеулермен расталады. Еркін молекула үшін екі конформердің пайда болу жылуының айырмашылығы 6.3 кДж/моль болатындығы белгілі болды.

Кілт сөздер: ЯМР спектроскопиясы, ИҚ спектроскопиясы, масс-спектрометрия, рентгендік дифракциялық талдау, Пятаева танацетопсисі, эндемикалық, 3-оксо-10β-гидрокси-5,7α(Н),6β(Н)-гвай-1,11(13)-диен-6,12-олид, сесквитерпенді лактондар.

К.М. Турдыбеков, С.А. Ивасенко, Д.М. Турдыбеков,
А.С. Махмутова, Ю.В. Гатилов, С.М. Адекенов

Выделение и структура нового сесквитерпенового лактона 3-оксо-10β-гидрокси-5,7α(Н),4,6β(Н)-гвай-1,11(13)-диен-6,12-олида

В статье приведены результаты химического исследования танацетопсиса Пятаева (*Tanacetopsis Pjataevae*), эндемичного растения Казахстана. Сумма экстрактивных веществ получена экстракцией хлороформом из воздушно-сухой измельченной надземной части растения, собранного в фазу цветения. Выделение соединений проведено методом колоночной хромотографии на колонке с силикагелем марки КСК при соотношении сумма–носитель = 1:20. При элюировании колонки смесью петролейный эфир–этилацетат (87,5:12,5) выделено бесцветное кристаллическое вещество состава C$_{15}$H$_{18}$O$_4$ с т. пл. 189–191 °С (перекристаллизация из диэтилового эфира). Строение полученного нового соединения (3-оксо-10β-гидрокси-5,7α(Н),6β(Н)-гвай-1,11(13)-диен-6,12-олида) установлено на основании анализа ИК-, ЯМР- и масс-спектров. Пространственная структура определена рентгеноструктурным методом. Установлено, что молекула 3-оксо-10β-гидрокси-5,7α(Н),6β(Н)-гвай-1,11(13)-диен-6,12-олида в кристалле разупорядочена по двум конформационным состояниям в соотношении 6:4. Устойчивость этих конформеров подтверждена квантово-химическими полуэмпирическими расчетами. Отмечено, что для свободной молекулы разница теплот образования двух конформеров составляет 6,3 кДж/моль.

Ключевые слова: ЯМР-спектроскопия, ИК-спектрпоскопия, масс-спектрометрия, рентгеноструктурный анализ, танацетопсис Пятаева, эндемик, 3-оксо-10β-гидрокси-5,7α(Н),6β(Н)-гвай-1,11(13)-диен-6,12-олид, сесквитерпеновые лактоны.

References

1 Adekenov, S.M. (2013). Sesquiterpene lactones from endemic species of the family Asteraceae. *Chem. Natur. Comp., 49*(1), *158–162*. https://doi:10.1007/s10600-013-0543-y

2 Adekenov, S.M., Gabdullin, Ye.M., & Kuprianov, A.Kh. (2013). Rasteniia — istochniki novykh lekarstvennykh veshchestv [Plants — sources of new medicinal substances]. *Farmatsevticheskii biulleten — Pharmaceutical Bulletin*, 1, 2, 9–16 [in Russian].

3 Pavlov, N.B. (1966). *Flora Kazakhstana [Flora of Kazakhstan]*. Alma-Ata: Nauka [in Russian].

4 Abduazimov, B.C., Yunusov, A.I., & Sidyakin, G.P. (1983). Components of *Tanacetopsis mucronata. Chem. Natur. Comp.*, *19*(6), 764–765. https://doi.org/10.1007/BF00575207

5 Makhmudov, M.K., Abduazimov, B.K., Tashkhodzhaev, B., Ibragimov B.T., & Yagudaev, M.R. (1988). Crystal and molecular structure of the sesquiterpene lactone mucrin. *Chem. Natur. Comp.*, *24*(1), 49–53. https://doi.org/10.1007/BF00597573

6 Abduazimov, B.C., Tashkhodzhaev, B., Nasirov, S., Sham'yanov, I.D., Yagudaev, M.R., & Malikov, V.M. (1991). Structure of mucrolide. *Chem. Natur. Comp.*, *27*(1), 15–19. https://doi.org/10.1007/BF00629823

7 Izbosarov, M.B., Abduazimov, B.R., Vdovin, A., Kristallovich, E.L., & Yuldashev, M.P. (1999). Structure of mucroflavone B. *Chem. Natur. Comp.*, *35*(6), 625–627. https://doi.org/10.1007/BF02236287

8 Tashkhodzhaev, B., Abduazimov, B.K., Izbosarov, M.B., Sham'yanov, I.D., & Antipin, M.Y. (2002). 13α-Hydroxy-methylenedeacetyllaurenobiolide, a New Germacranolide from Tanacetopsis mucronata. *Chem. Natur. Comp.*, *38*(6), 557–560. https://doi.org/10.1023/A:1022682620162

9 Dusmatova, D.E., Bobakulov, K.M., Mukhamatkhanova, R.F., Turgunov, K.K., Terenteva, E.O., Tsay, E.A., Sham'yanov, I.D., Tashkhodzhaev, B., Azimova, S.S., & Abdullaev, N.D. (2021). Isolation of cytotoxic sesquiterpene lactones from the *Tanacetopsis karataviensis* (Kovalevsk.) Kovalevsk. *Natural product research*, *35*(12), 1939–1948. https://doi.org/10.1080/14786419.2019.1647423

10 Stewart, J.J.P. (2007). Optimization of parameters for semiempirical methods V: modification of NDDO approximations and application to 70 elements. *J. Mol. Modeling*, *13*, 1173–1213. https://doi:10.1007/s00894-007-0233-4

11 Bruker (2015). SAINT. Bruker AXS Inc., Madison, Wisconsin, USA.

12 Bruker (20015). SADABS. Bruker AXS Inc., Madison, Wisconsin, USA.

13 Sheldrick, G.M. (2008). Crystal structure solution with SHELXS. *Acta Crystaollogr., Sect. A*, *64*, 112–122. https://doi.org/10.1107/S0108767307043930

14 Sheldrick, G.M. (2015). Crystal structure refinement with SHELXL. *Acta Crystaollogr., Sect. C*, *71*, 3–8. https://doi.org/10.1107/S2053229614024218

15 Allen, F.H., Kennard, O., Watson, D.G., Brammer, L., Orpen, A.G., & Taylor, R. (1987). Tables of bond lengths determined by x-ray and neutron diffraction. *J. Chem. Soc. Perkin Trans. 2*, S1–S19. https://doi.org/10.1039/A701672G

16 Cox P.J. (1993). X-ray and molecular mechanics studies on the sesquiterpene lactone eupatocunin-o-bromobenzoate — An unusual case of disorder involving atropisomerism. *J. Crystallogr. Spectrosc. Res.*, *23*(3), 203–208. https://doi.org/10.1007/bf01190048

17 Quijano, L., Rios, T., Toscano, R.A., & Fronczek, F.R. (1996). Structures of 8α-(2′-methylbutyryloxy)-9α-hydroxymontahibisciolide, a new skeletal type of sesquiterpene lactone, and of its precursor 8α-isobutyryloxy-9-oxo-germacra-4E, 1(10)Z-dien-6β,12-olide. *J. Chem. Cryst.*, *26*(11), 753–757. https://doi.org/10.1007/BF01664652

18 Gonzalez, A.G., Bermejo, J., Massanet, G.M., Amaro, J.M., Dominguez B., & Fayos, J. (1977). Hypochaerin: a new sesquiterpene lactone from Hypochaeris setosus. *Cryst. Struct. Commun.*, *6*, 373–376.

19 Kitaigorodskii, A.I. (1971). *Molekuliarnye kristally [Molecular crystals]*. Moscow: Nauka [in Russian].

Information about authors*

Turdybekov, Koblandy Muboryakovich — Doctor of Chemical Sciences, Professor, Karagandy University of the name of academician E.A. Buketov, Universitetskaya street, 28, 100024, Karaganda, Kazakhstan; e-mail: xray-phyto@yandex.kz; https://orcid.org/0000-0001-9625-0060;

Ivasenko, Svetlana Alexandrovna — Associate Professor, Doctor of Pharmaceutical Sciences, School of Pharmacy, Karaganda Medical University, Gogol street, 40, 100008, Karaganda, Kazakhstan; e-mail: Ivasenko@qmu.kz; https://orcid.org/0000-0003-3074-5719;

Turdybekov, Dastan Mukhtarovich — Candidate of Chemical Sciences, Karaganda Technical University, N. Nazarbayev str., 56, 100010, Karaganda, Kazakhstan; e-mail: turdas@mail.ru; https://orcid.org/0000-0002-0245-022X;

Makhmutova, Almagul Satybaldievna — Candidate of Chemical Sciences, Associate Professor, Karaganda Medical University, Gogol str., 40, 100000, Karaganda, Kazakhstan; e-mail: almagul_312@mail.ru; https://orcid.org/0000-0002-0194-8739;

Gatilov, Yurii Vasilevich — Doctor of Chemical Sciences, Leading Researcher, N.N. Vorozhtsov Institute of Organic Chemistry of Siberian Branch of Russian Academy of Sciences, Novosibirsk, Lavrentiev Avenue, 9, 630090, Russia; e-mail: gatilov@nioch.ncs.ru; https://orcid.org/0000-0002-4128-7293;

Adekenov, Sergazy Mynzhasarovich — Doctor of Chemical Sciences, Professor, General Director, International Research and Production Holding "Phytochemistry", Gazaliev str. 4, 100009, Karaganda, Kazakhstan, e-mail: arglabin@phyto.kz; https://orcid.org/0000-0001-7588-6174.

_____

*The author's name is presented in the order: *Last Name, First and Middle Names*

R.N. Nurdillayeva[1*], A.N. Zhylysbayeva[2], A.K. Askarov[1], A. Bayeshov[3]

[1] Khoja Akhmet Yassawi International Kazakh-Turkish University, Turkistan, Kazakhstan;
[2] South Kazakhstan State Pedagogical University, Shymkent, Kazakhstan;
[3] D.V. Sokolsky Institute of Fuel, Catalysis and Electrochemistry, Almaty, Kazakhstan
(*Corresponding author's e-mail: raushan.nurdillayeva@ayu.edu.kz)

Electrochemical Method of Lead (II) Ions Removal from Wastewater Using Granular Graphite Electrodes

The article presents an electrochemical method of wastewater treatment from Pb (II) ions through granular graphite electrodes. The cathode was made of graphite particles and the anode was made of rod graphite. Features of wastewater treatment from heavy metals by using developed surface granular graphite electrodes were revealed. Electrochemical research was carried out in a flow mode in a two-chamber electrolyzer. Effect of different electrochemical parameters (current density, electrolyte flow rate, initial concentration of lead (II) ions in solution, size of graphite granules, and concentration of additional cations in solution) to the reduction process of Pb (II) on lump graphite was studied. Results revealed that the removal value of Pb (II) hit a peak at $150 A/m^2$ current density and gradually decreased at a higher value. The efficiency of electrolysis in the flow mode was demonstrated. It was found that the initial concentration of lead ions in the electrode process was insignificant, while the concentration of additional cations had a significant effect. Using very small particles of granular graphite electrodes caused an agglomeration. At an optimal condition, ($i=150 A/m^2$; $V=150$ ml/h; $[Pb^{2+}] = 200$ mg/l; $s= 0.05$ cm^3) treatment value of wastewater from Pb (II) ions reached 97.6 ± 0.3 %.

Keywords: lead (II) ions, granular graphite electrodes, wastewater, heavy metals, flow mode, current output, removal degree, current density.

Introduction

Rapid industrialization in the XXI century has led to problems such as heavy metal contaminated wastewater. Chemical industries are generating a large amount of wastewater contaminated with cadmium, zinc, lead, and copper. These heavy metals, which have a density of more than 5g/ cm^3, are known to be toxic [1]. Wastewater pollutants can be classified by measure and chemical-physical properties. It is necessary to choose a suitable treatment method for each type of wastewater pollution. Wastewater treatment methods can be classified as chemical, mechanical, physico-mechanical, and biological ones. They can be used together as a combined treating method [2]. Efficient methods of heavy metal removal from aqueous solutions include ion exchange, membrane filtration, coagulation, flotation, reverse osmosis, chemical precipitation, evaporation, solvent extraction, biosorption, adsorption, oxidation, electrochemical treatment, and others. Adsorption/ion exchange has been the most suitable method among these methods for heavy metal removal for great removal performance, cost-effectiveness, and simplicity [3].

Our previous work represented a wastewater treatment by the ion exchange adsorption method. The research object was a model of wastewater containing Zn^{2+}, Pb^{2+} and Cd^{2+} ions. A phosphorus-acidic cationite KRF-10P was used as a sorbent. Size of cationite, duration of interaction, and solution temperature were taken as affecting parameters and optimal condition was established. At an optimal condition, removal value of Zn^{2+}, Pb^{2+}, and Cd^{2+} reached 96.1 %, 89 %, and 91 %, respectively [4].

Industrial wastewater from oil and gas production contains high concentrations of cadmium and lead ions. J.E. Segundo and A. Feitoza developed an electrochemical reactor with a perforated steel cathode and expanded mesh three-dimensional DSA anode. Removal percentages were 96 % and 94 % for Pb^{2+} and Cd^{2+}, respectively [5]. Lead (II) ion adsorption of pristine graphite (6.13 % carbon, 93.87 % carbon) and oxidized graphite (15.97 % oxygen, 84.03 % carbon) was compared. The adsorption capacity of oxidized graphite was more than 70 %, while bare graphite showed only 41 % of adsorption capacity. This study results showed that graphite oxide was a suitable material for the Pb^{2+} absorption [6]. A hybrid biopolymer was used to extract Pb (II) ions from water. The hybrid biopolymer prepared by a simple one-step galvanostatic polymerization consisted of poly(3,4-ethylenedioxythiophene)/ polystyrene sulfonate (PEDOT/PPS) and the biopol-

ymer lignin (LG). The electrochemical results showed that the neutral solution of lead ions could be absorbed by applying a negative potential. LG can double the adsorption capacity of PEDOT/PSS from 245mg g^{-1} to 452 mg g^{-1} [7].

Research on a new electrochemical way of lead (II) ions removal from industrial wastewater showed that iron and aluminum electrodes had a high level of lead, zinc, and copper removal. At an initial concentration of 50 mg/l, and at optimal conditions, results showed 98.9 % of lead removal. However, these electrodes have a short lifetime [8].

The electrochemical way of Pb (II) removal from wastewater by using iron and aluminum electrodes at low voltage was studied. The removal procedure included three processes, i.e., chemical reduction, electrochemical reduction, and electrocoagulation. The result showed that the removal value was directly proportional to the voltage and affected by the distance between electrodes and solution acidity. At pH value of 6, an applied voltage of 6V, and electrode distance of 2 cm, removal value of lead (II) was more than 90 % [9]. Electroplating effluents contain a high concentration of lead (II) ions. Researchers developed the removal method of lead (II) by electrocoagulation using iron as a sacrificial electrode. Removal experiment results showed that pH was an important parameter. Anode consumption increased with a decrease in pH while energy consumption increased with an increase in pH of the solution. As a result of the 90 min removal process, the removal value of Pb (II) reached 91.3 % [10].

The Taguchi method is a good technique for improving removal process performance, yield, and productivity. It reduces manufacturing costs due to excessive variability in the process. Taguchi method contains several steps, such as determining the quality characteristics (current efficiency, energy consumption), identification of the noise factors and test conditions, control parameters, and their alternative levels, designing and conducting the matrix experiment, analyzing data, and determining the optimum levels [11]. A 3D reticulated vitreous carbon (RVC) cathode is used to remove lead (II) ions from aqueous solutions under acidic pH conditions. RVC cathode is coupled with a Zn anode. A batch electrochemical cell removed about 95 % of Pb (II) with a cell performance of 73 % [12]. Nanotechnology is also used for wastewater treatment. Yao Xing Lui and Jun Mei Yan used a stainless-steel net electrode coated with single-wall carbon nanotubes (SWCNTs@SSN). The mechanism of the electrochemical lead (II) removal method involved that Pb (II) ions were reduced and deposited on the surface of the SWCNTs@SSN cathode. An experiment was carried out under several parameters, such as electrolysis time, pH value, applied voltage and initial lead concentration. After 90 min electrolysis, with an initial Pb (II) concentration of 150 mg/l, removal value reached up to 95 %. After electrolysis with the same conditions, a good result was shown for other heavy metals [13].

The result of literature review designates that electrochemical methods promise a high lead (II) removal degree. Granular graphite electrode (GGE) using electrochemical method is acceptable for many reasons. GGE has a high value of Pb (II) removal, the electrolysis method is simple, and it is cheap.

The purpose of the research is to study electrochemical methods of wastewater treatment from heavy metals using lump electrodes as a cathode in a flow mode, the influence of different electrochemical parameters to the removal degree (RD) and current output (CO) of metals. We examine an opportunity of using a lump electrode, composites metallic or graphite electrodes with large, developed surface, to avoid pointed out demerits. This treatment method is chemical-free and environmentally friendly, therefore, it can be a perspective direction, and application of lumpy electrodes can intensify the process.

Experimental

This work presents the results of the electrolysis of solution with an initial lead concentration of 200 mg/l on granular graphite electrodes. The necessary methods were chosen for carrying out the research. The research was conducted under direct current. A granular graphite electrode was taken as a cathode; a rod graphite electrode was taken as an anode. $Pb(NO_3)_2$ was used to produce a model solution containing 200 mg/l of Pb^{2+} ions. Solution was acidified with 0.2 M of HNO_3 acid. Electrolysis was carried out in a flow mode in a two-chamber electrolyzer (Figure 1). Solution containing lead (II) ions was passed at a certain rate through the granular electrode layer. Current density (i), electrolyte flow rate (V), initial concentration of Pb (II) in a solution (C), size of graphite granule (s) and concentration of additional cations in the solution were taken as the main parameters of electrolysis during the study to determine the features of removal degree (RD) and current output (CO) of Pb^{2+} ions in the solution. The duration of electrolysis (t) and thickness of granular graphite layer (l) was constant. An analyzer CTA-1 voltammeter was used for determining a low concentration of Pb (II) ions with very high accuracy. The process of determining the concentration of Pb (II) ions is demonstrated in Figure 2.

The average mean of Pb (II) removal was determined by formula 1.

$$\underline{x} = \frac{\sum x_i}{n}.$$ (1)

Formula 2 was used to determine a standard deviation:

$$\Delta x = \frac{\sum |x_i - \underline{x}|}{n}.$$ (2)
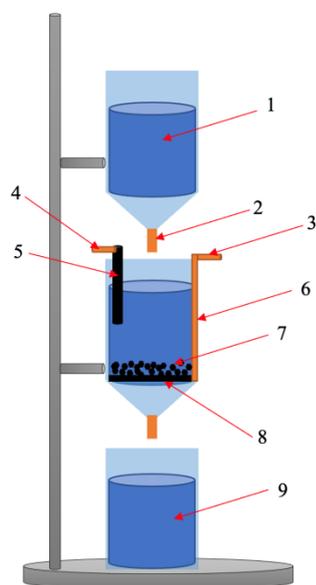
1 — Pb (II) containing wastewater sample; 2 — water flow controller;
3 — current input (-); 4 — current input (+); 5 — anode rod graphite;
6 — copper wire; 7 — granular graphite particles;
8 — cathode plate graphite; 9 — purified solution

Figure 1. Model of electrolyzer
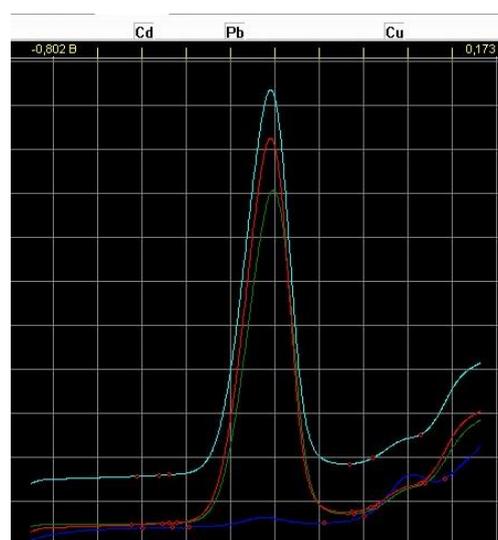
Figure 2. Determining Pb (II) concentration
with a CTA-1 voltammeter

Results and Discussion

The studies were based on the purification of wastewater from lead (II) ions by their electrolytic reduction on granular graphite cathode to an elemental state, according to the reaction:

$$Pb^{2+} + 2e^- \rightarrow Pb^0 \qquad E = -0.126 \text{ V.}$$ (3)
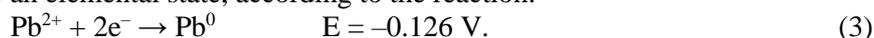
Discharge of water takes place at the anode:

$$2H_2O - 4e^- \rightarrow O_2 + 4H^+$$ (4)

Experiments were carried out between 50 and 250 A/m^2 current densities. It was observed that removal degrees grew steadily until the graphite electrode reached diffusion-limited current density (DLCD). Hydrogen emission occurred parallel to the lead removal at a high current density, consequently, removal of Pb (II) ions began to decrease (Fig. 3). The maximum degree of metal removal from the solution was achieved when the entire volume of the electrode operated at the limiting diffusion current mode. The decrease in the degree of lead extraction can be explained by the intensification of the competitive process of hydrogen evolution at high current densities.

The influence of electrolyte flow rate on lead (II) removal degree was determined. The range of electrolyte flow rate was between 50–350 ml/h. It was established that removal of lead (II) ions reached a maximum value at 150 ml/h electrolyte flow rate and decreased inversely proportional to the flow rate of electrolyte. When electrolyte flows at a high velocity, the reduction reaction of lead becomes less effective (Table 1). This phenomenon can be explained that at even higher flow rates, lead (II) ions cannot be properly reduced at the granular electrodes, and this leads to a decrease in the degree of metal extraction from the solution.
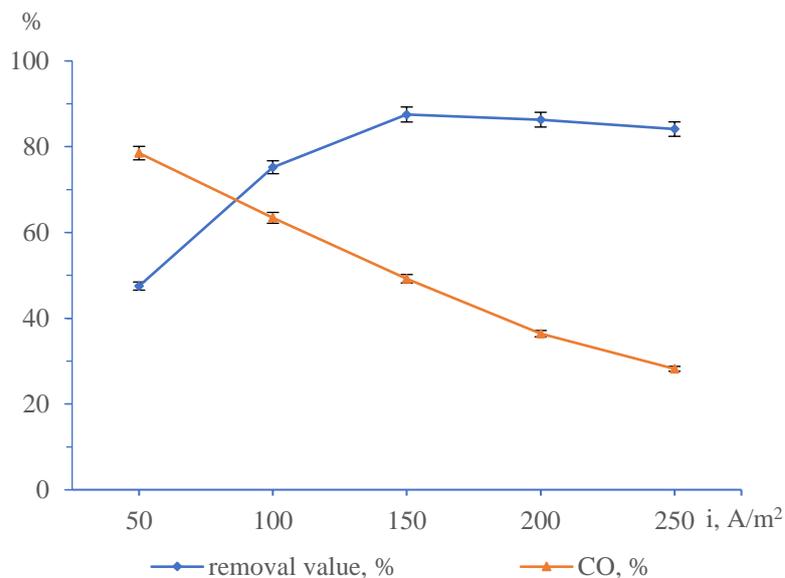
$[Pb^{2+}] = 200$ mg/l; s = 0.2 cm^3; $t = 0.5$ h; $V = 0$ ml/h; $l = 1$ cm

Figure 3. Effect of current density on Pb (II) ions removal degree

T a b l e 1

Effect of electrolyte flow on Pb (II) ions removal degree
(i = 150 A/m^2; [Pb^{2+}] = 200 mg/l; s = 0.2 cm^3; t = 0.5 h; l = 1 cm)

V, ml/h	50	100	150	250	350
α, %	89.2±1.5	91.7±1.3	92.8±1.5	86±1.0	80.5±1.2
CO, %	50.2±0.4	51.4±0.4	52.2±0.4	48.2±0.2	45.2±0.2

The removal value remains the same at a higher initial concentration of lead (II) ions. The rise of the initial concentration of Pb (II) ions causes saturation of solution and interferes with smooth polarization. It leads a process to occur in circumferential areas and the degree of Pb (II) ions removal gradually decreases. Current output gradually increases directly proportional to the initial Pb (II) concentration (Fig. 4).
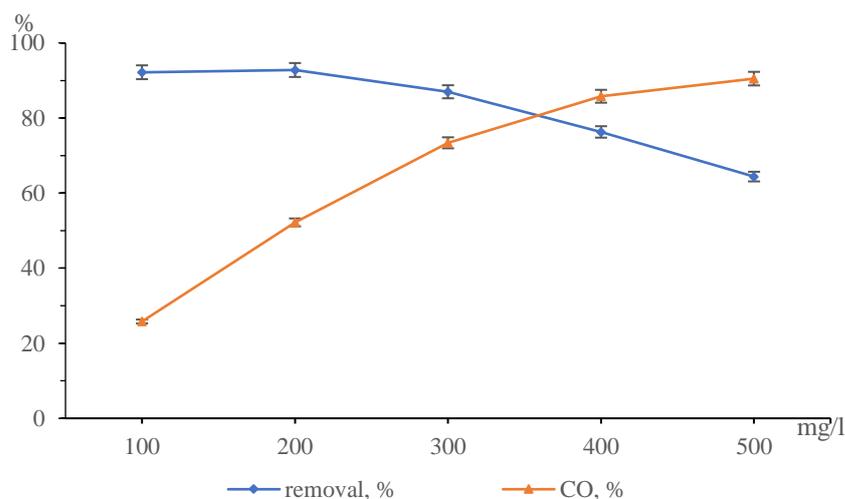
i = 150 A/m^2; V = 150 ml/h; s = 0.2 cm^3; t = 0.5 h; l = 1 cm

Figure 4. Effect of initial lead (II) ions concentration on Pb (II) removal degree

The influence of the electrode material on the electrolysis process is also considered. The maximum degree of extraction is observed on the graphite electrode (92.8 %), whereas on the lead electrode, this figure reached just under 68 %, as the copper electrode accounted for only 44 %. As a comparison, the experiment also was carried out without granular electrodes, which means only on a graphite substrate. It turned out that the degree of lead extraction didn't exceed even 15 %.

It was observed that change in graphite granule size affected the removal value of lead ions. Smaller granule size resulted in a higher removal degree and a higher current output while larger electrode granules resulted in a lower removal degree and less current output (Table 2). However, results of research carried out with the help of $1mm^3$ granular graphite electrode showed that removal degree decreased steadily. It was found that small granules (< 0.01 cm^3) agglomerated and became less effective because of the small reacting area.

T a b l e 2

Effect of graphite granular electrode size on Pb (II) ions removal degree
(i =150 A/m^2; V = 150 ml/h; [Pb^{2+}] = 200 mg/l; t = 0.5 h; l = 1 cm)

s, cm^3	0.25	0.2	0.15	0.1	0.05
α, %	89.9±0.7	92.8±0.8	94.4±0.8	96.7±0.6	97.6±0.3
CO, %	50.4±0.4	52.2±0.4	53±0.2	54.2±0,19	54.9±0.1

The influence of additional cations concentration in the solution on the Pb (II) ions removal degree and current output was determined during the electrolysis including copper ions. Lead (II) ions removal value and current output reduce gradually when copper concentration is increased in the solution (Table 3). This phenomenon can be explained by the reduction of copper ions parallel to the lead ions on the cathode.

T a b l e 3

Effect of additional cations concentration on Pb (II) ions removal degree
(i =150 A/m^2; V= 150 ml/h; [Pb^{2+}] = 200 mg/l; s = 0.05 cm^3; t = 0.5 h; l = 1 cm)

[Cu^{2+}]	50	100	150	200	250
α, %	90.6±0.9	88±0.7	85.2±0.8	79.7±0.8	74.3±0.7
CO, %	51±0.25	49.4±0.2	47.8±0.2	44.8±0.22	41.8±0.2

At an optimal condition, (i = 150 A/m^2; V = 150 ml/h; [Pb^{2+}] = 200 mg/l; s = 0.05 cm^3) removal value and current output of Pb (II) reached 97.6±0.3 % and 54.9±0.1 %, respectively. It should be noted that if the solution is passed through several such kinds of electrolyzers, the removal value of Pb (II) ions will be higher. Deposited lead can be extracted from the electrode by burning the graphite.

Conclusions

As a result of research, the influence of main factors affecting Pb (II) removal value was determined. It was observed that Pb (II) ions removal degree reached the maximum at 150 A/m^2 and decreased gradually because of hydrogen emission parallel to the lead (II) removal at higher current densities. At a high electrolyte flow rate, the reduction reaction of lead becomes less effective. A higher initial concentration of Pb (II) ions results in higher current output and lower removal value. The removal value and current output are inversely proportional to the size of cathode graphite particles, however, particles smaller than 0.01cm^3 become less effective because of particle agglomeration. Additional cations decreased the removal value and current output of Pb (II) ions. As a result of the research work the optimal conditions of electrolysis are established, at which (i = 150 A/m^2; V = 150 ml/h; [Pb^{2+}] = 200 mg/l; s = 0.05 cm^3) Pb (II) ions removal degree from wastewater accounted for 97.6±0.3 %.

The results of electrochemical research with the use of granular electrodes showed an opportunity of using electrochemical methods for wastewater treatment to intensify the electrode processes and to solve some ecological problems of the chemical and metallurgical industry. We consider that using granular electrodes is a new direction in the electrochemical branch on the solution of ecological problems.

References

1 Shrestha R. Technological trends heavy metals removal from industrial wastewater: A review / S. Ban, S. Devkota, S. Sharma, R. Joshi, A.P. Tiwari, M.K. Joshi // Journal of Environmental Chemical Engineering. — 2021. — Vol. 9, No. 4. — P. 105688. https://doi.org/10.1016/j.jece.2021.105688

2 Zhylysbayeva A. Electrochemical methods of wastewater treatment from heavy metals / A. Zhylysbayeva, R. Nurdillayeva, A. Bayeshov // In Integrated Water Cycle Management in Kazakhstan. P. 145–149. Eds. Meyer B.C. & Lundy L. Almaty: Al-Farabi Kazakh National Publishing House, 2014. — 304 p. ISBN: 978-601-04-0900-2

3 Khaligh N.G. Recent advances in water treatment using grapheme-based materials / N.G. Khaligh, M.R. Johan // Mini-Reviews in Organic Chemistry. — 2020. — Vol. 17. — P. 74–90. https://doi.org/10.2174/1570193X16666190516114023

4 Бабажанова С.З. Ақаба суларды ауыр және түсті металл иондарынан ион алмастырғыш адсорбция әдісімен тазарту / С.З. Бабажанова, Р.Н. Нұрділлаева, Өзлер Мехмет Али // ҚазҰУ Хабаршысы, Химия Сериясы — 2016 — Т. 83, № 3-4. – Б. 45–51.

5 Segundo J.E. Cadmium and lead removal from aqueous synthetic wastes utilizing Chemelec electrochemical reactor: Study of the operating conditions / J.E. Segundo, G.R. Salazar-Banda, A. Feitoza, E.O. Vilar, E.B. Cavalcanti // Separation and Purification Technology. — 2012. — Vol. 88. — P. 107–115. https://doi.org/10.1016/ j.seppur.2011.12.023

6 Selvanantharajah N. Removal of lead by oxidized graphite / N. Selvanantharajah, P. Iyngaran, P. Abiman, N. Kuganathan // Journal of Carbon Research. — 2021. — Vol. 7, No. 23. https://doi.org/10.3390/c7010023

7 Checkol F. Highly stable and efficient lignin-PEDOT/ PSS composites for removal of toxic metals / F. Checkol, A. Elfwing, G. Greczynski, S. Mehretie, O. Inganas, S. Admassie // Advanced Sustainable Systems. — 2018. — Vol. 2. https://doi.org/10.1002/adsu.201700114

8 Khue A.V. Research on a new electrochemical method combined with chemical coagulation in removal of lead, zinc, and copper from wastewater / A.V. Khue, J.X. Xiao, G.L. Tian, H.P. Rui, L.L. Shu & L.Y. Xiu // Desalination and Water Treatment. — 2015. — Vol. 57, No. 33. — P. 15343–15352. https://doi.org/10.1080/19443994.2015.1070757

9 Rao X. Simultaneous removal of lead (II) and nitrate from water at low voltage / X. Rao, Q. Li, C. Inoue, I. Ahmad, J. Yi, Y. Liu, J. Zhang // Journal of Water Process Engineering. — 2019. — Vol. 32, No. 100940. https://doi.org/10.1016/j.jwpe.2019.100940

10 Sharma D. Removal of chromium (VI) and lead from electroplating effluent using electrocoagulation / D. Sharma, P.K. Chaudhari, A.K. Prajapati // Separation Science and Technology. — 2019. — Vol. 55. — P. 321–331. https://doi.org/10.1080/01496395.2018.1563157

11 Kaminari N.M.S. Heavy metals recovery from industrial wastewater using Taguchi method / N.M.S. Kaminari, D.R. Schultz, M.J.J.S. Ponte, H.A. Ponte, C.E.B. Marino, A.C. Neto // Chemical Engineering Journal. — 2007. — Vol. 126. — P. 139–146. https://doi.org/10.1016/j.cej.2006.08.024

12 Ramalan N.H.M. Impulsive removal of Pb (II) at a 3-D reticulated vitreous carbon cathode / N.H.M. Ramalan, F.S. Karoonian, M. Etesami, S.Wen-Min, M.A. Hasnat, N. Mohamed // Chemical Engineering Journal. — 2012. — Vol. 202. — P. 123–129. https://doi.org/10.1016/j.cej.2012.07.006

13 Liu Y. The study of lead removal from aqueous solution using an electro-chemical method with a stainless-steel net electrode coated with wall carbon nanotubes / Y.X. Liu, J.M. Yan, D.X. Yuan, Q.L. Li, X.Y. Wu // Chemical Engineering journal. — 2013. — Vol. 218. — P. 81–88. https://doi.org/10.1016/j.cej.2012.12.020

Р.Н. Нұрділлаева, А.Н. Жылысбаева, А.Х. Асқаров, А. Баешов

Түйіршікті графит электродтарының көмегімен ақаба суды қорғасын (II) иондарынан тазалаудың электрохимиялық әдісі

Ақаба суларды құрамындағы ауыр металдардан тазалауда электрохимиялық әдіс өзге әдістерге қарағанда интенсивтілігі, тұрақтылығы және құрылғы конструкциясының қарапайымдылығы сияқты біршама қасиеттерімен ерекшеленеді. Мақалада түйіршікті графит электродтарын қолдану арқылы ақаба суларды Pb (II) иондарынан тазартудың электрохимиялық әдісі ұсынылған. Катод ретінде түйіршікті графит кесінділері, ал анод ретінде стерженді графит электроды қолданылды. Электролиз әдісі дамыған беті бар кесек графит электродтарындағы ағынды суларды ауыр металл иондарынан тазарту ерекшелігін көрсетеді. Электрохимиялық зерттеу екі камералы электролизерде ағынды режимде жүргізілді. Түйіршікті электродтарда қорғасын (II) ионының тотықсыздану үрдісіне негізгі электрохимиялық параметрлердің (ток тығыздығы, электролит ағынының жылдамдығы, ерітіндідегі Pb (II) ионының бастапқы концентрациясы, графит түйіршіктерінің мөлшері және ерітіндідегі қосымша катиондардың концентрациясы) әсері зерттелді. Зерттеу нәтижесінде, ақаба сулардың қорғасын (II) иондарынан тазалану дәрежесі түйіршікті графит электродында 150 А/м² ток тығыздығында ең жоғары мәнге ие болатындығы анықталды. Электролизді ағынды режимде жүргізудің тиімділігі көрсетілді. Электродтық үрдіске қорғасын иондарының бастапқы концентрациясының әсері елеусіз болса, қосымша катиондардың концентрациясы елеулі әсер

ететіндігі анықталды. Түйіршікті графит электродтарының өте майда ұнтақтарын пайдаланғанда, оларға агломерация құбылысы тән екендігі көрсетілді. Электролиздің оңтайлы жағдайларында (i = 150 а/м^2; V = 150 мл/сағ; [Pb^{2+}] = 200 мг/л; s = 0,05 см^3) ақаба сулардың Pb (II) иондарынан тазалану дәрежесі 97.6±0.3 % құрады.

Кілт сөздер: қорғасын (II) иондары, түйіршікті графит электродтары, ақаба сулар, ауыр металдар, ағынды режим, ток бойынша шығымы, тазалану дәрежесі, ток тығыздығы.

Р.Н. Нурдиллаева, А.Н. Жылысбаева, А.Х. Аскаров, А. Баешов

Электрохимический способ очистки сточных вод от ионов свинца (II) с применением кусковых графитовых электродов

Электрохимический метод очистки сточных вод от тяжелых металлов отличается от других методов рядом свойств, таких как интенсивность, стабильность и простота конструкции устройства. В статье предложен электрохимический способ очистки сточных вод от ионов Pb (II) с помощью кусковых графитовых электродов. В качестве катода использовались куски гранулированного графита, в качестве анодов — стержневые графитовые электроды. Методом электролиза показана особенность очистки сточных вод от ионов тяжелых металлов на кусковых графитовых электродах с развитой поверхностью. Электрохимические исследования проводились в двухкамерном электролизере в проточном режиме. Изучено влияние основных электрохимических параметров (плотности тока, расхода электролита, начальной концентрации ионов свинца в растворе, размера гранул графита и концентрации дополнительных катионов в растворе) на восстановительный процесс ионов свинца на кусковых электродах. В результате исследования установлено, что степень очистки сточных вод от ионов свинца имеет максимальное значение при плотности тока 150 А/м^2 на кусковом графитовом электроде. Показана эффективность электролиза в проточном режиме. Установлено, что начальная концентрация ионов свинца влияет на электродный процесс незначительно, в то же время существенное влияние оказывает концентрация дополнительных катионов. При использовании очень мелких кусковых графитовых электродов было показано, что для них характерно явление агломерации. При оптимальных условиях электролиза (i = 150 А/м^2; V = 150 мл/ч; [Pb^{2+}] = 200 мг/л; s = 0,05 см^3) степень очистки сточных вод от ионов Pb (II) составила 97,6±0,3 %.

Ключевые слова: ионы свинца (II), кусковые графитовые электроды, сточные воды, тяжелые металлы, проточный режим, выход по току, степень очистки, плотность тока.

References

1 Ban, S., Devkota, S., Sharma, S., Joshi, R., Tiwari, A.P., & Joshi, M.K. (2021). Technological trends heavy metals removal from industrial wastewater: A review. *Journal of Environmental Chemical Engineering, 9*(4), 105688. https://doi.org/10.1016/j.jece.2021.105688

2 Zhylysbayeva, A., Nurdillayeva, R., & Bayeshov, A. (2014). Electrochemical methods of wastewater treatment from heavy metals. 145–149. In *Integrated Water Cycle Management in Kazakhstan*. B.C. Meyer, L. Lundy (Ed.). Almaty: Al-Farabi Kazakh National Publishing House. 304. ISBN: 978-601-04-0900-2.

3 Khaligh, N.G., & Johan, M.R. (2020). Recent advances in water treatment using grapheme-based materials. *Mini-Reviews in Organic Chemistry, 17*, 74–90. https://doi.org/10.2174/1570193X16666190516114023

4 Babazhanova, S.Z., Nurdillayeva R.N., & Ozler Mehmet Ali (2016). Aqaba sulardy auyr zhane tusti metall iondarynan ion almastyrgysh adsorbatsiia adisimen tazartu [Wastewater treatment from ions of heavy and non-ferrous metals by ion-exchange adsorption]. *Vestnik KazNU. Seriia Khimiia. — Bulletin of KazNU. Chemistry Series, 87*(3-4), 45–51 [in Kazakh].

5 Segundo, J.E., Salazar-Banda, G.R., Feitoza, A., Vilar, E.O., & Cavalcanti, E.B. (2012). Cadmium and lead removal from aqueous synthetic wastes utilizing Chemelec electrochemical reactor: Study of the operating conditions. *Separation and Purification Technology, 88*, 107–115. https://doi.org/10.1016/j.seppur.2011.12.023

6 Selvanantharajah, N., Iyngaran, P., Abiman, P., & Kuganathan, N., (2021). Removal of lead by oxidized graphite. *Journal of Carbon Research, 7*(23). https://doi.org/10.3390/c7010023

7 Checkol, F., Elfwing, A., Greczynski, G., Mehretie, S., Inganas, O., & Admassie, S. (2018). Highly stable and efficient lignin-PEDOT/ PSS composites for removal of toxic metals. *Advanced Sustainable Systems, 2*. https://doi.org/10.1002/adsu.201700114

8 Khue, A.V., Xiao, J.X., Tian, G.L., Rui, H.P., Shu, L.L., & Xiu, L.Y. (2015). Research on a new electrochemical method combined with chemical coagulation in removal of lead, zinc, and copper from wastewater. *Desalination and Water Treatment, 57*(33), 15343–15352. https://doi.org/10.1080/19443994.2015.1070757

9 Rao, X., Li, Q., Inoue, C., Ahmad, I., Yi, J., Liu, Y., & Zhang, J. (2019). Simultaneous removal of lead (II) and nitrate from water at low voltage. *Journal of Water Process Engineering, 32*(100940). https://doi.org/10.1016/j.jwpe.2019.100940

10 Sharma, D., Chaudhari, P.K., & Prajapati, A.K. (2019). Removal of chromium (VI) and lead from electroplating effluent using electrocoagulation. *Separation Science and Technology, 55*, 321–331. https://doi.org/10.1080/01496395.2018.1563157

11 Kaminari, N.M.S., Schultz, D.R., Ponte, M.J.J.S., Ponte, H.A., Marino, C.E.B., & Neto, A.C. (2007). Heavy metals recovery from industrial wastewater using Taguchi method. *Chemical Engineering Journal, 126*, 139–146. https://doi.org/10.1016/j.cej.2006.08.024

12 Ramalan, N.H.M., Karoonian, F.S., Etesami, M., Wen-Min, S., Hasnat, M.A., & Mohamed, N. (2012). Impulsive removal of Pb (II) at a 3-D reticulated vitreous carbon cathode. *Chemical Engineering Journal, 202*, 123–129. https://doi.org/10.1016/j.cej.2012.07.006

13 Liu, Y.X., Yan, J.M., Yuan, D.X., Li, Q.L., & Wu, X.Y. (2013). The study of lead removal from aqueous solution using an electro-chemical method with a stainless-steel net electrode coated with wall carbon nanotubes. *Chemical Engineering journal, 218*, 81–88. https://doi.org/10.1016/j.cej.2012.12.020

Information about authors*

Nurdillayeva, Raushan Nurdillakyzy (corresponding author) — Candidate of Chemical Science, Professor, Head of Ecology and Chemistry Department of Natural Sciences Faculty, Khoja Akhmet Yassawi International Kazakh-Turkish University, B. Sattarkhanov Ave., 29, 161200, Turkistan, Kazakhstan; E-mail: raushan.nurdillayeva@ayu.edu.kz; https://orcid.org/0000-0001-9444-737X;

Zhylysbayeva, Akkongyr Nurdillayevna — Candidate of Chemical Science, Associate Professor, South Kazakhstan State Pedagogical University, A. Baitursynov St., 13, 160012, Shymkent, Kazakhstan; E-mail: zhylysbayeva.akkongyr@okmpu.kz; https://orcid.org/0000-0001-9114-7582;

Askarov, Akbar Khamdamovich — Khoja Akhmet Yassawi International Kazakh-Turkish University, 2nd year Master student of educational program 7M05324-Chemistry, B. Sattarkhanov Ave, 29, 161200, Turkistan, Kazakhstan; E-mail: akbar.askarov@ayu.edu.kz; https://orcid.org/0000-0001-6182-188X;

Bayeshov, Abduali — Doctor of Chemical Science, Professor, Academician of the National Academy of Sciences of the Republic Kazakhstan, D.V. Sokolsky Institute of Fuel, Catalysis and Electrochemistry, Kunaev St., 142, 050010, Almaty, Kazakhstan; E-mail: bayeshov@mail.ru; https://orcid.org/0000-0003-0745-039X

_____

*The author's name is presented in the order: *Last Name, First and Middle Names*

I.L. Stadnik[1*], F.Zh. Abilkanova[1], Ye.V. Kudryavtseva[1], S.N. Nikolskiy[1,2], A.S. Masalimov[1]

[1]Karagandy University of the name of academician E.A. Buketov, Kazakhstan;
[2]Altay State University, Barnaul, Russia
*(*Corresponding author's e-mail: i.stadnik@mail.ru)*

ESR-Study of the Proton Exchange with Aliphatic Amino Acids in Toluene

This paper presents the results of an ESR spectroscopic study of the intermolecular proton exchange kinetics with some isomers of aminocaproic acid, such as 2-aminohexanoic and 6-aminohexanoic acids in the toluene indifferent medium. A stable semiquinone radical, namely 3,6-di-*tert*-butyl-2-hydroxyphenoxyl, is used as a spin probe. The ESR spectra have been recorded on a RE-1306 spectrometer. The article provides the obtained dynamic spectra of the intermolecular proton exchange process. Modeling of the proton exchange ESR spectra has been carried out using a previously developed program, which is based on a four-jump model of this reaction and modified Bloch equations. The kinetic parameters of the process of acid-base interaction of the spin probe with amino acids and the activation barrier of the reaction have been estimated with a minimum error based on a comparison of the model spectra with the experimental ones. The obtained data have been analyzed and compared with previous studies. It has been found that the reaction rate of the intermolecular proton exchange between 3,6-di-tert-butyl-2-hydroxyphenoxy and studied aliphatic amino acids is comparable to the same with aliphatic carboxylic acids. Hoewever, in our case, there is an increase in the activation barrier, which apparently is associated with a negative effect on the intramolecular hydrogen bonding process between the amino and the carboxyl groups in the amino acid molecule.

Keywords: ESR-spectroscopy, proton exchange reactions, spin probe, semiquinone radical, Bloch equation, aminohexanoic acid, 3,6-di-*tert*-butyl-2-hydroxyphenoxyl, OH-acids.

Introduction

The acid-base interactions are common phenomena in nature. They are widely used in scientific and practical activities. Theoretical ideas about acids and bases are often of primary importance in the formation of all conceptual systems of chemistry and have a versatile influence on the development of many theoretical concepts in all fundamental chemical disciplines. Typical acid-base interactions, according to the Bronsted–Lowry theory, include protolytic reactions involving proton. The proton exchange reaction is one of the varieties of such reactions. To date, plenty of papers are devoted to acid-base interactions. However, as can be seen from the literature analysis, most studies of protolytic reactions have been carried out in aqueous media, and there are data on such studies in non-aqueous media [1–6].

Previously, we have carried out ESR spectroscopic studies of proton exchange reactions between a stable semiquinone radical as a spin probe and various organic acids in non-aqueous media [7, 8]. It seems interesting to study the proton exchange reaction with aminohexanoic acids (1), namely 2-aminohexanoic (α-aminocaproic) and 6-aminohexanoic (ε-aminocaproic):

                                                                                                         (1)

          2-aminohexanoic acid   6-aminohexanoic acid
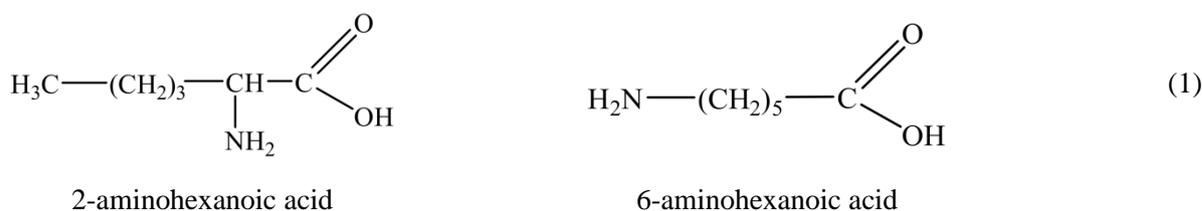
This study will make it possible to determine the protolytic ability of these acids and to evaluate the influence of their structure on the rate of the proton exchange reaction.

Amino acids play an important role in various biochemical processes. The scientists pay the attention to this class of compounds. This is confirmed by a large number of publications devoted to the study of their physicochemical properties [9–14].

Experimental

The method of recrystallization from tetrahydrofuran was used to purify 3,6-di-*tert*-butylcyclohexa-3,5-diene-1,2-dione (3,6-di-*tert*-butyl-*o*-benzoquinone) (N.D. Zelinsky Institute of Organic Chemistry of the Russian Academy of Sciences, >98 % purity) and 3,6-di-*tert*-butylbenzene-1,2-diol (3,6-di-*tert*-butylcatechol) (N.D. Zelinsky Institute of Organic Chemistry of the Russian Academy of Sciences, >98 % purity).

Toluene (CJSC "Ekos-1", >98 % purity) was purified by distillation under atmospheric pressure over sodium hydroxide.

Amino acids, namely 2-aminohexanoic and 6-aminohexanoic (AppliChem GmbH), were used without additional purification since their purity exceeded 99 %. Amino acids were placed in the desiccator for 48 hours before use [15].

The studied system of 3,6-di-*tert*-butyl-2-hydroxyphenoxyl — amino acids was obtained by direct mixing of 3,6-di-*tert*-butylcyclohexa-3,5-diene-1,2-dione with 3,6-di-*tert*-butylbenzene-1,2-diol in a glass ampoule followed by the addition of an amino acid solution in toluene of a given concentration. Then the ampoule was degassed and sealed. The spectra were recorded on a RE-1306 spectrometer (Russia) with a unit for temperature control in the range of 200–400K. The spectrometer was upgraded with a device that converts the analog signal to digital. The ESR EXCHANGE program was used to process the experimental data. Previously, we developed this program in the FORTRAN algorithmic language [16]. The ESR EXCHANGE program includes calculation of the theoretical spectrum, comparison of this spectrum with the experimental spectrum, calculation of the kinetic parameters of the intermolecular proton exchange reaction, Least-squares processing with determination of the standard error of measurement.

Results and Discussion

The ESR spectrum of 3,6-di-*tert*-butyl-2-hydroxyphenoxyl is a triplet of doublets. It is formed by the interaction of an unpaired electron with ring protons ($a_H = 0.392$ mT) and with a proton of the hydroxyl group ($a_{OH} = 0.162$ mT). The advantage of the used spin probe is the hyperfine structure of the radical's ESR spectrum, which is sensitive to acid-base interactions [7, 8].

A four-jump model can describe the process of intermolecular proton exchange with H-acids:

$$(2)$$
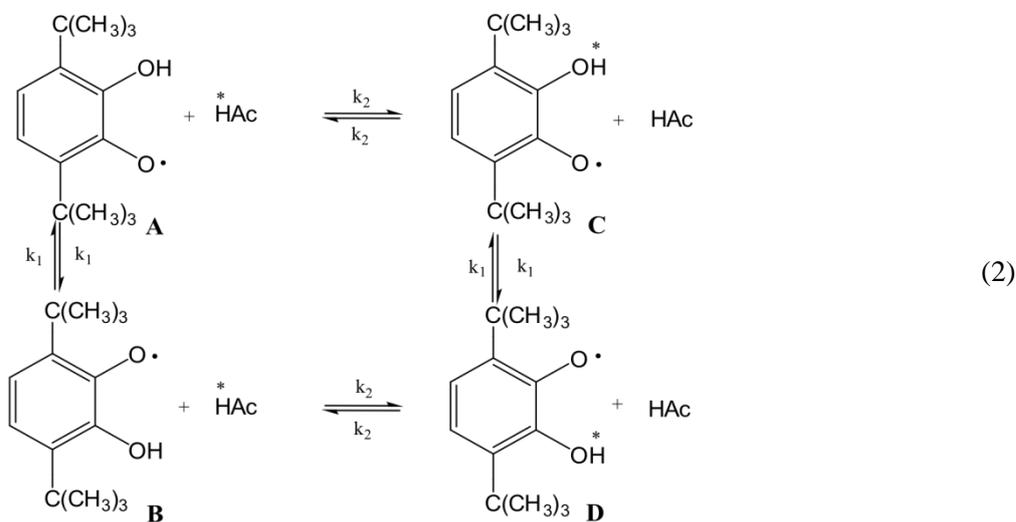
Along with the above reaction (A↔C, B↔D), it includes tautomeric transformations of a semiquinone radical, i.e., intramolecular migration of the hydrogen atom of the hydroxyl group between oxygen atoms (A↔B, C↔D) [17].

This four-jump model (2) and the modified Bloch equation formed the basis of the previously developed program for modeling intermolecular proton exchange. In this program, the ESR spectra are calculated from the coupling constants, rate constants, and linewidths of all chemical configurations of 3,6-di-*tert*-butyl-2-hydroxyphenoxyl. The rate constants of the reaction of intermolecular proton exchange, the activation energy of the process, and the measurement error can be found by comparing the model spectra with the

experimental ones. It should be noted that the proton exchange process presumably has a "cooperative" mechanism, that is, a cyclic hydrogen-bonded complex is formed during the reaction. The lifetime of this complex directly affects the rate of the whole process [17].

The ESR spectra of the 3,6-di-*tert*-butyl-2-hydroxyphenoxyl — aminohexanoic acid system were obtained by the ESR method. The broadening of the hyperfine structure lines was noted with increasing temperature. This is characteristic of proton exchange and confirms that an intermolecular reaction of proton exchange is observed in the system under study.

Figure 1 shows experimental and simulated ESR spectra of the 3,6-di-*tert*-butyl-2-hydroxyphenoxyl — 6-aminohexanoic acid system in toluene.
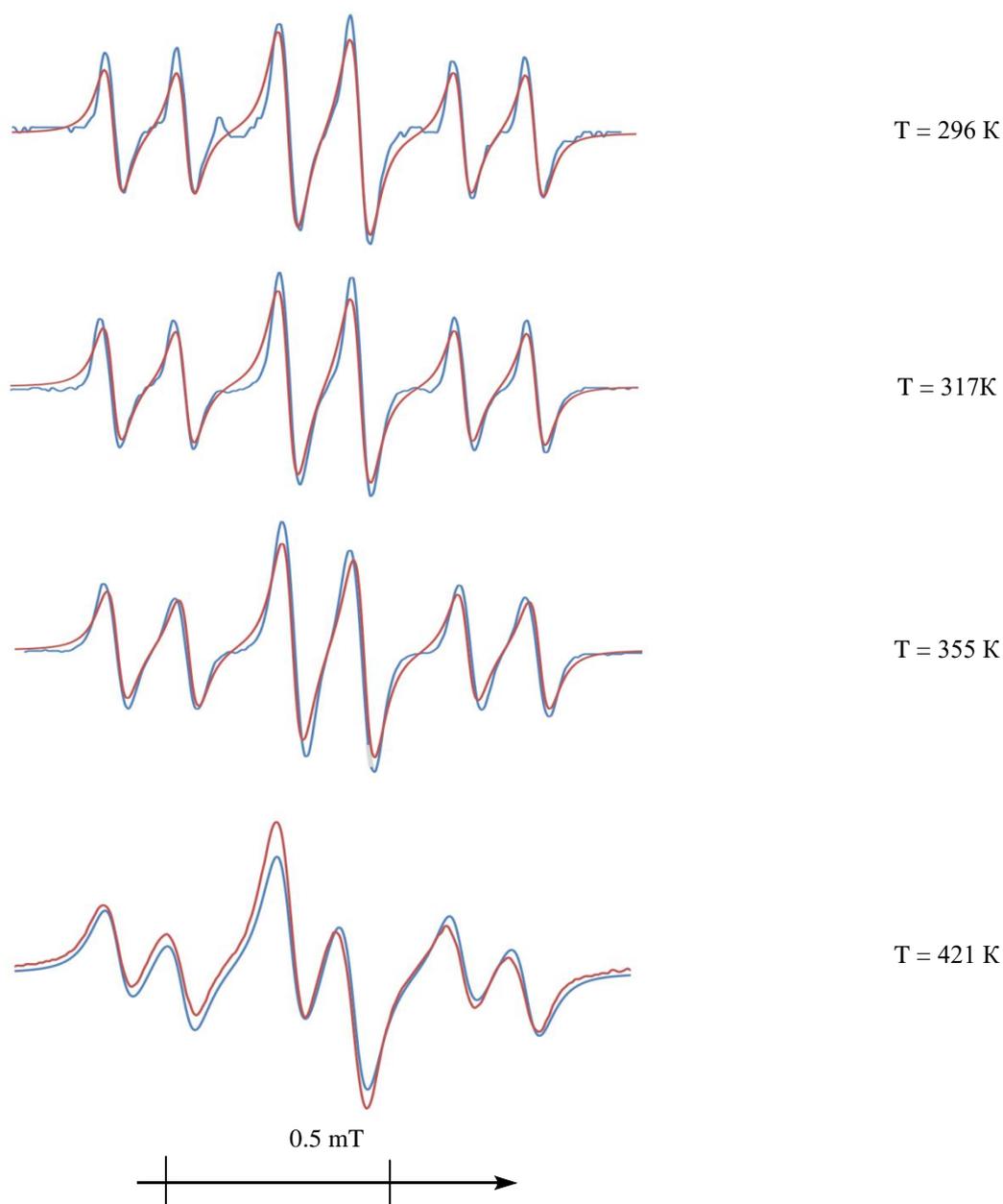
Figure 1. ESR spectra of 3,6-di-*tert*-butyl-2-hydroxyphenoxyl — 6-aminohexanoic acid (0.05 mol/l) system in toluene at different temperatures. Blue line is an experimental spectrum; red line is a simulated spectrum

The decrease in the central components of the ESR spectrum triplet (Fig. 1) indicates a slowdown in proton migration between oxygen atoms in the radical. This means that the resulting intermediate of semiquinone radical with acid is sufficiently stable.

The Arrhenius plot showed a good linear relationship between $\lg k_{exch}$ and $1/T$ (Fig. 2). The plot in Figure 2 also demonstrates the values of the standard measurement error calculated by the ESR EXCHANGE program.
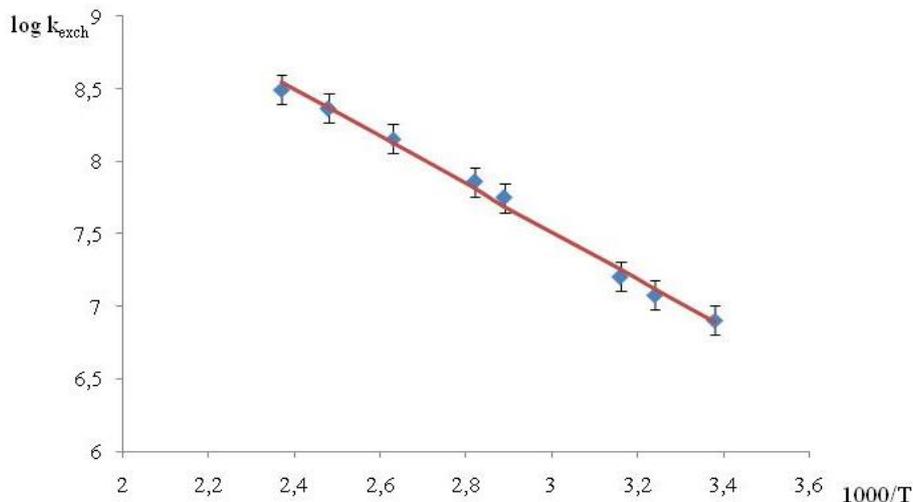
Figure 2. Arrhenius plot of the intermolecular rate constant (k_{exch}) for 3,6-di-*tert*-butyl-2-hydroxyphenoxyl — 6-aminohexanoic acid system in toluene obtained from the experimental and theoretical ESR spectra

Kinetic parameters of intermolecular proton exchange reaction between 3,6-di-*tert*-butyl-2-hydroxyphenoxyl and aminohexanoic acids were calculated using the ESR EXCHANGE program. Table 1 presents the obtained data and measurement error.

Table 1

**Kinetic parameters of the intermolecular proton exchange reactions
between 3,6-di-*tert*-butyl-2-hydroxyphenoxyl and H-acids in toluene solution**

H-acid	k_{exch} (293K), l/mol·s	k^o_{exch}, l/mol·s	E_a, kJ/mol	pK_a
2-Aminohexanoic acid	$(3.58\pm0.44)\cdot10^7$	$1.96\cdot10^{10}$	15.4 ± 0.7	2.34 9.83
6-Aminohexanoic acid	$(2.90\pm0.23)10^7$	5.9510^{10}	18.6 ± 3.6	4.43
Hexanoic acid	$(8.01\pm0.24)\cdot10^7$	$2.78\cdot10^9$	8.7 ± 0.5	4.88
Hexanedioic acid	$(7.22\pm0.70)\cdot10^8$	$5.09\cdot10^9$	4.8 ± 0.8	4.43 5.28
2-Anilinobenzoic acid	$(3.15\pm0.20)\cdot10^7$	$9.25\cdot10^9$	13.8 ± 1.1	5.28
Dodecan-1-amine	$(1.02\pm0.02)\cdot10^9$	$3.64\cdot10^9$	3.1 ± 0.2	10.63

Table 1 shows similar parameters of hexanoic, hexanedioic, 2-anilinobenzoic acids and dodecan-1-amine for comparison [17, 18]. Analysis of available data suggests that despite their amphoteric nature 2- and 6-aminohexanoic acids in toluene react with the spin probe at a rate comparable to the rate of the proton exchange reaction with aliphatic monocarboxylic acids (hexanoic acid is given for an example). The value of this rate is far from the rates with aliphatic amines [18]. Therefore, a proton of the carboxyl group of aminohexanoic acid is involved in the proton exchange. It is assumed that the proton exchange will occur both in the amino group and in the carboxyl group simultaneously. At the same time, an increase in the rate should be recorded at least by an order of magnitude, as in the case of dicarboxylic hexanedioic acid, but we do not observe this. It should be noted that the high activation energy of the process is a feature of the proton exchange reaction with 2- and 6-aminohexanoic acids. There are competing reactions of the intra- and intermolecular interaction of the amino group with the carboxyl group of aminohexanoic acid. Also, this interaction is more pronounced in 6-aminohexanoic acid, where these functional groups occupy terminal positions, and the flexibility of the carbon skeleton of the molecule makes it possible to form fairly stable structures. All these processes have a negative effect on the resulting intermolecular complex with the spin probe and lead

to an increase in the activation barrier. A similar situation is observed in the reaction of 3,6-di-*tert*-butyl-2-hydroxyphenoxyl with 2-anilinobenzoic acid.

Conclusions

The intermolecular proton exchange reaction of the spin probe, namely 3,6-di-*tert*-butyl-2-hydroxyphenoxyl, with 2-aminohexanoic and 6-aminohexanoic acids, was carried out with the carboxyl group participation. The protolytic ability of aminohexanoic acid isomers in the toluene is comparable to that of aliphatic monocarboxylic acids and aromatic amino acids. The high activation barrier of the intermolecular proton exchange is due to the presence in the system of intramolecular and intermolecular interactions between the carboxyl and amino groups, which are typical of amino acids. This has a destructive effect on the intermediate reaction complex.

References

1   Wang C.H. A comparative study on intermolecular hydrogen bond interactions in molecular dimers using different levels of computational methods / C.H. Wang, R.Q. Zhang, Z.J. Lin // Journal of Theoretical & Computational Chemistry. — 2012. — No. 11(6). — P. 1237–1259. https://doi.org/10.1142/s0219633612500836

2   Bureiko S.F. The kinetic spectroscopy of hydrogen exchange processes in systems with hydrogen bond / S.F. Bureiko // 16th International Conference on Spectroscopy of Molecules and Crystals; Minist E., Sci Ukraine. – T. 5507: Proceedings of the Society of Photo-Optical Instrumentation Engineers (Spie) – Sevastopol, UKRAINE, 2003. — P. 143–153.

3   Limbach H.H. Double Proton Tautomerism via Intra- or Intermolecular Pathways? The Case of Tetramethyl Reductic Acid Studied by Dynamic NMR: Hydrogen Bond Association, Solvent and Kinetic H/D Isotope Effects / H.H. Limbach, S. Baumgartner, R. Franke, F. Mannle, G. Scherer, G.S. Denisov // Molecules. — 2021. — Vol. 26, No. 14. https://doi.org/10.3390/molecules26144373

4   Grabowski S.J. Reaction pathway of proton transfer from the neutral to zwitterionic forms of amino acids. Support for a water molecule-mediated mechanism / S.J. Grabowski, T.M. Krygowski, B. Stepien // Journal of Physical Organic Chemistry. — 2000. — No. 13(11). — P. 740–744. https://doi.org/10.1002/1099-1395(200011)13:11<740:: aid-poc304>3.3.co;2-t

5   Wu Z.C. Proton affinity of arginine measured by the kinetic approach / Z.C. Wu, C. Fenselau // Rapid Communications in Mass Spectrometry. — 1992. — No. 6(6). — P. 403–405. https://doi.org/10.1002/rcm.1290060610

6   Bureiko S.F. Structure and intermolecular interactions in complexes with hydrogen bond of a series of bifunctional nitrogen-containing compounds / S.F., Bureiko, S.Y. Kucherov // Journal of Structural Chemistry. — 2009. — No. 50(4). — P. 712–721. https://doi.org/10.1007/s10947-009-0109-9

7   Masalimov A.S. EPR-spectroscopy of the fast proton exchange reactions in solutions / A.S. Masalimov, A.F. Kurmanova, A.U. Ospanov, A.A. Tur, S.N. Nikolskiy // Bulletin of the Karaganda university — Chemistry. — 2014. — No. 73. — P. 30–35.

8   Nikolskiy S.N. Investigation of intermolecular proton exchange 3,6-di-tert-butyl-2-oxyphenoxyl with phenol by ESR spectroscopy method / S.N. Nikolskiy, A.A. Tur, A.A. Yelchibekova, K.Zh. Kutzhanova // Bulletin of the Karaganda university — Chemistry. — 2015. — No. 77. — P. 47–50.

9   Rozman M. Proton affinity of several basic non-standard amino acids / M. Rozman // Chemical Physics Letters. — 2012. — No. 543. — P. 50–54. https://doi.org/10.1016/j.cplett.2012.06.048

10   Zhao G.D. Amino acid clusters supported by cellulose nanofibers for proton exchange membranes / G.D. Zhao, X.L. Xu, Y.B. Di, H. Wang, B.W. Cheng, L. Shi., Y. Yin // Journal of Power Sources. — 2019. — No. 438, Article 227035. https://doi.org/10.1016/j.jpowsour.2019.227035

11   Li W. Measurement and Correlation of the Solubility of Aminocaproic Acid in Some Pure and Binary Solvents / W. Li, S.C. Du, D.D. Han, S.G. Wu // Journal of Chemical and Engineering Data. — 2019. — No. 64(12). — P. 5312–5323. https://doi.org/10.1021/acs.jced.9b00543

12   Kutzhanova K.Z. Nonempirical modeling of protolytic processes in dimeric molecules of amino acids / K.Z. Kutzhanova, A.F. Kurmanova, I.A. Pustolaikina, B.M. Ismagulov // Bulletin of the University of Karaganda — Chemistry. — 2018. — No. 90. — P. 58–63. https://doi.org/10.31489/2018ch2/58-63

13   Topol I.A. Protonation of glycine and alanine: proton affinities, intrinsic basicities and proton transfer path / I.A. Topol, S.K. Burt, M. Toscano, N. Russo // Journal of Molecular Structure — Theochem. — 1998. — No. 430. — P. 41–49.

14   Miyamoto H. Allergic contact dermatitis from epsilon-aminocaproic acid / H. Miyamoto, M. Okajima // Contact Dermatitis. — 2000. — No. 42(1). — P. 50.

15   Romero C.M. Effect of Temperature on The Solubility of α-Amino Acids and α,ω-Amino Acids in Water / C.M. Romero, C.D. Oviedo // Journal of Solution Chemistry. — 2013. — No. 42(6). — P. 1355–1362. doi: 10.1007/s10953-013-0031-9

16   Никольский С.Н. Моделирование спектров ЭПР 3,6-ди-трет-бутил-2-оксифеноксила в реакции межмолекулярного протонного обмена / С.Н. Никольский // Вестн. Евраз. нац. ун-та. Сер. Химия. — 2007. — No. 60 (6). — С. 160–167.

17 Nikolskiy S.N. Investigation of intermolecular proton exchange of 3,6-di-tert-butyl-2-oxyphenoxyl with N-phenylanthranilic acid by ESR spectroscopy method / S.N. Nikolskiy, F.Z. Abilkanova, A.S. Golovenko, I.A. Pustolaikina, A.S. Masalimov // Bulletin of the University of Karaganda-Chemistry. — 2020. — No. 98. — P. 35–41. https://doi.org/10.31489/2020Ch2/35-41

18 Masalimov A.S. Protolytic Reactions of 3,6-Di-tert-Butyl-2-Hydroxyphenoxyl with Nitrogen Bases / A.S. Masalimov, A.A. Tur, S.N. Nikolskiy // Theoretical and Experimental Chemistry. — 2016. — No. 52(1). — P. 57–65. DOI: 10.1007/s11237-016-9451-0

И.Л. Стадник, Ф.Ж. Абилканова, Е.В. Кудрявцева, С.Н. Никольский, А.С. Масалимов

Толуол ортадағы кейбір алифаттық аминқышқылдарымен протон алмасу реакциясын ЭПР әдісімен зерттеу

Мақалада толуол сияқты индифферентті еріткіштегі 2-аминогексан қышқылы және 6-аминогексан қышқылы сияқты аминокапрон қышқылының кейбір изомерлерімен молекулаааралық протон алмасу кинетикасын ЭПР-спектроскопиялық зерттеу нәтижелері келтірілген. Спиндік зонд ретінде 3,6-ди-трет-бутил-2-гидроксифеноксил тұрақты семихинон радикалы пайдаланылды. ЭПР спектрлері РЭ-1306 спектрометрінде тіркелінді. Молекулаааралық протон алмасу процесінің алынған динамикалық спектрлері осы жұмыста келтірілген. Протон алмасуының ЭПР спектрлерін модельдеу осы реакция-ның төрт секірмелі моделіне және модифицирленген Блох теңдеулеріне негізделген бұрын әзірленген бағдарлама арқылы жүзеге асырылды. Модель спектрлерін эксперимент нәтижесінде алынғандармен салыстыру спиндік зондтың аминқышқылдарымен қышқылдық-негіздік әрекеттесуінің кинетикалық параметрлерін ең аз қателікпен анықтауға және реакцияның активтену кедергісін бағалауға мүмкіндік берді. Осылайша алынған мәліметтер талданып, бұрын белгілі ақпаратпен салыстырылды. Зерттелетін алифатты амин қышқылдары спиндік зондпен 3,6-ди-трет-бутил-2-гидроксифеноксилдің алифаттық карбон қышқылдарымен молекулаааралық протон алмасу реакциясының жылдамдығымен салыстыры-латын жылдамдықпен әрекеттесетіні анықталды. Бірақ, біздің жағдайда, активтену тосқауылының жоғарылауы байқалады, бұл шамасы, амин қышқылы молекуласындағы амин тобы мен карбоксил то-бы арасындағы молекулаішілік сутегі байланысы процесіне теріс әсер етумен байланысты.

Кілт сөздер: ЭПР спектроскопия, протон алмасу реакциялары, спиндік зонд, семихинонды радикал, Блох теңдеуі, аминогексан қышқылы, 3,6-ди-трет-бутил-2-гидроксифеноксил, ОН-қышқылдары.

И.Л. Стадник, Ф.Ж. Абилканова, Е.В. Кудрявцева, С.Н. Никольский, А.С. Масалимов

ЭПР-исследование реакции протонного обмена с некоторыми алифатическими аминокислотами в толуольной среде

В статье представлены результаты ЭПР-спектроскопического исследования кинетики межмолекуляр-ного протонного обмена с некоторыми изомерами аминокапроновой кислоты, такими как 2-аминогексановая кислота и 6-аминогексановая кислота в среде индифферентного растворителя — то-луола. В качестве спинового зонда был использован стабильный семихинонный радикал — 3,6-ди-трет-бутил-2-гидроксифеноксил. Спектры ЭПР регистрировали на спектрометре РЭ–1306. Получен-ные динамические спектры процесса межмолекулярного протонного обмена приведены в настоящей работе. Моделирование спектров ЭПР протонного обмена проводилось с помощью ранее разработан-ной программы, в основе которой лежит четырехпрыжковая модель данной реакции и модифициро-ванные уравнения Блоха. Сопоставление модельных спектров с экспериментальными позволило нам с минимальной ошибкой определить кинетические параметры процесса кислотно-основного взаимо-действия спинового зонда с аминокислотами и оценить активационный барьер реакции. Полученные таким образом данные были проанализированы и сопоставлены с ранее известными сведениями. Было обнаружено, что исследуемые алифатические аминокислоты реагируют со спиновым зондом со ско-ростями, сопоставимыми со скоростями реакции межмолекулярного протонного обмена 3,6-ди-трет-бутил-2-гидроксифеноксила с алифатическими карбоновыми кислотами. Но при этом в нашем случае наблюдается рост активационного барьера, который, видимо, связан с негативным влиянием на про-цесс внутримолекулярной водородной связи между амино- и карбоксильной группами в молекуле аминокислоты.

Ключевые слова: ЭПР-спектроскопия, реакции протонного обмена, спиновый зонд, семихинонный ра-дикал, уравнение Блоха, аминогексановая кислота, 3,6-ди-трет-бутил-2-гидроксифеноксил, ОН-кислоты.

References

1   Wang, C.H., Zhang, R.Q., & Lin, Z.J. (2012).A comparative study on intermolecular hydrogen bond interactions in molecular dimers using different levels of computational methods. *Journal of Theoretical & Computational Chemistry*, 11(6), 1237–1259. https://doi.org/10.1142/S0219633612500836

2   Bureiko, S.F. (2003, May 25-Jun 01). The kinetic spectroscopy of hydrogen exchange processes in systems with hydrogen bond. Paper presented at the 16th International Conference on Spectroscopy of Molecules and Crystals, Sevastopol, Ukraine.

3   Limbach, H.H., Baumgartner, S., Franke, R., Mannle, F., Scherer, G., & Denisov, G.S. (2021). Double Proton Tautomerism via Intra- or Intermolecular Pathways? The Case of TetramethylReductic Acid Studied by Dynamic NMR: Hydrogen Bond Association, Solvent and Kinetic H/D Isotope Effects. Molecules, 26(14), Article 4373. https://doi.org/10.3390/molecules26144373

4   Grabowski, S.J., Krygowski, T.M., & Stepien, B. (2000).Reaction pathway of proton transfer from the neutral to zwitterionic forms of amino acids. Support for a water molecule-mediated mechanism. *Journal of Physical Organic Chemistry*, *13*(11), 740–744. https://doi.org/10.1002/1099-1395(200011)13:11<740:: aid-poc304>3.3.co;2-t

5   Wu, Z.C., & Fenselau, C. (1992). Proton affinity of arginine measured by the kinetic approach. *Rapid Communications in Mass Spectrometry*, *6*(6), 403–405. https://doi.org/10.1002/rcm.1290060610

6   Bureiko, S.F., & Kucherov, S.Y. (2009). Structure and intermolecular interactions in complexes with hydrogen bond of a series of bifunctional nitrogen-containing compounds. *Journal of Structural Chemistry*, *50*(4), 712–721. https://doi.org/10.1007/s10947-009-0109-9

7   Masalimov, A.S., Kurmanova, A.F., Ospanov, A.U., Tur, A.A., & Nikolskiy, S.N. (2014). EPR-spectroscopy of the fast proton exchange reactions in solutions. *Bulletin of the University of Karaganda – Chemistry, 1(73),* 30–35.

8   Nikolskiy, S.N., Tur, A.A., Yelchibekova, A.A., & Kutzhanova, K.Zh. (2015). Investigation of intermolecular proton exchange 3,6-di-tert-butyl-2-oxyphenoxyl with phenol by ESR spectroscopy method. *Bulletin of the University of Karaganda – Chemistry, (77)*, 47–50.

9   Rozman, M. (2012). Proton affinity of several basic non-standard amino acids. *Chemical Physics Letters*, *543*, 50–54. https://doi.org/10.1016/j.cplett.2012.06.048

10   Zhao, G.D., Xu, X.L., Di, Y.B., Wang, H., Cheng, B.W., Shi, L., & Yin, Y. (2019). Amino acid clusters supported by cellulose nanofibers for proton exchange membranes. *Journal of Power Sources*, *438*, Article 227035. https://doi.org/10.1016/j.jpowsour.2019.227035

11   Li, W., Du, S.C., Han, D.D., & Wu, S.G. (2019). Measurement and Correlation of the Solubility of Aminocaproic Acid in Some Pure and Binary Solvents. *Journal of Chemical and Engineering Data*, *64*(12), 5312–5323. https://doi.org/10.1021/acs.jced.9b00543

12   Kutzhanova, K.Z., Kurmanova, A.F., Pustolaikina, I.A., & Ismagulov, B.M. (2018). Nonempirical modeling of protolytic processes in dimeric molecules of amino acids. *Bulletin of the University of Karaganda – Chemistry (90)*, 58–63. https://doi.org/10.31489/2018ch2/58-63

13   Topol, I.A., Burt, S.K., Toscano, M., & Russo, N. (1998). Protonation of glycine and alanine: proton affinities, intrinsic basicities and proton transfer path. *Journal of Molecular Structure – Theochem*, *430*, 41–49.

14   Miyamoto, H., & Okajima, M. (2000). Allergic contact dermatitis from epsilon-aminocaproic acid. *Contact Dermatitis*, *42*(1), 50–50.

15   Romero, C.M., & Oviedo, C.D. (2013). Effect of Temperature on The Solubility of α-Amino Acids and α,ω-Amino Acids in Water. *Journal of Solution Chemistry, 42(6),* 1355–1362. doi: 10.1007/s10953-013-0031-9

16   Nikolskiy, S.N. (2007). Modelirovanie spektrov EPR 3,6-di-tret-butil-2-oksifenoksila v reaktsii mezhmolekuliarnogo protonnogo obmena [Simulation of ESR spectra of 3,6-di-tert-butyl-2-oxyphenoxyl in the reaction of intermolecular proton exchange]. *Vestnik Evraziiskogo natsionalnogo univetrsiteta. Seriia Khimiia — Bulletin of the L.N. Gumilyov Eurasian National University – Chemistry*, 60(6), 160–167 [in Russian].

17   Nikolskiy, S.N., Abilkanova, F.Z., Golovenko, A.S., Pustolaikina, I.A., & Masalimov, A.S. (2020). Investigation of intermolecular proton exchange of 3,6-di-tert-butyl-2-oxyphenoxyl with N-phenylanthranilic acid by ESR spectroscopy method. *Bulletin of the University of Karaganda – Chemistry, 2*(98), 35–41. https://doi.org/10.31489/2020Ch2/35-41

18   Masalimov, A.S., Tur, A.A., & Nikolskiy, S.N. (2016). Protolytic Reactions of 3,6-DI-tert-Butyl-2-Hydroxyphenoxyl with Nitrogen Bases. *Theoretical and Experimental Chemistry, 52(1),* 57–65. https://doi.org/10.1007/s11237-016-9451-0

Information about authors*

Stadnik, Irina Leonidovna (corresponding author) — Candidate of Chemical Sciences, Assistant Professor, Physical and Analytical Chemistry Department, Karagandy University of the name of academician E.A. Buketov, Universitetskaya street, 28, 100024, Karaganda, Kazakhstan; e-mail: i.stadnik@mail.ru; https://orcid.org/0000-0002-9497-4177;

Abilkanova, Farida Zhumageldyevna — PhD student, Physical and Analytical Chemistry Department, Karagandy University of the name of academician E.A. Buketov, Universitetskaya street, 28, 100024, Karaganda, Kazakhstan; e-mail: Farida_b88@mail.ru; https://orcid.org/0000-0002-6894-5276;

Kudryavtseva, Yelizaveta Vasilyevna — 1st year Master's student, Physical and Analytical Chemistry Department, Karagandy University of the name of academician E.A. Buketov, Universitetskaya street, 28, 100024, Karaganda, Kazakhstan; e-mail: kudryavcevaev99@gmail.com; https://orcid.org/0000-0002-1672-1318;

Nikolskiy, Sergey Nikolayevich — Doctor of Chemical Sciences, Professor, Physical and Analytical Chemistry Department, Karagandy University of the name of academician E.A. Buketov, Universitetskaya street, 28, 100024, Karaganda, Kazakhstan; Professor, Physical and Inorganic Chemistry Department, Altay State University, 656049, Barnaul, Russia, e-mail: sergeynikolsky@mail.ru; https://orcid.org/0000-0003-3175-6938;

Masalimov, Abay Sabirzhanovich — Full Professor, Doctor of Chemical Sciences, Physical and Analytical Chemistry Department, Karagandy University of the name of academician E.A. Buketov, Universitetskaya street, 28, 100024, Karaganda, Kazakhstan; e-mail: masalimov-as@mail.ru; https://orcid.org/0000-0002-6405-7108

_____

*The author's name is presented in the order: *Last Name, First and Middle Names*

UDC 544.18+544.43   https://doi.org/10.31489/2022Ch2/2-22-20

A.V. Ryabykh[1], O.A. Maslova[1], S.A. Beznosyuk[1*], A.S. Masalimov[2]

[1]Altai State University, Barnaul, Russia;
[2]Karagandy University of the name of academician E.A. Buketov, Karaganda, Kazakhstan
*(*Corresponding author's e-mail: bsa1953@mail.ru)*

The Role of Zinc Ion in the Active Site of Copper-Zinc Superoxide Dismutase

The interaction of the superoxide radical ion O_2^- with the active site of Cu, Zn-superoxide dismutase is studied by computer simulation using the ORCA software package version 5.0.2 at the level of density functional theory using the PBE functional and the basis sets of functions def2-SVP, def2-SVPD and def2-TZVPD. The main characteristics for two processes of electron transfer in the catalytic cycle of radical ion deactivation are obtained: reaction potential ΔG^0, total reorganization energy λ_{tot}, activation energy $\Delta G^{\neq}$, overlap matrix element H_{DA}, and transfer rate constant k according to Marcus. The variable factor in the modeling is the presence of the Zn^{2+} ion at the active site of the enzyme. Two variants of the electron transfer mechanism are considered: one carried out through ligands and another occurring in the immediate vicinity of an oxygen-containing particle and a copper ion. It has been established that the presence of the Zn^{2+} ion contributes to a large extent only to the second electron transfer from the Cu^+ ion to the protonated form of the radical ion, to the hydroperoxide radical HO_2. Other things being equal, the zinc ion increases the electron transfer rate constant by five times through specific interactions.

Keywords: Cu, Zn-superoxide dismutase, superoxide radical ion, enzyme, reactive oxygen species, antioxidants, condensed state physical chemistry, computer simulation.

Introduction

Molecular oxygen O_2 is an integral part of the energy chains of aerobic organisms. In addition to the benefits that oxygen brings to the body when it is reduced to a water molecule during the redox process, the oxidative power of O_2 can also harm the cellular components of the body. During metabolic transformations, oxygen is able to turn into extremely reactive particles, such as the superoxide radical ion O_2^- considered in this article, the hydroxyl ion OH^-, the hydroxyl radical OH, hydrogen peroxide H_2O_2, etc. These are the so-called reactive oxygen species (ROS). Their accumulation can adversely affect the state of cell components, destroying them and leading to various diseases of the body as a whole. This phenomenon is called oxidative stress [1, 2].

Antioxidants and antioxidant enzymes provide protection against excessive production of ROS in a healthy body; for example, enzymes of the superoxide dismutase group (SOD) ensure the neutralization of superoxide O_2^- by dismuting it into molecular oxygen and a hydrogen peroxide molecule:

$$2O_2^- + 2H_3O^+ = O_2 + H_2O_2 + 2H_2O.$$

These metalloenzymes include ions of 3d transition elements, such as Cu^{2+} and Zn^{2+} (Cu, Zn-SOD or SOD1), Mn^{3+} (Mn-SOD or SOD2), Fe^{3+} (Fe-SOD), and Ni^{3+} (Ni-SOD) [3, 4].

There are various approximate models for describing the quantum mechanisms of electron transport in condensed states. The model for the case of an electron passing through a one-dimensional static potential barrier over a distance of the order of the barrier width is justified for solid crystalline bodies. This model is not suitable for liquid water-protein media of "living" biochemical systems, where significant relaxation changes occur in the geometry of atoms surrounding the electron transfer channel. Therefore, when conducting this study, we were under the paradigm of the Marcus electron transfer theory for liquid biochemical systems. In this approach, a significant contribution to the value of the potential barrier $\Delta G^{\neq}$ is made by the energy of reorganization of the condensed medium and the structure of the nearest environment of the electron transfer channel. In this study, we evaluated all the main characteristics of an effective potential barrier $\Delta G^{\neq}$ for transfer between an electron donor and an acceptor. At the same time, the matrix element of the overlapping of the electron molecular orbitals of the donor and acceptor H_{DA} makes it possible to estimate the efficiency of electron tunneling in the semi-quantitative approximation, as a decrease in the height of the classical barrier $\Delta G^{\neq}$ due to its quantum "smearing".

Previously, we studied the stability of the superoxide ion O_2^- [5] in a dielectric medium. Also, using a semi-quantitative technique for such a system as oxygen-SOD1, we evaluated the effect of the properties of a continuous dielectric medium on the primary electron transfer [6]. This technique can be associated with frozen strongly perturbed states during electron transfer. To fully appreciate the electronic and intermolecular effects of interaction in such a system, we apply the opposite but complementary method associated with the Marcus continuum approximation. This is the subject of our consideration in the present study.

This paper considers the main aspects and specifics of the interaction between the superoxide radical ion and the Cu, Zn-SOD active center. The details of the catalytic mechanism are still debatable. Thus, the mechanism of electron transfer is debatable: Does it proceed through the inner-sphere mechanism (in this case, O_2^- comes close enough to the copper ion and acts as a ligand) or through the outer-sphere (in this case, the electron is transferred over a long distance through other ligands associated with the copper ion)? In addition, if the presence of the copper ion Cu^{2+} is necessary for the creation of a redox potential through the formation of a Cu^{2+}/Cu^+ redox pair, then what is the role of the zinc ion Zn^{2+} in the active site? There is evidence that the zinc ion maintains the structure of the site and the Zn-deficient enzyme copes worse with the reduction of O_2^- to H_2O_2 during the secondary electron transfer from Cu^+, while the secondary transfer becomes pH-dependent [7]. This paper aims to study the processes of electron transfer at two stages of the catalytic process of O_2^- deactivation by enzyme SOD1 and identify the role of the Zn^{2+} ion in this case by comparing the transfer characteristics with "normal" and "Zn-deficient" active sites.

Experimental

Modeling was carried out using the ORCA software package version 5.0.2 [8]. As a calculation method, we applied the level of density functional theory using the GGA density functional of Perdew–Burke-Ernzerhof PBE [9]. The def2-TZVPD basis set [10, 11] was used to optimize the geometry and calculate single point energies of small particles (O_2^-, O_2, HO_2, HO_2^-, H_2O, H_3O^+). When optimizing the geometry of the active site, a simplified def2-SVP basis [10] was used with additional restrictions in the form of pinning 8 hydrogen atoms of the methyl end groups to simulate the fact that the active site is retained by the protein environment [12]. After geometry optimization, the one-point energy of the active center structure was calculated with the def2-SVPD basis. In addition, in all cases, when calculating the active center, the oxygen atoms O, copper Cu, and zinc Zn were always subject to the def2-TZVPD basis set. To speed up the hardware calculation, the RI approximation with the basis set def2/J [13] was automatically applied. In any calculation, to consider fine dispersion interactions, the atomic pair dispersion correction algorithm based on rigidly coupled partial charges D4 was used [14, 15]. The influence of the dielectric medium was taken into account using the CPCM continuum model. The surface type is Gaussian VdW [16]. The adequacy of the selection of such calculation parameters was evaluated by one of the important characteristics for molecular oxygen O_2, which participates in these reactions, namely, by electron affinity in the gas phase. The experimental value A = -0.451 ± 0.007 eV [17]. Our value A = -0.414 eV. This approach made it possible to balance the accuracy of the calculation and the cost of hardware time.

To begin with, we should briefly describe the catalytic cycle of the enzyme. Figure 1 shows a simplified process diagram.

The **II–III** and **IV–I** transitions are key to electron transfer. It can be seen that these transitions are complex since the transfer of an electron is coupled with the transfer of a proton H^+. Since the proton is 1836 times heavier than the electron, the same formalism cannot be applied to it as to the electron. Therefore, the transitions should be divided into more simplified stages in order to be able to describe directly the electron transfer separately from the proton.

It is rather easy to separate transitions **II–III**. Since molecular oxygen O_2 is formed in this case, it is reasonable to assume that the act of electron transfer from O_2^- to the copper ion Cu^{2+} occurs first in a distorted square environment. Then, monovalent copper Cu^+, which is no longer able to maintain a complex with a coordination number of 4, weakens the bond with the bridging histidine ligand and passes into a trigonal environment, followed by protonation of the nitrogen atom.
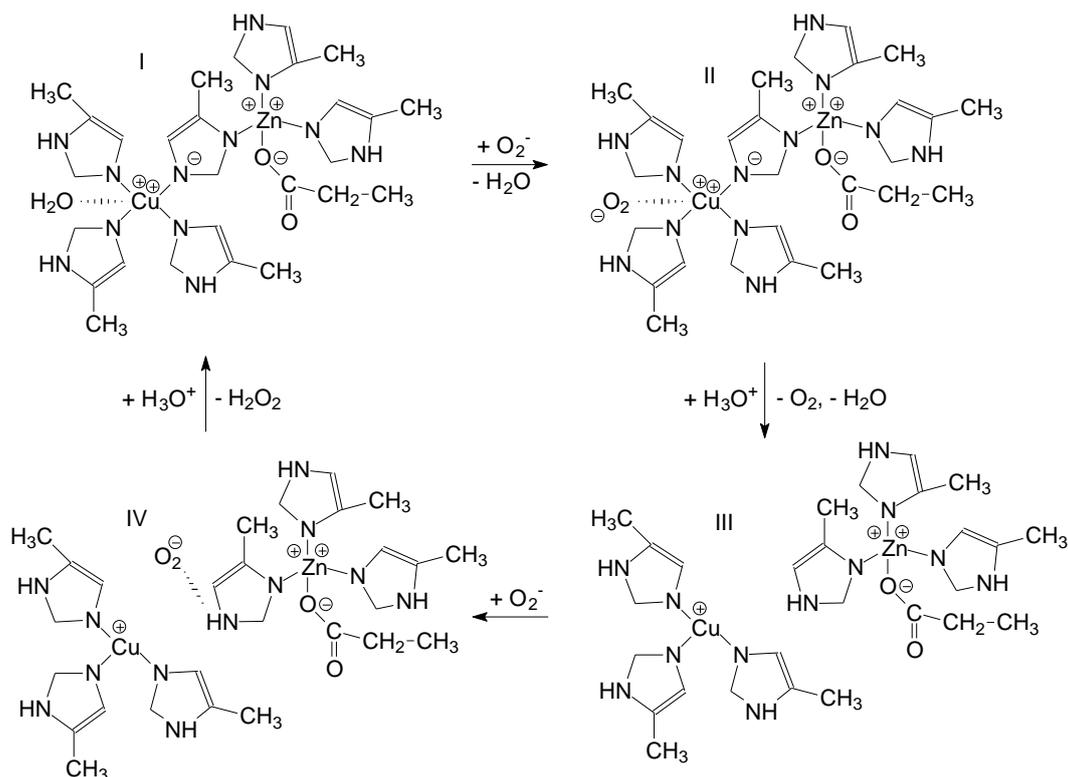
Figure 1. Scheme of the catalytic cycle of dismutation of the superoxide radical ion O_2^-
at the active site of copper-zinc superoxide dismutase

IV–I transition is more difficult to separate. This is where the bifurcation occurs. 1. The copper ion Cu^+ in the trigonal environment first donates the electron to the O_2^- ion with the formation of a peroxide ion O_2^{2-} that is not stable in a condensed medium, followed by its protonation to the H_2O_2 molecule. 2. The O_2^- ion accepts a proton from the N–H bond to form the HO_2 hydroperoxide radical, and then the Cu^+ copper ion in the trigonal environment donates the electron to the radical to form the HO_2^- hydroperoxide ion. The simulation showed the predominant flow of process 2, which will be reflected in the results. Figure 2 reflects the above considerations regarding the choice of stages for electron transfer.
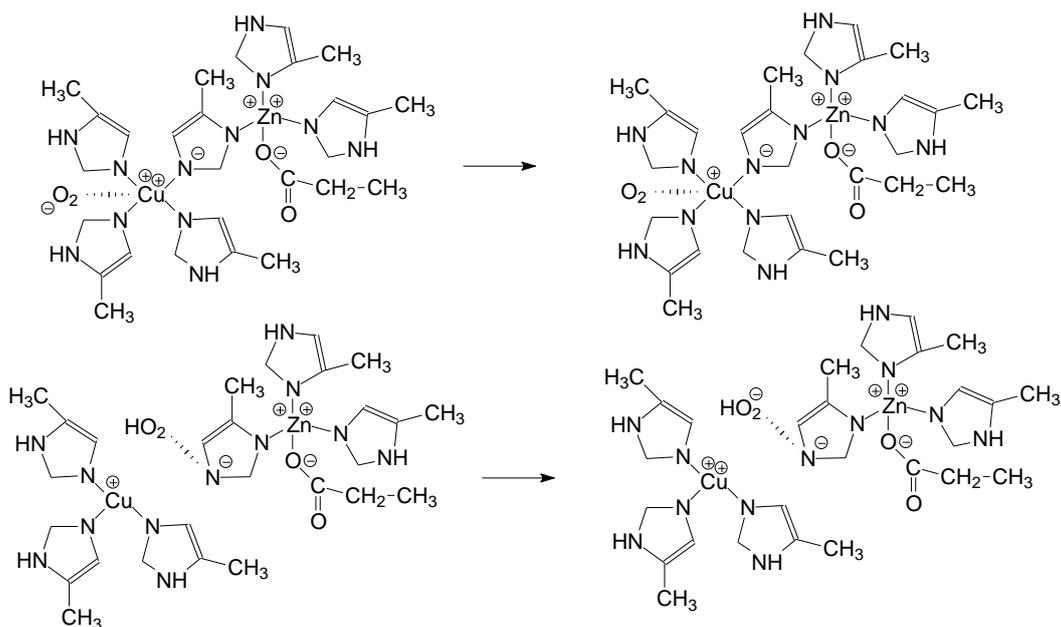
Figure 2. Separately distinguished stages of primary and secondary electron transfers

Besides, for the case of a Zn-deficient active site, the Zn^{2+} ion was removed from the structure of the active site and replaced by two equivalent H^+ protons. The first of them was attached to the oxygen atom of the former zinc ligand, and the second, to the nitrogen atom of the former bridging ligand. Figure 3 presents the scheme for the removal of zinc ion.
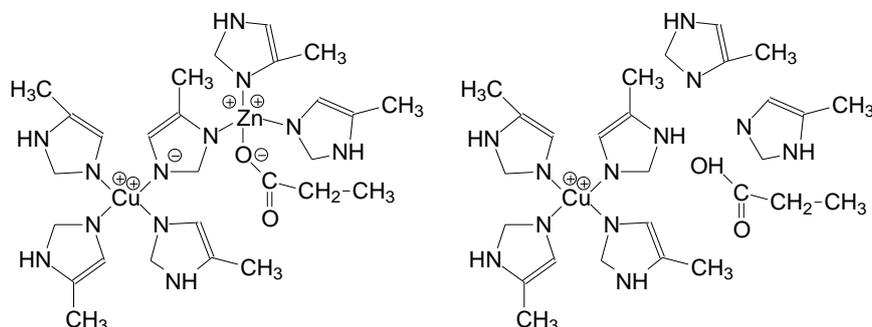
Figure 3. Scheme for the removal of zinc ion from the active site

The efficiency of electron transfer can be estimated to a complete extent by obtaining the value of the second-order transfer rate constant k (hereinafter, we denote *I* as primary transfer and *II* as secondary):

$$O_2^- + ICu^{2+}SOD = O_2 + ICu^+SOD \tag{1}$$

$$\frac{dC}{dt} = -k_I \cdot [O_2^-] \cdot [Cu^{2+}] ; \tag{2}$$

$$HO_2 + IICu^+SOD = HO_2^- + IICu^{2+}SOD \tag{3}$$

$$\frac{dC}{dt} = -k_{II} \cdot [HO_2] \cdot [Cu^+]. \tag{4}$$

In general, the rate constant k for reactions (1) and (3) can be estimated using an analogue of the Eyring equation for the activated complex theory [18]:

$$k = k_{et} \cdot K_{pre}^{\neq}, \tag{5}$$

where k_{et} — the frequency factor of electron transfer according to Marcus, s-1; $K_{pre}^{\neq}$ — the concentration equilibrium constant of the formation of the precursor complex from the electron donor and acceptor, M-1.

The frequency factor k_{et} or the first-order rate constant of electron transfer can be calculated using the Marcus formalism [19]:

$$k_{et} = \frac{4 \cdot \pi^2}{h} \cdot \frac{H_{DA}^2}{\sqrt{4 \cdot \pi \cdot \lambda_{tot} \cdot k_B \cdot T}} \cdot e^{\frac{-\Delta G^{\neq}}{k_B \cdot T}} . \tag{6}$$

where h — the Planck's constant, J·s; H_{DA} — the matrix element of overlapping molecular orbitals of the electron donor and acceptor, J; λ_{tot} — the total energy of the system reorganization, J; k_B — the Boltzmann constant; J/K; T — temperature, K; $\Delta G^{\neq}$ — the transfer activation energy, J.

a. Calculation of the reaction potential ΔG^0

According to the Hess law and the principle of the quantum dimension of the system, the change in the potential of the electron transfer reaction was calculated according to the scheme:

$$\Delta G_I^0 = G^0(O_2) + G^0(ICu^+SOD) - G^0(O_2^-) - G^0(ICu^{2+}SOD) ; \tag{7}$$

$$\Delta G_{II}^0 = G^0(HO_2^-) + G^0(IICu^{2+}SOD) - G^0(HO_2) - G^0(IICu^+SOD) . \tag{8}$$

It is also necessary to calculate the "corrected" value of $\Delta G^{0\backprime}$ — adjusted for the fact that the electron transfer occurs not at infinity, but at a specific finite distance R. To do this, we use the expression proposed in [20]:

$$\Delta G^{0\backprime} = \Delta G^0 + (Z_A - Z_D - 1) \cdot \frac{1}{4 \cdot \pi \cdot \varepsilon_0} \cdot \frac{q_e^2}{\varepsilon \cdot R} . \tag{9}$$

where Z_A — the charge number of the acceptor; Z_D — the charge number of the donor; ε_0 — the electrical constant, F/m; q_e — the electron charge, C; R — the transfer distance, m; ε — the static permittivity of the medium.

The transfer distance R is an extremely ambiguous value and can vary greatly. The principle of choosing R values is presented below.

b. Calculation of the total reorganization energy λ_{tot}

The reorganization energy is the energy that must be expended to bring the system into a state as if the electron transfer had already occurred, but *de facto* without it. The total reorganization energy consists of two components. The first one is the internal λ_{in}, which includes the energy spent on rearranging the structure of the donor and acceptor for electron transfer. The second is the external λ_{out}, which includes the energy consumption for the rearrangement of the structure of the environment surrounding the donor and acceptor, the solvent.

The calculation of λ_{in} is generally similar to the calculation of the reaction potential, but with a difference in the products. Here it is necessary to take perturbed structures as finite particles, for example, if in its ground state the superoxide ion O_2^- has, according to our modeling, an equilibrium internuclear distance of 1.353 Å in the charge state –1, then the perturbed structure corresponding to it will have an internuclear distance of 1.218 Å (as in molecular oxygen O_2) in the charge state –1. Single point energy without optimization of the geometry of such structures is denoted by *.

$$\lambda_{in}^{I} = G^{0*}(O_2^-) + G^{0*}(ICu^{2+}SOD) - G^0(O_2^-) - G^0(ICu^{2+}SOD);\qquad (10)$$

$$\lambda_{in}^{II} = G^{0*}(HO_2) + G^{0*}(IICu^+SOD) - G^0(HO_2) - G^0(IICu^+SOD).\qquad (11)$$

Markus and Sutin proposed the calculation of λ_{out} in the approximation of the solvent continuum model [19]:

$$\lambda_{out} = \frac{\Delta q^2}{4\cdot\pi\cdot\varepsilon_0}\cdot\left(\frac{1}{2r_D}+\frac{1}{2r_A}-\frac{1}{R}\right)\cdot\left(\frac{1}{n^2}-\frac{1}{\varepsilon}\right),\qquad (12)$$

where Δq — the value of the transferred charge, C; r_D — the donor radius, m; r_A — the acceptor radius, m; n — the refractive index of the medium.

The size of the transfer participants was estimated from the following considerations. All reagents were presented as spheres with certain radii r. Thus, the radius of the superoxide ion O_2^- was calculated as the sum of the radius of the oxygen atom according to the continuum model (this is 1.52 Å) and half the length of the O–O bond (this is 0.6765 Å from 1.353 Å). In the case of such a small particle, a solvent correction is also needed [20]. When using the continuum model, it makes sense to add half of the probe radius (this is 0.65 Å from 1.3 Å). We have the radius of the donor sphere centered in the middle of the bond $r_{DI}(O_2^-) = 2.8465$ Å. By using a similar approach, we can obtain $r_{AII}(HO_2) = 2.8365$ Å for the HO_2 acceptor. Also, for the active site, it is logical to choose only such a region that changes significantly during the redox process. This is the first ligand environment of the copper ion. A sphere centered on a copper ion with an average radius extending to the second nitrogen atom in the imidazole ring of the ligands was chosen with the addition of the radius of the nitrogen atom according to the continuum model of 1.89 Å. We have $r_{AI}(Cu^{2+}SOD) = 6.035$ Å. By analogy, for the monovalent copper state, one can obtain $r_{DII}(Cu^+SOD) = 6.040$ Å. For the Zn-deficient active site, the corresponding values are 6.047 Å and 6.034 Å.

To estimate the transfer rate constant by the outer-sphere mechanism, two reference values of R can be chosen. The first of them is the sum of the donor and acceptor radii. In our case, this is 8.88 Å. The second value is 6 Å, chosen from the consideration that a positively charged aspartic group adjoins the active center at this distance, which is capable of directing O_2^- to the reaction. Also, for the inner-sphere mechanism, the distance R is determined, for the most part, by optimizing the O_2^- geometry in close proximity to the copper ion.

c. Calculation of the transfer activation energy $\Delta G^{\neq}$

Knowing the values of the reaction potential $\Delta G^{0`}$ and λ_{tot}, it is possible to determine the value of the activation energy [20] according to the equation:

$$\Delta G^{\neq} = \frac{1}{4\cdot\pi\cdot\varepsilon_0}\cdot\frac{Z_D\cdot Z_A\cdot q_e^2}{\varepsilon\cdot R} + \frac{1}{4}\cdot\lambda_{tot}\cdot\left(1+\left(\frac{\Delta G^{0`}}{\lambda_{tot}}\right)^2\right).\qquad (13)$$

d. Calculation of the overlap matrix element H_{DA}

The overlapping matrix element of the molecular orbitals of the electron donor and acceptor can be estimated using the generalized Mulliken–Hush (GMH) approximation [21]:

$$H_{DA} = \frac{\Delta E_{12} \cdot \mu_{12}}{\sqrt{\Delta \mu_{12}^2 + 4 \cdot \mu_{12}^2}} , \tag{14}$$

where ΔE_{12} — the energy of electron transition from the MO of the donor to the MO of the acceptor, J; μ_{12} — the transition dipole moment, C·m; $\Delta \mu_{12}$ — the difference between dipole moments before and after electron transfer, C·m.

The values included in (14) were estimated using the time-dependent density functional theory (TD-DFT) using the default TDA approximation.

e. Calculation of the equilibrium constant for the formation of the precursor complex $K_{pre}^{\neq}$

The equilibrium constant $K_{pre}^{\neq}$ can be obtained based on various considerations. We used one of the expressions presented in [18], in which it suffices to know the work of approach of the donor and acceptor W_R and the electron transfer distance R:

$$K_{pre}^{\neq} = \frac{4}{3} \cdot \pi \cdot N_A \cdot R^3 \cdot e^{\frac{-W_R}{k_B \cdot T}} , \tag{15}$$

where N_A — the Avogadro constant, mol^{-1}; R — the transfer distance, dm; W_R — the electrostatic work of bringing the reagents together at a distance R, J.

$$W_R = \frac{1}{4 \cdot \pi \cdot \varepsilon_0} \cdot \frac{Z_D \cdot Z_A \cdot q_e^2}{\varepsilon \cdot R} . \tag{16}$$

Here and below, when calculating according to the above expressions, the temperature value T is equal to the standard 298.15 K.

Results and Discussion

To begin with, we point out that the experimental values of k for both primary and secondary electron transfers do not depend on the charge of the copper ion and are equal to $2 \cdot 10^9$ M^{-1}·s^{-1} [22].

Thus, let us consider the main characteristics of the primary electron transfer of the **II–III** transition between the superoxide radical ion O_2^- and the copper ion Cu^{2+} according to the outer-sphere mechanism at a distance of 6 Å perpendicular to the square environment of copper (Table 1).

T a b l e 1

Characteristics of primary electron transfer at R = 6 Å

Parameter	SOD1	Zn-deficient SOD1
ΔG^0, eV	–0.444	–0.491
$\Delta G^{0\backprime}$, eV	–0.385	–0.431
λ_{tot}, eV	1.754	1.686
$\Delta G^{\neq}$, eV	0.208	0.174
H_{DA}, eV	$1.68 \cdot 10^{-2}$	$2.51 \cdot 10^{-3}$
k_{et}, s^{-1}	$1.11 \cdot 10^9$	$9.37 \cdot 10^7$
$K_{pre}^{\neq}$, M^{-1}	5.56	5.56
k, M^{-1}·s^{-1}	$6.15 \cdot 10^9$	$5.21 \cdot 10^8$

Similar values of the rate constants of electron transfer at the same distance with and without zinc ion indicate that the zinc ion does not play an important role in the first stage of deactivation of the superoxide ion.

It should be noted that the overlap of the donor and acceptor molecular orbitals decays with increasing transfer distance. Since the overlap matrix element, along with the activation energy, makes the most significant contribution to the rate constant, we can compare how the matrix element decays with the transfer distance for the active site with and without zinc ion. The dependence of the overlap matrix element was assumed to be exponential [23]:

$$H_{DA} = H_{DA}^0 \cdot e^{-\alpha \cdot (R - R_0)} , \tag{17}$$

where H^0_{DA} — the value of the matrix element at the distance $R_0 = r_D + r_A$; α — the overlap damping constant, Å^{-1}.

We obtained the following correlation equations for SOD1 $\alpha = 1.173$ Å^{-1} and Zn-deficient SOD1 $\alpha = 0.573$ Å^{-1}. For SOD1, the overlap integrals of molecular orbitals decay 2 times faster than for zinc-

deficient. However, such a value is not particularly critical, given the similar values of the rate constants we obtained.

Next, we consider the main characteristics of the secondary electron transfer of the ***IV–I*** transition between the hydroperoxide radical HO_2 and the copper ion Cu^+ according to the outer-sphere mechanism at a distance of 6 Å. Let us give an explanation regarding the bifurcation discussed above. Why was HO_2 chosen as the electron acceptor, and not O_2^-? Does this mean that the proton transfer occurs before the electron transfer? It is necessary to study the potentials of the corresponding reactions to answer this question:

$$O_2^- + IICu^+(SODH^+) = O_2^{2-} + IICu^{2+}(SODH^+); \tag{18}$$

$$O_2^{2-} + IICu^{2+}(SODH^+) = HO_2^- + IICu^{2+}(SOD); \tag{19}$$

$\Delta G^0{}_{20} = +2.84$ eV. $\Delta G^0{}_{21} = -1.90$ eV. Sum: 0.94 eV.

$$O_2^- + IICu^+(SODH^+) = HO_2^- + IICu^+(SOD); \tag{20}$$

$$HO_2 + IICu^+(SOD) = HO_2^- + IICu^{2+}(SOD); \tag{21}$$
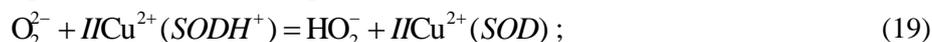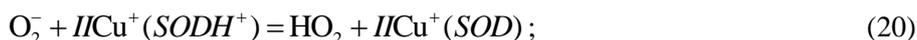
$\Delta G^0{}_{22} = +0.354$ eV. $\Delta G^0{}_{23} = -0.39$ eV. Sum: -0.036 eV.

It is natural to choose scheme 2 (20–21) as the model scheme for secondary transfer. Further, it should be pointed out that the superoxide ion O_2^- is no longer bound by the copper ion Cu^+ in the trigonal environment that is stable for such a valence state, but elsewhere. According to the geometry optimization results, O_2^- tends to the source of protons, in this case, to the N–H bond of the bridging ligand. This proton is split off from the nitrogen atom and goes to the radical.

Table 2

Characteristics of secondary electron transfer at R = 6 Å

Parameter	SOD1	Zn-deficient SOD1
ΔG^0, eV	–0.390	–0.044
$\Delta G^{0\backslash}$, eV	–0.449	–0.104
λ_{tot}, eV	1.603	1.672
$\Delta G^{\neq}$, eV	0.208	0.368
H_{DA}, eV	$1.91 \cdot 10^{-1}$	$3.70 \cdot 10^{-2}$
k_{et}, s^{-1}	$1.49 \cdot 10^{11}$	$1.08 \cdot 10^7$
$K_{pre}{}^{\neq}$, M^{-1}	0.545	0.545
k, M$^{-1} \cdot$ s^{-1}	$8.12 \cdot 10^{10}$	$5.86 \cdot 10^6$

As can be seen, the effects mainly concern only the secondary electron transfer. This indicates that the copper ion Cu^+ in the absence of Zn^{2+} becomes less labile with respect to the loss of an electron with the formation of Cu^{2+}. The effect is on all quantities that determine the value of the rate constant. Significant differences in the rate constants, both of the first order and of the second order, indicate that zinc-deficient SOD1 copes much worse with the role of a catalyst. The frequency transfer factor in this case is less by five orders of magnitude than for the "normal" SOD1.

The removal of the zinc ion increases the value of the isobaric-isothermal transfer potential ΔG^0 by 0.35 eV. Let's write its value as:

$$\Delta G^0 = z \cdot F \cdot \left(E^0 \left(SOD^{2+} \middle/ SOD^+ \right) - E^0 \left(HO_2 \middle/ HO_2^- \right) \right) \tag{22}$$

where z — the number of transferred electrons; F — the Faraday constant, C/mol; E^0 — the standard electrode potential, V.

It can be seen that the value of the standard electrode potential of the SOD active center increases. The oxidizing properties of the center are enhanced and the reducing properties are weakened. The oxidizing properties of the center are weakened and the reducing properties are enhanced. The reorganization energy somewhat increases by 0.07 eV due to the structural component. The zinc ion in a tetrahedral environment more stabilizes the system and limits the geometric transformations of the active center after electron transfer. Thus, with a change in these parameters, the activation energy of the second transfer for the Zn-deficient center increases by about 16 kJ/mol. Given that the rate constant has a quadratic dependence on H_{DA}, this effect is more significant than the increase in the transfer activation energy.

There is clear participation of the bridging histidine ligand in the formation of the donor MO of the active site, which promotes electron transfer. When the zinc ion is removed, the ligand is no longer bridging and becomes more independent, while it does not take part in the formation of the donor MO.

As for the primary transfer, let us analyze the attenuation coefficient of the orbital overlap for the secondary transfer. For SOD1 $\alpha = 0.047$ Å^{-1} and Zn-deficient SOD1 $\alpha = 0.569$ Å^{-1}. Here, we observe a significant difference in the values of the indicator. The extremely low value for SOD1 indicates that the attenuation of the orbital overlap is extremely weak and can reach significant values for the implementation of electron transfer, even at large distances through ligands. The obtained molecular orbitals for SOD1 and zinc-deficient SOD1 for secondary transfer show that the bridging ligand connecting copper and zinc ions is also involved in the formation of the outer orbital. This indicates the low attenuation and the participation of ligands in the transfer.

It is reasonable to trace the distribution of an atomic-molecular characteristic, such as atomic charge, throughout the active center before and after electron transfer. Let us look at the changes in atomic charges according to Löwdin during the transition from $IICu^+SOD$ to $IICu^{2+}SOD$ with secondary (II) electron transfer:

– "normal" SOD1: $\Delta_qCu = +0.177$; $\Delta_qZn = +0.008$. The contribution of zinc is 4.3 %.

– Zn-deficient SOD1: $\Delta_qCu = +0.188$.

The difference between the atomic charges according to Löwdin for the copper atom Cu in $IICu^+SOD$ with and without the zinc ion Zn^{2+} is $\Delta_qCu = {}_qCu - {}_qCu(Zn) = +0.021$ (increase by 45 %). Based on the above results on the population, we can conclude that, in addition to the structural organization of the active site, the zinc ion Zn^{2+} contributes to the partial delocalization of the electron density, accepting part of it through the ligand bridge together with the copper ion Cu^+.

Let us now look at the changes in atomic charges according to Löwdin during the transition from $ICu^{2+}SOD$ to ICu^+SOD during the primary (I) electron transfer.

– "normal" SOD1: $\Delta_qCu = -0.314$; $\Delta_qZn = -0.007$. The contribution of zinc is 2.2 %.

– Zn-deficient SOD1: $\Delta_qCu = -0.321$.

The difference between atomic charges according to Löwdin for copper atom Cu in ICu^+SOD with and without zinc ion Zn^{2+} is $\Delta_qCu = {}_qCu - {}_qCu(Zn) = 0.0006$. This implies another proof of the fact that the zinc ion Zn^{2+} has a much greater influence only on the secondary electron transfer.

It has been experimentally established that the reaction catalyzed by Zn-deficient superoxide dismutase becomes pH-dependent on secondary electron transfer [7]. We present the calculated values of ΔG^0 for the processes of O_2^- protonation from the N–H bond before the secondary electron transfer in SOD1 and Zn-deficient SOD1: +0.354 eV and +0.712 eV, respectively. In the absence of zinc, the cost of protonation doubles, which indicates the stabilization of the protonated form of the histidine ligand, which is free of both the zinc ion Zn^{2+} and the copper ion Cu^+. Such an increase in energy creates certain difficulties for the preliminary formation of HO_2; therefore, the presence of an external proton from the solvent molecules is required. For example, its source can be the hydronium ion H_3O^+. This explains why the removal of zinc results in a pH-dependent electron transfer.

Conclusions

All two-electron transfer processes are associated with proton transfer. The primary electron transfer occurs somewhat earlier than the proton transfer. In the case of secondary transfer, the situation is reversed. A proton from the N–H bond of the bridging ligand is able to attach to the superoxide ion to form HO_2, which then readily accepts an electron. The zinc ion Zn^{2+} has little effect on the primary electron transfer from O_2^- to the copper ion Cu^{2+}. Its presence in the active site creates a suitable conformation for efficient overlapping of the donor and acceptor MOs and creates an additional minor electron density delocalization. At the same time, the zinc ion Zn^{2+} has a significant effect on the secondary electron transfer from Cu^+ to HO_2. When the zinc ion is removed, the transfer rate constant decreases by five times. This is due to a significant positive increase in the value of the transfer reaction potential, which in turn increases the activation energy. Thus, the zinc ion, by its presence in the active center, stabilizes the structure in such a way that during the secondary electron transfer from the active center, its redox potential increases and the reduction properties decrease. According to the results obtained, it follows that the redox potential increases by 0.35 V. The bridging ligand retained by the zinc ion is able to participate in the formation of orbital overlap during transfer, in contrast to the case of zinc removal. The participation of the ligand reduces the degree of damping of the overlap integrals and promotes rapid electron transfer. In addition, the electron density distribution

between copper and zinc ions makes it easier for the proton to break away from the ligand and then attach to the oxygen-containing particle.

References

1 Barja, G. (1999). Mitochondrial Oxygen Radical Generation and Leak: Sites of Production in States 4 and 3, Organ Specificity, and Relation to Aging and Longevity. *J. Bioenergetics and Biomembranes*, *31*, 347–366. https://doi.org/10.1023/A:1005427919188

2 Dawson, T.M., & Dawson, V.L. (2003). Molecular Pathways of Neurodegeneration in Parkinson's Disease. *Science*. *302*, 5646. https://doi.org/10.1016/B978-0-323-88460-0.00010-2

3 Fridovich, I. (1997). Superoxide anion radical (O_2^-), superoxide dismutase and related matters. *J. Biol. Chem.*, *272*, 18515–18517. https://doi.org/10.1074/jbc.272.30.18515

4 Cabelli, D.E., Riley, D., Rodriguez, J.A., Valentine, J.S., & Zhu, H. (1999). *Models of superoxide dismutases. Biomimetic Oxidations Catalyzed by Transition Metal Complexes*. Imperial College Press, 461–508. https://doi.org/10.1142/9781848160699_0010

5 Ryabykh, A.V., Maslova, O.A., Beznosyuk, S.A., Zhukovsky, M.S., & Masalimov, A.S. (2020). Computer Simulation of the O_2^- Superoxide Ion Stability in a Continuous Dielectric Medium. *Izvestiya of Altai State University*, *1*(111), 36–40. https://doi.org/10.14258/izvasu(2020)1-05

6 Maslova, O.A., Ryabykh, A.V., & Beznosyuk, S.A. (2020). Computer simulation of SOD interaction with reactive oxygen species in low-sized membrane cell nanostructures. *AIP Conference Proceedings, 2310,* 020196. https://doi.org/10.1063/5.0034337

7 Ellerby, L.M., Cabelli, D.E., Graden, J.A., & Valentine, J.S. (1996). Copper-Zinc Superoxide dismutase: Why Not pH-Dependent. *J. Am. Chem. Soc.*, *118*, 6556–6561. https://doi.org/10.1021/ja953845x

8 Neese, F. (2012). The ORCA program system. *Wiley interdisciplinary Reviews — Computational Molecular Science*, *2*(1), 73–78. https://doi.org/10.1002/wcms.81

9 Perdew, J.P., Burke, K., & Ernzerhof, M. (1996). Generalized Gradient Approximation Made Simple. *Phys. Rev. Letters*, *77*, 3865. https://doi.org/10.1103/physrevlett.77.3865

10 Weigend, F. & Ahlrichs, R. (2005). Balanced basis sets of split valence, triple zeta valence and quadruple zeta valence quality for H to Rn: Design and assessment of accuracy. *Phys. Chem. Chem. Phys.*, *7*, 3297. https://doi.org/10.1039/b508541a

11 Rappoport, D. & Furche, F. (2010). Property-optimized Gaussian basis sets for molecular response calculations. *J. Chem. Phys.*, *133*, 134105. https://doi.org/10.1063/1.3484283

12 Xerri, B., Petitjean, H., Dupeyrat, F., Flament, J.-P., Lorphelin, A., Vidaud, C., et al. (2014). Mid- and Far-Infrared Marker Bands of the Metal Coordination Sites of the Histidine Side Chains in the Protein Cu, Zn-Superoxide Dismutase. *European Journal of Inorganic Chemistry, 2014*(27)*, 4650–4659. https://doi.org/10.1002/ejic.201402263

13 Weigend, F. (2006). Accurate Coulomb-fitting basis sets for H to Rn. *Phys. Chem. Chem. Phys.*, *8*, 1057. https://doi.org/10.1039/b515623h

14 Grimme S., Antony, J., Ehrlich, S. & Krieg, H. (2010). A consistent and accurate ab initio parametrization of density functional dispersion correction (DFT-D) for the 94 elements H-Pu. *J. Chem. Phys.*, *132*, 154104. https://doi.org/10.1063/1.3382344

15 Caldeweyher, E., Bannwarth, C. & Grimme, S. (2017). Extension of the D3 dispersion coefficient model. *J. Chem. Phys.*, *147*, 034112. https://doi.org/10.1063/1.4993215

16 Cossi, M., Rega, N. & Scalmani, G. et al. (2003). Energies, structures and electronic properties of molecules in solution with the C-PCM solvation model. *Chem. Phys.*, *24*, 669–681. https://doi.org/10.1002/jcc.10189

17 Rienstra-Kiracofe, J.C., Tschumper, G.S., & Shaefer, H.F. (2002). Atomic and molecular electron affinities: photoelectron experiments and theoretical computations. *Chem. Rev.*, *102*, 231–282. https://doi.org/10.1021/cr990044u

18 Lippard, S.J. (1978). Theory of Electron Transfer Reactions: Insights and Hindsights. *Progress in Inorganic Chemistry*, *30*, 441–498. https://doi.org/10.1002/9780470166314.ch9

19 Marcus, R.A., & Sutin, N. (1985). Electron transfers in chemistry and biology. *Biochimica et Biophysica Acta*, *811*, 265–322. https://doi.org/10.1016/0304-4173(85)90014-x

20 Eberson, L. (1985). The Marcus theory of electron transfer, a sorting device for toxic compounds. *Advances in Free Radical Biology & Medicine, 1*, 19–90. https://doi.org/10.1016/8755-9668(85)90004-3

21 Cave, R.J., & Newton, M.D. (1997). Calculation of electronic coupling matrix elements for ground and excited state electron transfer reactions: Comparison of the generalized Mulliken-Hush and block diagonalization methods. *Journal of Chemical Physics, 106*, 9213–9226. https://doi.org/10.1063/1.474023

22 Takahashi, M.A., & Asada, K. (1982). A flash-photometric method for determination of reactivity of superoxide: application to superoxide dismutase assay. *Journal of biochemistry, 91*(3), 889–896. https://doi.org/10.1093/oxfordjournals.jbchem.a133777

23 Hopfield, J.J. (1974). Electron transfer between biological molecules by thermally activated tunneling. *Proceedings of the National Academy of Sciences of the United States of America, 71*(9), 3640–3644. https://doi.org/10.1073/pnas.71.9.3640

А.В. Рябых, О.А. Маслова, С.А. Безносюк, А.С. Масалимов

Мыс-мырыш супероксид дисмутазасының белсенді орталығындағы мырыш ионының рөлі

PBE функционалын және def2-SVP, def2-SVPD мен def2-TZVPD функцияларының базистік жиынтықтарын пайдалана отырып, тығыздық функционалы теориясының деңгейінде ORCA 5.0.2 нұсқасының бағдарламалық пакетінің көмегімен компьютерлік модельдеу арқылы O_2^- супероксидті ион-радикалының Cu, Zn-супероксиддисмутазаның белсенді орталығымен өзара әрекеттесуіне зерттеу жүргізілді. Ион-радикалды дезактивациялаудың каталитикалық циклiндегі электрон тасымалдаудың екі процесінің негізгі сипаттамалары алынған: ΔG^0 реакция потенциалы, λ_{tot} жалпы қайта құру энергиясы, $\Delta G^{\neq}$ активтену энергиясы, H_{DA} қабаттасатын матрица элементі және Маркус бойынша k тасымалдау жылдамдығының тұрақтысы. Модельдеу барысындағы өзгермелі фактор ретінде ферменттің белсенді орнында Zn^{2+} ионының орналасуы алынды. Лигандтардың көмегімен және құрамында оттегі бар бөлшек пен мыс ионының жақын орналасуы арқылы жүзеге асырылатын электронды тасымалдау механизмінің екі нұсқасы қарастырылды. Zn^{2+} ионының болуы тек Cu^+ ионынан ион-радикалының протондалған формасына — HO_2 гидропероксид радикалына екінші электронның өтуіне ғана үлкен дәрежеде ықпал ететіні анықталды. Арнайы өзара әрекеттесулер арқылы мырыш ионы, басқа жағдайлар бірдей болғанда электронды тасымалдау жылдамдығының константасын бес реттік шамаға арттырады.

Кілт сөздер: Cu, Zn-супероксиддисмутаза, супероксидті ион-радикал, фермент, реактивті оттегі түрлері, антиоксиданттар, конденсацияланған күйдің физика-химиясы, компьютерлік модельдеу.

А.В. Рябых, О.А. Маслова, С.А. Безносюк, А.С. Масалимов

Роль иона цинка в активном центре медно-цинковой супероксиддисмутазы

Проведено изучение взаимодействие супероксидного ион-радикала O_2^- с активным центром Cu, Zn-супероксиддисмутазы путем компьютерного моделирования при помощи программного пакета ORCA версии 5.0.2 на уровне теории функционала плотности с использованием функционала PBE и базисных наборов функций def2-SVP, def2-SVPD и def2-TZVPD. Получены основные характеристики для двух процессов переноса электрона в каталитическом цикле дезактивации ион-радикала: потенциал реакции ΔG^0, полная энергия реорганизации λ_{tot}, энергия активации $\Delta G^{\neq}$, матричный элемент перекрывания H_{DA} и константа скорости переноса k по Маркусу. Переменным фактором при моделировании являлось наличие иона Zn^{2+} в активном центре фермента. Были рассмотрены два варианта механизма переноса электрона, осуществляющихся при помощи лигандов и непосредственной близости кислородсодержащей частицы и иона меди. Установлено, что наличие иона Zn^{2+} способствует в значительной степени только второму переносу электрона от иона Cu^+ к протонированной форме ион-радикала — к гидропероксидному радикалу HO_2. Посредством специфических взаимодействий ион цинка при прочих равных условиях повышает константу скорости переноса электрона на пять порядков.

Ключевые слова: Cu, Zn-супероксиддисмутаза, супероксидный ион-радикал, фермент, активные формы кислорода, антиоксиданты, физикохимия конденсированного состояния, компьютерное моделирование.

Information about authors*

Ryabykh, Andrey Valerievich — Assistant and Engineer, Department of Physical and Inorganic Chemistry, Altai State University, Barnaul, Lenina avenue, 61; e-mail: ryabykh@chem.asu.ru; https://orcid.org/0000-0003-3699-3932;

Maslova, Olga Andreevna — Candidate of Physical and Mathematical Sciences, Associate Professor, Physical and Inorganic Chemistry Department, Altai State University, Barnaul, Lenina avenue, 61; e-mail: maslova_o.a@mail.ru; https://orcid.org/0000-0003-3862-3687;

Beznosyuk, Sergey Alexandrovich (corresponding author) — Doctor of Physical and Mathematical Sciences, Professor, Head of the Physical and Inorganic Chemistry Department, Altai State University, Barnaul, Lenina avenue, 61; e-mail: bsa1953@mail.ru; https://orcid.org/0000-0002-4945-7197;

Masalimov, Abay Sabirzhanovich — Full Professor, Doctor of Chemical Sciences, Physical and Analytical Chemistry Department, Karagandy University of the name of academician E.A. Buketov, Universitetskaya street, 28, 100024, Karaganda, Kazakhstan; e-mail: masalimov-as@mail.ru; https://orcid.org/0000-0002-6405-7108

---

*The author's name is presented in the order: *Last Name, First and Middle Names*

INORGANIC CHEMISTRY

I.V. Korolkov[1,2*], A.V. Zibert[2], L.I. Lisovskaya[1,2], K. Ludzik[3,4], M.V. Anisovich[5],
M.M. Vasilyeva[5], A.E. Shumskaya[6], A. Usseinov[2], A.B. Yeszhanov[1,2], M.V. Zdorovets[1,2]

[1]Institute of Nuclear Physic of the Republic of Kazakhstan, Almaty, Kazakhstan;
[2]L.N. Gumilyov Eurasian National University, Nur-Sultan, Kazakhstan;
[3]University of Lodz, Poland;
[4]Frank Laboratory of Neutron Physics, Joint Institute for Nuclear Research, Dubna, Russia;
[5]Republican Unitary Enterprise, Scientific-Practical Centre of Hygiene, Minsk, Belarus;
[6]Institute of Chemistry of New Materials, National Academy of Sciences of Belarus, Minsk, Belarus
(*Corresponding author's e-mail: i.korolkov@inp.kz)

Simultaneous Immobilization of Gadolinium Ions and Di(*o*-carborano-1,2-dimethyl)borate on Fe₃O₄ Nanoparticles

Neutron capture therapy is a promising method for cancer treatment based on the targeted delivery of specific isotopes into cancer cells and subsequent irradiation with epithermal neutrons. As a result, a large amount of energy is released at a distance comparable to the size of the cell, destroying it from the inside. Magnetic iron oxide nanoparticles can be used for the targeted delivery of isotopes. In this article, iron oxide nanoparticles (Fe₃O₄) were modified with silanes and polyelectrolyte complexes for simultaneous immobilization of gadolinium ions and carborane compounds through ionic interaction for potential application in targeted delivery into cancer cells for neutron capture therapy. Structure, size and element composition was elucidated by the Fourier-transform infrared spectroscopy (FTIR), Energy-dispersive X-ray spectroscopy (EDA), dynamic light scattering (DLS) and X-ray diffraction (XRD) analysis. It was found that, according to EDA, resulting nanoparticles consist of 15.4 % boron and 1.5 % gadolinium, with average hydrodynamical size of 386 nm measured by DLS. An in vitro cytotoxicity test using HepG2 (a cancer cell line) and human skin fibroblasts (a normal cell line) showed minor cytotoxicity in concentration range from 0.05 to 1 mg/mL.

Keywords: Fe₃O₄ nanoparticles, silane, surface modification, targeted delivery of payload, BNCT, carborane, cytotoxicity.

Introduction

The development of medicine has led to significant progress in cancer treatment during the past two decades. Nevertheless, cancer remains a problem; for example, there were 2.7 million new cases and 1.3 million lethal cases in 2020. Such an approach as radiotherapy has shown its effectiveness, 40 % of cancer types can be treated using it alone or combined with other methods [1]. However, there is a type of tumor considered to be radioresistant [2], and it cannot be treated with traditional radiotherapeutic approaches. Neutron capture therapy (NCT) could be one of the ways to solve this problem [3].

To treat cancer with this method, a drug labeled with specific isotopes (usually ¹⁰B and ¹⁵⁷Gd) is delivered to the tumor. After that, it is irradiated with epithermal neutron flux. As a result, we have a neutron capture reaction localized in tumor. In the case of B, the safety of nearby tissues can be achieved due to the pathlength of the resulting α-particles (4–9 μm) and its high cellular response efficiency [4]. Other studies indicate that the simultaneous use of Gd and B increases the efficiency of NCT by 80 % [5]. Currently, only clinical trials have been conducted with BPA (*p*-borophenylalanine) and BSH (disodium mercaptoundeca-

hydrododecaborate), and they have shown no selectivity. On the other hand, selectivity can be improved by using nanocarriers as a drug delivery system. Nanoparticles possess unique physical properties, such as a high surface-to-volume ratio, the ability to penetrate through vascular architecture and cellular membranes, and, in some cases, low cytotoxicity [6, 7].

In this study, we present a method for the simultaneous immobilization of Gd ions and di(o-carborano-1,2-dimethyl)borate to the core-shell Fe_3O_4 nanoparticles covered with polyacrylic acid/polyallylamine (PAA/PALAM) polyelectrolyte. This approach has the following goals: The presence of Gd can not only increase the efficiency of NCT, but also be used as a diagnostic agent for MRI, so after the injection of nanocarriers it is possible to determine the drug distribution in body area [8, 9]. On the other hand, the magnetic core makes it possible to manipulate nanoparticles using an external magnetic field. In addition, although di(o-carborano-1,2-dimethyl)borate has a large number of boron atoms in its structure, it is insoluble in water. Therefore, simple injection of it into the blood could be problematic. This problem can be avoided if it is immobilized on the nanocarriers surface. In contrast to our previous study [10], di(o-carborano-1,2-dimethyl)borate is bonded to PAA/PALAm through NH_3^+ groups via ionic bond, which may provide better drug release.

Experimental

Reagents and materials

Iron chloride (II) tetrahydrate, iron chloride (III) hexahydrate, acrylic acid (AA), polyallylamine hydrochloride (PALAm), aluminum oxide, 3-(trimethoxysilyl)propyl methacrylate (TMSPM), 2,2′-azobis(2-methylpropionamidine) dihydrochloride (AAPH), gadolinium (III) nitrate hexahydrate were purchased at Sigma-Aldrich (Germany). Ethanol, methanol, benzene, o-xylol, diethyl ether, hydrochloric acid, ammonium hydroxide aqueous solution, NaOH, and ethyl acetate were analytical grade (Russia).

Synthesis of iron oxide nanoparticles and its modification

Fe_3O_4 nanoparticles (NPs) were synthesized by the precipitation method described in our previous work [10]. Fe_3O_4 nanoparticles were modified according to the scheme presented in Figure 1.
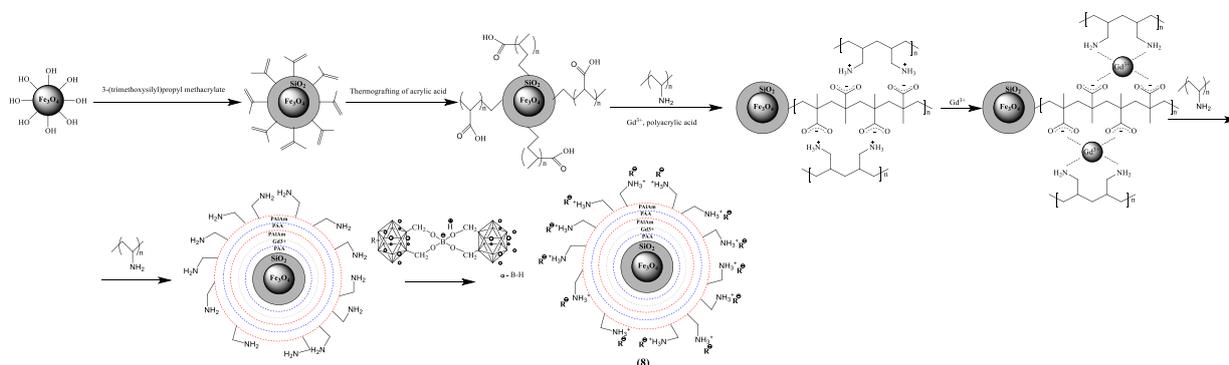
Figure 1. Schematic representation of iron oxide NPs modification,
and gadolinium and carborane immobilization via ionic interaction

To form methacrylate groups on iron oxide nanoparticles, 1 g of Fe_3O_4 NPs was added to a solution of 100 ml o-xylol, then it was ultrasonicated for 2 hrs, and bubbled with argon. After that, 3 ml of 3-(trimethoxysilyl)propyl methacrylate was dropped under vigorous stirring, then the reaction was heated to 80 °C and continued for 5 h. The precipitate was magnetically separated and washed with o-xylol and diethyl ether.

Then, for acrylic acid grafting, 1g of Fe_3O_4 NPs with methacrylate groups was ultrasonicated to 50 % ethanol (90 ml) for fine desperation and degassing, moreover, argon was bubbled during 15–20 min to remove oxygen. 10 ml of purified AA and 0.05 g of thermal initiator 2,2′-azobis(2-methylpropionamidine) dihydrochloride (AAPH) were added to the solution. The reaction was heated to 80 °C and kept at this temperature for 24 h. After that, obtained precipitate was magnetically separated and washed with water several times.

To form a polyelectrolyte complex on modified nanoparticles, 1 g of grafted NPs was ultrasonicated in a 0.012 g/ml of polyallylamine solution for desperation for 2 h and then shaken using tube shaker for 24 h.

Then, Gd ions formed complexes from 0.016 g/ml of gadolinium (III) nitrate solution in ethanol and were shaken for 48 hrs. Samples were washed several times in ethanol and water and magnetically separated from the solution.

Synthesis of di(o-carborano-1,2-dimethyl)borate

0.62 g (0.01 M) of an aqueous solution of boric acid was added to 4.08 g (0.02 M) of a dioxane solution of 1,2-bis(oxymethyl)-o-carborane, and the reaction was stirred for 2 h. The precipitate was filtered. The extract was dried over Na_2SO_4 and evaporated. The yield was 3.58 g (86 %), m.p. > 400 °C.

FTIR (ν, cm^{-1}): 3000 (CH), 2625, 2596, 2568 (BH), 1350 (B–O).

NMR ^{1}H (DMSO-d6, δ, ppm): 0.3–3.7 (m., 20H, B–H); 4.02 (s., 8H, CH_2).

NMR ^{11}B (DMSO-d6, δ, ppm): 4.47 (s., 1B, B–O); 4.66 (s., 6B, B–H); 11,29 (s., 14B, B–H).

Complexation of di(o-carborano-1,2-dimethyl)borate on modified Fe₃O₄

1 g of NPs was dispersed in a 0.5 % solution of di(o-carborano-1,2-dimethyl)borate in $CH_3COOC_2H_5$ for 1 h and then it was additionally shacked for 1 h. The samples were washed several times in ethyl acetate and aceton, magnetically separated from the solution, and dried.

Methods of characterization

InfraLum FT-08 FTIR (Russia) was used to record FTIR spectra in KBr pellets. The scanning range was 4000–400 cm^{-1}, the resolution was 2 cm^{-1}, and the number of scans was 25.

Hitachi TM3030 (Japan) was used for EDA. Samples were magnetron sputtered with gold before the analysis.

D8 ADVANCE ECO diffractometer (Germany) was used for X-ray diffraction analysis. To identify the phases and study the crystal structure, the software BrukerAXSDIFFRAC.EVAv.4.2 and the international database ICDD PDF-2 were used.

ZetaSizer Nano-ZS (United Kingdom) was used for evaluation of average hydrodynamical size and zeta potential at different pH.

To determine the concentration of carboxyl groups, a colorimetric assay was applied [11]. The concentration of carboxyl groups was determined using toluidine blue.

Cytotoxicity Assay

Cytotoxicity was evaluated using HepG2 cancer cell line and human skin fibroblasts as normal cells. Cells were grown in a CO_2 incubator (Herra Cell) at 37 °C, 5 % CO_2, 80 % relative humidity on 96-well plates (50–70 thousand cells/ml was the seed concentration). Samples of NPs dissolved in Fetal Bovine Serum were added to wells with adherent cells (second day of cultivation). After 24-hours of sample exposure, total cell mitochondrial dehydrogenase activity in each well was measured photometrically in the methyltetrazolium test (MTT).

Results and Discussion

The surface of Fe₃O₄ nanoparticles was functionalized according to the scheme presented in Figure 1 to immobilize gadolinium ions and carborane compounds. At the first stage, iron oxide nanoparticles were covered with silane shell using 3-(trimethoxysilyl)propyl methacrylate (TMSPM) by reaction of hydrolysis and condensation. This reaction is based on the removal of CH₃O- from alkoxysilane and attaching it to the OH group of Fe₃O₄ nanoparticles. The reaction temperature of 80 ^{0}C makes it possible to remove effectively the reaction product (methanol), forming an azeotropic mixture with xylene. The FTIR spectra presented in Figure 2 confirm the formation of Si-O-Si and C=C bonds at 1175, 1015 cm^{-1} and 1640 cm^{-1}. Also, Si-OH bond was detected at 935 cm^{-1}, it points to incompleteness of polycondensation reaction [12, 13]. EDA detected silicon in elemental composition.

At the second stage, thermoinitiated graft polymerization of acrylic acid (AA) was performed on silanized iron oxide nanoparticles. The effect of reaction time, temperature, concentration of initiator and monomer on the efficiency of graft polymerization was studied. Considering the solubility of monomer and initiator, and the good dispersion of NPs, 50 % ethanol is the optimal solvent.

The main peaks in the FTIR spectra, which can be seen after graft polymerization on iron oxide NPs, appear at 2950 cm^{-1} (C–H), and at 1725 cm^{-1} (C=O of carboxyl group). The amount of grafted polymeric chains can be evaluated using ratio of intensities or area under the peak at 575 cm^{-1} (Fe–O) and 1725 cm^{-1} (C=O of PAA) [14]. Table 1 demonstrates the results. The amount of grafted polymer chain continuously increased with time and decreased with the increase in the concentration of monomer due to homopolymerization but not grafting. Additionally, colorimetric assay was used to evaluate concentration of carboxylic group on modified nanoparticles. Concentration of COOH groups was 174.61 µM/g (at 0.03125 % AAPH,

10 % AA and 24 hour reaction time). This additionally confirms the grafting of PAA on the surface of nano-particles.

Then, the samples were soaked in PAlAm solution to form polyelectrolyte layer on the surface of NPs. In the FTIR spectra, the peaks were detected at around 1500–1600 cm^{-1}, which may be related to COO$^-$ and NH$_3^+$, 3340 cm^{-1} (O–H/N–H), 1635 cm^{-1} (N–H stretching), 1452 cm^{-1} (C–H stretching) and 1178 cm^{-1} (C–N stretching) [12].

After the formation of polyelectrolyte complexes, the immobilization of Gd ions from their nitrate salt was performed. After the complexation of Gd ions and the formation of chelates, as presented in Figure 1, the FTIR spectra show a shift of the peak of the COO$^-$ group from 1319 to 1399 cm^{-1}. A peak was in addition recorded at 1386 cm^{-1} (NO$_3^-$) with low intensity. 2.9 % gadolinium has also been found in the EDA.

T a b l e 1

Effect of different parameters on efficiency of PAA grafting

	Concentration of AAPH, %			Concentration of AA, %			Time, h		
	0.0125	0.03125	0.05	10	20	30	2	6	24
I$_{1725}$/I$_{575}$	0.15	0.184	0.181	0.184	0.181	0.103	0.162	0.181	0.184
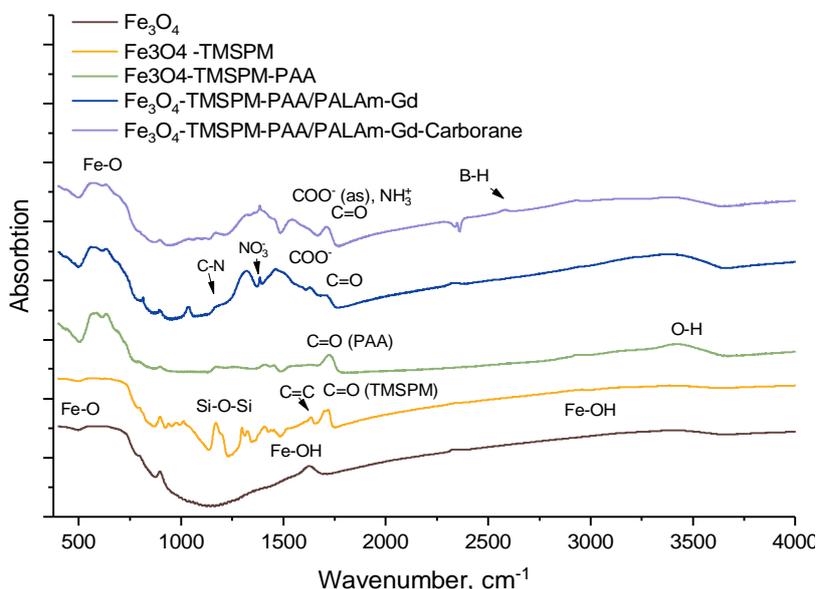
Figure 2. FTIR spectra of Fe$_3$O$_4$ at different stages of modification and carborane immobilization

After that, a second layer of polyelectrolyte was formed for attaching the di(*o*-carborano-1,2-di-methyl)borate through ionic interaction, while in our recent article [10], attaching of carborane diborate was performed by covalent bonding. A new peak at around 2600 cm^{-1} (B–H stretching) of diborate [15] was detected in the FTIR spectra. Moreover, B was found in EDA in the amount of 15.4 at.%. This sample was also characterized by DLS analyses to evaluate hydrodynamic diameters and zeta potential at different pH. Figure 3 represents the results. It was found out that the average hydrodynamic diameter of the Fe$_3$O$_4$-TMSPMS-PAA/PAlAm-Gd-diborate sample is 386 nm. DLS analyzes the solvated state of the sample, in which H$_2$O molecules associate with nanoparticle [16], it should also be noted that the obtained sample is unstable and tends to agglomerate, so it is necessary to find a method for suspension stabilization (for instance, surfactants can be used for this purpose). Figure 3b provides the results of zeta potential measurements at different pH. It is clearly seen that the modified samples are negatively charged at pH range of 3.5–7.5 due to an excess of negatively charged carboxylic groups of the grafted polyacrylic acid.
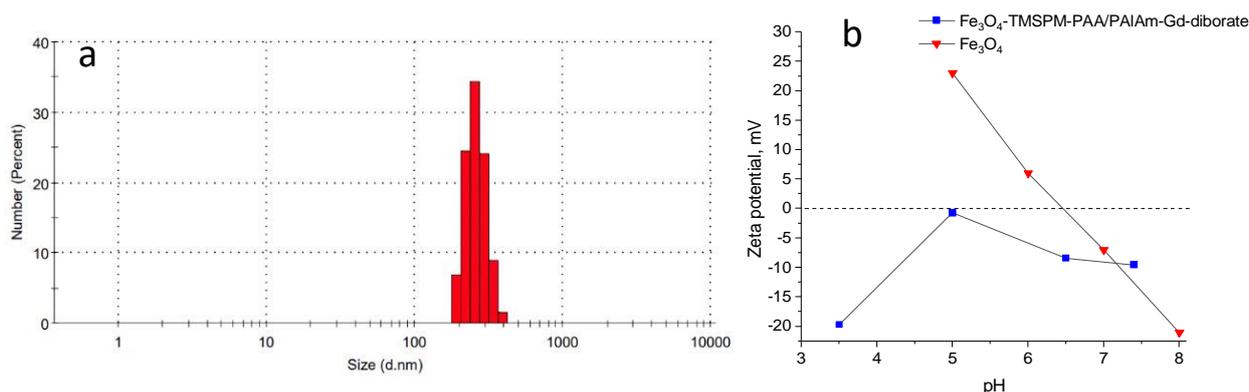
Figure 3. Size distribution (*a*) and zeta-potential as function of pH (*b*)
of Fe$_3$O$_4$-TMSPM-PAA/PALAm-Gd-diborate

Figure 4 illustrates the results of XRD analysis of the initial Fe$_3$O$_4$ and after diborate immobilization. The diffraction patterns are characteristic for polycrystalline-like nanopowders, moreover, there are disordered regions that are typical for oxide nanoparticles synthesized by wet chemistry. Full-profile analysis shows that the presented peaks are attributed to cubic phase of magnetite with broadened reflections, in addition, the presence of altered positions of the interplanar distances indicates the disordering of the structure. Modification is accompanied by partial ordering and an increase in the intensity of diffraction reflections due to changes in the stoichiometry and defect structures. Fe$_3$O$_4$ NPs are characterized by a large number of disordered regions [13, 17].
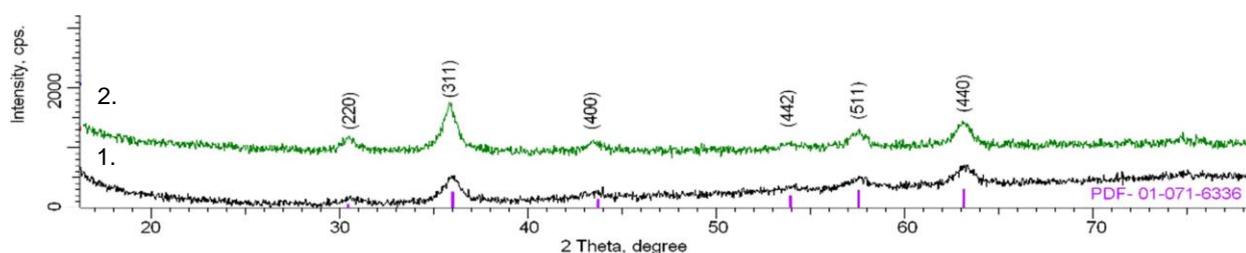
Figure 4. XRD patterns of: 1) initial Fe$_3$O$_4$; 2) Fe$_3$O$_4$-TMSPM-PAA/PAlAm-Gd-diborate

Table 3 shows the results of XRD analysis; the stoichiometry was calculated according to method presented in [18]. It is seen that Fe (II) oxidizes after modification and diborate immobilization. Thus, the initial NPs have the Fe$_{2.88}$O$_4$ stoichiometry, and the final NPs have Fe$_{2.78}$O$_4$ stoichiometry.

T a b l e 3

Data of XRD analysis

Sample	Lattice parameter, Å	Crystalline size, nm	Degree of structural ordering, %	Stoichiometry
Fe$_3$O$_4$	$a = 8.29402$	10.5	53.6	Fe$_{2.88}$O$_4$
Fe$_3$O$_4$-TMSPM-PAA/ PALAm-Gd-diborate	$a = 8.30408$	21.5	59.7	Fe$_{2.78}$O$_4$

The cytotoxicity of Fe$_3$O$_4$-TMSPM-PAA/PALAm-Gd-diborate nanoparticles was elucidated by cell vitality by the example of HepG2 and human fibroblasts cell lines. Figure 5 presents the results.
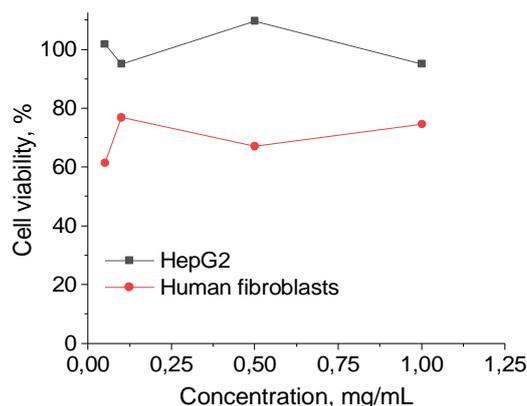
Figure 5. Cell viability after incubation depends of NPs concentrations
for HepG2 and human fibroblast cell lines

The cytotoxicity of Fe_3O_4/TMSPM/PAA/PALAm/Gd-diborate towards HepG2 and human fibroblasts is low even at the heist concentration of 1 mg/mL, so, it is not possible to determinate the IC_{50} for the considered cell lines. Thus, the obtained nanoparticles can be further studied for targeted delivery of di(o-carborano-1,2-dimethyl) borate for BNCT.

Conclusions

This study presents the results of simultaneous immobilization of gadolinium ions and carborane compound on modified iron oxide nanoparticles through ionic interaction. Average hydrodynamic radius of the prepared nanoparticles was 386 nm, the boron content was 15.4 %, and the Gd content was 1.5 % according to EDA. An *in vitro* test using HepG2 (cancer cell) and human fibroblasts (normal cell line) showed minor cytotoxicity in concentration range from 0.05 to 1 mg/mL.

Acknowledgments

References

1 Grilo, A.M., Santos, B., Baptista, I., & Monsanto, F. (2021). Exploring the cancer patients' experiences during external radiotherapy: A systematic review and thematic synthesis of qualitative and quantitative evidence. *European Journal of Oncology Nursing*, *52*, 101965. https://doi.org/10.1016/j.ejon.2021.101965

2 Cohen-Jonathan-Moyal, Vendrely, V., Motte, L., Balosso, J., & Thariat, J. (2020). Radioresistant tumours: From identification to targeting. *Cancer/Radiotherapie*, *24* (6–7), 699–705. https://doi.org/10.1016/j.canrad.2020.05.005

3 Vares, G., Jallet, V., Matsumoto, Y., Rentier, C., Takayama, K., Sasaki, T., Hayashi, Y., Kumada, H., & Sugawara, H. (2020). Functionalized mesoporous silica nanoparticles for innovative boron-neutron capture therapy of resistant cancers. *Nanomedicine: Nanotechnology, Biology, and Medicine*, *27*, 102195. https://doi.org/10.1101/471128

4 Issa, F., Ioppolo, J.A., & Rendina, L.M. (2013). Boron and Gadolinium Neutron Capture Therapy. *Comprehensive Inorganic Chemistry II (Second Edition): From Elements to Applications*, *3*(9), 877–900. https://10.1016/C2009-0-63454-1

5 Yoshida, F., Yamamoto, T., Nakai, K., Zaboronok, A., & Matsumura, A. (2015). Additive effect of BPA and Gd-DTPA for application in accelerator-based neutron source. *Applied Radiation and Isotopes*, *106*, 247–250. https://doi.org/10.1016/j.apradiso.2015.07.030

6 Huang, S., Li, C., Cheng, Z., Fan, Y., Yang, P., Zhang, C., Yang, K., & Lin, J. (2012). Magnetic Fe_3O_4@mesoporous silica composites for drug delivery and bioadsorption. *Journal of Colloid And Interface Science*, *376*(1), 312–321. https://doi.org/10.1016/j.jcis.2012.02.031

7 García-Fernández, A., Sancenón, F., & Martínez-Máñez, R. (2021). Mesoporous silica nanoparticles for pulmonary drug delivery. *Advanced Drug Delivery Reviews*, *177*, 113953. https://doi.org/10.1016/j.addr.2021.113953

8   Farhood, B., Samadian, H., Ghorbani, M., Zakariaee, S.S., & Knaup, C. (2018). Physical, dosimetric and clinical aspects and delivery systems in neutron capture therapy. *Reports of Practical Oncology and Radiotherapy*, *23*(5), 462–473. https://doi.org/10.1016/j.rpor.2018.07.002

9   Lee, W., Jung, K.H., Park, J.A., Kim, J.Y., Lee, Y.J., Chang, Y., & Yoo, J. (2021). In vivo evaluation of PEGylated-liposome encapsulating gadolinium complexes for gadolinium neutron capture therapy. *Biochemical and Biophysical Research Communications*, *568*, 23–29. https://doi.org/10.1016/j.bbrc.2021.06.045

10   Korolkov, I.V., Zibert, A.V., Lissovskaya, L.I., Ludzik, K., Anisovich, M., Kozlovskiy, A.L., Shumskaya, A.E., Vasilyeva, M., Shlimas, D.I., Jażdżewska, M., Marciniak, B., Kontek, R., Chudoba, D., & Zdorovets, M.V. (2021). Boron and gadolinium loaded Fe₃O₄ nanocarriers for potential application in neutron cancer therapy. *International Journal of Molecular Sciences*, *22*(16), 8687. https://doi.org/10.3390/ijms22168687

11   Ho, A., Ho, K., Thiele, T., & Schedler, U. (2012). Scope and Limitations of Surface Functional Group Quanti Fi Cation Methods: Exploratory Study with Poly(Acrylic Acid)-Grafted Micro- and Nanoparticles. *Journal of American Chemical Society, 134* (19), 8268–8276. https://doi.org/10.1021/ja302649g

12   Shahbazi, M., Bahari, A., & Ghasemi, S. (2016). Studying saturation mobility, threshold voltage, and stability of PMMA-SiO₂-TMSPM nano-hybrid as OFET gate dielectric. *Synthetic Metals*, *32*, 100–108. https://doi.org/10.1088/1361-6528/aa87fa

13   Korolkov, I.V., Ludzik, K., Lisovskaya, L.I., Zibert, A.V., Yeszhanov, A.B., & Zdorovets, M.V. (2021). Modification of magnetic Fe₃O₄ nanoparticles for targeted delivery of payloads. *Bulletin of the University of Karaganda – Chemistry*, *101*(1), 99–108. https://doi.org/10.31489/2021Ch1/99-108

14   Purwar, R., Rajput, P., & Srivastava, C.M. (2014). Composite Wound Dressing for Drug Release. *Fibers and Polymers, 15*(7), 1422–1428. https://doi.org/10.1007/s12221-014-1422-2

15   Yue, J., Li, Y., Zhao, Y., Xiang, D., & Dai, Y. (2016). Thermal degradation behavior of carborane-containing phenylethynyl terminated imide systems. *Polymer Degradation and Stability*, *129*, 286–295. https://doi.org/10.1016/j.polymdegradstab.2016.05.006

16   Eaton, P., Quaresma, P., Soares, C., Neves, C., de Almeida, M.P., Pereira, E., & West, P. (2017). A direct comparison of experimental methods to measure dimensions of synthetic nanoparticles. *Ultramicroscopy*, *182*, 179–190. https://doi.org/10.1016/j.ultramic.2017.07.001

17   Kozlovskiy, A.L., Ermekova, A.E., Korolkov, I.V., Chudoba, D., Jazdzewska, M., Ludzik, K., Nazarova, A., Marciniak, B., Kontek, R., Shumskaya, A.E., & Zdorovets, M.V. (2019). Study of phase transformations, structural, corrosion properties and cytotoxicity of magnetite-based nanoparticles. *Vacuum*, *163*, 236–247. https://doi.org/10.1016/j.vacuum.2019.02.029

18   Bondarenko, L.S., Kovel, E.S., Kydralieva, K.A., Dzhardimalieva, G.I., Illés, E., Tombácz, E., Kicheeva, A.G., & Kudryasheva, N.S. (2020). Effects of modified magnetite nanoparticles on bacterial cells and enzyme reactions. *Nanomaterials*, *10*(8), 1499. https://doi.org/10.3390/nano10081499

И.В. Корольков, А.В. Зиберт, Л.И. Лисовская, К. Луджик, М.В. Анисович, М.М. Васильева, А.Е. Шумская, А. Усеинов, А.Б. Есжанов, М.В. Здоровец

Fe₃O₄ нанобөлшектеріне ди(*о*-карборан-1,2-диметил)борат және гадолиний иондарды қатар иммобилизациялау

Нейтрондыбасып алу терапиясы — рак клеткаларына арнайы изотоптарды мақсатты түрде жеткізуге және эпитермиялық нейтрондармен кейіннен сәулелендіруге негізделген қатерлі ісік ауруын емдеудің перспективті әдісі. Нәтижесінде жасушаның өлшемімен салыстырылатын қашықтыққа үлкен мөлшерде энергия бөлініп, оны ішінен жояды. Изотоптарды мақсатты жеткізу үшін магниттік темір оксидінің нанобөлшектерін пайдалануға болады. Мақалада темір оксиді нанобөлшектері (Fe₃O₄) нейтрондыбасып алу терапиясы қатерлі ісік жасушаларының мақсатты жеткізуде әлеуетті пайдалану үшін иондық өзара әрекеттесу арқылы гадолиний иондары мен карборан қосылыстарын бір уақытта иммобилизациялау үшін силандармен және полиэлектролиттік кешендермен модификацияланды. Құрылымы, өлшемі және элементтік құрамы инфрақызыл спектроскопия, энергодисперсиялық рентген спектроскопиясы, жарықтың динамикалық шашырауы және рентгендік фазалық талдаудың көмегімен зерттелді. Алынған нанобөлшектерде 15,4% бор және 1,5% гадолиний бар (EDA мәліметтері бойынша) және олардың орташа гидродинамикалық мөлшері 386 нм құрайды (DLS мәліметтері бойынша). HepG2 (қатерлі ісік жасушаларының желісі) және адам терісінің фибробласттары (қалыпты жасуша сызығы) қолданылған *in vitro* зерттеулер 0,05–1 мг/мл концентрация диапазонында төмен цитоуыттылықты көрсетеді.

Кілт сөздер: Fe₃O₄ нанобөлшектері, силан, беттік модификациялау, пайдалы жүктемені мақсатты жеткізу, БНҰТ, карборан, цитоуыттылық.

И.В. Корольков, А.В. Зиберт, Л.И. Лисовская, К. Луджик,
М.В. Анисович, М.М. Васильева, А.Е. Шумская, А. Усеинов, А.Б. Есжанов, М.В. Здоровец

Одновременная иммобилизация ионов гадолиния и ди($о$-карборано-1,2-диметил)бората на наночастицы Fe_3O_4

Нейтронозахватная терапия — перспективный метод лечения рака, основанный на адресной доставке специфических изотопов в раковые клетки и последующем облучении эпитепловыми нейтронами. В результате выделено большое количество энергии на расстояние, сравнимое с размером клетки, разрушая ее изнутри. Для адресной доставки изотопов могут быть использованы магнитные наночастицы оксида железа. В статье наночастицы оксида железа (Fe_3O_4) были модифицированы силанами и полиэлектролитными комплексами для одновременной иммобилизации ионов гадолиния и карборановых соединений посредством ионного взаимодействия для потенциального применения в целевой доставке в раковые клетки для нейтронно-захватной терапии. Структура, размер и элементный состав были изучены с помощью инфракрасной спектроскопии, энергодисперсионной рентгеновской спектроскопии, динамического рассеяния света и рентгенофазового анализа. Полученные наночастицы содержат 15,4 % бора и 1,5 % гадолиния (по данным EDA), а их средний гидродинамический размер составляет 386 нм (по данным DLS). In vitro исследования с использованием HepG2 (линия раковых клеток) и фибробласты кожи человека (нормальная линия клеток) показывают низкую цитотоксичность в диапазоне концентраций 0,05–1 мг / мл.

Ключевые слова: наночастицы Fe_3O_4, силан, модификация поверхности, адресная доставка полезного груза, БНЗТ, карборан, цитотоксичность.

Information about authors*

Korolkov, Ilya Vladimirovich (corresponding author) — PhD, Senior Researcher of the Institute of Nuclear Physics, Abylay khana 2/1, 010000, Nur-Sultan, Kazakhstan; e-mail: i.korolkov@inp.kz, https://orcid.org/0000-0002-0766-2803

Zibert, Aleksandr Vitalevich — Student of L.N. Gumilyov Eurasian National University, Satbayev str., 2, 010000, Nur-Sultan, Kazakhstan; e-mail: alexandr.zibert@bk.ru, https://orcid.org/0000-0003-0218-4790

Lisovskaya, Lana Igorevna — Engineer of the Institute of Nuclear Physics, Abylay khana 2/1, 010000, Nur-Sultan, Kazakhstan; e-mail: ms.defrance@mail.ru, https://orcid.org/0000-0002-3894-6366

Ludzik, Katarzyna — Researcher of Department of Physical Chemistry, University of Lodz, 90-137, ul. Uniwersytecka 3, 90-137 Łódź, Poland; e-mail: katarzynaludzik82@gmail.com, https://orcid.org/0000-0003-1749-808X.

Anisovich, Marina Vladimirovna — Senior Researcher of Republic Unitary Enterprise, Scientific-Practical Centre of Hygiene, 220012, 8 Akademicheskaya st., Minsk, Belarus, e-mail: m_anisovich@mail.ru, https://orcid.org/0000-0002-9179-7523

Vasilyeva, Marina Maksimovna — researcher of Republican Unitary Enterprise, Scientific-Practical Centre of Hygiene, 220012, 8 Akademicheskaya st., Minsk, Belarus, e-mail: m_vasilyeva@gmail.com, https://orcid.org/0000-0002-8548-1960

Shumskaya, Alena Evgenievna — Senior Researcher of the Institute of Chemistry of New Materials, National Academy of Sciences of Belarus, 220072 Minsk, Belarus, e-mail: lunka7@mail.ru, https://orcid.org/0000-0001-5429-820X

Usseinov, Abay — Senior Lecturer at L.N. Gumilyov Eurasian National University, 010008 Astana, 2 Satpayev str., Kazakhstan, e-mail: usseinov_ab@enu.kz, https://orcid.org/0000-0002-4066-8422

Yeszhanov, Arman Bachitzhanovich — Junior Researcher of the Institute of Nuclear Physics, Abylay khana 2/1, 010000, Nur-Sultan, Kazakhstan; e-mail: arman_e7@mail.ru, https://orcid.org/0000-0002-1328-8678

Zdorovets, Maxim Vladimirovich — Candidate of Physical and Mathematical Sciences, Director of the Astana Branch of the Institute of Nuclear Physics, Abylay khana 2/1, 010000, Nur-Sultan, Kazakhstan; e-mail: mzdorovets@inp.kz, https://orcid.org/0000-0003-2992-1375

_____
*The author's name is presented in the order: *Last Name, First and Middle Names*

N.A. Medvedeva[1*], A.A. Mironova[1], N.E. Skryabina[1], M.D. Plotnikova[1], D. Fruchart[2], M.G. Shcherban'[1]

[1]Perm State University, Perm, Russia;
[2]Institut Néel-CNRS, Grenoble, France
(*Corresponding author's e-mail: nata-kladova@yandex.ru)

The Effect of Aging on the Microstructure of Alloys (TiCr$_{1.8}$)$_{100–x}$V$_x$ after Electrolytic Hydrogen Charging

The microstructure transformation of ternary Ti-Cr-V alloys after introduction of hydrogen has been analyzed for a long time. Assessment of the impact of vanadium concentration and ratio of Ti and V concentrations on composition stability has been carried out. Investigated alloys system corresponds to relation (TiCr$_{1.8}$)$_{100–x}$V$_x$. The atomic ratio Ti/Cr is constant. Vanadium content changes with the step 20 at.%. The hydrogen charging has been carried out in a thermostatic three-electrode electrochemical cell using 1M KOH electrolyte (i_c = 10–30 mA/cm^2) at 293 K for three hours. It was established that the hydrogen introduction leads to surface migration of alloy components. Their distribution oscillates as time passed. This is due to the fact that hydrogen interacts differently with titanium and vanadium. The electrolytic hydrogen introduction initiates deformation of the crystal lattice and self-diffusion of alloy atoms. The statistically nonuniform distribution of electrolytic hydrogen increases the intensity of the process. The relaxation of internal stresses leads to further redistribution of components. The observed changes depend on the vanadium content in the alloys and have a different character inside the grain and near grain boundaries. A significant change has been established for (TiCr$_{1.8}$)$_{60}$V$_{40}$.

Keywords: (TiCr$_{1.8}$)$_{100–x}$V$_x$, alloys, electrochemical hydrogen saturation, stability, elements, concentration, self-diffusion.

Introduction

Body-centered cubic (bcc) alloys have been studied as hydrogen storage materials for a long time. As an example, the system of TiVCr alloys can absorb and store hydrogen better, than most metal compounds. In fact, basic elements of TiVCr alloys have broad mutual solubility in solid state and can form solid solution with bcc crystal structure. However, optimal conditions of TiVCr hydrogenation are determined by different external factors: method of alloy obtaining, heat treatment, etc. Reversible hydrogen absorption fully depends on (Ti+V)/Cr ratio at normal conditions. Optimized alloy compositions demonstrate maximum of hydrogen absorption, which achieves 3.7 wt. % [1, 2]. Furthermore, for high and stable reversible properties (sorption/desorption of hydrogen) it is particularly important to have a stable and the same structure before each hydrogenation cycle.

To propose a formula for the basic bcc alloys, that provide optimal properties for hydrogenation / dehydrogenation, it is necessary to understand well the progressive effect of the influence of the composition on the H-sorption parameters associated with the saturation conditions. The correlation between the relative amount of Ti, V elements in alloy and the stability of Ti$_\alpha$V$_\beta$Cr$_\gamma$-H hydrides formed in the gas-solid reaction was shown in [3]. Increasing of concentration of hydride forming elements (Ti, V) leads to decreasing of hydrides stability and the temperature of hydrogen desorption [3–5]. Moreover, the investigations of hydrogen diffusion characteristics to Ti-V binary system [6, 7] demonstrated dependence of hydrides stability on Ti/V ratio. This could mean that nature of chemical bonding into metal-hydrogen interaction also not the same for each element of the metal in ternary alloy.

In this work, the effect of change in composition of (TiCr$_{1.8}$)$_{100–x}$V$_x$ system was researched. For this purposes vanadium concentration in alloys was changed in the range from 0 to 60 at.%. Usually hydrogen sorption characteristics of alloys was studied by plotting diagrams "pressure–composition–temperature" as a result of hydrogen gaseous saturation of alloys under certain pressure at different temperatures [8–11]. As part of this work, the electrolytic saturation method was used, which allows the process to be carried out at room temperature [7, 12, 13] and there is the correspondence between cathode current density (electrochemical

method) and hydrogen partial pressure on the sample surface (gaseous saturation). In addition, the surface of sample is a barrier to hydrogen penetration into the material regardless of hydrogen saturation method, so it is possible to define surface condition and its influence on sorption characteristics of alloys by electrochemical method [13, 14].

Experimental

The $(TiCr_{1.8})_{100-x}V_x$ alloys were obtained in two steps. At the first step $TiCr_{1.8}$ alloy (Laves phase, C14) was prepared in high-frequency melting furnace in a water-cooled crucible under argon atmosphere (components purity ~99.97 %). The $TiCr_{1.8}$ alloy was re-melted three times for homogeneity of structure. At the second step $Ti_\alpha V_\beta Cr_\gamma$ alloy was obtained by co-melting of the $TiCr_{1.8}$ ingot and vanadium (99.99 % purity). The ratio of $TiCr_{1.8}$ and V corresponds with the content of elements in ternary system $(TiCr_{1.8})_{100-x}V_x$ ($x = 20, 40,$ 60). The samples were made in the CRETA laboratory (Center for National Research, Grenoble, France).

The samples for electrochemical hydrogen saturation were cut from ingots by mechanical method. The surface of samples was treated by grinds "Sic-Paper" class 220÷1000 (grain diameter 100÷50 μm). After the samples were polished with discs "MC-Dac" (Struers) (grain size 9÷10 μm) and diamond paste "DiaDuo" (Diamond Suspension and Lubricant in One) by polishing machine "STRUERS LaboPol-2", electrodes for electrochemical saturation were obtained from prepared samples. After hydrogen saturation the electrodes were stored in a desiccator.

The electrochemical measurements were carried out in three-electrode electrochemical cell with cathodic and anodic compartments separated by a porous glass diaphragm. The temperature of electrolyte was 21±1 °C. The electrolyte was the 1M KOH solution prepared from high-purity reagent and de-ionized water. Hydrogen saturation condition (current of cathodic polarization) was chosen based on polarization studies conducted earlier [15]. Registration of cathodic polarization curves (rate of potential sweep 2 mV/sec) was carried out for determination of linear section (Tafel section). This section of potentials was used for electrochemical hydrogen saturation. Hydrogen saturation of samples was implemented at cathodic current density ($i_c = 10–30$ mA/cm^2) for three hours. As a result of electrochemical investigation the amount of reversible storage of hydrogen for all alloys was calculated [12, 16].

The microstructure study of samples surface before and after hydrogen saturation was carried out by scanning electron microscope "Hitachi" S-3400 with energy dispersing device, which allowed determining amount of alloys elements on the required point.

Results and Discussion

The following samples of $(TiCr_{1.8})_{80}V_{20}$, $(TiCr_{1.8})_{60}V_{40}$, $(TiCr_{1.8})_{40}V_{60}$ alloys were chosen for analysis of stability of microstructure after hydrogen saturation. These alloys were selected due to possibility of practical use because alloys with high vanadium content (80 at.% and higher) are much more expensive systems. For the other hand, Laves phase appears in alloy with low vanadium concentration (lower 20 at.%) [17]. Before hydrogen saturation all samples of alloys were tested by scanning electron microscope for determination of homogeneity of the material. Table 1 demonstrates the results (errors are obtained for each sample by averaging 5 measurements). Figure 1 illustrates an example of the distribution of elements in the samples.
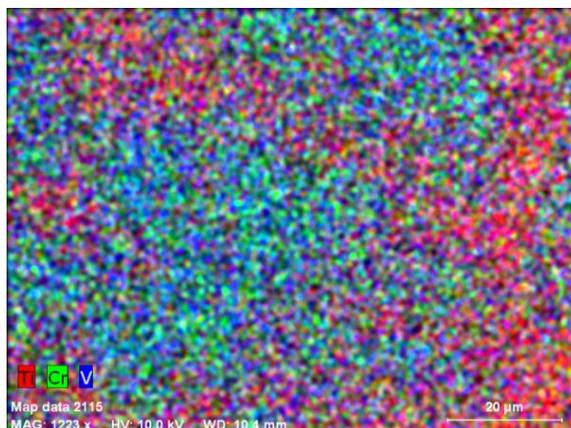
Figure 1. Image of elements distribution in $(TiCr_{1.8})_{80}V_{20}$ (×1200)

**Composition of $(TiCr_{1.8})_{100-x}V_x$ alloys and concentration of Ti, Cr and V in grain
and on grain boundary before hydrogen saturation**

x, at.% V	Elements of alloy	Composition, at.%			
		Grade composition	Initial	Distribution of elements	
				Grain	Grain boundary
20	Ti	28.56	27.10±2.15	27.96±2.23	39.19 ±2.63
	Cr	51.44	52.47±4.13	51.05±3.40	46.01± 5.06
	V	20	20.43±3.78	20.99±6.23	14.80±5.80
40	Ti	21.42	20.60±2.43	20.01±2.06	31.89±2.48
	Cr	38.58	37.45±4.16	36.59±3.40	33.92±2.94
	V	40	41.95±6.00	43.36±6.10	34.17±5.91
60	Ti	14.28	13.77±0.93	11.32±1.13	18.44±1.87
	Cr	25.72	25.05±1.74	25.93±3.02	25.93±3.27
	V	60	61.18±3.93	62.76±4.80	55.62±6.15

From these results, it can be concluded that all samples correspond to the specified composition within the scatter of results. It is important to emphasize that all of the alloys have a single-phase **bcc** structure; however, the heterogeneity in the distribution of the components between the grain (**G**) and near grain boundary (**GB**) exists. Furthermore, increasing of vanadium concentration leads to decreasing of the difference in distribution of elements between grain and grain boundary. This result was previously confirmed by SEM investigations in secondary electrons [15]. The results (Table 1) demonstrate that initial state of the $(TiCr_{1.8})_{40}V_{60}$ alloy (before hydrogenation) has more homogeneity structure than others. Figure 2 represents the results of investigation of the degree of homogeneity of elements distribution of the alloy in the process of aging after hydrogen saturation. After saturation, all samples were washed with de-ionized water and dried. Samples were stored in a desiccator between studies. The point on the vertical scale corresponding to "0" on the time scale indicates the amount of elements in initial state of the alloys.

Experimental data demonstrate insignificant influence of the aging after charging with hydrogen on elements distribution in alloys. However, there is an exception — it is $(TiCr_{1.8})_{60}V_{40}$ alloy (Fig. 2). This alloy has significant fluctuations all of elements near grain boundary and as well titanium inside of grain. The fact of oscillating change of crystal structure occurring in alloy after electrochemical hydrogen saturation was presented in studies [18, 19]. It should be pointed out that this effect can be caused by instability of structural states of microgroups of atoms due to the hydrogen charging method. Moreover, radii of titanium, vanadium and chromium atoms have close sizes (1.45, 1.31 and 1.25 Å, respectively) and ratio of these elements at grain boundary of $(TiCr1.8)_{60}V_{40}$ alloy is approximately equal, therefore is more likely formation of unstable complexes of hydrogen with a metal and/or with couple of metal-defect. In this case, defect can be any irregularity of the regular structure of the crystal lattice, for example, vacancy and dislocation. The existence of these defects is especially likely near the grain boundaries. There is a relaxation of internal stresses in the hydrogen-saturated alloy over time, and the system passes into the equilibrium state.

On the other hand, there are no significant changes in the concentration of chromium in all the investigated alloys. It can be assumed, that relaxation process exists not only because of decreases of "mechanical" stresses during hydrogen charging, but also because of influence of type of chemical bond between hydrogen and metal atoms of alloys. Hydrogen dissolves in vanadium and forms hydrides according to the principle of a solid solution [20]. The chemical bonding between the metal atom and hydrogen is observed for titanium hydride [20]. It is noticeable that metals in $(TiCr_{1.8})_{100-x}V_x$ alloys are distributed statistically uniformly. However, it cannot be excluded that hydrogen distribution is not statistically even especially because of lack of saturate hydrogen saturation. In this case, unstable metal-hydrogen complexes will migrate and create another character of local ordering because of the relaxation processes and self-diffusion of metal atoms. Apparently, this phenomenon is observed in the experiment.

1 — Cr; *2* — V; *3* — Ti
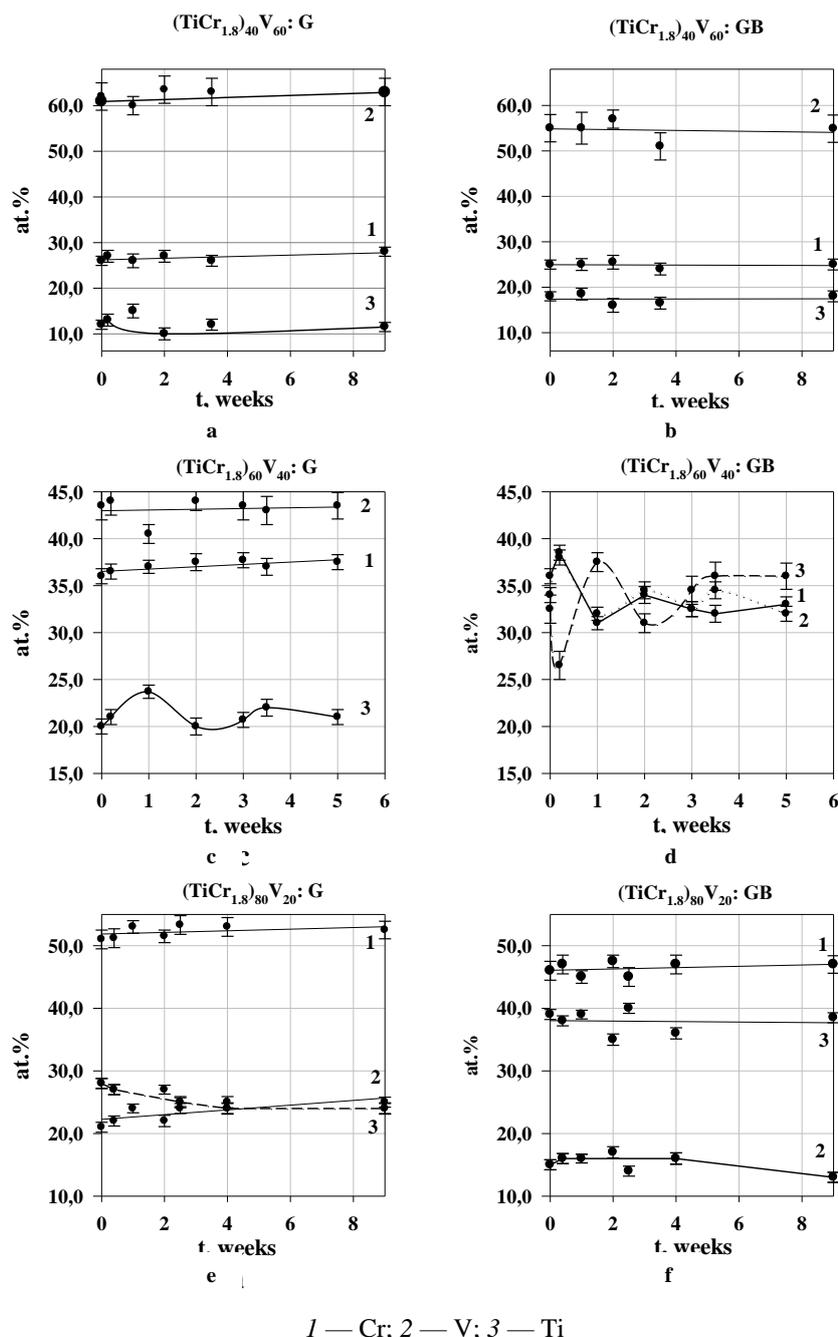
Figure 2. Influence of retention time of alloys samples after hydrogen saturation
on character of element distribution in grain (*a, c, e*) and on grain boundary (*b, d, f*)

Conclusions

In this work, we investigated the effect of electrochemical hydrogen saturation on surface migration of components of $(TiCr_{1,8})_{100-x}V_x$ alloys. Assessment of the impact of vanadium concentration and ratio Ti/V concentrations on composition stability was carried out. It was established that element distribution after hydrogen injection oscillates as time passed. Also, the electrolytic hydrogen introduction initiates deformation of the crystal lattice and self-diffusion of alloy atoms. The statistically nonuniform distribution of electrolytic hydrogen increases the intensity of the process. The relaxation of internal stresses leads to a further redistribution of alloy components. The observed changes depend on the V concentration in the alloys and have a different character inside the grain and near grain boundaries. A significant change was established for $(TiCr_{1,8})_{60}V_{40}$.

References

1   Itoh H. The influence of microstructure on hydrogen absorption properties of Ti-Cr-V alloys/ H. Itoh, H. Arashima, K. Kubo, T. Kabutomori // J. Alloys Comp. — 2002. — Vol. 330–332. — P. 287–291.

2   Arashima H. Correlation between hydrogen absorption properties and homogeneity of Ti–Cr–V alloys/ H. Arashima, F. Takahashi, T. Ebisawa, H. Itoh, T. Kabutomori // J. Alloys & Compds. — 2003. — Vol. 356–357. — P. 405–408.

3   Skryabina N.E. Phase transformations in Ti-V-Cr-H composition / N.E. Skryabina, D. Fruchart, S. Miraglia, P. de Rango, M.G. Shelyapina // Solid State Phenomena. –2011. — Vol. 170. — P. 302–306. — DOI: 10.4028/www.scientific.net/SSP.170.302.

4   Kurenkova E. ^{1}H NMR study of hydrogen site occupancy in hydrides of disordered / E. Kurenkova, A. Vyvodtseva, M.G. Shelyapina, V.I. Chizhik, A.V. Ievlev, N.E. Skryabina, A.G. Aleksanyan, D. Fruchart // Solid State Phenomena. — 2013. — Vol. 194. — P. 254–257. — DOI: 10.4028/www.scientific.net/SSP.194.254

5   Medvedeva N.A. Electrochemical behavior of Ti–V–Cr alloys in alkaline solution / N.A. Medvedeva, N.E. Skryabina // Chem. Met. Alloys. — 2013. — Vol. 6. — P. 158–162. — http://www.chemetal-journal.org/ejournal13/CMA0253.pdf

6   Skryabina N.E. Phases transformation in Ti-V-H hydrides / N.E. Skryabina, D. Fruchart, M.G. Shelyapina, S. Dolukhanyan, A. Aleksanyan // J. Alloys Compds. — 2013. — Vol. 580. — P. 94–97. — DOI: 10.1016/j.jallcom.2013.03.114.

7   Головин П.В. Сорбционная способность сплава состава Ti$_x$V$_{1-x}$ по отношению к водороду / П.В. Головин, Н.А. Медведева, Н.Е. Скрябина // Конденсированные среды и межфазные границы. — 2013. — Т. 15, № 2. — С. 99–105. — URL: http://www.kcmf.vsu.ru/resources/t_15_2_2013_002.pdf

8   Akib E. Hydrogen absorption by Laves phase related BCC solid solution / E. Akib, H. Iba // Intermetallics. — 1998. — Vol. 6. — P. 461-470.

9   Cho S. The hydrogen storage characteristics of Ti–Cr–V alloys / S. Cho, C. Han, C. Park, E. Akiba // J. Alloys Compd. — 1999. — Vol. 288 — P. 294–298. — DOI 10.1016/S0925-8388(99)00096-1.

10   Kuriwa T. New V-based alloys with high protium absorption and desorption capacity / T. Kuriwa, T. Tamura, T. Amemiya, T. Fusa, A. Kamegawa, T. Takemura, M. Okada // J. Alloys Compd. — 1999. — Vol. 293–295. — P. 433–436. — DOI: 10.1016/S0925-8388(99)00325-4.

11   Seo C. Hydrogen storage properties of vanadium-based b.c.c. solid solution metal hydrides. / C. Seo, J. Kim, P.S. Lee, J. Lee // J. Alloys Compd. — 2003. — Vol. 348. — P. 252–257. — DOI: 10.1016/S0925-8388(02)00831-9.

12   Крапивный Н.Г. Определение кинетических параметров стадии проникновения водорода в металлы нестационарным электрохимическим методом / Н.Г. Крапивный // Электрохимия. — 1981. — Т. 17, № 5. — С. 672–677.

13   Вигдорович В.И. Некоторые вопросы реакции выделения водорода и его диффузии через стальную мембрану/ В.И. Вигдорович, Л.Е. Цыганкова, И.В. Зарапина, Н.В. Шель, М.В. Матвеева // Изв. высш. учеб. завед. Химия и химическая технология. — 2006. — Т. 49, № 11. — С. 86–92. — https://cyberleninka.ru/article/n/nekotorye-voprosy-reaktsii-vydeleniya-vodoroda-i-ego-diffuzii-cherez-stalnuyu-membranu

14   Введенский А.В. Кинетика катодного выделения водорода на переходных металлах. I. Теоретический анализ / А.В. Введенский, И.А. Гуторов, Н.Б. Морозова // Конденсированные среды и межфазные границы. — 2010. — Т. 12, № 3. — С. 288–300.

15   Skryabina N.E. Correlation between the Hydrogen Absorption Properties and the Vanadium Concentration of Ti-V-Cr Based Alloys. / Skryabina N.E., Fruchart D., Medvedeva N.A., de Rango P., Mironova A.A // Solid State Phenomena. — 2017. — Vol. 257. — P. 165–172. — DOI: 10.4028/www.scientific.net/SSP.257.165

16   Крапивный Н.Г. Применение электрохимической экстракции для изучения наводороживания металлов / Н.Г. Крапивный // Электрохимия. — 1982. — Т.18, № 9. — С. 1174–1178.

17   Patent No. 6153032 A US. Hydrogen-absorbing alloy and process for preparing the same / Toyota Jidosha Kabushiki Kaisha. Publ.28.11.2000.

18   Авдюхина В.М. Дискретный характер немонотонных структурных превращений в системе Pd–Ta–H при релаксации / В.М. Авдюхина, А.А. Анищенко, А.А. Кацнельсон, А.И. Олемской, Г.П. Ревкевич // Вестн. Моск. гос. ун-та. Сер. 3. Физика. Астрономия. — 2003. — № 6. — С. 62–67. — PA.dvi (msu.ru)

19   Авдюхина В.М. Особенности индуцированной водородом дискретной (прыжковой) эволюции структуры в сплавах Pd–Ta–H и Pd–Mo–H / В.М. Авдюхина, А.А. Анищенко, А.А. Кацнельсон, Г.П. Ревкевич // ФТТ. — 2005. — Т. 47, № 3. — С. 387–394. — iss03-05.dvi (ioffe.ru)

20   Hydrogen in Metals. Application-Oriented Properties / Edited by G. Alefeld, J. Völkl. — Berlin: Springer-Verlag. NY.: Heidelberg, 1978. — 388p.

Н.А. Медведева, А.А. Миронова, Н.Е. Скрябина,
М.Д. Плотникова, Д. Фрушарт, М.Г. Щербань

Сутегімен электролиттік қаныққаннан кейінгі $(TiCr_{1,8})_{100-x}V_x$ қорытпалар микроқұрылымының эволюциясы

Ti-Cr-V үштік қорытпаларының сутегімен қанығуынан кейінгі микроқұрылымының өзгеруі бірнеше сағат бойы талданды. Қорытпадағы ванадий құрамының және Ti мен V-дің өзара қатынасының қорытпаның тұрақтылығына әсері бағаланды (қорытпа құрамдары %-бен берілген). Барлық зерттелген үлгілер үшін Ti және Cr мөлшерінің өзара қатынасы тұрақты болды. Мақалада $(TiCr_{1.8})_{100-x}V_x$ құрамды қорытпалар зерттелді. Ванадий мөлшері 20 % қадаммен өзгерді. Қорытпа үлгілерін сутегімен қанықтыру 1 М KOH термостатталған үш электродты электрохимиялық ұяшықта катодтық токтың тығыздығы ic = 10–30 мА/см^2 кезінде үш сағат бойы 293 K температурада жүргізілді. Сутекті енгізу нәтижесінде қорытпа компоненттерінің беттік миграциясы жүретіні анықталды. Олардың беткі қабатта таралуы уақыт бойынша тербеледі. Бұл сутегі қорытпаның құрамына кіретін титан және ванадиймен әртүрлі әрекеттесетініне байланысты. Қорытпаның сутегімен электролиттік қанығуы кристалдық тордың деформациясына және қорытпа атомдарының өздігінен диффузиясына әкеледі. Сутектің статистикалық біркелкі емес таралуы оны енгізудің бұл әдісімен процестің қарқындылығын арттырады. Ішкі кернеулердің босаңсуы компоненттердің қорытпаның бетінде одан әрі қайта бөлінуіне әкеледі. Байқалатын өзгерістер қорытпалардағы ванадийдің мөлшеріне байланысты және ішкі жағында сондай-ақ, шекара маңайында әртүрлі сипатта болады. $(TiCr_{1,8})_{60}V_{40}$. құрамының едәуір өзгергені анықталған.

Кілт сөздер: $(TiCr_{1.8})_{100-x}V_x$, қорытпалар, электрохимиялық гидрлеу, тұрақтылық, элементтер концентрациясы, өздігінен диффузия.

Н.А. Медведева, А.А. Миронова, Н.Е. Скрябина,
М.Д. Плотникова, Д. Фрушар, М.Г. Щербань

Эволюция микроструктуры сплавов $(TiCr_{1,8})_{100-x}V_x$ после электролитического насыщения водородом

Трансформация микроструктуры тройных сплавов Ti–Cr–V после их насыщения водородом анализировалась в течение нескольких часов. Была проведена оценка влияния содержания ванадия в сплаве и соотношения компонентов Ti и V на стабильность сплава (составы сплавов приведены в ат.%). Соотношение количеств Ti и Cr было постоянным для всех исследованных образцов. В статье исследованы сплавы состава $(TiCr_{1.8})_{100-x}V_x$. Содержание ванадия изменялось с шагом в 20 ат.%. Насыщение образцов сплавов водородом проводилось в термостатированной трехэлектродной электрохимической ячейке из 1 М KOH при плотности катодного тока $i_c = 10–30$ мА/см^2 в течение трех часов при 293К. Установлено, что введение водорода приводит к поверхностной миграции компонентов сплава. Их распределение по поверхности осциллирует во времени. Это связано с тем, что водород по-разному взаимодействует с титаном и ванадием, входящими в состав сплава. Электролитическое насыщение сплава водородом приводит к деформации кристаллической решетки и самодиффузии атомов сплава. Статистически неравномерное распределение водорода при таком способе его введения усиливает интенсивность протекания процесса. Релаксация внутренних напряжений приводит к дальнейшему перераспределению компонентов по поверхности сплава. Наблюдаемые изменения зависят от содержания ванадия в сплавах, имеют различный характер внутри зерна и вблизи межзёренных границ. Установлено значительное изменение состава $(TiCr_{1.8})_{60}V_{40}$.

Ключевые слова: $(TiCr_{1.8})_{100-x}V_x$, сплавы, электрохимическое наводороживание, стабильность, концентрация элементов, самодиффузия.

References

1   Itoh, H., Arashima, H., Kubo, K., & Kabutomori, T. (2002). The influence of microstructure on hydrogen absorption properties of Ti-Cr-V alloys. *J. Alloys Compd,* 330–332, 287–291. DOI: 10.1016/S0925-8388(01)01530-4

2   Arashima, H., Takahashi, F., Ebisawa, T., Itoh, H., & Kabutomori, T. (2003). Correlation between hydrogen absorption properties and homogeneity of Ti–Cr–V alloys. *J. Alloys Compd,* 356–357, 405–408. DOI: 10.1016/S0925-8388(03)00363-3

3   Skryabina, N.E., Fruchart, D., Miraglia, S., de Rango, P. & Shelyapina, M.G. (2011). Phase transformations in Ti-V-Cr-H composition. *Solid State Phenomena*, 70, 302–306. DOI: 10.4028/www.scientific.net/SSP.170.302.

4 Kurenkova, E., Vyvodtseva, A., Shelyapina, M.G., Chizhik, V.I., Ievlev, A.V., Skryabina, N.E., Aleksanyan, A.G., & Fruchart, D. (2013). H-NMR study of hydrogen site occupancy in hydrides of disordered. *Solid State Phenomena*, 194, 254–257. DOI: 10.4028/www.scientific.net/SSP.194.254

5 Medvedeva, N.A., & Skryabina, N.E. (2013). Electrochemical behavior of Ti–V–Cr alloys in alkaline solution. Chem. Met. Alloys, 6, 158–162. Retrieved from http://www.chemetal-journal.org/ejournal13/CMA0253.pdf

6 Skryabina, N.E., Fruchart, D., Shelyapina, M.G., Dolukhanyan, S., & Aleksanyan, A. (2013). Phases transformation in Ti-V-H hydrides. *J. Alloys Compds*, 580, 94–97. DOI: 10.1016/j.jallcom.2013.03.114.

7 Golovin, P.V., Medvedeva, N.A. & Skryabina, N.E. (2013). Sorbtsionnaia sposobnost splava sostava Ti$_x$V$_{1-x}$ po otnosheniiu k vodorodu [Sorption capacity of Ti$_x$V$_{1-x}$ alloys in relation to hydrogen]. Kondensirovannnye sredy i mezhfaznye granitsy – *Condensed Matter and Interphases*, 15, 2, 99–105. Retrieved from http://www.kcmf.vsu.ru/resources/t_15_2_2013_002.pdf [in Russian].

8 Akib, E. & Iba, H. (1998). Hydrogen absorption by Laves phase related BCC solid solution. Intermetallics, 6, 461–470.

9 Cho, S., Han, C., Park, C., & Akiba, E. (1999). The hydrogen storage characteristics of Ti–Cr–V alloys. *J. Alloys Compd*, 288, 294–298. DOI 10.1016/S0925-8388(99)00096-1.

10 Kuriwa, T., Tamura, T., Amemiya, T., Fusa, T., Kamegawa, A., Takemura, T., & Okada, M. (1999). New V-based alloys with high protium absorption and desorption capacity. *J. Alloys Compd.*, 293–295, 433–436. DOI: 10.1016/S0925-8388(99)00325-4

11 Seo, C., Kim, J., Lee, P.S. & Lee. J. (2003). Hydrogen storage properties of vanadium-based b.c.c. solid solution metal hydrides. *J. Alloys Compd.*, 348, 252–257. DOI: 10.1016/S0925-8388(02)00831-9.

12 Krapivny, N.G. (1981). Opredelenie kineticheskih parametrov stadii proniknoveniia vodoroda v metally nestatsionarnym elektrokhimicheskim metodom [Determination of kinetic parameters of the stage of penetration of hydrogen in metals nonstationary electrochemical method]. *Elektrokhimiia – Electrochemistry*, 17, 5, 672–677 [in Russian].

13 Vigdorovich, V.I., Cygankova, L.E., Zarapina, I.V., SHel, N.V., & Matveeva, M.V. (2006). Nekotorye voprosy reaktsii vydeleniia vodoroda i ego diffuzii cherez stalnuiu membranu [Some questions of hydrogen evolution reaction and its diffusion through a steel membrane]. *Izvestiia vysshikh uchebnykh zavedenii. Khimiia i khimicheskaia tekhnologiia – Russian Journal of Chemistry and Chemical Technology*, 49, 11, 86–92. Retrieved from https://cyberleninka.ru/article/n/nekotorye-voprosy-reaktsii-vydeleniya-vodoroda-i-ego-diffuzii-cherez-stalnuyu-membranu [in Russian].

14 Vvedenskii, A.V., Gutorov, I.A., & Morozova, N.B. (2010). Kinetika katodnogo vydeleniia vodoroda na perekhodnykh metallakh. I. Teoreticheskii analiz [The Kinetics of Cathodic Hydrogen Evolution on Transition Metals. I. Theoretical Analysis]. *Kondensirovannye sredy i mezhfaznye granitsy – Condensed Matter and Interphases,* 12, 3, 288–300 [in Russian].

15 Skryabina, N.E., Fruchart, D., Medvedeva, N.A., de Rango, P., & Mironova, A.A. (2017). Correlation between the Hydrogen Absorption Properties and the Vanadium Concentration of Ti-V-Cr Based Alloys. *Solid State Phenomena*, 257, 165–172. DOI: 10.4028/www.scientific.net/SSP.257.165.

16 Krapivny, N.G. (1982). Primenenie elektrokhimicheskoi ekstraktsii dlia izucheniia navodorozhivaniia metallov [The use of electrochemical extraction to study hydrogenation metals]. *Elektrokhimiia – Electrochemistry*, 18, 9, 1174–1178 [in Russian].

17 Patent No. 6153032 A US. Hydrogen-absorbing alloy and process for preparing the same / Toyota Jidosha Kabushiki Kaisha. Publ. 28.11.2000.

18 Avdyukhina, V.M., Anishchenko, A.A., Katsnel'son, A.A., Olemskoi, A.I., & Revkevich, G.P. (2003). Diskretnyi kharakter nemonotonnykh strukturnykh prevrashchenii v sisteme Pd–Ta–H pri relaksatsii [Discrete character of nonmonotonic structural transformations in the Pd-Ta-H system during relaxation]. *Vestnik Moskovskogo gosudarstvennogo universiteta — Bulletin of Moscow State University. Series 3. Physics. Astronomy*, 6, 62–67. Retrieved from PA.dvi (msu.ru) [in Russian].

19 Avdyukhina, V.M., Anishchenko, A.A., Katsnel'son, A.A., & Revkevich, G.P. (2003). Osobennosti indutsirovannoi vodorodom diskretnoi (pryzhkovoi) evoliutsii struktury v splavakh Pd–Ta–H i Pd–Mo–H [Specific Features of the hydrogen-induced discrete (jumplike) structural evolution in Pd-Ta-H and Pd-Mo-H alloys]. *Fizika tverdogo tela – Physics of the Solid State*, 47(3), 387–394. Retrieved from iss03-05.dvi (ioffe.ru) [in Russian].

20 Alefeld, G., & Völkl, J. (Eds.). (1978). Hydrogen in Metals. Application-Oriented Properties. Berlin: Springer-Verlag & New York, NY: Heidelberg.

Information about authors*

Medvedeva, Natalia Aleksandrovna (corresponding author) — Candidate of Chemical Sciences, Associate Professor, Physical Chemistry Department, Perm State National Research University, 15 Bukireva st., 614990, Perm, Russia; e-mail: nata-kladova@yandex.ru; https://orcid.org/0000-0002-0042-5418;

Mironova, Anastasiya Andreevna — Postgraduate student, Physical Chemistry Department, Perm State National Research University, 15 Bukireva st., 614990, Perm, Russia; e-mail: milissochka@mail.ru; https://orcid.org/0000-0002-9152-092X;

Skryabina, Nataliya Evgen'evna — Doctor of Physical and Mathematical Sciences, Professor, Faculty of Physics, Perm State National Research University, 15 Bukireva st., 614990, Perm, Russia; e-mail: natskryabina@mail.ru; https://orcid.org/0000-0002-4009-406X;

Plotnikova, Mariya Dmitrievna — Candidate of Chemical Sciences, Assistant Professor, Physical Chemistry Department, Perm State National Research University, 15 Bukireva st., 614990, Perm, Russia; e-mail: plotnikova-md@mail.ru; https://orcid.org/0000-0002-4050-5682;

Fruchart, Daniel — Research Director at Department of QUEST, Institut Néel CNRS et UGA, BP 166, 38042 Grenoble Cedex 9, France; e-mail: daniel.fruchart@neel.cnrs.fr; https://orcid.org/0000-0002-2387-7089;

Shcherban', Marina Grigor'evna — Candidate of Chemical Sciences, Assistant Professor, Physical Chemistry Department, Perm State National Research University, 15 Bukireva st., 614990, Perm, Russia; e-mail: ma-sher74@mail.ru; https://orcid.org/0000-0002-6905-6622.

_____

*The author's name is presented in the order: *Last Name, First and Middle Names*

Ya.A. Vissurkhanova[*], N.M. Ivanova, E.A. Soboleva, A.K. Mukhamedzhanova

Institute of Organic Synthesis and Coal Chemistry, Karaganda, Kazakhstan
*(*Correspondence author's e-mail: yakhavisurkhanova@bk.ru)*

Mono- and Bimetallic Silver-Containing Nitrogen-Doped Carbon Composites and Their Electrocatalytic Activity

The N-doped metal-carbon composites based on the carbonized melamine-formaldehyde polymer (MFP) with silver, silver-copper, and silver-cobalt particles were synthesized. Mono- and bimetallic silver-containing composites were prepared by the reduction of metal nitrates with hydrazine hydrate in an aqueous ethanol medium in the presence of carbon black particles obtained by the heat treatment of MF-polymer at 500 °C. The structural-phase changes before and after the use of metal-carbon composites as electrocatalysts in the electrohydrogenation of *p*-nitroaniline (*p*-NA) were studied by X-ray diffraction analysis. The morphological features of the created MFBC + Ag, MFBC + (Ag+Cu) and MFBC + (Ag+Co) composites were studied by electron microscopy. It was established that the synthesized composites mainly contain crystalline phases of the corresponding reduced metals or their alloys. The monometallic MFBC(1) + Ag(1) composite contains reduced silver crystallites of various shapes and localization on porous MF carbon black particles. Higher electrocatalytic activity of the synthesized Ag-containing composites in the *p*-NA electrohydrogenation was shown in comparison not only with the electrochemical reduction of *p*-NA but also with MFBC + (Ag+Cu) composites with electrocatalytic hydrogenation of *p*-NA on Ag + Cu particles (without MFBC). It was found that the use of the studied MFBC-composites increases the selectivity of the formation of the main hydrogenation product (*p*-phenylenediamine) and decreases the yields of by-products.

Keywords: N-doped metal-carbon composites, silver, melamine-formaldehyde polymer, carbonization, bimetallic catalysts, Ag-Cu particles, Ag-Co particles, electrocatalytic hydrogenation, *p*-nitroaniline.

Introduction

Currently, much attention is paid to catalytic systems with metal nanoparticles (NPs) deposited on a carbon carrier, metal-carbon composites with the distribution of metal NPs over the entire carbon matrix, as well as metal NPs encapsulated in carbon, which exhibits catalytic activity in various chemical reactions [1–3]. To create metal-carbon composites, modern carbon materials are used, such as carbon nanotubes (CNTs), fullerenes, graphene, etc., which are subjected to oxidative treatment to form oxygen-containing functional groups on their surface. The interaction of such groups with metal NPs promotes their confinement in the carbon support. Also, for the same purpose, carbon-doped with nitrogen atoms (C–N) is produced [4–7]. Such metal-carbon N-doped (M/C–N) composites have improved the electrochemical, adsorption and catalytic properties.

Silver-containing carbon composites are of particular interest since, in addition to the listed properties, they exhibit optical and antibacterial properties [8–10]. The methods for preparing Ag/C composites are generally similar to those described in the literature using carbon nanotubes [11, 12]. Among these are methods of powder metallurgy, methods using melting and solidification, thermal spraying, electrochemical deposition and a whole group of methods, which includes the so-called molecular-level mixing method. Some procedures frequently used for the production of Ag/C composites belong to the method, and primarily it is the chemical reduction of silver cations in the presence of suspended particles of a carbon material [8, 10, 13, 14].

One of the main methods for preparing nitrogen-doped metal-carbon composites is the carbonization of a metal-organic compound or polymer structurally enriched in nitrogen [6, 7]. Acrylamide, cyanamide, melamine, polyacrylonitrile, polyaniline, and other nitrogen-containing materials are often used as such sources of C–N-carbon material, on which then (or *in situ*) metal NPs are deposited [15–17].

This work aims at the synthesis of mono- and bimetallic silver-containing composites based on carbonized melamine-formaldehyde polymer (MFP) and the study of their structure and electrocatalytic activity in the electrohydrogenation of *p*-nitroaniline (*p*-NA) as a model compound. It should be noted that there are some studies in the literature devoted to the creation of various porous N-doped carbon materials based on an

MF polymer as a carbon source with high nitrogen content [18–20]. However, there are no works on the creation of Ag/C-N composites based on them. Examples of such composites include a composite with silver nanoparticles in the N/S doped carbon material (AgNPs@NSC), which was produced by the hydrothermal treatment at 700 °C of a silver polymer complex synthesized by the polycondensation of diphenylthiourea with formaldehyde [21]. The authors of the article found that the highly porous nanocomposite AgNPs@NSC shows excellent catalytic activity in the reduction of *p*-nitrophenol. A silver-containing N-doped carbon nanocomposite was also prepared by thermolysis at 450 °C of the melamine with oxalic acid complex, followed by the reduction of silver nitrate with sodium borohydride [22]. It is noted in many papers that the metal NPs/N-doped carbon composites exhibit high catalytic activity, stability, and reusability due to the interaction between metal nanoparticles including silver and nitrogen-containing groups. Furthermore, the preparation of metal nanoparticles in the presence of carbon supports prevents particle aggregation and increases catalytic activity.

Experimental

Mono- and bimetallic carbon composites based on a carbonized N-containing MF polymer and silver, silver-copper, and silver-cobalt particles were created by chemical reduction of metal cations in an aqueous ethanol medium in the presence of the carbonized MF polymer (MF-black carbon). Figure 1 demonstrates the general scheme for preparing mono- and bimetallic silver-containing N-doped carbon composites.
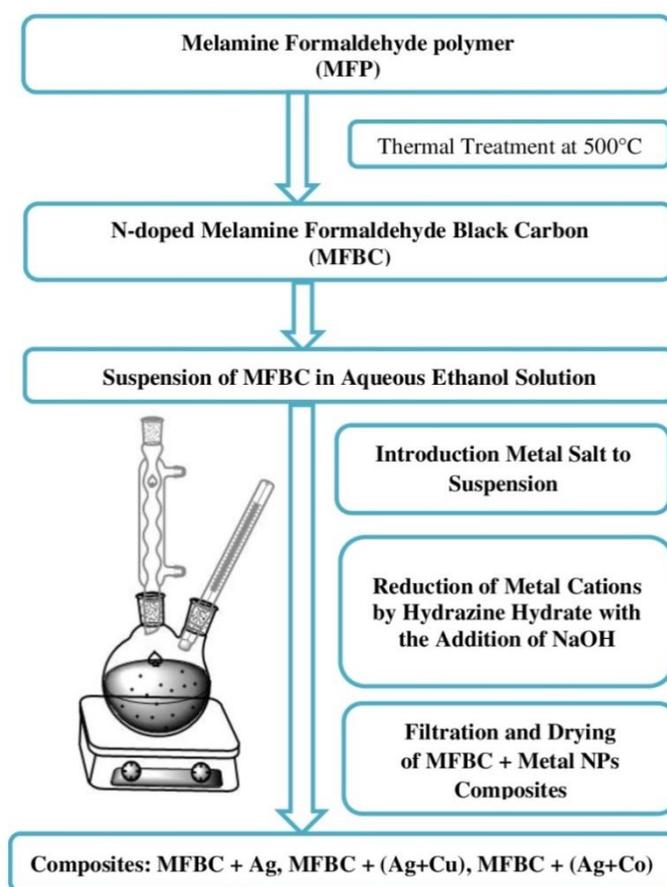
Figure 1. General scheme for preparing mono- and bimetal silver-containing
carbon composites based on carbonized MF polymer

The MF polymer was synthesized by the polycondensation of melamine with formaldehyde in an alkaline solution and the use of oxalic acid as a hardener [23]. The preparation and milling of MF polymer were then thermally treated at 500 °C for 2 h under conditions with limited oxygen access in a high-temperature chamber electric furnace (PL 5/12.5, Nakal, Russia). As a result, an MF soot (or black carbon) powder with a loose structure was produced. Monometallic carbon MFBC + Ag composites were synthesized according to the following procedure.

A weighed amount of MF black carbon in the ratio of 1:1 and 2:1 (MFBC/silver) by weight was put into a round-bottom flask (500 mL). 100 mL of water-ethanol solution was added (the ratio of distilled water and ethanol was 1:1 by volume). The suspension was stirred at room temperature for 1 hour. Then, 3.15 g of silver nitrate $AgNO_3$ was added. Stirring was continued at 40 °C. Separately, the alkaline solution of hydrazine hydrate was prepared by mixing 24 mL of 64 % $N_2H_4·H_2O$ and 20 mL of an aqueous solution of sodium hydroxide (content of NaOH was 1.60 g). This solution was added to the first reaction mixture by drops under constant stirring and temperature of 40 °C. The obtained precipitate was separated and washed with distilled water and ethyl alcohol that was heated to 40 ºC. It was dried at 80 ºC and at a pressure of 0.06 MPa.

The bimetallic MFBC + (Ag+Cu) and MFBC + (Ag+Co) composites were created by a similar procedure with the use of both metal nitrates (with a ratio of Ag/M = 1:1) and the metals reduction at a higher temperature: 60 °C for Ag+Cu and 70 °C for Ag+Co.

MFBC + Ag, MFBC + (Ag+Cu), and MFBC + (Ag+Co) composites were also prepared with the injection of the polyvinyl alcohol (PVA) into the reaction medium as a polymeric stabilizer. To reduce the particle size of the MFBC, the ultrasonic pre-treatment of the black carbon for 30 min was carried out, and then MFBC + Ag + UST composites were also obtained.

The processes of metal cations reduction using hydrazine hydrate are described by the following reaction equations [24, 25]:

$$4AgNO_3 + N_2H_4 + 4NaOH \rightarrow 4Ag^0\downarrow + N_2\uparrow + 4NaNO_3 + 4H_2O$$

$$2Cu(NO_3)_2 + N_2H_4 + 4NaOH \rightarrow 2Cu^0\downarrow + N_2\uparrow + 4NaNO_3 + 4H_2O$$

$$2Co(NO_3)_2 + N_2H_4 + 4NaOH \rightarrow 2Co^0\downarrow + N_2\uparrow + 4NaNO_3 + 4H_2O$$
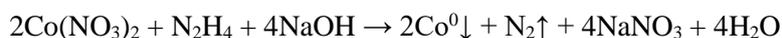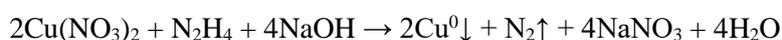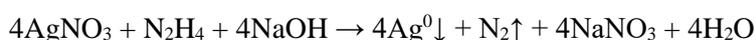
In the filtrates after the synthesis of MFBC + Ag, MFBC + (Ag+Cu), and MFBC + (Ag+Co) composites, the silver content was determined by the Mohr method, and copper and cobalt contents by the method of complexometric titration [26, 27]. According to the titration results, the lack of metal cations in the produced transparent filtrates was established, which indicates their complete reduction.

The structure and phase constitution of the synthesized metal-carbon composites were determined by X-ray diffraction analysis using a D8 ADVANCE ECO diffractometer (Bruker, Germany) with Cu-Kα radiation in the 15–80 2theta range. The morphological features of metal-carbon composites were studied by electron microscopy on the MIRA 3LMU scanning electron microscope (TESCAN, Czech Republic) using secondary (SE) and backscattered (BSE) electron detectors. The samples were analyzed with the deposition of a conductive layer of carbon. Elemental analysis of the composites was performed using an energy dispersive detector X-Act (Oxford Instruments) (EDS analysis).

The electrocatalytic activity of the prepared silver-containing N-doped carbon composites was studied in the electrohydrogenation of *p*-nitroaniline. According to the procedure from our report [28], the experiments were carried out in an alcohol-aqueous-alkaline catholyte of the diaphragm cell at a current of 1.5 A and a temperature of 30 °C. The cathode was a copper plate tightly adjacent to the bottom of the electrolyzer, on which the powder of composite was deposited as a catalyst (by a weight of 1 g), the anode was a platinum gauze. The initial concentration of *p*-NA was 0.066 mol/L. The composite powders deposited on the cathode were first saturated with hydrogen. Then, an organic compound was injected into the catholyte, and its electrocatalytic hydrogenation was carried out. The volume of hydrogen absorbed (V_t, mL), the hydrogenation rate (W, mL H_2/min), hydrogen utilization coefficient (η) and conversion of the hydrogenated compound (α) were calculated from the volumes of gases (oxygen and hydrogen) evolved. The hydrogenation products were extracted from the catholyte with chloroform, and the extracts were analyzed on a Kristallyuks-4000M chromatograph (Meta-Chrom, Russia).

Results and Discussion

The phase constitutions of silver-containing carbon composites prepared based on the carbonized N-reached MF polymer are determined after their thermal treatment and application in electrochemical experiments. Figure 2 illustrates the X-ray diffraction (XRD) patterns of the monometallic MFCB(1) + Ag(1) composite. As it follows from the XRD patterns, the composite contains crystalline phases of reduced silver, and amorphous carbon is present. The intensity of its peaks is much lower than the intensity of the silver peaks and therefore they are not visible on the XRD patterns. The sizes of Ag particles for the (111) phase with a peak at a diffraction angle of 2θ = 38.26° are ~20 nm. The particle sizes were calculated using the Scherrer formula via the Bruker diffractometer software. It may be noted that the XRD patterns of this composite, as

also of other monometallic composites, practically coincide after synthesis and electrochemical experiments, indicating their stability in the aqueous-ethanol-alkaline medium of the catholyte.
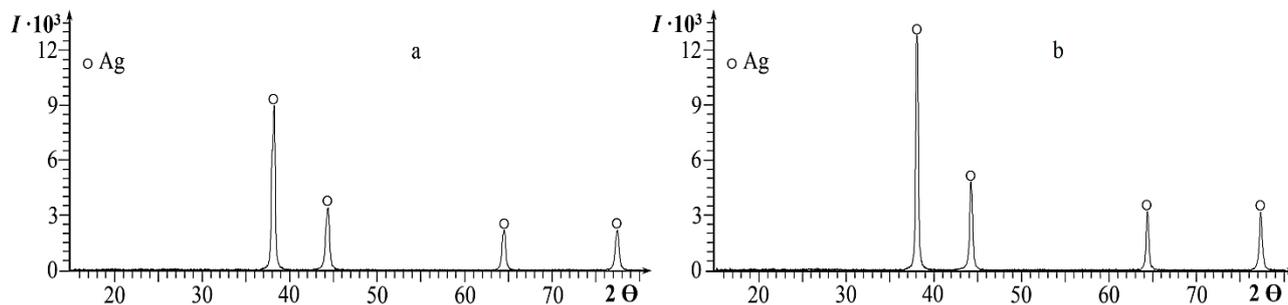
Figure 2. XRD patterns of MFBC(1) + Ag(1) composite before (*a*) and after (*b*) hydrogenation

The microscopic studies (Fig. 3) showed that the enlarged silver crystallites of two types are contained in the MFBC(1) + Ag(1) composite after synthesis: some are located directly on the surface of the carbonized polymer with a distance from each other and have rounded and other crystalline forms, their size changing within 50–220 nm. Their interaction with the carbon support probably occurs through nitrogen atoms in the structure of MF polymer carbonization products. Others are located in the pores of the MFBC and represent an accumulation of interconnected rounded or elongated granules combined into short chains.
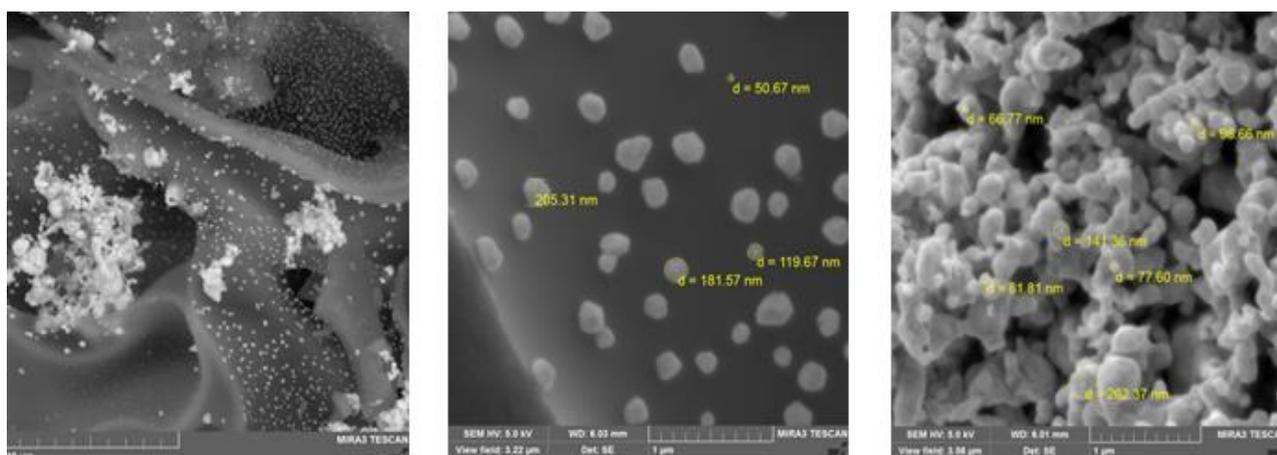
Figure 3. Micrographs of MFBC(1) + Ag(1) composite after synthesis

Figure 4 represents the X-ray patterns of bimetallic MFBC(1) + (Ag+Cu)(1) and MFBC(1) + (Ag+Co)(1) composites. Their phase constitutions are also practically similar after syntheses and after application in electrochemical experiments; therefore, they have been chosen with the best reproduction of reflections for crystalline phases.

According to the XRD pattern in Figure 4, *a*, the MFBC(1) + (Ag+Cu)(1) composite contains crystalline phases of both silver and copper metals reduced with hydrazine hydrate in the presence of MF black carbon. Herewith, the intensity of the peaks corresponding to the crystalline phases of silver is noticeably higher than copper. For the Ag (111) crystalline phase, the particles have sizes of ~39 nm, while Cu (111) particles (at the angle of $2\theta = 43.5°$) they are ~43 nm, according to calculations using the Scherrer formula.

In addition to the crystalline phases of both metals (Ag and Co) reduced, some peaks of which are localized at the same diffraction angles, the MFBC(1) + (Ag+Co)(1) composite (Fig. 4, b) contains the crystalline phases of cobalt hydroxide, β-$Co(OH)_2$. Its presence is explained by the incomplete reduction of cobalt cations during the synthesis of this composite. Probably, this was due to an unsuitable temperature regime for the reduction of Co^{2+} cations. In the case of using hydrazine hydrate as a reducing agent, the authors of the research work [29] recommend temperatures of 90 °C for Co^{2+} and 40 °C for Ag^+ cations. In the experiments, the joint reduction of cations of both metals was carried out at 70 °C, which is indicated in the description of the procedure for synthesizing composites. From the XRD data, it was determined that the Ag

(111) particle sizes in the MFBC(1) + (Ag+Co)(1) composite after electrohydrogenation are ~37 nm, particles of the joint crystalline phase of the Ag–Co alloy (at the angle of $2\theta = 44.5°$) are ~31 nm.
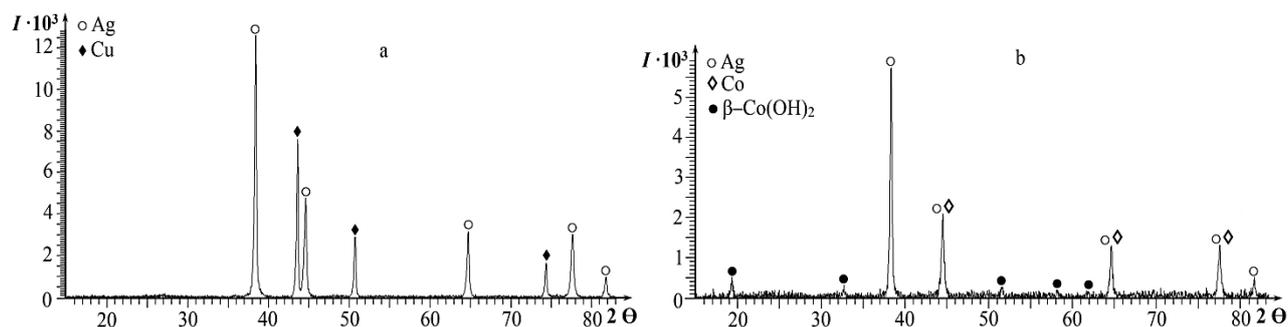
Figure 4. XRD patterns of MFBC(1) + (Ag+Cu)(1) composite (*a*) before
and MFBC(1) + (Ag+Co)(1) composite (*b*) after electrohydrogenation
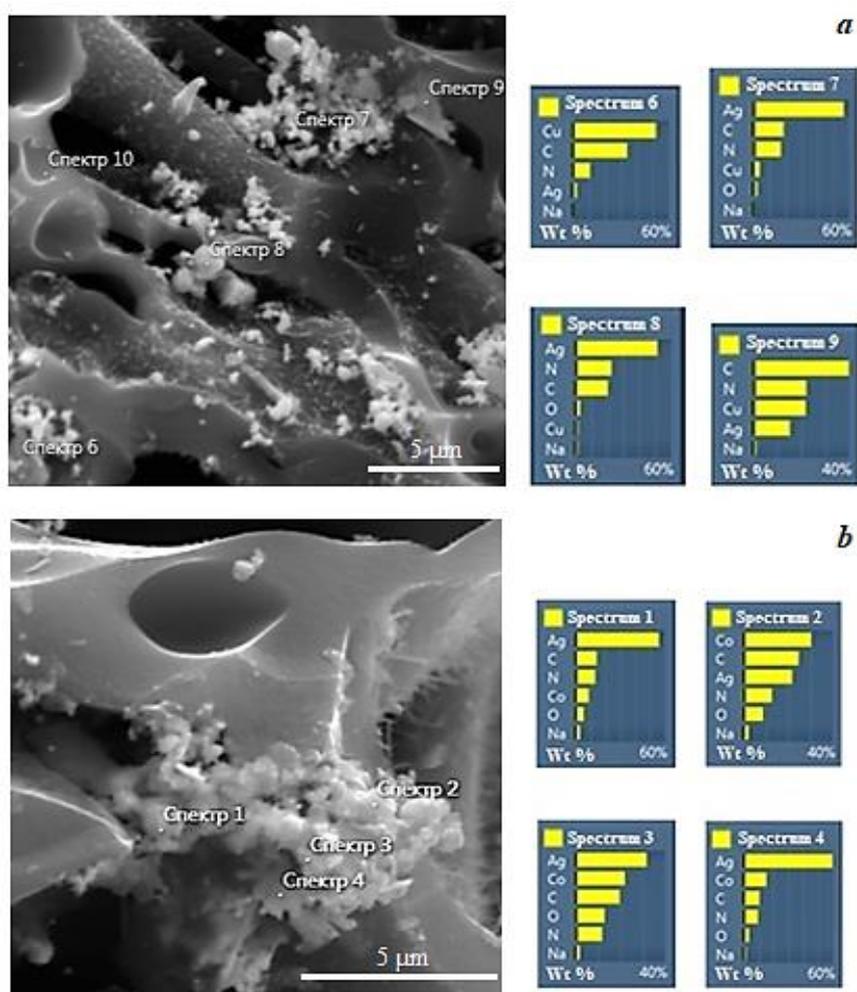
Figure 5. Micrographs of the MFBC(1) + (Ag+Cu)(1) (*a*) and MFBC(1) + (Ag+Co)(1) (*b*) composites
and EDS data for the surface of their particles

Microscopic studies and EDS analyses of the MFBC(1) + (Ag+Cu)(1) composite (Figure 5, *a*) revealed that on the surface of the MF carbon black, the crystallites are formed, consisting almost entirely of silver or copper, as well as crystallites with the joint presence of both metals (Spectrum 9). The joint chemical reduction of both metals is accompanied by the formation of bimetallic alloys particles in the MFBC(1) + (Ag+Co)(1) composite, which follows from the EDS spectral data (Fig. 5, *b*). It is also evident from these

data that the particles of bimetallic Ag-Co alloys are formed with different metal contents. Additionally, these data confirm the relatively high nitrogen content in the MF black carbon composition.

The synthesized MFBC + Ag, MFBC + (Ag+Cu) and MFBC + (Ag+Co) metal-carbon composites based on carbonized MF polymer were studied for the manifestation of electrocatalytic activity in the electrohydrogenation of *p*-nitroaniline:

p-Nitroaniline (*p*-NA) *p*-Phenylenediamine (*p*-PDA)
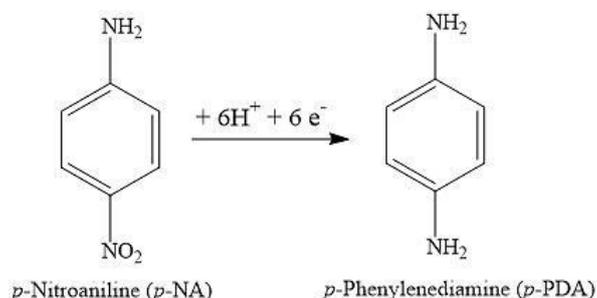
The main product of the electrocatalytic hydrogenation of *p*-nitroaniline is *p*-phenylenediamine, which is used in cosmetics for the production of permanent hair dyes and henna, in the synthesis of pharmaceuticals, in industry for the production of Kevlar and Twaron synthetic fibers, as an analytical reagent for determining ozone in the air, hydrogen sulfide, chlorine, bromine, vanadium sulfides, in microscopy to detect oxidative enzymes of the oxidoreductase class, as well as antiozonants in the production of rubber products.

Table 1 presents the results of the experiments on the electrocatalytic hydrogenation of *p*-NA on silver-containing composites deposited on the MFBC particles.

T a b l e 1

Results of electrocatalytic hydrogenation of *p*-NA on silver-N-carbon composites

Composites	Metals content in 1 g of composite, g		Hydrogen saturation stage		Electrocatalytic hydrogenation of *p*-NA		Composition products, %		
	Ag	Cu (Co)	τ, min	V_{H2}, mL	W, mL H_2/min ($\alpha = 0.25$)	α, %	*p*-PDA	*p*-NA	by-products
Cu cathode	–		0	0.0	6.9	83.1	57.8	0.2	42.0
Ag	1.000	–	0	0.0	10,0	100.0	80.0	0.2	19.8
MFBC(1) + Ag (1)	0.498	–	0	0.0	8.6	95.4	92.5	0.1	7.4
MFBC(1) + Ag (1) + UST	0.508	–	0	0.0	9.0	100.0	97.2	–	2.8
MFBC(1) + Ag (1) + PVA	0.497	–	0	0.0	9.3	100.0	96.8	–	3.2
MFBC(2) + Ag (1)	0.341	–	0	0.0	8.6	100.0	91.6	–	8.4
Ag(1) + Cu(1)	0.500	0.500	20	17.4	9.0	100.0	84.5	0.1	15.4
MFBC(1) + (Ag+Cu)(1)	0.255	0.255	20	13.2	8.8	100.0	82.3	0.1	17.6
MFBC(1) + (Ag+Cu)(1)+ PVA	0.251	0.251	20	17.5	9.2	99.5	83.2	0.1	16.7
MFBC(2) + (Ag+Cu)(1)	0.165	0.165	10	8.7	9.8	98.1	94.1	0.1	5.8
Ag(1) + Co(1)	0.500	0.500	20	17.5	8.3	98.7	91.8	–	8.2
MFBC(1) + (Ag+Co)(1)	0.231	0.231	20	30.0	8.2	96.0	99.0	0.1	0.9
MFBC(1) + (Ag+Co)(1)+ PVA	0.224	0.224	10	8.7	6.5	91.6	96.2	0.2	3.6
MFBC(2) + (Ag+Co)(1)	0.156	0.156	20	17.4	5.0	82.7	95.5	0.2	4.3

A comparison of obtained results was done with data on the electrochemical reduction of *p*-NA on a copper cathode under similar conditions. According to these results (Table 1), *p*-nitroaniline is electrochemically reduced on a Cu cathode at a high rate (6.9 ml H_2/min), and conversion of the initial substance of 83.1 % with formation of *p*-PDA (57.8 %). However, as it follows from chromatographic analyses, the electrochemical reduction of *p*-NA is attended to with the formation of a rather large amount of side products (42.0 %). Additionally, Table 1 shows the results of *p*-NA hydrogenation on the Ag, Ag-Cu and Ag-Co particles, prepared without the addition of MF black carbon. It should be noted that the hydrogenation of *p*-NA using these particles occurs at high rates: 10.0, 9.0, and 8.3 mL H_2/min, respectively.

The total content of metals in the created composites was calculated considering the titrimetric results for determining metal cations amounts in the filtrates after the synthesis of these composites. The metal contents in 1 g of the resulting composites were also calculated, which can affect the electrocatalytic activity of the catalysts.

According to data in Table 1, almost all studied silver-carbon composites manifested the electrocatalytic activity in the electrohydrogenation of *p*-NA. Their use increases both hydrogenation rates and *p*-NA conversion. The yields of the main product *p*-PDA increase with a sharp decrease in the formation of by-products.

The hydrogen saturation of monometallic MFBC + Ag composites is not accompanied by hydrogen absorption, i.e., the silver cations were completely reduced during the synthesis of these composites (Fig. 2). The application of ultrasonic treatment and the polymeric stabilizer improved the main characteristics of the process of electrocatalytic hydrogenation of *p*-NA. A slightly higher hydrogenation rate was obtained in this process for silver particles synthesized without MF black carbon compared to the MFBC + Ag composites. However, according to Table 1, the silver content in 1 g of these particles is significantly higher than in the Ag-carbon composites.

Bimetallic MFBC + (Ag+Cu) composites exhibited the similar and slightly higher electrocatalytic activity in the studied process as compared to monometallic Ag/C-N composites and even with bimetallic Ag+Cu particles (without MFBC) with a high content of the metals (Table 1), showing the synergistic effect of two metals in the composites. During the hydrogen saturation, these composites absorb the small volumes of hydrogen, which indicates the performing of additional electrochemical reduction of cations of both metals, or copper cations from its oxides, which probably are present in the composites in small amounts and are not indicated in X-ray patterns due to weak reflections of their crystalline phases (Fig. 4, *a*). A capacity of copper and silver cations incorporated in polymer-metal composites for electrochemical reduction under similar conditions was established by us earlier [30, 31].

In the bimetallic MFBC + (Ag+Co) composites, the silver cations are subjected to electrochemical reduction and cobalt cations to a lesser extent. At saturation of these composites with hydrogen, its absorption occurs in small volumes, evidently with additional reduction of both metal cations (Table 1). These composites exhibited lower electrocatalytic activity in electrohydrogenation of *p*-NA among all silver-carbon composites investigated, but with higher *p*-PDA yields and less formation of by-products than at MFBC + (Ag+Cu) composites application. Their lower activity is due to the presence of cobalt hydroxide in these composites, which decreases the content of reduced cobalt catalyzing the electrohydrogenation process. In addition, the resulting particles of silver and cobalt metal alloys in various ratios may have a lower electrocatalytic activity than reduced metals.

Conclusions

Mono- and bimetallic N-doped metal-carbon composites based on carbonized melamine-formaldehyde polymer with silver, silver-copper, and silver-cobalt particles were synthesized by the reduction of metal cations from their nitrates with hydrazine hydrate in an aqueous ethanol medium in the presence of dispersed MF black carbon powder. MF carbon black was prepared by heat treatment of MF polymer at 500 °C. According to the X-ray diffraction analysis and microscopic studies, the resulting MFBC + Ag composites contain crystalline silver phases with an average particle size of 20 nm, which form the larger crystallites with different shapes and arrangements on the surface of the MF black carbon particles. Bimetallic carbon composites contain crystallites of both individual metals and their alloys. The synthesized silver-containing N-doped carbon composites were tested for the manifestation of electrocatalytic properties in the electrohydrogenation of *p*-nitroaniline. The investigations performed were established that almost all prepared MFBC + Ag, MFBC + (Ag+Cu) and MFBC + (Ag+Co) composites were electrocatalytically active in the process under study, especially as to the increasing of *p*-nitroaniline conversion, the selective formation of *p*-phenylenediamine, as the main product of the *p*-NA hydrogenation, and the decreasing of by-product contents. The highest electrocatalytic activity in the electrohydrogenation of *p*-NA among all prepared silver-containing composites was shown by MFBC + (Ag+Cu) composites. The hydrogenation rate of *p*-NA on these composites exceeded its own value obtained by carrying out this process with the use of reduced Ag+Cu bimetallic particles (without MF black carbon) with the increased metal content per 1 g of these particles used to activate the cathode. It can be concluded that the created silver-containing N-doped carbon composites can be used as electrocatalysts or catalysts in various chemical catalytic processes.

References

1   Rodrigues-Reinoso F. The role of carbon materials in heterogeneous catalysis / F. Rodrigues-Reinoso // Carbon. — 1998. — Vol. 36, No. 3. — P. 159–175. https://doi.org/10.1016/S0008-6223(97)00173-5

2   Gopiraman M. Carbon Nanocomposites: Preparation and Its Application in Catalytic Organic Transformations / M. Gopiraman, I.S. Kim // In Book "Nanocomposites — Recent Evolutions". — London: IntechOpen, 2019. — 230 p. https://doi.org/10.5772/intechopen.81109

3   Gerber I.C. A theory/experience description of support effects in carbon-supported catalysts. / I.C. Gerber, Ph. Serp // Chem. Reviews. — 2020. — Vol. 120, No. 2. — P. 1250–1349. https://doi.org/10.1021/acs.chemrev.9b00209

4   Shen W.Z. Nitrogen-containing porous carbons: synthesis and application / W.Z. Shen, W.B. Fan // J. Mater. Chem. A. — 2013. — Vol. 1. — P. 999–1013. https://doi.org/10.1039/C2TA00028H

5   Majeed S. Synthesis and electrochemical applications of nitrogen-doped carbon nanomaterials / S. Majeed, J. Zhao, L. Zhang, S. Anjum, Zh. Liu, G. Xu // Nanotechnol. Rev. — 2013. — Vol. 2, No. 6. — P. 615–635. https://doi.org/10.1515/ntrev-2013-0007

6   He L. Synthesis, characterization, and application of metal nanoparticles supported on nitrogen-doped carbon: catalysis beyond electrochemistry / L. He, F. Weniger, H. Neumann, M. Beller // Angew. Chem. Int. Ed. — 2016. — Vol. 55, No. 41. — P. 12582–12594. https://doi.org/10.1002/anie.201603198

7   Rangraz Ya. Recent advances on heteroatom-doped porous carbon/metal materials: fascinating heterogeneous catalysts for organic transformations / Ya. Rangraz, V.V. Heravi, A. Elhampour // Chem. Rec. — 2021. — Vol. 21, No. 8. — P. 1985–2073. https://doi.org/10.1002/tcr.202100124

8   Maaz Kh. Silver nanoparticles — Fabrication, characterization and application / Kh. Maaz. — London: IntechOpen, 2018. — 288 p. https://doi.org/10.5772/intechopen.71247

9   Wu Ch. Synthesis and application of silver nanocomposites: A review / Ch. Wu, Sh. Xu, W. Wang // J. Phys.: Conf. Ser. — 2021. — Vol. 1948. — P. 012216. https://doi.org/10.1088/1742-6596/1948/1/012216

10 Haider A.J. Deposition of silver nanoparticles on multiwalled carbon nanotubes by chemical reduction process and their antimicrobial effects / A.J. Haider, A.D. Thamir, D.S. Ahmed, M.R. Mohammad // AIP Conf. Proceedings. — 2016. — Vol. 1758. — P. 030003. http://dx.doi.org/10.1063/1.4959399

11 Bakshi S.R. Carbon nanotube reinforced metal matrix composites / S.R. Bakshi, D. Lahiri, A. Agarwal // Intern. Mater. Rev. — 2010. — Vol. 55, No. 1. — P. 41–64. https://doi.org/10.1179/095066009X12572530170543

12 Agarwal A. Carbon nanotubes: Reinforced metal matrix composites. / A. Agarwal, S.R. Bakshi, D. Lahiri. — New York: CRC Press, 2018. — 325 p.

13 Daoush W.M. Synthesis of multi-walled carbon nanotubes/silver nanocomposite powders by chemical reduction in aqueous solution / W.M. Daoush, S.H. Hong // J. Exp. Nanosci. — 2013. — Vol. 8, No. 5. — P. 742–751. https://doi.org/10.1080/17458080.2011.604959

14 Pontoreau M. Synthesis of composite powders composed of silver and carbon nanotubes by liquid-phase reduction method / M. Pontoreau, B. Thomas, E. Le Guen, Ch. Bourda, N. Kraiem, L. Andrey, J.-F. Silvain // Nano-Structures & Nano-Objects. — 2020. — Vol. 24. — P. 100622. https://doi.org/10.1016/j.nanoso.2020.100622

15 Tachibana N. Highly porous nitrogen-doped carbon nanoparticles synthesized via simple thermal treatment and their electrocatalytic activity for oxygen reduction reaction / N. Tachibana, S. Ikeda, Y. Yukawa, M. Kawaguchi // Carbon. — 2017. — Vol. 115. — P. 515–525. https://doi.org/10.1016/j.carbon.2017.01.034

16 Муратов Д.Г. Формирование нанокомпозитов Ni/C на основе полиакрилонитрила под действием ИК-излучения / Д.Г. Муратов, Е.В. Якушко, Л.В. Кожитов, А.В. Попкова, М.А. Пушкарев // Материалы электронной техники. — 2013. — № 1. — С. 61–65. https://doi.org/10.17073/1609-3577-2013-1-61-65

17 Jiang Sh. Metal/N-doped carbon (metal = Ag, Cu, Ni) nanocatalysts for selective hydrogenation of 4-nitrophenol / Sh. Jiang, H. Ni, P. Li, J. Wang, H. Ren // Catalysis Communications. — 2021. — Vol. 151. — P. 106280. https://doi.org/10.1016/j.catcom.2021.106280

18 Tiwari D. Melamine-formaldehyde derived porous carbons for adsorption of CO2 capture / D. Tiwari, Ch. Goel, H. Bhunia, P. Bajpai // J. Environmental Management. — 2017. — Vol. 197. — P. 415–427. https://doi.org/10.1016/j.jenvman.2017.04.013

19 Zhong H. Nitrogen-enriched carbon from melamine resins with superior oxygen reduction reaction activity / H. Zhong, H. Zhang, S. Liu, Ch. Deng, M. Wang // ChemCusChem. — 2013. — Vol. 6, No. 5 — P. 807–812. https://doi.org/10.1002/cssc.201200919

20 Balla P.K. Nano casting fabrication of porous N-doped carbon using melamine-formaldehyde resins / P.K. Balla, B.V.N. Kumar, K. Ganesan, E.B. Shaik, K.R. Rao // AIP Conference Proceedings. — 2018. — Vol. 1992. — P. 040016. https://doi.org/10.1063/1.5047981

21 Ahamad T. N/S-doped carbon embedded with AgNPs as a highly efficient catalyst for the reduction of toxic organic pollutants / T. Ahamad, M. Naushad, S.I. Al-Saeedi, S.M. Alshehri // Materials Letters. — 2020. — Vol. 264, No. 1. — P. 127310. https://doi.org/10.1016/j.matlet.2020.127310

22 Bhaduri B. Facile synthesis of carbon-supported silver nanoparticles as an efficient reduction catalyst for aqueous 2-methyl-p-nitrophenol / B. Bhaduri, T. Polubesova // Materials Letters. — 2020. — Vol. 267, No. 5. — P. 127546. https://doi.org/10.1016/j.matlet.2020.127546

23 Visurkhanova Ya.A. Synthesis and the characteristic melamine formaldehyde composites / Ya.A. Visurkhanova, N.M. Ivanova, G.K. Tusupbekova, D.S. Izbastenova // Advanced Materials Research. — 2014. — Vol. 1040. — P. 393–398. https://doi.org/10.4028/www.scientific.net/AMR.1040.393

24 Formenti D. Reduction of nitro compounds using 3d-non-noble metal catalysts / D. Formenti, F. Ferretti, F.K. Scharnagl, M. Beller // Chemical Reviews. – 2019. — Vol. 119, No. 4. — P. 2611–2680. https://doi.org/10.1021/acs.chemrev.8b00547

25 Hong H.-J. Synthesis of Copper Nanoparticles from Cu^{2+}-spiked wastewater via adsorptive separation and subsequent chemical reduction / H.-J. Hong, J. Ryu // Nanomaterials. — 2021. — Vol. 11. — P. 2051. https://doi.org/10.3390/nano11082051

26 Калюкова Е.Н. Осадительное и комплексонометрическое титрование. Методические указания к лабораторной работе по аналитической химии / Е.Н. Калюкова. — Ульяновск: Ульянов. гос. техн. ун-т, 2003. — 28 с.

27 Васильев В.П. Практикум по аналитической химии / В.П. Васильев, Р.П. Морозова, Л.А. Кочергина. — М.: Химия, 2000. — 328 с.

28 Vissurkhanova Y.A., Soboleva E.A., Ivanova N.M., Muldakhmetov Z.M. Thermal and electrochemical reduction of nickel (II) ferrite under the influence of polymer stabilizers // Bulletin of the University of Karaganda – Chemistry. – 2020. — Vol. 98, No. 2. — P. 42–50. https://doi.org/10.31489/2020Ch2/42-50

29 Помогайло А.Д. Наночастицы металлов в полимерах / А.Д. Помогайло, А.С. Розенберг, И.Е. Уфлянд. — М.: Химия, 2000. — 672 с.

30 Иванова Н.М. Электрокаталитическая активность полианилин-медных композитов в электрогидрировании *n*-нитроанилина / Н.М. Иванова, Е.А. Соболева, Я.А. Висурханова, И.В. Кирилюс // Электрохимия. — 2015. — Т. 51, № 2. — С. 197–204. https://doi.org/10.7868/S042485701502005X

31 Иванова Н.М. Структурно-фазовые изменения полимерных композитов с введённым нитратом серебра и их электрокаталитическая активность / Н.М. Иванова, Е.А. Соболева, Я.А. Висурханова, Е.С. Лазарева // Электрохимия. — 2018. — Т. 54, № 11. — С. 1010–1017. https://doi.org/10.1134/S042485701813025X

Я.А. Висурханова, Н.М. Иванова, Е.А. Соболева, А.К. Мухамеджанова

Құрамында күміс бар моно-және биметалл N-қоспаланған көміртекті композиттер және олардың электрокаталитикалық белсенділігі

Күміс, күміс–мыс және күміс–кобальт бөлшектері бар көміртекті меламинформальдегидті полимер (МФП) негізіндегі N-қоспаланған металл-көміртекті композиттер синтезделді. Құрамында күміс бар моно- және биметалл композиттері МФ-полимерін 500°С температурада термиялық өңдеу нәтижесінде алынған күйе бөлшектерінің қатысуымен сулы–этанол ортасында металл нитраттарын гидразингидратпен тотықсыздандыру арқылы алынды. *n* -нитроанилинді (*n*-НА) электрогидрлеуде катализатор ретінде металл-көміртекті композиттерді қолданғанға дейінгі және одан кейінгі құрылымдық-фазалық өзгерістер рентгендік фазалық талдау арқылы зерттелді. Алынған МФС + Ag, МФС + (Ag+Cu) және МФС + (Ag+Co) композиттерінің морфологиялық ерекшеліктері электронды микроскопия әдісімен зерттелді. Синтезделген композиттердің құрамында негізінен сәйкес тотықсызданған металдардың немесе олардың қорытпаларының кристалдық фазалары болатыны анықталды. МФС(1) + Ag(1) монометалл композиті құрамындағы кеуекті МФ-күйе бөлшектерінде әртүрлі пішіндер мен локализацияға ие тотықсыздандырылған күмістің кристаллиттері бар. *n*-НА электрогидрлеу процесінде синтезделген Ag-құрамды композиттердің жоғары электрокаталитикалық белсенділігі *n*-НА-ның электрохимиялық тотықсыздануымен ғана емес, сонымен қатар МФС+(Ag+Cu) композиттерінің *n*-НА-ның Ag+Cu бөлшектерінде электрокаталитикалық гидрленуі (МФ-күйесіз) жағдайында да көрсетілген. Зерттелген МФС-композиттердің қолдану жағдайында негізгі гидрлеу өнімінің (*n*-фенилендиаминнің) түзілу селективтілігі артатыны және жанама өнімдердің шығымдылығы төмендейтіні анықталды.

Кілт сөздер: N-қоспаланған металл-көміртекті композиттер, күміс, меламинформальдегидті полимер, карбонизация, биметалл катализаторлары, Ag–Cu бөлшектері, Ag–Co бөлшектері, электрокаталитикалық гидрлеу, *n*-нитроанилин.

Я.А. Висурханова, Н.М. Иванова, Е.А. Соболева, А.К. Мухамеджанова

Моно- и биметаллические серебросодержащие N-допированные углеродные композиты и их электрокаталитическая активность

Синтезированы N-допированные металлоуглеродные композиты на основе карбонизированного меламиноформальдегидного полимера с частицами серебра, серебра–меди и серебра–кобальта. Моно- и биметаллические серебросодержащие композиты были получены восстановлением нитратов металлов гидразингидратом в водно-этанольной среде в присутствии частиц сажи, полученной в результате термической обработки МФ-полимера при 500 °С. Методом рентгенофазового анализа изучены структурно-фазовые изменения до и после применения металл-углеродных композитов в качестве катализаторов в электрогидрировании *n*-нитроанилина (*n*-НА). Морфологические особенности полученных композитов МФС + Ag; МФС + (Ag+Cu) и МФС + (Ag+Co) исследованы методом электронной микроскопии. Установлено, что в составе синтезированных композитов, в основном, присутствуют кристаллические фазы соответствующих восстановленных металлов или их сплавов. В монометаллическом композите МФС(1) + Ag(1) содержатся кристаллиты восстановленного серебра, имеющие разную форму и локализацию на пористых частицах МФ-сажи. Показана более высокая электрокаталитическая активность синтезированных Ag-содержащих композитов в процессе электрогидрирования *n*-НА по сравнению не только с электрохимическим восстановлением *n*-НА, но и в случае МФС + (Ag+Cu) композитов с электрокаталитическим гидрированием *n*-НА на частицах Ag + Cu (без МФ-сажи). Установлено, что при применении исследованных МФС-композитов возрастает селективность образования основного продукта гидрирования (*n*-фенилендиамина) и снижаются выходы побочных продуктов.

Ключевые слова: N-допированные металл-углеродные композиты, серебро, меламиноформальдегидный полимер, карбонизация, биметаллические катализаторы, Ag–Cu частицы, Ag–Co частицы, электрокаталитическое гидрирование, *n*-нитроанилин.

References

1 Rodríguez-Reinoso, F. (1998). The role of carbon materials in heterogeneous catalysis. *Carbon*, 36(3), 159–175. https://doi.org/10.1016/S0008-6223(97)00173-5

2 Gopiraman, M., & Kim, I.S. (2019). *Carbon Nanocomposites: Preparation and Its Application in Catalytic Organic Transformations*. In Book "Nanocomposites — Recent Evolutions". London: IntechOpen. https://doi.org/10.5772/intechopen.81109

3 Gerber, I.C., & Serp, P. (2019). A Theory/Experience Description of Support Effects in Carbon-Supported Catalysts. *Chemical Reviews*, 120(2), 1250–1349. https://doi.org/10.1021/acs.chemrev.9b00209

4 Shen, W., & Fan, W. (2013). Nitrogen-containing porous carbons: synthesis and application. *J. Mater. Chem. A*, 1(4), 999–1013. https://doi.org/10.1039/C2TA00028H

5 Majeed, S., Zhao, J., Zhang, L., Anjum, S., Liu, Zh., & Xu, G. (2013). Synthesis and electrochemical applications of nitrogen-doped carbon nanomaterials. *Nanotechnology Reviews*, 2(6), 615–635. https://doi.org/10.1515/ntrev-2013-0007

6 He, L., Weniger, F., Neumann, H., & Beller, M. (2016). Synthesis, Characterization, and Application of Metal Nanoparticles Supported on Nitrogen-Doped Carbon: Catalysis beyond Electrochemistry. *Angewandte Chemie International Edition*, 55(41), 12582–12594. https://doi.org/10.1002/anie.201603198

7 Rangraz, Y., Heravi, M.M., & Elhampour, A. (2021). Recent Advances on Heteroatom-Doped Porous Carbon/Metal Materials: Fascinating Heterogeneous Catalysts for Organic Transformations. *The Chemical Record*, 21(8), 1985–2073. https://doi.org/10.1002/tcr.202100124

8 Maaz, Kh. (2018). *Silver nanoparticles — Fabrication, characterization and application*. London: IntechOpen. https://doi.org/10.5772/intechopen.71247

9 Wu, C., Xu, S., & Wang, W. (2021). Synthesis and applications of silver nanocomposites: A review. *Journal of Physics: Conference Series*, 1948(1), 012216. https://doi.org/10.1088/1742-6596/1948/1/012216

10 Haider, A.J., Thamir, A.D., Ahmed, D.S., & Mohammad, M.R. (2016). Deposition of silver nanoparticles on multiwalled carbon nanotubes by chemical reduction process and their antimicrobial effects. *AIP Conf. Proceedings*, 1758, 030003 http://dx.doi.org/10.1063/1.4959399

11 Bakshi, S.R., Lahiri, D., & Agarwal, A. (2010). Carbon nanotube reinforced metal matrix composites — a review. *International Materials Reviews*, 55(1), 41–64. https://doi.org/10.1179/095066009X12572530170543

12 Agarwal A., Bakshi S.R., & Lahiri, D. (2018). *Carbon nanotubes: Reinforced metal matrix composites*. New York: CRC Press.

13 Daoush, W.M., & Hong, S.H. (2013). Synthesis of multi-walled carbon nanotube/silver nanocomposite powders by chemical reduction in aqueous solution. *Journal of Experimental Nanoscience*, 8(5), 742–751. https://doi.org/10.1080/17458080.2011.604959

14 Pontoreau, M., Thomas, B., Le Guen, E., Bourda, C., Kraiem, N., Andrey, L., & Silvain, J.-F. (2020). Synthesis of composite powders composed of silver and carbon nanotubes by liquid-phase reduction method. *Nano-Structures & Nano-Objects*, 24, 100622. https://doi.org/10.1016/j.nanoso.2020.100622

15 Tachibana, N., Ikeda, S., Yukawa, Y., & Kawaguchi, M. (2017). Highly porous nitrogen-doped carbon nanoparticles synthesized via simple thermal treatment and their electrocatalytic activity for oxygen reduction reaction. *Carbon*, 115, 515–525. https://doi.org/10.1016/j.carbon.2017.01.034

16 Muratov, D.G., Yakushko, E.V., Kozhitov, L.V., Popkova, A.V., & Pushkarev, M.A. (2015). Formirovanie nanokompozitov Ni/C na osnove poliakrilonitrila pod deistviem IK-izlucheniia [Formation of Ni/C nanocomposites based on polyacrylonitrile under the influence of IR radiation]. *Izvestiia vysshikh uchebnykh zavedenii. Materialy Elektronnoi Tekhniki — Materials of Electronic Engineering*, (1), 61–65 [in Russian]. https://doi.org/10.17073/1609-3577-2013-1-61-65

17 Jiang, S., Ni, H., Li, P., Wang, J., & Ren, H. (2021). Metal/N-doped carbon (Metal = Ag, Cu, Ni) nanocatalysts for selective hydrogenation of 4-nitrophenol. *Catalysis Communications*, 151, 106280. https://doi.org/10.1016/j.catcom.2021.106280

18 Tiwari, D., Goel, C., Bhunia, H., & Bajpai, P.K. (2017). Melamine-formaldehyde derived porous carbons for adsorption of CO_2 capture. *Journal of Environmental Management*, 197, 415–427. https://doi.org/10.1016/j.jenvman.2017.04.013

19 Zhong, H., Zhang, H., Liu, S., Deng, C., & Wang, M. (2013). Nitrogen-Enriched Carbon from Melamine Resins with Superior Oxygen Reduction Reaction Activity. *ChemSusChem*, 6(5), 807–812. https://doi.org/10.1002/cssc.201200919

20 Balla, P.K., Kumar, B.V.N., Ganesan, K., Shaik, E.B., & Rao, K.R. (2018). Nano casting fabrication of porous N-doped carbon using melamine-formaldehyde resins. *AIP Conference Proceedings,* 1992, 040016. https://doi.org/10.1063/1.5047981

21 Ahamad, T., Naushad, M., Al-Saeedi, S.I., & Alshehri, S.M. (2020). N/S-doped carbon embedded with AgNPs as a highly efficient catalyst for the reduction of toxic organic pollutants. *Materials Letters*, 264, 127310. https://doi.org/10.1016/j.matlet.2020.127310

22 Bhaduri, B., & Polubesova, T. (2020). Facile synthesis of carbon-supported silver nanoparticles as an efficient reduction catalyst for aqueous 2-methyl-p-nitrophenol. *Materials Letters*, 267(5), 127546. https://doi.org/10.1016/j.matlet.2020.127546

23 Visurkhanova, Y., Ivanova, N., Tusupbekova, G., & Izbastenova, D. (2014). Synthesis and Characteristics of Melamine Formaldehyde Composites. *Advanced Materials Research*, 1040, 393–398. https://doi.org/10.4028/www.scientific.net/AMR.1040.393

24 Formenti, D., Ferretti, F., Scharnagl, F.K., & Beller, M. (2018). Reduction of Nitro Compounds Using 3d-Non-Noble Metal Catalysts. *Chemical Reviews*, 119(4), 2611–2680. https://doi.org/10.1021/acs.chemrev.8b00547

25 Hong, H.-J., & Ryu, J. (2021). Synthesis of Copper Nanoparticles from Cu^{2+}-Spiked Wastewater via Adsorptive Separation and Subsequent Chemical Reduction. *Nanomaterials*, 11(8), 2051. https://doi.org/10.3390/nano11082051

26 Kalyukova, E.N. (2003). *Osaditelnoe i kompleksonometricheskoe titrovanie. Metodicheskie ukazaniia k laboratornoi rabote po analiticheskoi khimii [Precipitation and complexometric titration. Guidelines for laboratory work in analytical chemistry]*. Ulyanovsk: Ulyanovskii gosudarstvennyi tekhnicheskii universitet [in Russian].

27 Vasil'ev, V.P., Morozova, R.P., & Kochergina, L.A. (2000). *Praktikum po analiticheskoi khimii [Workshop on analytical chemistry]*. Moscow: Khimiia [in Russian].

28 Vissurkhanova, Y.A., Soboleva, E.A., Ivanova, N.M., & Muldakhmetov, Z.M. (2020). Thermal and electrochemical reduction of nickel (II) ferrite under the influence of polymer stabilizers. *Bulletin of the University of Karaganda – Chemistry,* 98(2), 42–50. https://doi.org/10.31489/2020Ch2/42-50

29 Pomogailo, A.D., Rozenberg, A.D., & Uflyand, I.E. (2000). *Nanochastitsy metallov v polimerakh [Metal Nanoparticles in Polymers]*. Moscow: Khimiia [in Russian].

30 Ivanova, N.M., Soboleva, E.A., Visurkhanova, Ya.A., & Kirilyus, I.V. (2015). Elektrokaticheskaia aktivnost polianilin-mednykh kompozitov v elektrogidrirovanii *n*-nitroanilina [Electrocatalytic activity of polyaniline-copper composites in the electrohydrogenation of *n*-nitroyaniline]. *Elektrokhimiia – Electrochemistry*, 51, 2, 197–204 [in Russian]. https://doi.org/10.7868/S042485701502005X

31 Ivanova, N.M., Soboleva, E.A., Visurkhanova, Y.A., & Lazareva, E.S. (2018). Strukturno-fazovye izmeneniia polimernykh kompozitov s vvedennym nitratom serebra i ikh eletktrokataliticheskaia aktivnost [Structure-Phase Changes in Polymer Composites Doped with Silver Nitrate and Their Electrocatalytic Activity]. *Elektrokhimiia – Electrochemistry,* 54, 11, 1010–1017 [in Russian]. https://doi.org/10.1134/S042485701813025X

Information about authors*

Vissurkhanova, Yakha Amkhadovna (corresponding author) — Researcher, Institute of Organic Synthesis and Coal Chemistry of the Republic of Kazakhstan, Karaganda, Alikhanova street, 1, 100008, Kazakhstan; e-mail: yakhavisurkhanova@bk.ru; https://orcid.org/0000-0001-7279-1145;

Ivanova, Nina Mikhailovna — Doctor of Chemical Sciences, Professor, Head of Laboratory "Electrocatalysis and Quantum Chemical Investigations" of the Institute of Organic Synthesis and Coal Chemistry of the Republic of Kazakhstan, Karaganda, Alikhanova street, 1, 100008, Kazakhstan; e-mail: nmiva@mail.ru; https://orcid.org/0000-0001-8564-8006;

Soboleva, Elena Anatolyevna — Candidate of Chemical Science, Leading Researcher, Institute of Organic Synthesis and Coal Chemistry of the Republic of Kazakhstan, Karaganda, Alikhanova street, 1, 100008, Kazakhstan; e-mail: esoboleva-kz@mail.ru; https://orcid.org/0000-0002-1089-367X;

Mukhamedzhanova, Aizhan Kudabaevna — Master's degree of Chemical Technology, Junior Researcher, Institute of Organic Synthesis and Coal Chemistry of the Republic of Kazakhstan, Karaganda, Alikhanova street, 1, 100008, Kazakhstan; e-mail: aijan_08@mail.ru; https://orcid.org/0000-0003-4369-3102

_____

*The author's name is presented in the order: *Last Name, First and Middle Names*

CHEMICAL TECHNOLOGY

Z.M. Muldakhmetov[1], A.T. Ordabaeva[1*], M.G. Meiramov[1], A.M. Gazaliev[1], Zh.S. Shaikenova[1], G.K. Mukusheva[2], T.S. Zhivotova[1]

[1]Institute of Organic Synthesis and Coal Chemistry, Karaganda, Kazakhstan;
[2]Karagandy University of the name of academician E.A. Buketov, Karaganda, Kazakhstan
(*Corresponding author's e-mail: aigul_serik_kz@mail.ru)

Obtaining Carbon Sorbent from "Euromet" LLP Coke Breeze

The paper presents the results of a physicochemical analysis of a coke sample from "Euromet" LLP (Karaganda, Kazakhstan), which is carbonaceous material with high carbon content, the absence of volatiles matter and low ash content. Carbon sorbents were obtained from low-value fractions of carbonized materials of the Karaganda region coke production by the steam-gas activation. An important advantage of using screenings (coke breeze class 0–10 mm, which was crushed and fractionated to a particle size of 2–5 mm.) is the exclusion of the energy-intensive carbonization stage from the technological process, which releases a large amount of environmentally harmful substances (phenols, cresols, gaseous emissions etc.). The optimal conditions for obtaining a sorbent from low-value coke breeze are a temperature of 850 °C and an activation time of 2 hours. The physicochemical properties (ash content, bulk density, sorption capacity for iodine and methylene blue, total pore volume for water) of carbon sorbents were determined.

Keywords: coke breeze, coals, sorbents, activation, sorption capacity, ash content, burning, bulk density.

Introduction

Environmental pollution by the oil, coal and metallurgical industries is one of the reasons for the severe environmental consequences and the negative impact on human health. Industrial enterprises of the republic discharge insufficiently treated wastewater into water sources. In addition, the water resources of Kazakhstan are polluted by household and agricultural waste. Currently, there is a tightening of requirements for the standards of discharges and emissions from production and economic activities. The high sorption activity of active carbons determines a wide range of their application, including the possibility of using them for purification from pollutants. The use of this product in the world is steadily growing with the development of industrial production of activated carbon. So in Western Europe, activated carbons are used as the main material for wastewater treatment and gas emissions, in accordance with current environmental regulations. The areas of application of carbon sorbents are inextricably linked both with the knowledge of their sorption properties in relation to various pollutants and with their physicochemical properties.

Also, in addition to activation gases, various chemical reagents are used at the stages of carbonization and preparation of raw materials. Different vegetable raw materials such as wood, nutshell, remains of stems and seed coats [1, 2], as well as processed carbon-containing substances such as plastics, rubber, oil, coal [3], are used as raw materials for the production of carbon sorbents.

A large amount of low-value fraction (screenings) remains during the preparation of products for sale at enterprises producing coke using different technologies. The use of this material will make it possible to obtain highly effective carbon sorbents for the public utilities, chemical, oil, gas, and mining industries with certain processing.

The advantage of using screenings is the exclusion from the technological process of the energy-consuming carbonization stage, which releases a large amount of environmentally harmful substances (phenols, cresols, gaseous emissions, etc.). The ash content, bulk density, and average particle diameter are linearly related to the degree of burning during activation. However, it is necessary to consider the specifics of the norms of sorbents for various purposes. Most of them require such parameters as grain size, total pore volume in water, mass fraction of moisture, bulk density, and abrasion resistance.

The grade of coal should be considered when activating hard coal [4]. Bituminous coals with a high tar and volatiles content, sinter or swell when heated, and therefore require pre-treatment. Another activation process [5] for coals of the "bituminous C" class with a high content of volatiles and moisture is carried out on grained raw materials, which are first subjected to drying and preliminary oxidation at 150–215 °C. Anthracite, which contains significantly fewer volatiles, can be activated immediately under appropriate conditions. To do this, anthracite is first crushed, the finely dispersed powder is briquetted with a binder, re-crushed, and after sieving into fractions, it is subjected to carbonization and activation. Direct activation of granular anthracite is difficult to implement and requires a long time in conventional rotary kilns. Low-grade bituminous coals (fat coals) with a relatively high volatile content, which coke poorly and produce grains of low strength, can also be used to produce activated carbons if crushed and washed with dilute mineral acid (hydrochloric, sulfuric, or phosphoric). Then after drying, the grains are crushed, the powders are granulated with binders, carbonized, and activated [6]. It is possible to activate the products of various stages of molded coke production with gas [7]. Coal-based activated carbons are not produced in Central Kazakhstan. The quality of the finished activated carbon depends on the correct set of technological parameters for the preparation of the initial material, activation modes. At present, the production of activated carbon is promising due to the possibility of obtaining materials with a developed structure for solving various problems, including protection of the biosphere from anthropogenic impact, in nuclear power engineering, and in modern devices for energy storage and transmission. At the same time, the scale of the use of nanoporous carbon is limited by the rather high cost of materials. This leads to the search for new methods for obtaining carbon materials with the required set of properties from cheap types of raw materials, which is an urgent task for science and industry [8]. For example, the cost of adsorbents is 450 times higher than the cost of raw materials with a huge sales market, and the total world production of porous carbon materials is currently about 1 million tons/year [9, 10].

With the high rates of development of heavy and light industry, motor transport entail an increasing load on surface waters [11, 12]. The quality of some natural water sources is unacceptable for their use not only for food purposes but also for technical needs. Hazardous organic substances, heavy metals, and radionuclides may be present in water bodies. Such water is of poor quality and certainly needs to be cleaned. The use of powdered activated carbon to capture mercury is actual for the Karaganda region (Nura river). In [13], the porous carbon materials obtained from the coal of the Maikuben basin, the Shoptykol deposit (Kazakhstan), with a specific surface area (348.99 m^2/g) were tested to treat waste sewage water taken from the SUC "Astana Water Canal" (Nur-Sultan, Kazakhstan). Active carbon is the only type of sorbent that has a high adsorption capacity when extracting toxic organic contaminants from water. All drinking water supply and deep (below maximum permissible concentrations) wastewater treatment are based on the use of powdered and granular activated carbons. For these purposes, 30 % of the global production of activated carbon is spent.

According to experts, it is necessary to produce at least 0.5 kg of activated carbon per capita per year for an environmentally safe and healthy lifestyle of people. This rate is undoubtedly higher in regions with high environmental pollution (for the Republic of Kazakhstan, at least 7.5 thousand tons per year). The main areas of use of carbon sorbents are associated with technological processes of adsorption purification, separation, isolation and concentration in gaseous and liquid media. Volatile organic compounds are the main pollutants of various industrial installations [14–16]. Some volatile organic compounds, such as toluene vapor released into the atmosphere as a result of their use, lead to serious environmental problems, therefore the concentration of which should be reduced to low levels in the environment [17–19]. Adsorption by activated carbon is one of the most common processes for the removal of volatile organic compounds, especially toluene from gaseous media [20, 21] and phenol from chemical wastewater [22].

In the world market, the main producer of activated carbon in the United States accounts for 34 % of the annual production of this product category. Europe, with a share of 24 %, ranks second in terms of activated carbon production. Kazakhstan accounts for only 0.7 % of the global activated carbon production, while Russia accounts for 2 % (Fig. 1).

Demand for activated carbon is growing due to its usefulness as a carbonaceous material in the fight against pollution. As a result, the cost of activated carbon rises depending on the application. The research of scientists is carried out in the direction of searching for a raw material base for the production of activated carbon for its low cost, availability, high carbon content and low ash content. The cost of coke breeze in the Republic of Kazakhstan is 60–90 thousand tenge/t. Activated coals based on coal, depending on the brand, cost from 800 thousand tenge/t. This indicates the need to organize their own production facilities for their production.
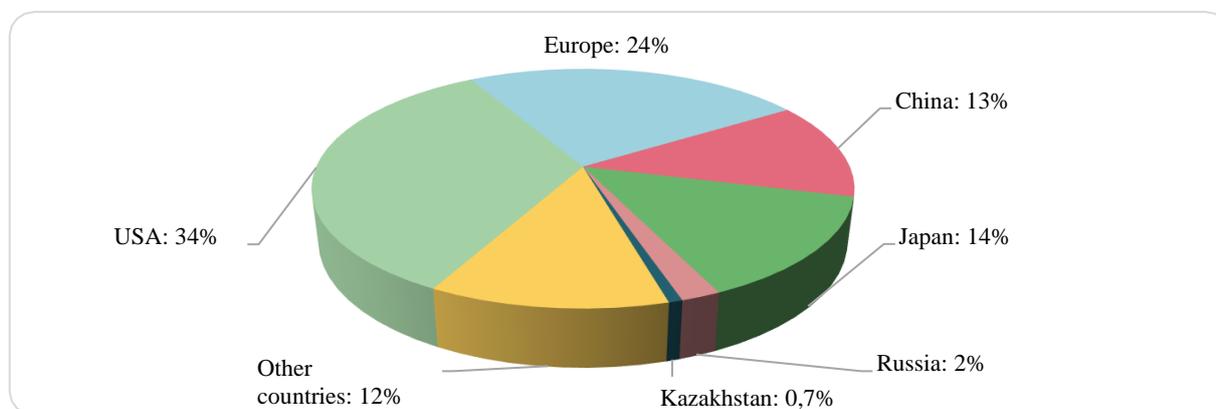
Figure 1. Share distribution of the annual production of activated carbon by country

This paper aims to determine the possibility of using a low-value fraction of the coke production of "Euromet" LLP (Karaganda, Kazakhstan) as a feedstock for the production of carbon sorbents.

Experimental

The object of the study was the coke breeze of the 0–10 mm class, which was subjected to crushing and fractionation to a particle size of 2–5 mm. Activation of coke from Karaganda coal was carried out on a laboratory unit based on a high-temperature tube furnace with maximum heating of 1100 °C and a quartz reactor. The amount of steam produced is controlled by the steam generator heater.

To work out the optimal conditions for obtaining active carbon, the feedstock was dried at a temperature of 120 °C for 3 hours, then 150–180 grams were loaded into the reactor, and, after connecting all systems, heating of the furnace was turned on. At 550–700 °C, the components absorbed during the quenching of coke are removed. At a temperature of 800 °C, steam is supplied to the reactor from the steam generator. After reaching the temperature of the set mode, activation continued for 1–2 hours, while the volatile substances condensed in the receiving flask cooled with water, and the resulting gases were removed carbon of the studied coke. The temperature at which the process of interaction of water vapor with the carbon of the coke under study begins was determined using GLC analysis on the "Crystallux 4000 M" (Research and Production Association "MetaKhrom", Russia) chromatograph. The relative average quadratic change in the output signal for a detector of an accident chromatograph "Crystallux 4000 M" is no more than 2 %. The accuracy of measurement results was estimated using a standard deviation (δ) according to [23, 24]. The correction factor T is 2.7760 for a 95 % level of reliability (trust probability) of a series of 5 measurements. To calculate the critical value F, the MS Excel program was used, where regression equations were obtained for the indicators: burnt, ash content, bulk density, sorption capacity for iodine and methylene blue, total pore volume for water, and structural strength.

250–300 g of dry coke with a grain size of 2–5 mm was placed in the reactor, the steam generator was turned on and, after boiling water, the furnace was turned on. Activation temperatures were 750, 800 and 850 °C. The set time for heating the oven to the set temperature was 10 minutes; the duration of activation was 60 and 120 minutes. At the end of the activation time, the heating and steam supply were stopped and, after the reactor cooled down, the yield of the obtained sorbent, the degree of burning, and bulk density were determined. The analysis of the obtained products was carried out according to the procedures [25].

Results and Discussion

Table 1 shows the main indicators of coke breeze from "Euromet" LLP.

Indicators of physico-chemical analysis of coke breeze from "Euromet" LLP

The name of indicators	UM	Medium
Mass fraction of carbon, C^d	%	upto 84
Ash content on dry state, A^d	%	upto 18.0
Mass fraction of total moisture	%	upto 5.0
Structural strength of dry coke	%	78–82

According to the given parameters, coke breeze from the coals of "Euromet" LLP can be used as a raw material for the production of carbon sorbents. Table 2 shows the data and test results from the laboratory of "Coal Research and Development Center" LLP, characterizing the degree of coke activation for the "Euromet" LLP coals in terms of its burning, ash content, bulk density, total pore volume in water, iodine and methylene blue activity.

Tables 2 and 3 demonstrate the boundaries of the confidence interval ($\pm\Delta$) of the measured characteristics of the "Euromet" LLP sorbent, determined considering the Student's criterion.

Conditions for obtaining and characteristics of the "Euromet" LLP sorbent

The mode for sorbent obtaining		Combustion loss, %	Ash content, %	Bulk density, g/dm³
T, °C	duration of activation, hour			
750	2	20.71±0.63	23.33±0.49	330±4.5
800	1	20.90±0.32	24.04±0.50	333±4.3
800	2	22.00±0.42	24.75±0.51	335±4.2
850	1	23.11±0.49	25.78±0.54	338±3.9
850	2	34.76±0.49	29.82±0.45	339±3.8

Conditions for obtaining and characteristics of the "Euromet" LLP sorbent

The mode for sorbent obtaining		Sorption capacity		Total pore volume by water, cm³/g	Structural strength, %
T, °C	duration of activation, hour	for iodine, %	Methylene blue, mg/g		
750	2	22.50±0.41	55±0.9	0.5258±0.0102	9.50±0.115
800	1	23.05±0.53	50±1.1	0.3533±0.0089	9.40±0.207
800	2	24.20±0.58	20±1.2	0.5975±0.0081	9.70±0.158
850	1	25.50±0.60	100±1.4154	0.5711±0.0167	9.60±0.207
850	2	27.94*±0.63	130±1.4	0.7501*±0.0086	9.80*±0.158

For the combustion loss index, the regression equation with different variations in the temperature and time modes of coal processing (Table 2) is described by the following equation:

$$Y \text{ (combustion loss)} = 0.1244T + 9.32t - 92.34. \qquad (1)$$

The coefficient of determination R-square is 0.83, the critical value F is 5.03, which is greater than the significance criterion F, equal to 0.16, which confirms the significance of the burn value from the mode of obtaining the sorbent. From equation (1), the amount of combustion loss increases linearly with increasing temperature and duration of the process.

The following equation describes the regression equation for the ash content index from the temperature and time modes of coal processing (Table 2):

$$Y \text{ (ash content)} = 0.030902T + 3.00523t - 3.923233. \qquad (2)$$

In this case, the value of R-square is 0.15, the critical value of F is 0.18, which is less than the significance criterion F, equal to 0.84, which indicates the significance of the value of the composition of the initial coal, but does not depend on the mode of its processing. Analysis of equations (2) shows that the ash content depends on the temperature and duration of the process, due to a decrease in the mass fraction of carbon.

The regression equation linking the obtained indicators for bulk density with different variations in the temperature and time modes of coal processing (Table 2) is as follows:

$$Y \text{ (bulk density)} = 0.144T + 1.4t - 471.4. \tag{3}$$

The value of the R-square is 0.03, and the critical value F 0.03 is less than the significance criterion F 0.96, which also indicates the significance of the value of the composition of the initial coal, but does not depend on the processing mode. An analysis of equation (3) shows that the bulk density value slightly depends on the process temperature and increases with the length of the processing time.

A regression equation has been obtained that relates the obtained indicators for the iodine sorption capacity with different variations in the temperature and time modes of coal processing (Table 3):

$$Y \text{ (sorption capacity for iodine)} = 0.05332T + 1.938t - 21.652. \tag{4}$$

The R-square value is 0.96; the critical value F 25.19 is greater than the significance criterion F 0.03, which indicates the significance of the indicator from the mode of obtaining the sorbent.

A regression equation was obtained that relates the obtained indicators for the sorption capacity for methylene blue with different variations in the temperature and time modes of coal processing (Table 3):

$$Y \text{ (sorption capacity for methylene blue)} = 0.8T + 13.33t - 598.333. \tag{5}$$

The value of the R-square is 0.53, the critical value F 1.36 is greater than the significance criterion F 0.46, which indicates the significance of the indicator from the mode of obtaining the sorbent.

A regression equation has been obtained that relates the obtained indicators for the total pore volume in water with different variations in the temperature and time regimes of coal processing (Table 3):

$$Y \text{ (total pore volume by water)} = 0.002666T + 0.228907t - 1.96583. \tag{6}$$

The R-square value is 0.93, the critical value F 13.68 is greater than the significance criterion F 0.06, which indicates the significance of the indicator from the mode of obtaining the sorbent.

A regression equation has been obtained that relates the obtained indicators for structural strength with different variations in the temperature and time modes of coal processing (Table 3):

$$Y \text{ (structural strength)} = 0.0032T + 0.246667t - 6.613333. \tag{7}$$

The R-square value is 0.97, the critical value F 36.5 is greater than the significance criterion F 0.02, which indicates the significance of the indicator from the mode of obtaining the sorbent.

Equations (4–7) show that the contribution of temperature to the increase in sorption capacity is significant for the indicator of sorption capacity for iodine and methylene blue, and for indicators of the total pore volume for water and structural strength, which will allow us to conclude that macropores in the sorbent increase. The value of the sorption capacity for iodine increases with increasing temperature treatment, which is consistent with theoretical ideas about the process.

Methylene blue activity indicates the AC surface formed by pores larger than 1.5 nm since the indicator molecule is relatively large. Therefore, low activity indicators for iodine, which is adsorbed on the surface of pores with a diameter significantly more than 1 nm, and methylene blue are not an indicator of the low quality of the carbon sorbent [26]. With a large specific surface, the proportion of thin pores increases, which do not fit large molecules, for example, persistent organic pollutants such as phenols, aromatic and polyaromatic hydrocarbons, etc. The results of sorption activity for iodine (MRTU No6-16-1003-67) [27] and clarifying ability for methylene blue (GOST 4453–74) [28] showed that the optimal conditions for obtaining a sorbent from coke breeze are: temperature 850 °C and activation time 2 hours. Properties of activated carbons depend on the choice of the appropriate raw material, method, and activation conditions. At the same time, a number of conditions can affect certain properties. Thus, the number and distribution of pore sizes depend, in particular, on the nature of the raw material, type and conditions of the activation process. The formation of gaseous products (H_2, CO, CO_2, CH_4) begins at a temperature of 670^0C, which indicates the presence of water vapor with the carbon of the coke breeze.

It is established that the exhaust gas contains hydrogen, carbon dioxide, methane, and carbon monoxide. When carbon interacts with water vapor or carbon dioxide, the following reactions occur simultaneously (Equations 8–10):

$$H_2O + C = CO + H_2 \qquad \Delta H = +117 \text{ kJ}; \qquad (8)$$

$$2H_2O + C = CO_2 + 2H_2 \qquad \Delta H = +75 \text{ kJ}; \qquad (9)$$

$$CO_2 + C = 2CO \qquad \Delta H = +159 \text{ kJ}. \qquad (10)$$
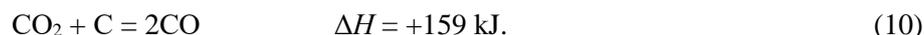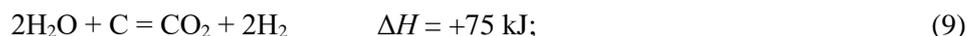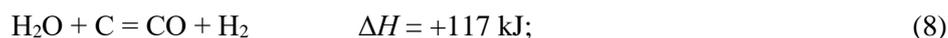
Table 4 shows the composition of gases obtained during the activation of coke breeze of "Euromet" LLP.

Table 4

The composition of the gas obtained during the activation of "Euromet" LLP coke breeze

Gas	Gas outlet mode							
	T,°C	τ, min	T,°C	τ, min	T,°C	τ, min	T,°C	τ, min
	670	120	750	120	800	120	850	120
H_2	50.33		55.23		59.08		53.7	
O_2	–		–		–		–	
N_2	0.780		0.80		0.95		0.95	
CO_2	18.90		20.40		15.43		10.74	
CH_4	3.35		3.05		3.38		0.89	
CO	17.42		20.52		21.16		33.72	

Thus, a carbon sorbent with a high adsorbing property was obtained as a result of the high-temperature process of activation of the coke breeze with water vapor on the basis of "Euromet" LLP (Karaganda, Kazakhstan) coal.

Conclusions

Physical and chemical analyzes showed that a sample of coke breeze from "Euromet" LLP (Karaganda, Kazakhstan) is a highly active carbonaceous material with high carbon and low ash content. The optimal technological parameters for obtaining carbon sorbents from screenings of coke production at a laboratory facility (temperature 850 °C and activation time 2 hours) were established. The conditions for coke breeze activation and characteristics (combustion loss, ash content, bulk density, total pore volume in water, and activity in terms of iodine and methylene blue) of the obtained sorbent were determined.

Acknowledgements

References

1   Ali I. Low cost adsorbents for the removal of organic pollutants from wastewater / I. Ali, M. Asim, T.A. Khan. // Journal of Environmental Management. — 2012. — Vol. 113. — P. 170–183. https://doi.org/10.1016/j.jenvman.2012.08.028

2   Gisi S.D. Characteristics and adsorption capacities of low-cost sorbents for wastewater treatment: A review / S.D. Gisi, G. Lofrano, M.C. Grassi, M. Notarnicola // Sustainable Materials and Technologies. — 2016. — Vol. 9. — P. 10–40. https://doi.org/10.1016/j.susmat.2016.06.002

3   Simate G.S. Coal-based adsorbents for water and wastewater treatment / G.S. Simate, N. Maledi, A. Ochieng, S. Ndlovu, J. Zhang, L.F. Walubita // Journal of Environmental Chemical Engineering. — 2016. — Vol. 4, No. 2. — P. 2291–2312. https://doi.org/10.1016/j.jece.2016.03.051

4   Еремин И.В. Марочный состав углей и их рациональное использование / И.В. Еремин, Т.М. Броновец. — М.: Недра, 1994. — 268 с.

5   Камнева А.И. Химия горючих ископаемых / А.И. Камнева. — М.: Химия, 1974. — 271 с.

6   Штах Э. Петрология углей / Э. Штах, М.Т. Маковский, М. Тейхмоллер. — М.: Мир, 1973. — С. 54–96.

7   Кельцев Н.В. Основы адсорбционной техники / Н.В. Кельцев. — М.: Химия, 1984. — 592 с.

8   Хабибуллин Е.Р. Комплексное исследование каменных углей Кузбасса ряда метаморфизма / Е.Р. Хабибуллин, З.Р. Исмагилов, Н.В. Журавлева, С.А. Созинов, С.Ю. Лырщиков, Р.И. Фурега, Л.М. Хицова, Р.Р. Потокина // VII Междунар. Рос.-Казахстан. симпоз. «Углехимия и экология Кузбасса». — Кемерово: ФИЦ УУХ СО РАН, 2018. — С. 99.

9   Ермагамбет Б.Т. Электрофизические свойства и теплоемкость сланца Кендырлыкского месторождения / Б.Т. Ермагамбет, Б.К. Касенов, Н.У. Нургалиев, М.А. Набиев, Ж.М. Касенова, М.К. Казанкапова, А.М. Зикирина // Химия твердого топлива. — 2018. — № 1. — С. 68–72. https://doi.org/10.7868/S0023117718010127

10 Ермагамбет Б.Т. Получение адсорбента из горючего сланца Кендырлыкского месторождения / Б.Т. Ермагамбет, Б.К. Касенов, Н.У. Нургалиев, М.К. Казанкапова, Ж.М. Касенова, А.М. Зикирина // Химия твердого топлива. — 2018. — № 5. — С. 27–32. https://doi.org/10.1134/S0023117718050043

11 Берлинтейгер Е.С. Изучение основных видов загрянений водных ресурсов Кузбасса / Е.С. Берлинтейгер // Междунар. журн. прикл. фунд. исслед. — 2013. — № 11–1. — С. 55.

12 Wang Guofa. Intelligent and ecological coal mining as well as clean utilization technology in China: Review and prospects / Wang Guofa, Xu Yongxiang, Ren Huaiwei // International Journal of Mining Science and Technology. — 2018. — Vol. 9. — P. 54–62. https://doi.org/10.1016/j.ijmst.2018.06.005

13 Ермагамбет Б.Т. Электрофизические свойства и теплоемкость пористо-углеродного материала из угля Майкубенского бассейна / Б.Т. Ермагамбет, Б.К. Касенов, М.К. Казанкапова, Н.У. Нургалиев, Ж.М. Касенова, Е.Е. Куанышбеков, А.Т. Наурызбаева // Химия твердого топлива. — 2020. — № 3. — С. 61–67. https://doi.org/10.31857/S0023117720030032

14 Singh K. Biofiltration of toluene using wood charcoal as the biofilter media / Singh K., Singh R.S., Rai B.N. and Upadhyay S.N. // Bioresource Technology. — 2010. — Vol. 101, No. 11. — P. 3947–3951. https://doi.org/10.1016/ j.biortech.2010.01.025

15 Mathur A.K. Combined removal of BTEX in air steam by using mixture of sugar cane bagasse, compost and GAC as biofilter media / A.K. Mathur, C.B. Majumber, S. Chatterjee // Journal of Hazardous Materials. — 2007. — Vol. 148, No. 1–2. — P. 64–74. https://doi.org/10.1016/j.jhazmat.2007.02.030

16 Farhadian M. In situ bioremediation of monoaromatic pollutants in groundwater: a review / M. Farhadian, C. Vachelard, D. Duchez, C. Larroche // Bioresource Technology. — 2008. — Vol. 99, No. 13. — P. 5296–5308. https://doi.org/10.1016/j.colsurfa.2009.10.025

17 Su F. Adsorption of benzene, toluene, ethylbenzene and pxylene by NaOCl — oxidized carbon nanotubes / Su F., Lu C., and Hu S. // Colloids and Surfaces A. — 2010. — Vol. 353, No. 1. — P. 83–91. https://doi.org/10.1016/j.colsurfa.2009.10.025

18 Nourmoradi H. Removal of benzene, toluene, ethylbenzene and xylene (BTEX) from aqueous solutions by montmorillonite modified with nonionic surfactant: equilibrium, kinetic and thermodynamic study / Nourmoradi H., Nikaeen M. and Nejad M.H. // Chemical Engineering Journal. — 2012. — Vol. 191. — P. 341–348. https://doi.org/10.1016/j.cej.2012.03.029

19 Yang C. nBiomass accumulation and control strategies in gas biofiltration / Yang C., Chen H., Zeng G., Yu G. and Luo S. // Biotechnology Advances. — 2010. — Vol. 28, No. 4. — P. 531–540. https://doi.org/10.1016/j.biotechadv.2010.04.002

20 Pei J. Determination of adsorption isotherm and diffusion coefficient of toluene on activated carbon at low concentrations / Pei J. and Zhang J.S. // Building and Environment. — 2012. — Vol. 48. — P. 66–76. https://doi.org/10.1016/j.buildenv.2011.08.005

21 Kim K.D., Effect of thin hydrophobic films for toluene adsorption and desorption behavior on activated carbon fiber under dry and humid conditions / Kim K. D., Park E. J., Seo H. O., Jeong M.G., Kim Y.D. and Lim D.C. // Chemical Engineering Journal. — 2012. — Vol. 200–202. — P. 133–139. https://doi.org/10.1016/j.cej.2012.06.044

22 Тамаркина Ю.В. Адсорбция фенола активированными углями на основе ископаемых углей разной степени метаморфизма / Ю.В. Тамаркина, В.Н. Анищенко, А.Н. Редько, В.А. Кучеренко // Химия твердого топлива. — 2021. — № 3. — С. 3–11. https://doi.org/10.31857/S0023117721030105

23 Акегян Т.А. Основы теории ошибок / Т.А. Акегян. — М.: Наука, 1972. — 170 с.

24 Гордон А. Спутник химика / А. Гордон, Р. Форд. — М.: Наука, 1976. — 541 с.

25 Колышкин Д.А. Активные угли. Свойства и методы испытаний / Д.А. Колышкин, К.К. Михайлова. — М.: Химия, 1972. — С. 52–54.

26 Кинле Х. Активные угли и их промышленное применение / Х. Кинле, Э. Бадер. — Л.: Химия, 1984. — 216 с.

27 МРТУ № 6-16-1003-67. Активные угли. Методы испытаний. Метод определения сорбционной активности по йоду.

28 ГОСТ 4453-74. Уголь активный осветляющий древесный порошкообразный. Технические условия. — Взамен ГОСТа 4453-48; Введ. с 01.01.76 г. по 01.01.96 г. — М.: Изд-во стандартов, 1993. — 23 с.

З.М. Молдахметов, А.Т. Ордабаева, М.Г. Мейрамов, А.М. Ғазалиев,
Ж.С. Шайкенова, Г.К. Мұқышева, Т.С. Животова

«Евромет» ЖШС кокс ұнтағынан көміртекті сорбент алу

Мақалада құрамында көміртегі жоғары, ұшпа және күлділігі төмен көміртекті материал болып табылатын «Евромет» ЖШС (Қарағанды қ.) кокс ұнтағы үлгісінің физика-химиялық талдау нәтижелері келтірілген. Көміртекті сорбенттер Қарағанды облысының коксхимия өндірісінің карбонизацияланған материалдарының аз ликвидті фракцияларынан бу-газды активтендіру әдісімен алынды. Қалдықтарды пайдаланудың маңызды артықшылығы (ұсақтауға және 2–5 мм-ге дейін фракциялауға ұшыраған 0–10 мм класты кокс ұсақтары) технологиялық процестен экологиялық зиянды заттардың көп мөлшері (фенолдар, крезолдар, газтәрізді шығарындылар және т.б.) шығарылатын карбонизацияның энергияны ысырап ететін сатысын алып тастау болып табылады. Аз ликвидті кокс ұнтағынан сорбент алудың оңтайлы шарттары активтендіру уақыты 2 сағат болған кезде 850 °C температура болып табылады. Көміртегі сорбенттерінің физика-химиялық қасиеттері

(күлділігі, үйінділік тығыздығы, йод және көк метилен бойынша сорбциялық сыйымдылығы, су бойынша кеуектердің жиынтық көлемі) анықталды.

Кілт сөздер: коксты ұсақ-түйек, көмір, сорбенттер, активтендіру, сорбциялық сыйымдылық, күлділік, күйдіру, үйінділік тығыздығы.

З.М. Мулдахметов, А.Т. Ордабаева, М.Г. Мейрамов, А.М. Газалиев, Ж.С. Шайкенова, Г.К. Мукушева, Т.С. Животова

Получение углеродного сорбента из коксовой мелочи ТОО «Евромет»

В статье приведены результаты физико-химического анализа образца коксовой мелочи ТОО «Евромет» (г. Караганда), представляющего собой углеродистый материал с высоким содержанием углерода, отсутствием летучих веществ и низкой зольностью. Углеродные сорбенты были получены из малоликвидных фракций карбонизованных материалов коксохимического производства Карагандинской области методом парогазовой активации. Важным преимуществом использования отсевов (коксовая мелочь класса 0–10 мм, которая подвергалась дроблению и фракционированию до крупности 2–5 мм) является исключение из технологического процесса энергозатратной стадии карбонизации, при которой выделяется большое количество экологически вредных веществ (фенолы, крезолы, газообразные выбросы и т.д.). Оптимальным условием получения сорбента из малоликвидной коксовой мелочи является температура 850^{0}С при времени активации 2 ч. Определены физико-химические свойства (зольность, насыпная плотность, сорбционная емкость по йоду и по метиленовому голубому, суммарный объем пор по воде) углеродных сорбентов.

Ключевые слова: коксовая мелочь, угли, сорбенты, активация, сорбционная емкость, зольность, обгар, насыпная плотность.

References

1   Ali, I., Asim, M., & Khan, T.A. (2012). Low cost adsorbents for the removal of organic pollutants from wastewater. *Journal of Environmental Management*, 113, 170–183. https://doi.org/10.1016/j.jenvman.2012.08.028

2   Gisi, S.D., Lofrano, G., Grassi, M.C., & Notarnicola, M. (2016). Characteristics and adsorption capacities of low-cost sorbents for wastewater treatment: A review. *Sustainable Materials and Technologies*, 9, 10–40. https://doi.org/10.1016/j.susmat.2016.06.002

3   Simate, G.S., Maledi, N., Ochieng, A., Ndlovu, S., Zhang, J., & Walubita, L.F. (2016). Coal-based adsorbents for water and wastewater treatment. *Journal of Environmental Chemical Engineering, 4(2)*, 2291–2312. https://doi.org/10.1016/j.jece.2016.03.051

4   Yeremin, I.V., & Bronovets, T.M. (1994). Marochnyi sostav uglei i ikh ratsionalnoe ispolzovanie [Grade composition of coals and their rational use]. Moscow: Nedra [in Russian].

5   Kamneva, A.I. (1974). Khimiia goriuchikh iskopaemykh [Chemistry of fossil fuels]. Moscow: Khimiia [in Russian].

6   Shtakh, E., Makovsky, M.T., & Teykhmollerr, M. (1973). Petrologiia uglei [Petrology of coals]. Moscow: Mir [in Russian].

7   Keltsev, N.V. (1984). Osnovy adsorbtsionnoi tekhniki [Fundamentals of adsorption technology]. Moscow: Khimiia [in Russian].

8   Xabibullin, E.R., Ismagilov, Z.R., Zhuravleva, N.V., Sozinov, S.A., Ly`rshhikov, S.Yu., Furega,, R.I., Xiczova, L.M., & Potokina, R.R. (2018). Kompleksnoe issledovanie kamennykh uglei Kuzbassa riada metamorfizma [Comprehensive study of coals of Kuzbass of a series of metamorphism]. "Carbon chemistry and ecology of the Kuzbass": VII Mezhdunarodnyi Rossiisko-Kazakhstanskii simpozium – 7th International Russia and Kazakhstan symposium. Kemerovo: Federalnyi issledovatelskii tsentr uglia i uglekhimii Sibirskogo otdeleniia rossiiskoi akademii nauk [in Russian].

9   Ermagambet, B.T., Kasenov, B.K., Nurgaliev, N.U., Nabiev, M.A., Kasenova, Zh.M., Kazankapova, M.K., & Zikirina, A.M. (2018). Elektrofizicheskie svoistva i teploemkost slantsa Kendyrlykskogo mestorozhdeniia [Electrophysical properties and heat capacity of shale from the Kendyrlyk deposit]. *Khimiia tverdogo topliva – Solid Fuel Chemistry*, 1, 68–72 [in Russian]. https://doi.org/10.7868/S0023117718010127

10 Ermagambet, B.T., Kasenov, B.K., Nurgaliev, N.U., Kazankapova, M.K., Kasenova, Zh.M., & Zikirina, A.M. (2018). Poluchenie adsorbenta iz goriuchego slantsa Kendyrlykskogo mestorozhdeniia [Obtaining an adsorbent from oil shale of the Kendyrlyk deposit]. *Khimiia tverdogo topliva – Solid Fuel Chemistry*, 5, 27–32 [in Russian]. https://doi.org/10.1134/S0023117718050043

11 Berlinteyger, Ye.S. (2013). Izuchenie osnovnykh vidov zagrianenii vodnykh resursov Kuzbassa [A study of the main types of pollution of water resources in Kuzbass]. *Mezhdunarodnyi zhurnal prikladnykh i fundamentalnykh issledovanii – International Journal of Applied and Fundamental Research, 11–1*, 55 [in Russian].

12 Wang, G., Xu, Y., & Huaiwei, R. (2018). Intelligent and ecological coal mining as well as clean utilization technology in China: Review and prospects. *International Journal of Mining Science and Technology*, (9), 54–62. https://doi.org/10.1016/j.ijmst.2018.06.005

13 Ermagambet, B.T., Kasenov, B.K., Kazankapova, M.K., Nurgaliev, N.U., Kasenova, Zh.M., Kuanyshbekov, E.E., & Nauryzbaeva, A.T. (2020). Elektrofizicheskie svoistva i teploemkost poristo-uglerodnogo materiala iz uglia Maikubenskogo basseina

[Electrophysical properties and heat capacity of porous carbon material from the Maikuben coal basin]. *Khimiia tverdogo topliva – Solid Fuel Chemistry,* 3, 61–67 [in Russian]. https://doi.org/10.31857/S0023117720030032

14 Singh, K., Singh, R.S., Rai, B.N., & Upadhyay, S.N. (2010). Biofiltration of toluene using wood charcoal as the biofilter media. *Bioresource Technology,* 101(11), 3947–3951. https://doi.org/10.1016/j.biortech.2010.01.025

15 Mathur, A.K., Majumber, C.B., & Chatterjee, S. (2007). Combined removal of BTEX in air steam by using mixture of sugar cane bagasse, compost and GAC as biofilter media. *Journal of Hazardous Materials. 148(1-2),* 64–74. https://doi.org/10.1016/j.jhazmat.2007.02.030

16 Farhadian, M., Vachelard, C., Duchez, D., & Larroche, C. (2008). In situ bioremediation of monoaromatic pollutants in groundwater: a review. *Bioresource Technology,* 99(13), 5296–5308. https://doi.org/10.1016/j.colsurfa.2009.10.025

17 Su, F., Lu C., & Hu, S. (2010). Adsorption of benzene, toluene, ethylbenzene and pxylene by NaOCl — oxidized carbon nanotubes. *Colloids and Surfaces A.* 353(1), 83–91. https://doi.org/10.1016/j.colsurfa.2009.10.025

18 Nourmoradi, H., Nikaeen, M., & Nejad, M.H. (2012). Removal of benzene, toluene, ethylbenzene and xylene (BTEX) from aqueous solutions by montmorillonite modified with nonionic surfactant: equilibrium, kinetic and thermodynamic study. *Chemical Engineering Journal,* (191), 341–348. https://doi.org/10.1016/j.cej.2012.03.029

19 Yang, C., Chen, H., Zeng, G., Yu, G., & Luo, S. (2010). Biomass accumulation and control strategies in gas biofiltration. *Biotechnology Advances, 28(4),* 531–540. https://doi.org/10.1016/j.biotechadv.2010.04.002

20 Pei, J. & Zhang, J.S. (2012). Determination of adsorption isotherm and diffusion coefficient of toluene on activated carbon at low concentrations. *Building and Environment,* 48(66–76). https://doi.org/10.1016/j.buildenv.2011.08.005

21 Kim, K.D., Park, E.J., Seo, H.O., Jeong, M.G., Kim, Y.D., & Lim, D.C. (2012). Effect of thin hydrophobic films for toluene adsorption and desorption behavior on activated carbon fiber under dry and humid conditions. *Chemical Engineering Journal,* 200–202, 133–139. https://doi.org/10.1016/j.cej.2012.06.044

22 Tamarkina, Yu.V., Anishhenko, V.N., Redko, A.N., & Kucherenko, V.A. (2021). Adsorbtsiia fenola aktivirovannymi ugliami na osnove iskopaemykh uglei raznoi stepeni metamorfizma [Adsorption of phenol by activated carbons based on fossil coals of varying degrees of metamorphism]. *Khimiia tverdogo topliva – Solid Fuel Chemistry*, 3, 3–11 [in Russian]. https://doi.org/10.31857/S0023117721030105

23 Akegyan, T.A. (1972). Osnovy teorii oshibok [Fundamentals of error theory]. Moscow: Nauka [in Russian].

24 Gordon, A., & Ford, R. (1976). Sputnik khimika [Chemist's companion]. Moscow: Nauka [in Russian].

25 Kolyshkin, D.A., & Mikhaylova, K.K. (1972). Aktivnyye ugli. Svoistva i metody ispytanii [Active carbons. Properties and test methods]. Moscow: Khimiia [in Russian].

26 Kinle, K.H., & Bader, E. (1984). Aktivnyye ugli i ikh promyshlennoe primenenie [Active coals and their industrial application]. Leningrad: Khimiia [in Russian].

27 MRTU № 6–16–1003–67. (1967). Aktivnye ugli. Metody ispytanii. Metod opredeleniia sorbtsionnoi aktivnosti po iodu [Active coals. Test methods. Method for determination of sorption activity by iodine] [in Russian].

28 GOST 4453–74. (1993). Ugol aktivnyi osvetliaiushchii drevesnyi poroshkoobraznyi. Tekhnicheskie usloviia [Charcoal active brightening wood powder. Specifications]. Vzamen GOSTa 4453–48; Vveden s 01.01.76 g. po 01.01.96 g.. Moscow: Izdatelstvo standartov, 23. [in Russian].

Information about authors*

Muldakhmetov, Zeynulla Muldakhmetovich — Doctor of Chemical Sciences, Academician, Director of the Institute of Organic Synthesis and Coal Chemistry of the Republic of Kazakhstan, Alikhanov str. 1, 100008, Karaganda, Kazakhstan; e-mail: zmm_ioscc@mail.ru; https://orcid.org/0000-0001-9497-2545;

Ordabaeva, Aigul Tanirbergenovna — Candidate of Chemical Sciences, Head of the Laboratory of Coal Chemistry, Institute of Organic Synthesis and Coal Chemistry of the Republic of Kazakhstan, Alikhanov str. 1, 100008, Karaganda, Kazakhstan; e-mail: aigul_serik_kz@mail.ru; https://orcid.org/0000-0002-4413-1163;

Meiramov, Mazhit Gabdullovich — Candidate of Chemical Sciences, Institute of Organic Synthesis and Coal Chemistry of the Republic of Kazakhstan, Alikhanov str. 1, 100008, Karaganda, Kazakhstan; e-mail: majit_m@mail.ru; https://orcid.org/0000-0003-2498-6516;

Gazaliev, Arstan Maulenovich — Doctor of Chemical Sciences, Academician, Deputy Director for Science of the Institute of Organic Synthesis and Coal Chemistry of the Republic of Kazakhstan, Alikhanov str. 1, 100008, Karaganda, Kazakhstan; e-mail: gazaliyev51@mail.ru; https://orcid.org/0000-0003-2161-0329;

Shaikenova, Zhazira Sergalievna — Researcher, Master of Biological Sciences, Institute of Organic Synthesis and Coal Chemistry of the Republic of Kazakhstan, Alikhanov str. 1, 100008, Karaganda, Kazakhstan; e-mail: plant-2019@mail.ru; https://orcid.org/0000-0001-8440-6056;

Mukusheva, Gulim Kenesbekovna — Candidate of Chemical Sciences, Associate Professor, Karaganda University of the name of academician E.A. Buketov, Universitetskaya str., 28, 100024, Karaganda, Kazakhstan; e-mail: mukusheva1977@list.ru; https://orcid.org/0000-0001-6706-4816;

Zhivotova, Tatyana Sergeevna — Doctor of Chemical Sciences, Chief Scientific Secretary of the Institute of Organic Synthesis and Coal Chemistry of the Republic of Kazakhstan, Alikhanov str. 1, 100008, Karaganda, Kazakhstan; e-mail: zhts2004@mail.ru; https://orcid.org/0000-0002-0793-4653

_____

*The author's name is presented in the order: *Last Name, First and Middle Names*

V.M. Skachkov[*], L.A. Pasechnik, I.S. Medyankina, S.A. Bibanaeva, N.A. Sabirzyanov

Institute of Solid State Chemistry of the Ural Branch of RAS, Ekaterinburg, Russia
(*Corresponding author's e-mail: skachkov@ihim.uran.ru)

Improvement of Extraction Technology and Electrotechnological Equipment for Obtaining Gallium from Alumina Production Solutions

High-purity gallium, not worse than 6N, with the concentration of controlled impurities (except H, C, N, O) of maximum 0.00007, including, wt.%·10^{-8}: Fe — 2, Cu — 5, Pb — 4, Mn — 1, In — 2, and Sn — 2.5 was produced by electrolysis of preliminarily purified aluminate solutions of alumina production. An improved design of electrolyzer with increased efficiency has been developed for gallium electroextraction. It was proposed to divide the casing of the advanced-efficiency electrolyzer by longitudinal partitions into two parts, each of which was divided by transverse partitions into 8 sections. The width of these sections was one-third smaller than that of available electrolyzers. The dimensions of the sections and the arrangement of electrodes in them were reduced by half, from 140 to 70 mm — a distance covered by gallate and zincate ions from electrolyte depth to cathodes, which decreased the duration of electrolysis. The optimal current density of 7.5 kA/m^3 at the calculated density of 5.8 kA/m^3 was proposed, which allowed electrical energy consumption to be reduced. The polarization component of voltage on the electrolyzer was decreased by lowering the average current density achieved by a three-fold enhancement of the anode surface. The technological order of seven sequential operations of metallic gallium extraction from cycling aluminate solutions is shown: 1) purification of electrolyte by an air or vapor-air mixture; 2) purification of solution by lime; 3) galvanization of cathodes and dissolution of cathode precipitate; 4) purifying electrolysis; 5) basic electrolysis with precipitation of zinc-gallium alloy; 6) cementation of gallium by aluminum gallam; 7) removal of impurities. Preliminary purification of gallate-zincate alkaline solution allows decreasing the granular aluminum consumption to the weight ratio Al : Ga = 1 : 1 during gallium cementation.

Keywords: gallium, electrolysis, aluminate solution, solution purification, alumina production, interelectrode distance.

Introduction

Gallium is a dispersed metal, contained in small concentrations in non-ferrous metal ores. In the world, gallium is obtained mainly as a by-product during the processing of bauxite, the basic technological scheme of the Bayer process is shown in Figure 1, where the source of gallium is recycled solutions of alumina production.
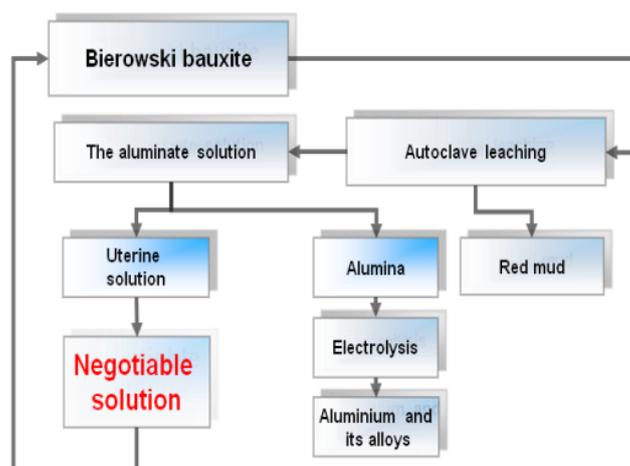

Figure 1. Schematic diagram of bauxite processing by the Bayer method

---

The main field of application of gallium is the electronic industry. LEDs, solar panels, smartphones "eat up" much more than half of the gallium produced, about 6 % goes to alloys, the most important use of gallium is the synthesis of compounds of the $A^{III}B^{V}$ type (GaN, GaP, GaAs, GaSb) — basic materials for modern opto- and microelectronics. The main producer of gallium is China and it continues to increase production, despite the fall in metal prices [1, 2], and subsequently came close to becoming a global monopolist, because the output of primary gallium in China this year amounted to 90 % of the world [3, 4]. The CIS countries, on the contrary, reduce the production of gallium. The main reason is the lack of demand in the Russian Federation due to absence of factories for the production of LEDs, semiconductors, etc. However, according to Rusnano, there are potential producers and consumers of semiconductors [5]. Gallium arsenide can rightfully be considered the engine of progress in the field of electronics [6], and the rise to the modern level of industrial production of semiconductor materials will contribute to solving the problems facing the country [7].

This may require developing a theoretical and practical implementation of various methods for obtaining gallium based on various sources and by various physicochemical methods [8–11]. There are several methods for obtaining gallium from alkaline aluminate solutions of alumina production [12, 13], but the most effective is electrolytic extraction [14–20]. However, electroextraction of gallium from solutions that have not undergone preliminary preparation will not provide serious extraction, productivity, cost reduction and reliable release of high purity metal (6N). This is largely due to the change in the composition of bauxite extracted from the new mine to SUBR-e (for the plant of JSC "BAZ-SUAL") and the transfer of JSC "UAZ-SUAL" to 100 % use of bauxite from the STBR deposits. The conducted studies found that the indicators of JSC "BAZ-SUAL" deteriorated: the concentration of gallium in the electrolyte decreased from 0.36 to 0.33 kg/m^3 — by 10 %, and the extraction of gallium by electrolysis lessened by 5 %, the purity of gallium deteriorated to 5N, the indicators of JSC "UAZ-SUAL" deteriorated significantly more, for example, the purity of gallium reduced to 4N. A significant change in the impurity composition of the initial bauxite (for the plant of JSC "BAZ-SUAL" and to a lesser extent for JSC "UAZ-SUAL"), caused by the launch of a new mine at the SUBR, required a more thorough cleaning of the initial electrolyte. These changes require technological improvements, first of all, to improve the purification of the initial electrolyte, which will increase the extraction of gallium, reduce the time of operations and increase the number of gallium concentration cycles to increase its release.

The purpose of this work was to improve the technological scheme for the extraction of gallium from alumina solutions, which will allow the production of high-purity metal gallium (6N), suitable for semiconductor production (Fig. 2).
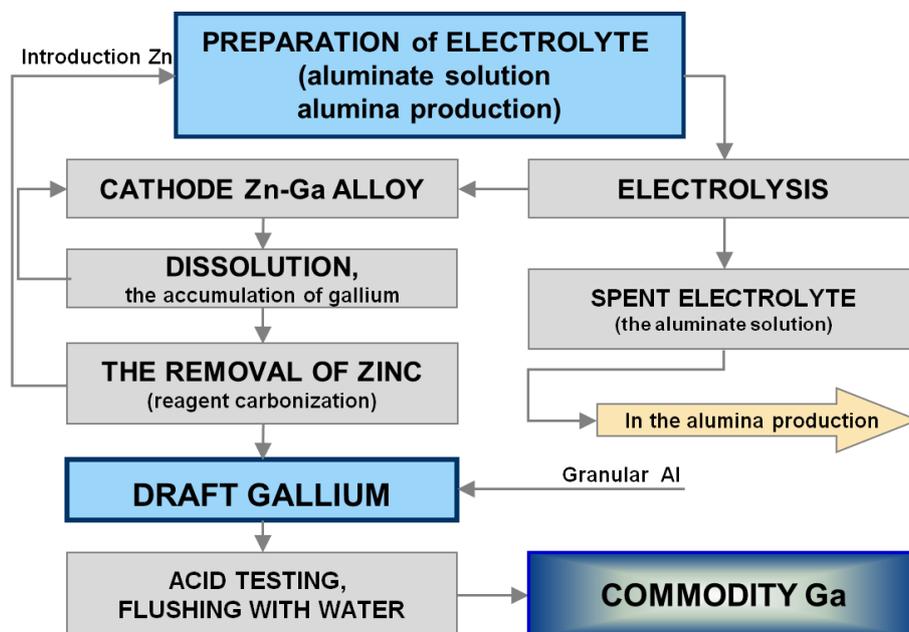

Figure 2. Technological scheme for obtaining gallium from aluminate solutions

Experimental

The separation of gallium from aluminate solutions was performed via the electrochemical method using an electrolytic bath made of stainless steel 1X18H9T with external water cooling (Fig. 3), a cathode made of the same stainless steel and two nickel anodes. Nickel prolongs anode lifespan by 2–2.5 times due to a decrease in the anode potential by ~0.2 V, and the thiosulfate ion is reduced to sulfur on the nickel anode, forming a protective layer of NiS. Direct current was supplied from the T1021 charger through a laboratory rheostat and an ammeter.

Figure 3. Water-cooled electrolyzer for laboratory extraction of gallium from alkaline-aluminate solutions

The studies were carried out on solutions of alumina production of JSC "UAZ-SUAL" and JSC "AZ-SUAL". The results are presented by average values considering previous production experience.

The probable discharge mechanism during gallium electrodeposition can be represented as follows [21]:

$$[H_2GaO_3]^- + \bar{e} \rightarrow [HGaO_2]^- + OH^-$$

$$2[HGaO_2]^- + H_2O + \bar{e} \rightarrow Ga° + [H_2GaO_3]^- + 2OH^-$$
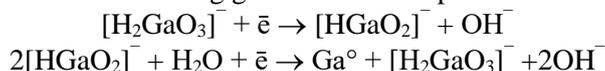
standard electrode potential in acidic solution of gallium salts (Ga/Ga^{3+}): –0.56 V, in alkaline solution: –1.226 V.

The chemical composition of the starting materials and products was monitored on an inductively coupled plasma mass spectrometer ELAN 9000, Perkin Elmer.

Results and Discussion

1. Comparison of electrolyte purification by air and steam-air mixture by bubbling hot solution

The initial mixture is prepared: 150 m³ of circulating solution (Table 1, p. 1), cooled to 30±5 °C and aged for at least a day in the reactor for the separation of soda-sulfate sludge, and 133 m3 of the mother (Table 1, p. 2) solution (volume ratio 1:0.887), this mixture of solutions is heated to a temperature of 85–90 °C and treated with a vapor-air mixture in the amount of 0.3–0.4 nm³/hour per 1 m³ for 2.0–2.5 hours with a ratio of air and steam volumes = 1.0 : 2.5 with a steady temperature at the outlet of the nozzle 250 °C. As a result, according to the analysis data, the content of organic substances decreases by 25–31 %, sulfide sulfur by 95 %, which is mainly oxidized into sulfate form (Table 1, p. 4). In comparison to the Chinese electrolyte processing method that uses only air and no steam, the operation time was reduced. Since aluminate solutions no longer require the introduction of sodium sulfide (up to 0.20 kg/m³, counting for sulfur), the corrosion of the equipment has decreased, a better removal of zinc (less than 0.010 kg/m³) and organic substances from solution was achieved.

2. Cleaning the solution with lime (consumption of 0.5 mol of CaO per mol of alumina in solution)

Lime milk (composition of 56 kg of CaO$_{act.}$ and 18 kg of water) is fed into the solution at a temperature of 80–90 °C with stirring for 1.5 hours. The precipitate is filtered out at a temperature of 70 °C to remove tricalcium hydroaluminate, on which iron, manganese, vanadium compounds and up to 25–30 % of organic

substances are sorbed (Table 1, p. 5). The precipitate is returned to alumina production. Reducing the content of impurities during lime cleaning: vanadium by 30 times (up to 0.01 kg/m^3), iron by 3 times (up to 0.002 kg/m^3), manganese is completely removed (Table 1, p. 5).

T a b l e 1

Compositions of solutions: alumina production (circulating (1), masterbatch (2), mixed (3), their double purification with a vapor-air mixture (4) and lime (5), synthetic alkali-zinc (6), purification electrolysis (7), initial and final (spent) electrolytes (8, 9), during carburization of the initial (10) and final (11), processing of slags of the initial (12) and final (13)

Components	Name (numbering) and compositions of solutions, kg/m^3												
	1	2	3	4	5	6	7	8	9	10	11	12	13
Na$_2$O$_{com.}$	314	157	240	230	235	220	210	233	235	105	103	170	168
Na$_2$O$_{caustic}$	290	145	222	220	231	200	200	230	232	100	100	165	165
Na$_2$O$_{soda.}$	24	12	18	18	4	20	10	3	3	3	4	5	4
Al$_2$O$_3$	138	69	106	105	87,5	–	87,0	87,0	88,0	50	63	4,2	4,3
Ga	0,46	0,23	0,35	0,34	0,33	–	0,34	0,34	0,18	10,2	0,25	100	100
Zn	0,06	0,03	0,04	0,004	0,004	20	0,003	0,45	0,04	3,0	0,06	2,9	1,25
S$^{2–}$	0,42	0,21	0,32	0,013	0,010	–	0,010	0,008	0,02	–	–	–	–
S$_2$O$_3^{2–}$	1,4	0,7	1,07	0,84	0,65	–	0,60	0,65	0,60	2,0	2,0	–	–
SO$_4^{2–}$	1,8	0,9	1,4	2,2	0,8	–	0,80	0,8	0,65	1,0	1,0	–	–
C$_{organic subst.}$	3,0	0,5	2,3	1,66	1,30	–	1,30	1,30	1,25	1,8	1,8	–	–
V$_2$O$_5$	0,42	0,21	0,32	0,31	0,01	–	0,08	0,01	0,005	–	–	–	–
Fe$_2$O$_3 \cdot 10^{-4}$	80	40	60	50	20	–	10	20	–	–	–	–	–
Cu 10^{-5}	13	10	12	12	10	–	1,1	1,0	6,0	10,0	1,0	12	1,0
Mn$\cdot 10^{-4}$	60	30	50	45	н/об.	–	12	–	–	–	–	–	–
Pb$\cdot 10^{-4}$	80	80	78	80	80	–	5	80	5,0	80	3,0	85	4,0

3. Galvanizing of cathodes and dissolution of cathode sediment

Before applying the zinc coating, the cathodes are cleaned by reverse current from the existing impurity sediment. To apply a zinc layer to the cathodes, a zinc solution prepared from a sodium hydroxide solution with an alkali concentration of 150–200 kg/m^3 and zinc oxide 15–20 kg/m^3 is used, followed by dilution before electrolysis with condensate to the composition, kg/m^3: sodium oxide ~125 and zinc ~12.5 (Table 1, p. 6). Electrolysis is carried out at a temperature of 45–55 °C and a volumetric current density of 4–5 kA/m^3. A layer of zinc 10–15 microns thick is increased in 12–15 minutes. This thickness of the cathode layer is sufficient for carrying out four to five operations of the main deposition of the zinc-gallium alloy and subsequent removal of the sediment after the last operation.

4. Purification electrolysis from impurities

Cleaning is carried out in a separate electrolyzer at low densities: cathode current (40–50 A/m^2), anode current densities 100–140 A/m^2 (volumetric current density 4–5 kA/m^3), temperature 60–70 °C and the voltage on the bath ~1.9 V (the bath body is also a cathode). The duration of the electrolyte cleaning operation is ~ 4-6 hours. The content of impurities during this period decreased by more than an order of magnitude, kg/m^3: copper from 0.000125 to 0.000011; lead from 0.0078 to 0.0005; iron and manganese by two to three times. The concentration of gallium in the electrolyte under the recommended electrolysis conditions practically does not decrease (Table 1 p.7). The precipitates isolated on the cathodes are dissolved in an alkaline synthetic solution at a temperature of 70–85 °C with the imposition of a reverse current. The resulting solution after settling is filtered out with the removal of impurities. The resulting purified alkaline solution is used for galvanizing the electrodes.

5. Conducting basic electrolysis with deposition of zinc-gallium alloy

Into the purified electrolyte with a content, kg/m^3: Na$_2$O$_3$ 220–230, Al$_2$O$_3$ 75–90, Ga$_2$O$_3$ 0.33–0.35 a dilute solution of zincate is introduced in an amount of ~1/30 of the volume of the initial electrolyte. As a result, the zinc content in the electrolyte reaches 0.2–0.3 kg/m^3. The electrolyte prepared and cooled to ~30 °C is poured into a water-cooled electrolyzer and electrolysis is carried out on galvanized cathodes at a volumetric current density of 6.0–6.2 kA/m^3, a process temperature of 25–30 °C and an electrolysis duration of 2.0–2.15 hours. During this time, about 43 % of gallium and at least 80 % of zinc are released (Table 1, p. 8, 9).

6. Cementation of gallium with aluminum gallam

Cementation is carried out in apparatuses with a capacity of up to 2.5 m^3 equipped with a stirrer, a device for filling granulated aluminum, level and potential sensors, a jacket for heating and the necessary hatches and pipes. For cementation, a settled filtered receiving solution, sufficiently rich in gallium (10.0 kg/m^3), and granular aluminum are used. ~2.0 m^3 of mortar and 40 kg of cement base are poured into the 2.5 m^3 cementator, aluminum is supplied according to the program with the EMF measurement of the cementation base – earth system. 97.5 % of gallium passes from the solution to the rough gallium (approximately 0.25 kg/m^3 remains in the solution) and almost all zinc (~4% remains). The consumption of aluminum is ~1.1 kg per 1 kg of isolated gallium (Table 1, p. 14, 15).

7. Removal of impurities from sludge

After dissolving the pressed sludge in a solution of sodium hydroxide (Na$_2$O — 150–200 kg/m^3), the impurities are removed by electrolysis under the following conditions: The cathode current density is 40–50 A/m^2, the anode current is 100–120 A/m^2, the volumetric current is 2–3 kA/m^3 and the process duration is up to 5 hours. The concentration of gallium ~100 kg/m^3 remains unchanged. The impurity content decreases by at least an order of magnitude (Table 1, p. 12, 13).

To organize the gallium production at alumina plants, based on existing experience, it is advisable to use the improved design of electrolyzers (Fig. 4) combined with the gallium electrolysis technology described above. The body of the electrolyzer is divided by a longitudinal partition into two parts, each of which in turn is divided by transverse partitions into 8 sections.
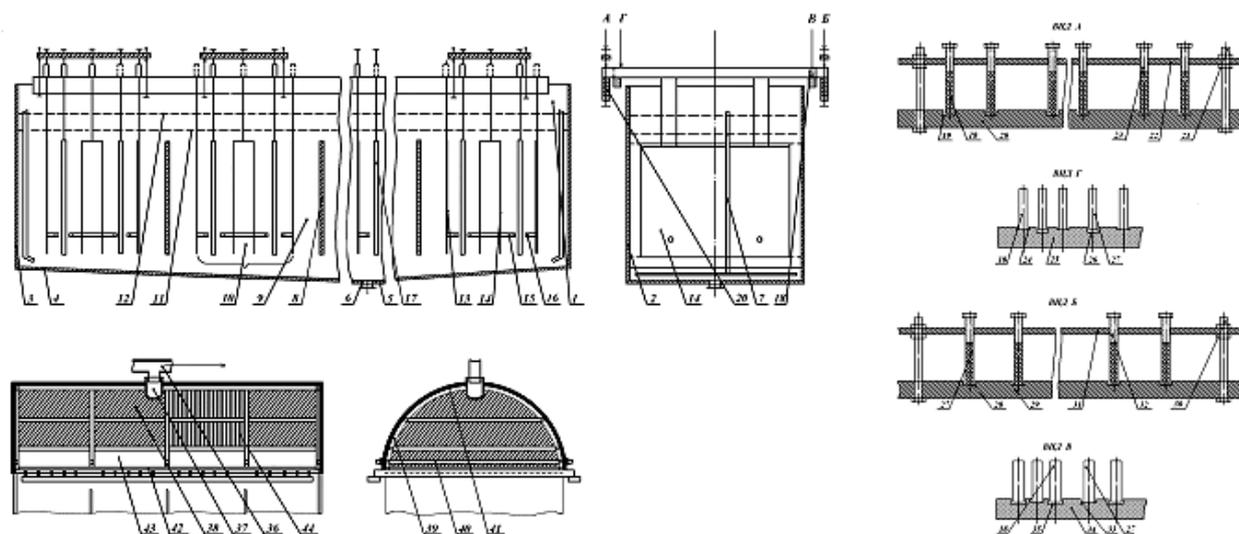
1 — steel case; *2* — the longitudinal wall; *3* — transverse, end wall; *4* — bottom; *5* — horizontal platform; *6* — drain hole; *7* — flushing device (flushing device); *8* — partition; *9* — section; *10* — a block of electrodes; *11* — electrolyte level during electrolysis; *12* — the initial level of the electrolyte; *13* — single anode; *14* — "П"-shaped anode; *15* — position lock; *16* — electrical insulation cap; *17* — box-shaped water-cooled cathode; *18* — anode rod; *19* — groove in the anode rod; *20* — anode tire; *21* — mounting bolts on the anode bus; *22* — steel plate for clamping anode rods; *23* — fixing screws for clamping anode rods; *24* — slots in the anode electrical insulation plate; *25* — anode electrical insulation plate; *26* — deep grooves in the anode electrical insulation plate; *27* — cathode rods; *28* — a groove in the cathode bus; *29* — cathode bus; *30* — mounting bolts on the cathode bus; *31* — steel plate for clamping cathode rods; *32* — fixing screws for clamping cathode rods; *33* — slots in the cathode insulating plate; *34* — cathode electrical insulation plate; *35* — deep grooves in the cathode insulating plate; *36* — exhaust ventilation; *37* — corrugated rubber pipe; *38* — the frame of the shelter; *39* — the arches of the frame; *40* — tie rods; *41* — covering the frame; *42* — horizontal support tube; *43* — an opening in the frame; *44* — sliding curtains

Figure 4. Gallium electrolyzer

The two sections are symmetrically arranged along the width of the housing, forming a compartment, where a package of electrodes is placed, divided in two along the length, and each half is connected to one copper rod resting on a conducting busbar of the corresponding polarity. The accepted dimensions of the sections and the location of the electrodes in them were reduced by 2 times, from 140 to 70 mm — the distance

that gallate and zinc ions pass from the depth of the electrolyte to the cathodes. Accordingly, the duration of electrolysis is reduced. In the space occupied by the sections, there is more than 80 % of the electrolyte with minimal gas filling, so it maintains an optimal current density of 7.5 kA/m^3 at an estimated density of 5.8 kA/m^3, which reduces electricity consumption. The polarization component of the voltage on the electrolyzer is reduced due to a reduction of the average current density achieved by a 1.5-fold increase in the surface of the anodes; a decrease in the interelectrode distance; a reduction of foaming, which increases the active component of the electrolyte resistance. As a result, the voltage on the bath is decreased by 16 %.

Conclusions

The refinement of gallate-zinc alkaline solution helps reduce the consumption of granular aluminum during carburization to a mass ratio of Al : Ga = 1 : 1. Sludge formation is also reduced. In practical terms [22], at least 2 kg of sludge is formed per 1 kg of obtained gallium, but this solution reduces the amount of sludge to 0.1 kg — twenty times less.

The gallium ingots obtained after purification using this technology have a total composition of controlled impurities (excluding impurities H, C, N, O) of no more than 0.00007, including $\% \cdot 10^{-8}$: Fe — 2, Cu — 5, Pb — 4, Mn — 1, In — 2, Sn — 2.5. The gallium content in the ingot is not less than 99.9999 %.

The effectiveness of the proposed solution has been tested on an industrial scale. The purity of gallium obtained at the industrial plant of JSC UAZ-SUAL was 5N (99.999 %), on solutions of JSC BAZ-SUAL using the proposed technology, the purity of metallic gallium was 6N (99.99995 %), produced at the plant in Ping-Guo (PRC) according to our technology (transferred under contract) also corresponds to the brand 6N.

For the production of 10 tons of gallium per year, it is technically and economically feasible to use electrolyzers developed at the IHTT of the Ural Branch of the Russian Academy of Sciences with increased productivity. It is recommended to use 10 electrolyzers of the described type for the convenience of their operation, rational organization, technological and production processes, and to create an optimal DC power supply system ensuring high energy security of the enterprise. The electrolyzers are connected in series by five in chain, forming 2 chains of gallium electrolysis; each circuit of gallium electrolyzers receives power from an individual DC converter unit; the power supply system of electrolytic gallium production should contain a third, backup converter unit; nominal output parameters of the converter unit: rectified voltage of 20 V, rectified current of 30 kA.

Acknowledgments

References

1   U.S. Geological Survey, Mineral Commodity Summaries, January 2015. 196 p. http://dx.doi.org/10.3133/70140094

2   U.S. Geological Survey, Mineral Commodity Summaries, February 2019. 200 p. https://doi.org/10.3133/70202434

3   U.S. Geological Survey, Mineral Commodity Summaries, January 2021. 200 p. https://doi.org/10.3133/mcs2021

4   U.S. Geological Survey, Mineral Commodity Summaries, January 2022. 202 p. https://doi.org/10.3133/mcs2022

5   Сетевое издание «Редкие земли / Rare Earth», Интернет ресурс: http://rareearth.ru/ru/news/20161026/02637.html

6   Baker I. Fifty Materials That Make the World / I. Baker. — Springer International Publishing AG, part of Springer Nature 2018. — P. 267–271. https://doi.org/10.1007/978-3-319-78766-4_50

7   Акчурин Р.Х. Производство полупроводниковых материалов: краткая история и современное состояние / Р.Х. Акчурин // Цветные металлы. — 2016. — № 11 (887). — С. 67–74. https://doi.org/10.17580/tsm.2016.11.07

8   Дюсенова С.Б. Комплексная гидрохимическая переработка шламовых хвостов обогащения хромитсодержащих руд / С.Б. Дюсенова, Б.К. Кенжалиев, Р.А. Абдулвалиев, С.В. Гладышев // Обогащение руд. — 2018. — № 6 (378). — С. 27–32. https://doi.org/10.17580/or.2018.06.05

9   Кольцов В.Б. Разработка технологии получения галлия полупроводниковой чистоты / В.Б. Кольцов, Н.М. Ларионов, С.А. Слесарев, Т.А.Б. Баркинкоева // Естественные и технические науки. — 2016. — № 4 (94). — С. 12–20.

10 Кольцов В.Б. Разработка технологии получения галлия высокой чистоты из отходов лантагаллиевых силикатов / В.Б. Кольцов, Е.А. Севрюкова, С.А. Слесарев // Актуальные проблемы повышения эффективности производств микроэлектроники: сб. науч. тр., под ред. В.И. Каракеяна. — М., 2016. — С. 140–145.

11 Потапов С.О. Приминение сорбционной технологии для получения галлия из гамма-Ga_2O_3 / С.О. Потапов, М.Н. Свиридова, И.Н. Танутров, Д.А. Толокнов // XX Менделеевский съезд по общей и прикладной химии: Тез. докл.: [В 5 т.]. — Уральское отд. РАН. — 2016. — Т. 3. — С. 235.

12 Дамаскин А.А. Усовершенствование технологии получения галлия из оборотных растворов глиноземного производства / А.А. Дамаскин, М.Н. Печенкин, В.Г. Кравченко, Е.В. Ковалев / В сб. Цветные металлы и минералы — 2017: сб. докл. Девятого междунар. конгр. — 2017. — С. 136–143.

13 Абдулвалиев Р.А. Электрохимическое извлечение галлия из щелочных растворов способом электролиза / Р.А. Абдулвалиев, Ата Акчил, Н.К. Ахмадиева, С.В. Гладышев, К.О. Бейсембекова // Комплексное использование минерального сырья. — 2016. — № 2 (297). — С. 76–82.

14 Копырин В.С. Энергоэффективная технология электролиза галлия из растворов глиноземного производства и электрооборудование / В.С. Копырин, Г.М. Рубинштейн, С.П. Яценко / Сб. докл. 3-й Междунар. науч.-практ. конф. «Эффективное и качественное снабжение и использование электроэнергии». — Екатеринбург: УрФУ, 2013. — С. 110–115.

15 Рубинштейн Г.М. Совершенствование технологии и электротехнологического оборудования электролиза галлия из растворов глиноземного производства / Г.М. Рубинштейн, С.П. Яценко, В.М. Скачков, В.С. Копырин / Сб. докл. 4-й Междунар. науч.-практ. конференции «Эффективное и качественное снабжение и использование электроэнергии». — Екатеринбург: УрФУ, 2015. — С. 102–105.

16 Рубинштейн Г.М. Извлечение галлия из щелочных растворов глиноземного производства / Г.М. Рубинштейн, Л.А. Пасечник, С.П. Яценко, И.Н. Пягай // Цветные металлы. — 2014. — № 3. — С. 37–43.

17 Skachkov V.M. Electrolytic recovery of gallium from alkali aluminate bayer process solutions / V.M. Skachkov, G.M. Rubinshtein, V.T. Surikov, I.S. Medyankina, L.A. Pasechnik, N.A. Sabirzyanov // Theoretical Foundations of Chemical Engineering. — 2017. — Vol. 51, No. 4. — P. 580–586. DOI: 10.1134/S0040579517040133

18 Полезная модель 14214 (РФ). Электролизер получения галлия. Опубл. БИ. — 2000. — № 19 / Школьников Р.М., Шаблаков В.С., Садовников В.Б., Кузнецов А.В., Рубинштейн Г.М., Яценко С.П.

19 Полезная модель 106248 (РФ). Электролизер для извлечения галлия из щелочно-алюминатных растворов процесса Байера. Опубл. БИ. — 2011. — № 19 / Рубинштейн Г.М., Яценко С.П., Сабирзянов Н.А.

20 Полезная модель 147934 (РФ). Электролизер для извлечения галлия из щелочно-алюминатных растворов процесса Байера. Опубл. БИ. — 2014. — № 45. Рубинштейн Г.М., Яценко С.П., Скачков В.М.

21 Яценко С.П. Галлий: Технологии получения и применение жидких сплавов: моногр. / С.П. Яценко, Л.А. Пасечник, В.М. Скачков, Г.М. Рубинштейн. — М.: РАН, 2020. — 344 с.

22 Патент РФ № 2553318. Способ получения галлия из щелочно-алюминатных растворов глиноземного производства. Опубл. БИ. — 2015. — № 16 / Рубинштейн Г.М., Яценко С.П., Скачков В.М., Лудская Л.П., Устич Е.П., Вайлерт А.В.

В.М. Скачков, Л.А. Пасечник, И.С. Медянкина, С.А. Бибанаева, Н.А. Сабирзянов

Жербалшық өндірісінің ерітінділерінен галлий алу үшін экстракция технологиясын және электротехнологиялық жабдықты жетілдіру

Жербалшық өндірісіне алдын ала тазартылған алюминатты ерітінділерді электролиздеу әдісімен тазалығы жоғары галлий алынды, 6н төмен емес, бақыланатын қоспалардың құрамы (H, C, N, O қоспаларын қоспағанда) 0,00007-ден аспайды, оның ішінде массалар %·10^{-8}: Fe — 2, Cu — 5, Pb — 4, Mn — 1, In — 2, Sn — 2,5. Галлийді электроэкстракциялау үшін өнімділігі жоғары электролизердің жетілдірілген конструкциясы жасалды, өнімділігі жоғары электролизер корпусын бойлық бөлімдермен екі бөлікке бөлу ұсынылды, олардың әрқайсысы өз кезегінде көлденең қалқалы 8 секцияға бөлінеді, ені бойынша бұл секциялар электролизерлердің қолданыстағы әзірлемелерінің секцияларынан үштен бір есеге аз. Секциялардың қабылданған өлшемдері мен олардағы электродтардың орналасуы 2 есе азайды, 140-тан 70 мм-ге дейін қысқарды, яғни электролит тереңдігінен катодтарға галлат пен цинкат иондары өтетін қашықтық, бұл электролиз ұзақтығын қысқартты. Токтың 5,8 кА/$м^3$ есептелген тығыздығы кезіндегі 7,5 кА/$м^3$ оңтайлы тығыздығы ұсынылған, бұл электр энергиясын тұтынуды азайтуға мүмкіндік береді. Электролизерде анодтар бетінің 1,5 есе ұлғаюымен қол жеткізілген орташа ток тығыздығының азаюы есебінен кернеудің поляризациясы төмендеді. Алюминатты айналым ерітінділерінен металл галлийді алу операцияларының технологиялық реттілігі көрсетілген, ол жеті жүйелі операциядан тұрады: 1) электролитті ауа және бу-ауа қоспасымен тазалау; 2) ерітіндіні әкпен тазалау; 3) катодтарды мырыштау және катод тұнбасын еріту; 4) тазарту электролизі; 5) мырыш-галлий қорытпасын тұндыратын негізгі электролиз; 6) алюминий галлийін цементтеу; 7) қоспаларды алып тастау. Галлат-мырыш сілтілі ерітіндісін алдын-ала тазарту галлий цементтеу кезінде түйіршікті алюминий шығынын Al : Ga = 1 : 1 массалық қатынасына дейін азайтуға мүмкіндік береді.

Кілт сөздер: галлий, электролиз, алюминатты ерітінді, ерітіндіні тазарту, глинозем өндірісі, электрод аралық қашықтық.

В.М. Скачков, Л.А. Пасечник, И.С. Медянкина, С.А. Бибанаева, Н.А. Сабирзянов

Совершенствование технологии извлечения и электротехнологического оборудования для получения галлия из растворов глиноземного производства

Методами электролиза предварительно очищенных алюминатных растворов глиноземного производства получен галлий высокой чистоты, не ниже 6N, состав контролируемых примесей (исключая примеси H, C, N, O) не более 0,00007, в том числе, масс.%·10⁻⁸: Fe — 2, Cu — 5, Pb — 4, Mn — 1, In — 2, Sn — 2,5. Разработана усовершенствованная конструкция электролизера повышенной производительности для электроэкстракции галлия, предложено разделить корпус электролизера повышенной производительности продольными перегородками на две части, каждая из которых, в свою очередь, разделяется поперечными перегородками на 8 секций, по ширине эти секции меньше на треть по сравнению с секциями имеющихся разработок электролизеров. Принятые размеры секций и расположение в них электродов уменьшили в 2 раза, со 140 до 70 мм, — расстояние, которое проходят ионы галлата и цинката из глубины электролита к катодам, что сократило продолжительность электролиза. Предложена оптимальная плотность тока — 7,5 кА/м³ при расчетной плотности 5,8 кА/м³, что позволяет снизить потребление электроэнергии. На электролизере снижена поляризационная составляющая напряжения за счет уменьшения средней плотности тока, достигнутого увеличением в 1,5 раза поверхности анодов. Показана технологическая последовательность операций извлечения металлического галлия из алюминатных оборотных растворов, состоящая из семи последовательных операций: 1) очистка электролита воздушной и паровоздушной смесью; 2) очистка раствора известью; 3) цинкование катодов и растворение катодного осадка; 4) очистительный электролиз; 5) основной электролиз с осаждением цинк-галлиевого сплава; 6) цементация галлия галламой алюминия; 7) удаление примесей. Предварительная очистка галлатно-цинкатного щелочного раствора позволяет снизить при цементации галлия расход гранулированного алюминия до массового отношения Al : Ga = 1 : 1.

Ключевые слова: галлий, электролиз, алюминатный раствор, очистка раствора, глиноземное производство, межэлектродное расстояние.

References

1 U.S. Geological Survey, Mineral Commodity Summaries, January 2015. 196 p. http://dx.doi.org/10.3133/70140094

2 U.S. Geological Survey, Mineral Commodity Summaries, February 2019. 200 p. https://doi.org/10.3133/70202434

3 U.S. Geological Survey, Mineral Commodity Summaries, January 2021. 200 p. https://doi.org/10.3133/mcs2021

4 U.S. Geological Survey, Mineral Commodity Summaries, January 2022. 202 p. https://doi.org/10.3133/mcs2022

5 Setevoe izdanie «Redkie zemli» [Online publication "Rare Earth"]. Retrieved from http://rareearth.ru/ru/news/20161026/02637.html [in Russian].

6 Baker, I. (2018). Zinc. In: Fifty Materials That Make the World. *Springer International Publishing AG, part of Springer Nature,* 267–271. https://doi.org/10.1007/978-3-319-78766-4_50

7 Akchurin, R.H. (2016). Proizvodstvo poluprovodnikovykh materialov: kratkaia istoriia i sovremennoe sostoianie [Production of semiconductor materials: a brief history and current state]. *Tsvetnye metally — Non-ferrous metals*, 11, 67–74 [in Russian]. https://doi.org/10.17580/tsm.2016.11.07

8 Dyusenova, S.B., Kenzhaliev, B.K., Abdulvaliev, R.A., & Gladyshev, S.V. (2018). Kompleksnaia gidrokhimicheskaia pererabotka shlamovykh khvostov obogashcheniia khromitosoderzhashchikh rud [Complex hydrochemical processing of sludge tailings for the enrichment of chromium-containing ores]. *Obogashchenie rud — Ore dressing,* 6, 27–32 [in Russian]. https://doi.org/10.17580/or.2018.06.05

9 Koltsov, V.B., Larionov, N.M., Slesarev, S.A., & Barkinkoeva, T.A.B. (2016). Razrabotka tekhnologii polucheniia galliia poluprovodnikovoi chistoty [Development of technology for obtaining gallium of semiconductor purity]. *Estestvennye i tekhnicheskie nauki — Natural and technical sciences,* 4, 12–20 [in Russian].

10 Koltsov, V.B., Sevryukova, E.A., & Slesarev, S.A. (2016). Razrabotka tekhnologii polucheniia galliia vysokoi chistoty iz otkhodov lantagallievykh silikatov [Development of technology for obtaining high-purity gallium from waste of lanthagallium silicates]. *Aktualnye problemy povysheniia effektivnosti proizvodstv mikroelektroniki:sbornik nauchnykh trudov — Actual problems of improving the efficiency of microelectronics production. Collection of scientific papers.* Moscow, 140–145 [in Russian].

11 Potapov S.O., Sviridova M.N., Tanutrov I.N., & Toloknov, D.A. (2016). The application of sorption technology for the produce of gallium from gamma-Ga₂O₃. *XX Mendeleev Congress on general and applied chemistry*. Ekaterinburg: Ural Branch of the Russian Academy of Sciences, 3, 214.

12 Damaskin, A.A., Pechenkin, M.N., Kravchenko, V.G., & Kovalev, E.V. (2017). Usovershenstvovanie tekhnologii polucheniia galliia iz oborotnykh rastvorov glinozemnogo proizvodstva [Improvement of technology for obtaining gallium from recycled

solutions of alumina production]. *Tsvetnye metally i mineraly. Sbornik dokladov Deviatogo mezhdunarodnogo kongressa — Non-ferrous metals and minerals. Collection of reports of the Ninth International Congress,* 136–143 [in Russian].

13 Abdulvaliev, R.A., Ata, Akchil, Akhmadieva, N.K., Gladyshev, S.V., & Beisembekova, K.O. (2016). Elektrokhimicheskoe izvlechenie galliia iz shchelochnykh rastvorov sposobom elektroliza [Electrochemical extraction of gallium from alkaline solutions by electrolysis]. *Kompleksnoe ispolzovanie mineralnogo syria – Complex use of mineral raw materials*, 2, 76–82 [in Russian].

14 Kopyrin, V.S., Rubinshtein, G.M., & Yatsenko, S.P. (2013). Energoeffektivnaia tekhnologiia elektroliza galliia iz rastvorov glinozemnogo proizvodstva i elektrooborudovanie [Energy-efficient technology of gallium electrolysis from alumina solutions and electrical equipment]. *Sbornik dokladov 3-i Mezhdunarodnoi nauchno-prakticheskoi konferentsii «Effektivnoe i kachestvennoe snabzhenie i ispolzovanie elektroenergii» — Collection of reports of the 3rd International Scientific and Practical Conference "Efficient and high-quality supply and use of electricity"*. Ekaterinburg: UrFU, 110–115 [in Russian].

15 Rubinshtein, G.M., Yatsenko, S.P., Skachkov, V.M., & Kopyrin, V.S. (2015). Sovershenstvovanie tekhnologii i elektrotekhnicheskogo oborudovaniia elektroliza galliia iz rastvorov glinozemnogo proizvodstva [Improvement of technology and electrotechnological equipment for gallium electrolysis from alumina solutions]. *Sbornik dokladov 4-i Mezhdunarodnoi nauchno-prakticheskoi konferentsii «Effektivnoe i kachestvennoe snabzhenie i ispolzovanie elektroenergii» — Collection of reports of the 4th International Scientific and Practical Conference "Efficient and high-quality supply and use of electricity"*. Ekaterinburg: UrFU, 102–105 [in Russian].

16 Rubinshtein, G.M., Pasechnik, L.A., Yatsenko, S.P., & Pyagai, I.N. (2014). Izvlechenie galliia iz shchelochnykh rastvorov glinozemnogo proizvodstva [Extraction of gallium from alkaline solutions of alumina production]. *Tsvetnye metally — Non-ferrous metals*. 3, 37–43 [in Russian].

17 SkachkovV.M. Rubinshtein G.M., Surikov, V.T., Medyankina, I.S., Pasechnik, L.A., & Sabirzyanov, N.A. (2017). Electrolytic recovery of gallium from alkali aluminate bayer process solutions. *Theoretical Foundations of Chemical Engineering*. 51, 4, 580–586. DOI: 10.1134/S0040579517040133.

18 Shkolnikov, R.M., Shablakov, V.S., Sadovnikov, V.B., Kuznecov, A.V., Rubinshtein, G.M., & Yatsenko, S.P. (2000). Poleznaia model No. 14214 RF [Utility model 14214 (RF)]. Gallium electrolyzer. Publ. BI. 19 [in Russian].

19 Rubinshtein, G.M., Yatsenko, S.P., & Sabirzyanov, N.A. (2011). Poleznaia model No. 106248 RF [Utility model 106248 (RF). Electrolyzer for the extraction of gallium from alkaline-aluminate solutions of the Bayer process]. Publ. BI. 19 [in Russian].

20 Rubinshtein, G.M., Yatsenko, S.P., & Skachkov, V.M. (2014). Poleznaia model No. 147934 RF [Utility model 147934 (RF). Electrolyzer for the extraction of gallium from alkaline-aluminate solutions of the Bayer process]. Publ. BI. 45 [in Russian].

21 Yatsenko, S.P., Pasechnik L.A., Skachkov, V.M., & Rubinshtein, G.M., (2020). Gallii: Tekhnologii polucheniia i primenenie zhidkikh splavov: monografiia [Gallium: Technologies for the production and application of liquid alloys: Monograph]. Moscow: Russian Academy of Sciences. ISBN 978-5-907036-93-2 ISBN 978-5-907036-93-2. Retrieved from https://elibrary.ru/item.asp?id=44605072 [in Russian].

22 Rubinshtein, G.M., Yatsenko, S.P., Skachkov, V.M., Ludskaya, L.P., Ustich, E.P., & Vailert, A.V. (2015). Patent RF № 2553318. Sposob polucheniia galliia iz shchelochno-aliuminatnykh rastvorov glinozemnogo proizvodstva. Opublikovano BI [Patent No. 2553318 RF. Method for obtaining gallium from alkaline-aluminate solutions of alumina production]. Publ. BI. 16 [in Russian].

Information about authors*

Skachkov, Vladimir Mikhailovich (corresponding author) – Candidate of Chemical Sciences, Senior Researcher, Laboratory of Heterogeneous Processes, Institute of Solid State Chemistry of the Ural Branch of the Russian Academy of Sciences, Pervomaiskaya street, 91, 620108, Ekaterinburg, Russian; e-mail: skachkov@ihim.uran.ru; https://orcid.org/0000-0003-2551-3235;

Pasechnik, Liliya Alexsandrovna — Candidate of Chemical Sciences, Leading Researcher, Laboratory of Heterogeneous Processes, Institute of Solid State Chemistry of the Ural Branch of the Russian Academy of Sciences, Pervomaiskaya street, 91, 620108, Ekaterinburg, Russian; e-mail: pasechnik@ihim.uran.ru; https://orcid.org/0000-0002-0631-5287;

Medyankina, Irina Sergeevna — Researcher, Laboratory of Heterogeneous Processes, Institute of Solid State Chemistry of the Ural Branch of the Russian Academy of Sciences, Pervomaiskaya street, 91, 620108, Ekaterinburg, Russian; e-mail: lysira90@mail.ru; https://orcid.org/0000-0002-8636-3755;

Bibanaeva, Svetlana Alexsandrovna — Researcher, Laboratory of Heterogeneous Processes, Institute of Solid State Chemistry of the Ural Branch of the Russian Academy of Sciences, Pervomaiskaya street, 91, 620108, Ekaterinburg, Russian; e-mail: bibanaeva@mail.ru; https://orcid.org/0000-0002-1181-8735;

Sabirzyanov, Nail Adelevich — Doctor of Technical Sciences, Chief Scientific Officer, Laboratory of Heterogeneous Processes, Institute of Solid State Chemistry of the Ural Branch of the Russian Academy of Sciences, Pervomaiskaya street, 91, 620108, Ekaterinburg, Russian; e-mail: sabirzyanov@ihim.uran.ru; https://orcid.org/0000-0002-0304-8160

---

*The author's name is presented in the order: *Last Name, First and Middle Names*

S.V. Kim[*1, 2], M.I. Baikenov[1], K.S. Ibishev[2], M.G. Meiramov[3], Fengyun Ma[4], T.O. Khamitova[5]

[1]Karagandy University of the name of academician E.A. Buketov, Karaganda, Kazakhstan;
[2]Zh. Abishev Chemical and Metallurgical Institute, Karaganda, Kazakhstan;
[3]Institute of Organic Synthesis and Coal Chemistry, Karaganda, Kazakhstan;
[4]Xinjiang University, Xinjiang, China;
[5]S. Seifullin Kazakh Agro Technical University, Nur-Sultan, Kazakhstan
(*Corresponding author's e-mail: vanquishV8@mail.ru)

Effect of Nickel Nanopowder on the Thermal Degradation of Coal Tar Distillate

Regularities of influence of nickel nanopowder on the thermal degradation of coal tar distillate were determined using model-free Kissinger, Flynn-Wall-Ozawa and model-fitting Coats-Redfern methods. Coal tar distillate with a boiling point of <350 °C was obtained by simple distillation of primary coal tar from the Shubarkol deposit. Nickel nanopowder was used as a catalyst and was added to coal tar distillate in a quantity of 1 % of the mass of the distillate and then the process of thermal degradation of coal tar distillate was conducted at heating rates 5, 10 and 20 °C/min in an inert gas medium. Nickel powder was obtained by high-voltage discharge impact on the dc electrolysis. X-ray diffraction (XRD) analysis showed that the obtained nickel powder has face-centered cubic structure and the average crystallite size calculated by the Scherrer equation was ~ 34 nm. Calculations of activation energy were performed via processing of thermogravimetric data. The Kissinger method showed that the activation energy value decreases from 145.19 kJ/mol to 43.65 kJ/mol, by the Flynn-Wall-Ozawa (FWO) method the value decreases from 152.82 kJ/mol to 51.65 kJ/mol, and by the Coats-Redfern method the value decreases from 143.38 kJ/mol to 52.64 kJ/mol. Applicability of these methods is ensured by the high values of correlation coefficients.

Keywords: thermal degradation, nickel, nanopowder, coal tar, distillate, crystallite, thermogravimetric analysis, activation energy.

Introduction

The increasing demands placed on the quality of technological processing of organic raw materials [1] are primarily related to more stringent environmental requirements [2], point to the need for in-depth research on the development of methods for obtaining effective catalytic systems [3]. Studies on the development and application of various nanoheterogeneous catalytic systems for the processing of organic raw materials have risen in recent decades [4]. Nickel and its compounds are widely used in the production of various catalytic systems. The processes of aquathermolysis in the presence of iron, cobalt, and nickel at 300 °C improve the quality of heavy oil increasing the amount of low-molecular alkanes and reducing content of resins, asphaltenes, polyaromatic compounds, sulfur and nitrogen [5]. For instance, it was found that the pumping hydrogen, nickel-molybdenum nanoparticles in the form of a suspension in a vacuum oil residue at 360 °C in carbonate reservoirs was leading to destruction of almost 50 % of asphaltenes thus causing heavy oil liquefaction and increasing oil recovery [6].

Palladium-nickel phosphide deposited on a silicone-aluminum phosphate molecular sieve contributes to a more orderly mechanism of hydroisomerization of *n*-hexadecane, which leads to a high yield of isomerization products [7].

Coal tar can serve as a raw material for producing gasoline, diesel fuel, etc. For example, the simultaneous use of NiW/γ-Al₂O₃ and NiW/SAPO-11 catalysts in the process of hydrotreating low-temperature resin in a two-stage reactor makes it possible to obtain jet fuel with a freezing point of –51 °C and a high heat value [8]. The catalytic hydrogenation of coal tar in a reactor with two fixed layers in the presence of two catalysts MoNi/γ-Al₂O₃ and of WNiP/γ-Al₂O₃-USY leads to formation of diesel and gasoline fractions with a reduced sulfur and nitrogen content [9]. The Ni/ZSM-5 catalyst obtained by decomposition of nickel tetracarbonyl promotes to deeper hydrogenation of low-temperature and high-temperature resins, and also contributes to the removal of sulfur and nitrogen [10].

Hydrogenation of a mixture of resin and oil distillation residue with the addition of nickel nitrate and elemental sulfur leads to formation of products which are suitable for coke producing with a more ordered structure and yield greater than with the use of industrial catalysts [11].

Mesoporous spherical NiO-containing catalyst promotes the complete decomposition of anthracene in the hydrogenation process at 300 °C [12]. High conversion of anthracene was observed when hydrogenation process of anthracene in the presence of NiCo supported on chrysotile [13].

NiO supported on chrysotile leads to a significant reduction of activation energy in the process of thermal destruction of primary coal tar/polymeric materials mixture [14].

In this work, the kinetics of thermal degradation of primary coal tar distillate from the Shubarkol deposit without a catalyst and with the addition of nickel nanopowder in a quantity of 1 % of the mass of the organic compound was studied. Nickel nanopowder obtained by the action of a high-voltage discharge on the electrolysis process was used as a catalyst [15].

Experimental

The composition of coal tar distillate obtained by simple distillation of primary coal tar to 350 ºC was determined using an Agilent 7890A gas chromatograph having an Agilent 5975C mass-selective detector. Column parameters Rxi-5ms: length — 30 m, diameter — 0.25 mm, column adsorbent thickness — 0.25 microns, column heating rate 8 °C/min, carrier gas — helium; gas pressure in the column 1.38×10^5 Pa; sample volume 2×10^{-4} cm^3; input mode — split, library — NIST08. The composition of fractions was determined by a semi-quantitative method relative to the peak area. Data processing was carried out using the GS-MSD Data Analysis program.

The surface morphology of the nickel powder was studied using the MIRA 3 TESCAN scanning electron microscope (SEM). Phase composition and crystallite size of nickel powder were determined using X-ray diffraction (XRD) analysis and energy dispersion spectroscopy (EDS). X-ray diffraction analysis was performed on Shimadzu XRD-6000 diffractometer with CuKα-radiation with a wavelength $\lambda = 0.15418$ nm. Phase identification was carried out using PDF 4+ databases, as well as the POWDER CELL 2.4 full-profile analysis program.

The average crystallite size of nickel powder was calculated for the largest diffraction peak (111), using the Scherrer equation for spherical particles of cubic symmetry:

$$D = \frac{0.94 \cdot \lambda}{B \cdot \cos \theta}, \qquad (1)$$

where D — the average crystallite size (nm); λ — the X-ray diffractometer wavelength (nm); B — the line broadening at half the maximum intensity (radians); θ — the Bragg angle. In this equation K — the numerical factor dependent on crystallite shape and in our case $K = 0.94$.

Thermogravimetric analysis was performed on the Labsys Evo TG-DTA/DSC 1600 °C derivatograph (Setaram, France) at heating rates of 5, 10 and 20 °C/min, in nitrogen atmosphere.

Since the distillate is a liquid organic mass, it was mixed with Al_2O_3 to avoid boiling and splashing. Al_2O_3 was pre-calcined at 600 °C for 4 hours. Distillate with the mass of 5 g was mixed with Al_2O_3 in the ratio of 1:4.

Sample containing nickel powder was prepared as follows: 5 g of the distillate was mixed with the 0.05 g (1 % of distillate weight) nickel powder and this mixture was thoroughly stirred. Then Al_2O_3 was added to obtained mixture with the same ratio as in the case of sample without nickel powder. $10 \cdot 10^{-3}$ g of obtained mixture was taken for thermal analysis.

The kinetic parameters were determined based on the assumptions that the rate of transformation of a substance is a linear function depending on the temperature T and conversion ω [16]:

$$\frac{d\omega}{dt} = k(T) f(\omega) , \qquad (2)$$

where ω — the conversion which can be found from the relation [17, 18]:

$$\omega = \frac{m_i - m_t}{m_i - m_e} , \qquad (3)$$

where m_i — the initial mass sample; m_t — the mass at time; m_e — the final mass.

The basic equation for non-isothermal conditions has the form:

$$\frac{d\omega}{dt} = \frac{Z}{\beta}\exp\left(-\frac{E}{RT}\right)f(\omega), \qquad (4)$$

where Z — the pre-exponential or frequency factor (sec⁻¹); $R = 8.314$ kJ/(mol·K) — the universal gas constant; T — the temperature (K); E — the activation energy (kJ/mol); β — the heating rate.

The Kissinger and Flynn-Wall-Ozawa model-free methods and the Coats-Redfern model method were used to evaluate the effect of nanosized nickel powder on changing the activation energy.

The calculation of kinetic parameters by the Kissinger iso-conversion method is based on the equation [19]:

$$\ln\left[\frac{\ln\beta}{T^2}\right] = \ln\left[\frac{ZR}{E}\right] - \frac{E}{RT}. \qquad (5)$$

The slope of the straight line plotted in coordinates $\ln\left[\dfrac{\ln\beta}{T^2}\right]$ versus $\left(\dfrac{1000}{T}\right)$ allows the activation energy E to be computed.

For the calculation kinetic parameters according to the Flynn-Wall-Ozawa model-free method was used the following equation, taking into account the Doyle's approximation [20]:

$$\ln\beta = \ln\left[\frac{Z \cdot E}{R \cdot g(\omega)}\right] - 5.331 - 1.052\frac{E}{RT}. \qquad (6)$$

("1000"/"T") along the slope of the straight line, the activation energy E was found.

A plot of $\ln\left[\dfrac{g(\omega)}{T^2}\right]$ versus $\left(\dfrac{1000}{T}\right)$ gives a straight line with the slope which allows the determination of the activation energy E.

A Coats-Redfern method, which refers to model-fitting methods, was also applied to determine the activation energy E [21]. The equation used in this method is of the form:

$$\ln\left[\frac{g(\omega)}{T^2}\right] = \ln\left[\frac{ZR}{\beta E}\left[1 - \frac{2RT}{E}\right]\right] - \frac{E}{RT}. \qquad (7)$$

All calculations are made under the condition that the reaction order is $n = 1$.

Results and Discussion

According to the result of the chromatography-mass spectrometric analysis, it was found that the obtained coal tar distillate comprised alkanes (C_{12}–C_{20}), alkenes (C_{13}–C_{16}), cycloalkanes (C_7–C_{11}), alkylbenzenes (C_7–C_{11}), bicyclic alkanes, phenyl-cycloalkanes, naphthalenes (alkylnaphthalenes), biphenyls (alkyl biphenyls), phenols and O-, N- and S-containing compounds. Table 1 shows the composition of distillate.

T a b l e 1

The composition of the obtained coal tar distillate (< 350 ºC)

№	Compound	Area, %	№	Compound	Area, %
1	2	3	4	5	6
1	3-Methylpyridine	0.15	12	5-Decanone	0.20
2	1,3-Dimethylbenzene	0.11	13	2-Ethylphenol	5.4
3	3,5-Dimethylpyridine	0.21	14	1,3-Cyclopentanedione, 2-chloro-	0.19
4	Phenol	3.78	15	3,5-Dimethylphenol	3.32
5	3-Methylbenzyl mercaptan	0.21	16	Triquinacene	0.53
6	1-Methylpropyl benzene	0.14	17	2,6-Dimethylanisole	0.27
7	2-Cyclopenten-1-one, 2,3-dimethyl	0.27	18	3-Ethylphenol	1.90
8	1-Propynyl benzene	0.13	19	(3-Methyl-2-butenyl) benzene	0.22
9	2-Methylphenol	3.21	20	1,2-Benzenediol	0.52
10	4-Methylphenol	7.50	21	4,7-Dimethylbenzofuran	0.28
11	2,6-Dimethylpyridine	0.18	22	2-Propylphenol	0.43

1	2	3	4	5	6
23	2-Ethyl-6-methylphenol	1.03	55	1-Naphthalenol	1.15
24	2,3-Dimethylanisole	0.14	56	2(1H)-Quinolinone, 4,8-dimethyl	1.76
25	1-Ethyl-4-methoxy benzene	1.05	57	1,6,7-Trimethyl naphthalene	2.5
26	2,4-Dimethylanisole	1.84	58	1,4,6-Trimethyl naphthalene	0.84
27	1,2-Benzenediol, 3-methyl-	1.35	59	4,6,8-Trimethylazulene	1.47
28	3,4-Dimethylanisole	0.48	60	1-Heptadecene	1.35
29	Cyclohexane, 1,2,3-trimethyl-, (1 alpha., 2.beta., 3.alpha.)	0.38	61	Heptadecane	5.11
30	1H-Indene, 2,3-dihydro-4,7-dimethyl	0.27	62	1-methyl-7-(1-methylethyl) naphthalene	0.70
31	3,5-dimethyl octane	0.76	63	1-Naphthalenol, 2-methyl-	2
32	1,2-Benzenediol, 4-methyl	1.45	64	Ethanol, 2-(5-amino-6-chloropyrimidin-4-ylamino)-	1.32
33	2-Methyl naphthalene	3.08	65	1-Methyl-7-(1-methylethyl) naphthalene	0.43
34	1-(2-Hydroxy-5-methylphenyl) ethanone	0.40	66	Methyl diisopropylphosphoramioridite	0.51
35	2-Methyl-5-(1-methylethyl) phenol	0.51	67	1,6-Dimethyl-4-(1-methylethyl) naphthalene	1.41
36	6,7-Dimethyl-1,2,3,4-tetrahydronaphthalene	0.54	68	9-Methoxyfluorene	0.53
37	1H-Inden-5-ol, 2,3-dihydro	0.86	69	1,4-Dihydro-2,5,8-tri methyl naphthalene	1.04
38	1,3-Benzenediol, 4-ethyl	0.71	70	1-Naphthol, 6,7-dimethyl-	1.19
39	6-Methyl-4-indanol	0.29	71	1-Naphthol, 5,7-dimethyl-	0.41
40	2-Ethyl-3-methoxypyrazine	1.61	72	N-Methoxy-2-carbomethoxy-2-carbeth ox-yaziridine	0.33
41	1-(2,4-Dimethylphenyl) ethanone	0.51	73	N-Methyl-1-hydroxycarbazole	0.64
42	1,2,3-Trimethylindene	0.71	74	3-Methyl tetradecane	3
43	1,3-Cyclohexanedione, 5-isopropyl	0.45	75	Phenanthrene	0.35
44	1-(2,4-Dimethyl-furan-3-yl) ethanone	2.75	76	6-Methoxy-2-(1-buten-3-yl) naphthalene	0.32
45	1,2,3,4-Tetrahydro-1,1,6-trimethyl naphthalene	1.08	77	3,4-Dimethyl(1H)pyrrole, 2-[(3,4-d imethyl-[2H]-pyrrol-2-ylidene	0.24
46	2,7-Dimethyl naphthalene	1.28	78	Trifluoroacetoxy hexadecane	0.19
47	2-Allyl-4-methylphenol	0.32	79	Eicosane	2.45
48	2,3-Dimethyl naphthalene	3.19	80	7-Hydroxycadalene	0.20
49	1-(2,5-Dimethylphenyl) ethanone	2.06	81	1-Hexadecene	0.24
50	1-Pentadecene	0.70	82	Heneicosane	1.58
51	Pentadecane	1.57	83	Octadecyl trifluoroacetate	0.26
52	Acenaphthene	0.58	84	1-Methyl-7-(1-methylethyl) phenanthrene	0.41
53	3-Ethyl-1,2,4,5-tetramethyl benzene	0.90	85	11-Tricosene	0.16
54	2,3,6-Trimethyl naphthalene	0.64	86	Hentriacontane	2.3

SEM analysis (Fig. 1) showed that the nickel powder consists of nanoscale particles with a form close to spherical forming aggregates. The presence of small amount of oxygen and carbon were found by EDS (Fig. 1).
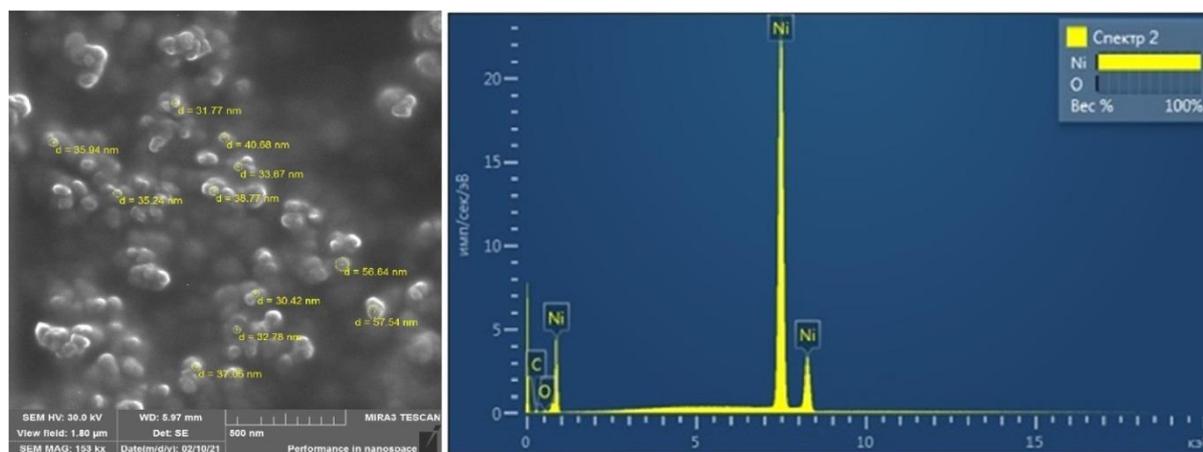

Figure 1. SEM image and EDS of nickel powder

On the XRD pattern (Fig. 2) basic peaks with the Miller indices (111), (200) and (220) were observed at the appropriate values of interplanar distances 2.034 Å, 1.762 Å and 1.246 Å. These parameters were in accordance with face-centered cubic structure. Calculation using the Equation (1) showed that medium crystallite size was approximately 34 nm.
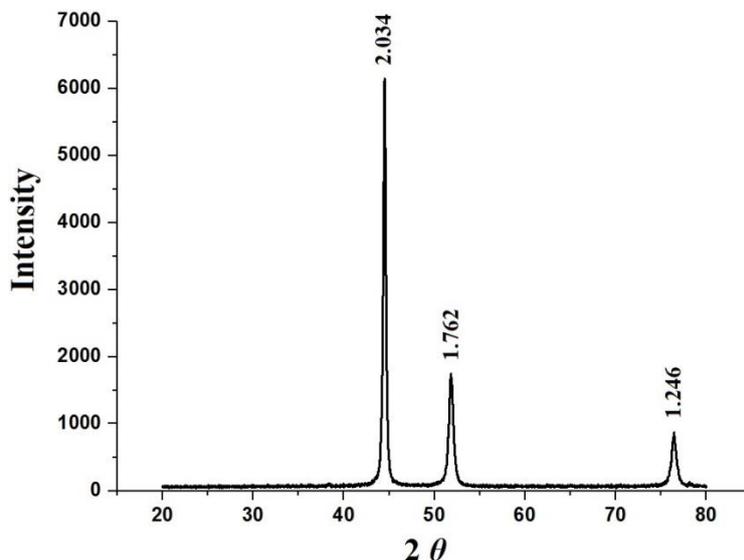

Figure 2. Diffraction pattern of the nickel powder

Figure 3 presents the effect of heating rate 5, 10 and 20 °C/min on weight loss (%).

The values of activation energies calculated by the Kissinger method showed that high correlation coefficients $R^2 = 0.966–0.9915$ were received for the conversion ω in the range of 20–60 % for thermal decomposition of primary coal tar distillate without a catalyst (Table 1).
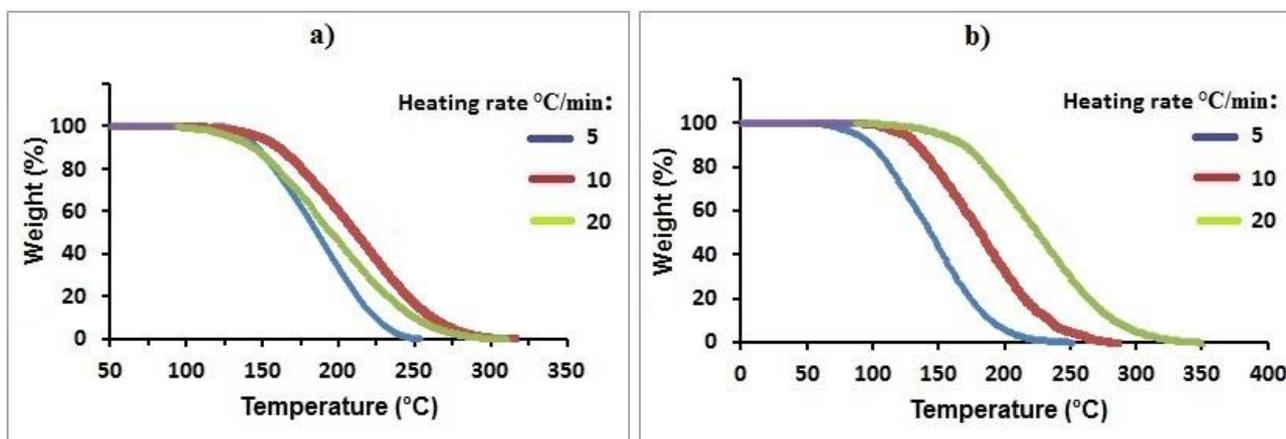
a — without a catalyst; b — in the presence of nickel powder

Figure 3. The effect of heating rate 5, 10 and 20 °C/min on weight loss (%)

At a heating rate of 5 °C/min, a temperature shift of the start of degradation is observed from ~140 °C without a catalyst versus ~90 °C in the presence of nickel powder. The shift was from ~150 °C to ~125 °C for the heating rate 10 °C/min. Also, for the heating rate 20 °C/min the temperature of the start of degradation was ~125 °C without the catalyst and ~160 °C in the presence of nickel powder.

Figure 4 designates the plots obtained by the Kissinger method.

*a* — without a catalyst; *b* — in the presence of nickel powder
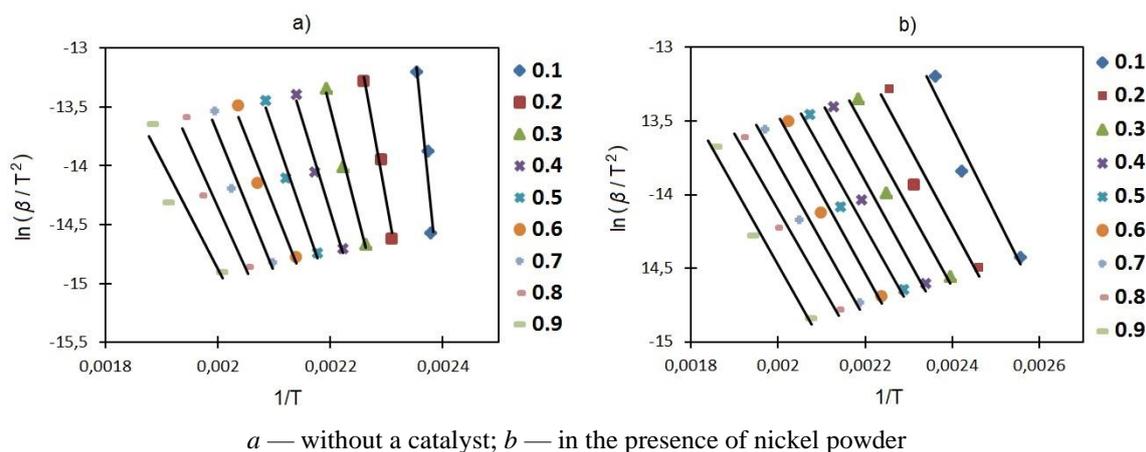
Figure 4. Kissinger approximation plots of thermal degradation of primary coal tar distillate

The average value of the activation energy $E_a = 145.19$ kJ/mol was calculated from the activation energy values for conversion (ω) in the range 0.2–0.6 with correlation coefficients $R^2 \geq 0.96$.

T a b l e 2

Calculation of activation energy at various conversions by the Kissinger method

Without a catalyst									
Conversion (ω)	0.1	0.2	0.3	0.4	0.5	0.6	0.7	0.8	0.9
Correlation coefficient (R^2)	0.8481	0.9847	0.9915	0.9857	0.9832	0.963	0.9352	0.9177	0.8913
Activation energy (E_a, kJ/mol)	392.98	220.04	158.42	131.9	114.97	100.62	96.77	87.07	76.62
In the presence of catalyst									
Conversion (ω)	0.1	0.2	0.3	0.4	0.5	0.6	0.7	0.8	0.9
Correlation coefficient (R^2)	0.9403	0.9177	0.9359	0.9404	0.9514	0.9606	0.9682	0.9667	0.9762
Activation energy (E_a, kJ/mol)	49.1	45.53	44.72	44.57	43.54	44.52	43.75	42.69	43.76

When calculating by the Kissinger method for the thermal decomposition of coal distillate with the addition of nanoscale nickel powder in a quantity of 1 % of distillate weight, the activation energies with correlation coefficients $R^2 \leq 0.98$ were obtained for all the range of $\omega = 0.1$–0.9 (Table 2). The average activation energy $E_a = 43.65$ kJ/mol was calculated from the activation energies obtained in the range of $\omega = 0.5$–0.9 with $R^2 = 0.9514$–0.9762.

Figure 5 illustrates the linear relationships obtained by the Flynn-Wall-Ozawa method.

*a* — without a catalyst; *b* — in the presence of nickel powder
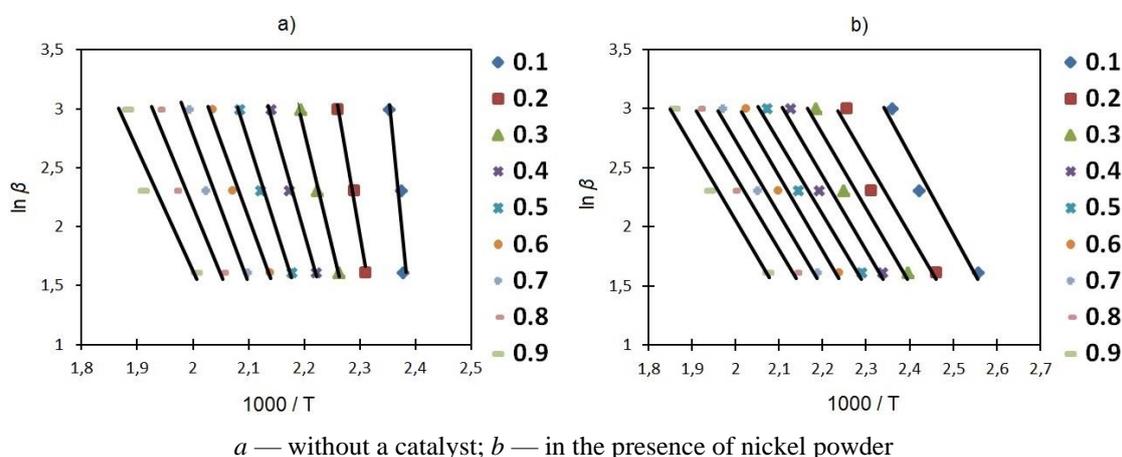
Figure 5. Linear relationships obtained by the Flynn-Wall-Ozawa method

The calculation of activation energies at various conversions by the FWO method (Table 3) showed that the highest correlation coefficients R^2 were in the range of conversions $\omega = 0.2$–0.6 for thermal decomposition of primary coal tar distillate without a catalyst. The average value of activation energy were calculated for ω in the range 0.2–0.6 and accounted for $E_a = 152.82$ kJ/mol.

Calculation of activation energy at various conversions by the FWO method

Without a catalyst									
Conversion (ω)	0.1	0.2	0.3	0.4	0.5	0.6	0.7	0.8	0.9
Correlation coefficient (R^2)	0.8527	0.9856	0.9922	0.9872	0.9852	0.9679	0.9441	0.9302	0.9098
Activation energy (E_a, kJ/mol)	400	227.32	165.89	122.77	140.27	108.58	104.88	95.39	85.15
In the presence of catalyst									
Conversion (ω)	0.1	0.2	0.3	0.4	0.5	0.6	0.7	0.8	0.9
Correlation coefficient (R^2)	0.9527	0.9364	0.9511	0.9549	0.9636	0.9705	0.9764	0.9756	0.9826
Activation energy (E_a, kJ/mol)	55.85	52.57	51.97	52	51.15	51.31	51.74	50.88	51.2

Calculation by the FWO method for thermal decomposition of distillate with the addition of nickel powder (in a quantity of 1 % of distillate weight) showed that the values of activation energies were received at correlation coefficients $R^2 < 0.99$ for all the range of conversion $\omega = 0.1$–0.9. The average activation energy $E_a = 51.65$ kJ/mol was calculated from the activation energies obtained in the range $\omega = 0.5$–0.9 with $R^2 = 0.9636$–0.9826.

Figure 6 demonstrates curves of thermal degradation of primary coal tar distillate in the presence of nickel powder constructed by the Coats-Redfern method.
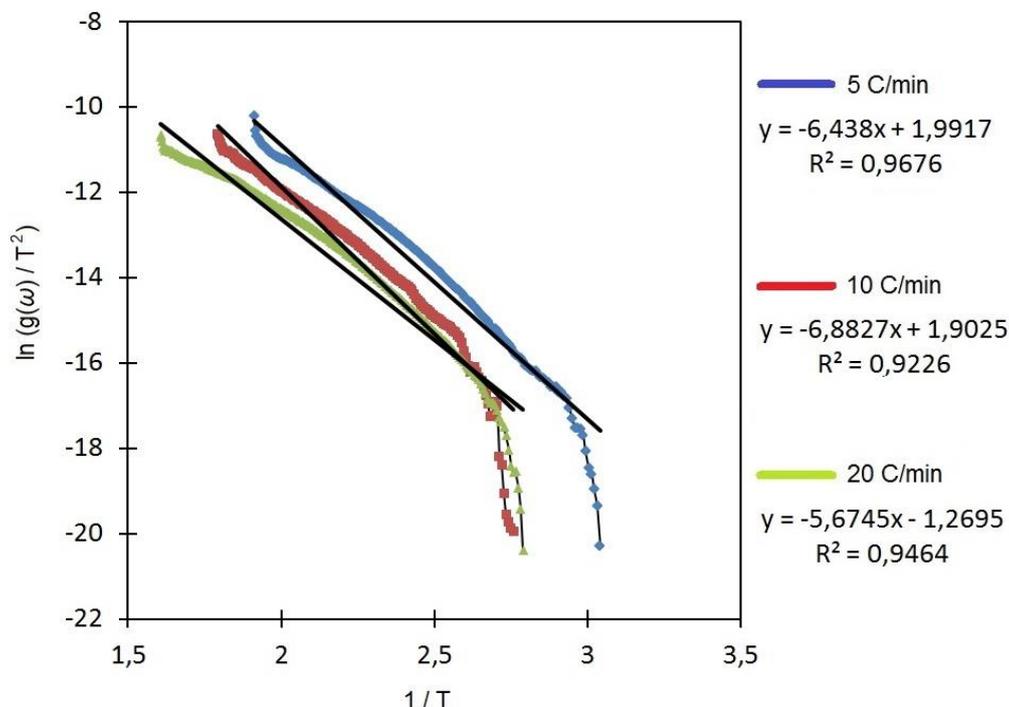

Figure 6. Curves of thermal degradation of primary coal tar distillate in the presence of nickel powder

The calculation of activation energies at different heating rates by the Coats-Redfern method is presented in Table 4.

Table 4

Calculation of activation energies at different heating rates by the Coats-Redfern method

Kinetic parameters	Without a catalyst			In the presence of nickel powder		
Heating rate (ºC/min)	5	10	20	5	10	20
Activation energy (E_a, kJ/mol)	178.753	119.185	132.203	52.525	57.22	47.18
Correlation coefficient (R^2)	0.9926	0.9909	0.9935	0.9676	0.9226	0.9446
The average value of E_a, kJ/mol	143.38			52.64		

According to the calculation received by the Coats-Redfern method for thermal degradation of primary coal tar distillate without a catalyst, the average activation energy was $E_a = 143.38$ kJ/mol without a catalyst and was close to activation energy value obtained by the Kissinger method.

In the presence of nickel powder the activation energy was $E_a = 52.64$ kJ/mol, which was close to activation energy value obtained by the FWO method.

Conclusions

The results of this study revealed that in the process of thermal degradation of primary coal tar distillate (<350 ºC) the values of activation energy calculated by the model-free Kissinger and Flynn-Wall-Ozawa methods are consistent with the model-fitting Coats-Redfern method. The differential between obtained values is insignificant. The calculation of the activation energy with high correlation coefficients is provided by the Kissinger and FWO methods for the process of thermal degradation of primary coal tar distillate (<350 °C) without a catalyst.

The Coats-Redfern method is also suitable for calculating the activation energy in the presence of nickel nanopowder, because obtained dependences are close to linear and have the high correlation coefficients. It was found that the addition of nanoscale nickel powder in a quantity of 1 % of distillate weight the activation energy reduces by approximately 3 times.

References

1   Zhang H. Selective hydrogenation of aromatics in coal-derived liquids over novel NiW and NiMo carbide catalysts / H. Zhang, G. Chen, L. Bai, N. Chang, Y. Wang // Fuel. — 2019. — Vol. 244. — P. 359–365. https://doi.org/10.1016/j.fuel.2019.02.015

2   Lei Z. Gas-Modified Pyrolysis Coke for in Situ Catalytic Cracking of Coal Tar / Lei, S. Hao S., Z. Lei, J. Yang // ACS Omega. — 2020. — Vol. 5. — P. 14911–14923. https://doi.org/10.1021/acsomega.0c00055

3   Baig N. Nanomaterials: a review of synthesis methods, properties, recent progress, and challenges / N. Baig, I. Kammakakam, W. Falathabe // Materials Advances. — 2020. — Vol. 2. — P. 1821–1871. https://doi.org/10.1039/D0MA00807A

4   Khalil M. Advanced nanomaterials in oil and gas industry: Design, application and challenges / M. Khalil, B.M. Jan, C.W. Tong, M.A. Berawi // Applied energy. — 2017. — Vol. 191. — P. 287–310. https://doi.org/10.1016/j.apenergy.2017.01.074

5   Suwaid M. In-situ catalytic upgrading of heavy oil using oil-soluble transition metal-based catalysts / M. Suwaid, V.A. Varfolomeev, A.A. Al-muntaser, C. Yuan, V.I. Starshinova, A. Zinnatullin, F.G. Vagizov, I.Z. Rakhmatullin, D.A. Emelian, A.E. Chemodanov // Fuel. — 2020. — Vol. 281. — No. 118753. https://doi.org/10.1016/j.fuel.2020.118753

6   Khoshooei M.A. Activity assessment of NiMo bimetallic nanocatalyst in presence and absence of steam in in-situ upgrading technology (ISUT) / M.A. Khoshooei, S.M. Elahi, L. Carbognani, C.E. Scott // Fuel. — 2021. — Vol. 288. — No. 119664. https://doi.org/10.1016/j.fuel.2020.119664

7   Wang W. Bifunctional catalysts for the hydroisomerization of n-alkanes: the effects of metal–acid balance and textural structure / W. Wang, C.J. Liu, W. Wu // Catalysis Science & Technology. 2019. — Vol. 9. — P. 4162–4187. https://doi.org/10.1039/C9CY00499H

8   Gang Y. Hydroprocessing of low-temperature coal tar to produce jet fuel / Y. Gang, X. Zhang, X. Lei, H. Guo, W. Li, D. Li // RSC Advances. — 2018. — Vol. 8, Issue 42. — P. 23663–23670. https://doi.org/10.1039/C8RA04531C

9   Kan T. Production of Gasoline and Diesel from Coal Tar via Its Catalytic Hydrogenation in Serial Fixed Beds / T. Kan, X. Sun, H. Wang, C. Li, U. Muhammad // Energy & Fuels. — 2012. — Vol. 26, Issue 6. — P. 3604−3611. https://doi.org/10.1021/EF3004398

10 Qi S.C. A highly active Ni/ZSM-5 catalyst for complete hydrogenation of polymethylbenzenes / S.C. Qi, X.Y. Wei, Z.M. Zong, J.I. Hayashi, X.H. Yuan, L.B. Sun L.B. // ChemCatChem. — 2013. — Vol. — 5, Issue 12. — P. 3543–3547. https://doi.org/10.1002/cctc.201300547

11 Малолетнев А.С. Гидрооблагораживание каменноугольной смолы в присутствии наногетерогенных никельсульфид-ных катализаторов / А.С. Малолетнев, Ж.К. Каирбеков, Н.Т. Смагулова // Кокс и химия. — 2020. — № 5. — С. 253–256. https://doi.org/10.3103/S1068364X20050038

12 Байкенов М.И. Влияние новых каталитических систем на процесс гидрогенизации антрацена / М.И. Байкенов, Г.Г. Байкенова, А.С. Исабаев, А.Б. Татеева, Ж.С. Ахметкаримова, А. Тусипхан, А.Ж. Матаева, К.К. Есенбаева // Химия твердого топлива. — 2015. — № 3. — С. 22–27. https://doi.org/10.7868/S0023117715030032

13 Baikenov M.I. Hydrogenation of polyaromatic compounds over NiCo/chrysotile catalyst / M.I. Baikenov, D.E. Aitbekova, N.Zh. Balpanova, A. Tusipkhan, G.G. Baikenova, Y.A. Aubakirov, A.R. Brodskiy, F. Ma, D.K. Makenov // Bulletin of the University of Karaganda — Chemistry. — 2021. — Vol. 103, No. 3. — P. 74–82. https://doi.org/10.31489/2021Ch3/74-82

14 Balpanova N.Zh. Thermokinetic parameters of the primary coal tars destruction in the presence of catalysts and polymeric materials / N.Zh. Balpanova, M.I. Baikenov, A.M. Gyulmaliev, Z.B. Absat, Zh. Batkhan, F. Ma, K. Su, S.V. Kim, G.G. Baikenova, D.E. Aitbekova, A. Tusipkhan // Bulletin of the University of Karaganda — Chemistry. — 2021. — Vol. 102, No. 2. — P. 86–95. https://doi.org/10.31489/2021Ch2/86-95

15 Ким С.В. Каталитические свойства ультрадисперсного порошка никеля при гидрогенизации антрацена и фенантрена / С.В. Ким, К.С. Ибишев, М.И. Байкенов, А. Тусупхан, В.П. Григорьева, А.М. Гюлмалиев // Химия твердого топлива. — 2022. — № 1. — С. 36–42. https://doi.org/10.31857/s0023117722010029

16 Vyazovkin S. ICTAC Kinetics Committee recommendations for performing kinetic computations on thermal analysis data / S. Vyazovkin, A.K. Burnham, J.M. Criado, L.A. Pérez-Maqueda, C. Popescu, N. Sbirrazzuoli // Thermochimica Acta. — 2011. — Vol. 520. — P. 1–19. https://doi.org/10.1016/j.tca.2011.03.034

17 Loy A. Thermogravimetric kinetic modelling of 1 in-situ catalytic pyrolytic conversion of rice husk to bioenergy using rice hull ash catalyst / A. Loy, D. Gan, S. Yusup, B. Chin, M.K. Lam, M. Shahbaz, P. Unrean, M.N. Acda, E. Rianawati // Bioresource Technology. — 2018. — Vol. 261. — P. 213–222. https://doi.org/10.1016/ j.biortech.2018.04.020

18 Heydari M. Kinetic Study and Thermal Decomposition Behavior of Lignite Coal / M. Heydari, M. Rahman, R. Gupta // International Journal of Chemical Engineering. — 2015. — Article ID 481739. https://doi.org/10.1155/2015/481739

19 Yao Z. Comparative study on the pyrolysis kinetics of polyurethane foam from waste refrigerators. / Z. Yao, S. Yu, W. Su, W. Wu, J. Tang, W. Qi // Waste Management & Research. — 2019. — Vol. 38, Issue 3. — P. 271–278. https://doi.org/10.1177/ 0734242X19877682

20 Balart R. Kinetic analysis of the thermal degradation of recycled acrylonitrile-butadiene-styrene by non-isothermal thermogravimetry / R. Balart, D. Garcia-Sanoguera, L. Quiles-Carrillo, N. Montanes, G. Torres-Giner // Polymers. — 2019. — Vol. 11, Issue 2. — No. 281. https://doi.org/10.3390/polym11020281

21 Козлов А.Н. Кинетический анализ термохимической конверсии твердых топлив / А.Н. Козлов, Д.А. Свищева, Д.И. Худякова, А.Ф. Рыжков // Химия твердого топлива. — 2017. — № 4. — С. 12–21. https://doi.org/10.7868/S0023117717040028

С.В. Ким, М.И. Байкенов, К.С. Ибишев,
М.Г. Мейрамов, Фен Юн Ма, Т.О. Хамитова

Таскөмір шайыры дистиллятының термиялық ыдырауына никель наноұнтағының әсері

Таскөмір шайыры дистиллятының термиялық ыдырау процесіне никель наноұнтағының әсер ету заңдылықтары Киссинджер, Флинн-Уолл-Озаваның динамикалық модельсіз әдістерін және Коутс-Редферннің модельді әдісін қолдана отырып анықталды. Қайнау температурасы <350 °C болатын таскөмір шайырының дистилляты Шұбаркөл кен орнының біріншілік таскөмір шайырын қарапайым айдау арқылы алынды. Катализатор ретінде қолданылған наноөлшемді никель ұнтағы таскөмір шайырының дистилляты массасына 1 % мөлшерде қосылды, содан кейін таскөмір шайыры дистиллятының термиялық ыдырау процесі инертті газ ортасында 5, 10 және 20 °C/мин қыздыру жылдамдықтарымен жүргізілді. Никель ұнтағы электролиз процесіне тұрақты токта жоғары вольтты разрядпен әсер еткен кезде алынды. Рентгендік фазалық анализ (РФА) алынған никель ұнтағы центрлікырлы текше құрылымды екенін көрсетті, ал Шеррер теңдеуімен есептелген кристаллиттердің орташа өлшемі шамамен 34 нм құрады. Активтелу энергиясын есептеу термогравиметриялық мәліметтерді өңдеу арқылы жүргізілді. Киссинджер әдісі бойынша есептеу активтелу энергиясының мәні 145,19 кДж/моль-ден 43,65 кДж/моль-ге дейін төмендейтінін көрсетті, Флинн-Уолл-Озава (FWO) әдісі бойынша активтелу энергиясының мәні 152,82 кДж/моль-ден 51,65 кДж/моль-ге дейін төмендейтіні анықталды және Коутс-Редферн модельдік әдісіне сәйкес активтелу энергиясының мәні 143,38 кДж/моль-ден 52,64 кДж/моль-ге дейін төмендейді. Алынған корреляция коэффициенттерінің жоғары мәндері бұл әдістердің қолданылу мүмкіншілігін анықтайды.

Кілт сөздер: термиялық деструкция, никель, наноұнтақ, таскөмір шайыры, дистиллят, кристаллит, термогравиметриялық анализ, активтелу энергиясы.

С.В. Ким, М.И. Байкенов, К.С. Ибишев,
М.Г. Мейрамов, Фен Юн Ма, Т.О. Хамитова

Влияние нанопорошка никеля на термическое разложение дистиллята каменноугольной смолы

Закономерности влияния нанопорошка никеля на процесс термического разложения дистиллята каменноугольной смолы были определены с использованием динамических безмодельных методов Киссинджера, Флинна–Уолла–Озавы и модельного метода Коутса–Редферна. Дистиллят каменноугольной смолы с температурой кипения < 350 °С был получен простой перегонкой первичной каменноугольной смолы с месторождения «Шубарколь». В качестве катализатора использовали наноразмерный порошок никеля, который добавляли в дистиллят каменноугольной смолы в количестве 1 % от массы дистиллята и затем проводили процесс термической деструкции дистиллята каменноугольной смолы при скоростях нагрева 5, 10 и 20 °С/мин в среде инертного газа. Порошок никеля был получен при воздействии высоковольтного разряда на процесс электролиза на постоянном токе. Проведенный рентгенофазовый анализ показал, что полученный порошок никеля имеет гранецентрированную кубическую структуру, а средний размер кристаллитов, рассчитанный по уравнению Шеррера, составил примерно 34 нм. Расчеты энергии активации проводились с помощью обработки термогравиметрических данных. Расчет по методу Киссинджера показал, что значение энергии активации уменьшается с 145,19 кДж/моль до 43,65 кДж/моль, по методу Флинна–Уолла–Озавы установлено, что значение энергии активации уменьшается с 152,82 кДж/моль до 51,65 кДж/моль, и согласно модельному методу Коутса–Редферна значение энергии активации уменьшается со 143,38 кДж/моль до 52,64 кДж/моль. Применимость данных методов обеспечивается полученными высокими значениями коэффициентов корреляции.

Ключевые слова: термическая деструкция, никель, нанопорошок, каменноугольная смола, дистиллят, кристаллит, термогравиметрический анализ, энергия активации.

References

1   Zhang, H., Chen, G., Bai, L., Chang, N., & Wang, Y. (2019). Selective hydrogenation of aromatics in coal-derived liquids over novel NiW and NiMo carbide catalysts. *Fuel, 244*, 359–365. https://doi.org/10.1016/j.fuel.2019.02.015

2   Lei, Z., Hao, S., Lei, Z., & Yang, J. (2020). Gas-Modified Pyrolysis Coke for in Situ Catalytic Cracking of Coal Tar. *ACS Omega, 5,* 14911–14923. https://doi.org/10.1021/acsomega.0c00055

3   Baig, N., Kammakakam, I., & Falathabe, W. (2021). Nanomaterials: a review of synthesis methods, properties, recent progress, and challenges. *Materials Advances, 2,* 1821–1871. https://doi.org/10.1039/D0MA00807A

4   Khalil, M., Jan, B.M., Tong, C.W., & Berawi, M.A (2017). Advanced nanomaterials in oil and gas industry: Design, application and challenges. *Applied energy, 191*, 287–310. https://doi.org/10.1016/j.apenergy.2017.01.074

5   Suwaid, M., Varfolomeev, V.A., Al-muntaser, A.A., Yuan, C., Starshinova, V.I., Zinnatullin, A., Vagizov, F.G., Rakhmatullin, I.Z., Emelian, D.A., & Chemodanov, A.E. (2020). In-situ catalytic upgrading of heavy oil using oil-soluble transition metal-based catalysts. *Fuel, 281*, 118753. https://doi.org/10.1016/j.fuel.2020.118753

6   Khoshooei, M.A., Elahi, S.M., Carbognani, L., & Scott, C.E. (2021). Activity assessment of NiMo bimetallic nanocatalyst in presence and absence of steam in in-situ upgrading technology (ISUT) *Fuel, 288*, 119664. https://doi.org/10.1016/j.fuel.2020.119664

7   Wang, W., Liu, C.J., & Wu, W. (2019). Bifunctional catalysts for the hydroisomerization of *n*-alkanes: the effects of metal–acid balance and textural structure. *Catalysis Science & Technology, 9*, 4162–4187. https://doi.org/10.1039/C9CY00499H

8   Gang, Y., Zhang, X., Lei, X., Guo, H., Li, W., & Li, D. (2018). Hydroprocessing of low-temperature coal tar to produce jet fuel. *RSC Advances, 8(42)*, 23663–23670. https://doi.org/10.1039/C8RA04531C

9   Kan T., Sun X., Wang H., Li, C., & Muhammad, U. (2012). Production of Gasoline and Diesel from Coal Tar via Its Catalytic Hydrogenation in Serial Fixed Beds. *Energy & Fuels, 26(6),* 3604−3611. https://doi.org/10.1021/EF3004398

10   Qi, S.C., Wei, X.Y., Zong, Z.M., Hayashi, J.I., Yuan, X.H., & Sun, L.B. (2013). A highly active Ni/ZSM-5 catalyst for complete hydrogenation of polymethylbenzenes. *ChemCatChem, 5(12)*, 3543–3547. https://doi.org/10.1002/cctc.201300547

11   Maloletnev, A.S., Kairbekov Zh.K., & Smagulova, N.T. (2020). Gidrooblagorazhivanie kamennougolnoi smoly v prisutstvii nanogeterogennykh nikelsukfidnykh katalizatorov [Refining of coal tar by hydrogenation in the presence of nanoheterogeneous nickel sulfide catalyst]. *Koks i khimiia — Coke and Chemistry, 63(5)*, 253–256. https://doi.org/10.3103/S1068364X20050038

12   Baikenov, M.I., Baikenova, G.G., Isabaev, A.S. *et al.* Effect of new catalytic systems on the process of anthracene hydrogenation. *Solid Fuel Chem.* 49, 150–155 (2015). https://doi.org/10.3103/S0361521915030039

13   Baikenov, M.I., Aitbekova, D.E., Balpanova, N.Zh, Tusipkhan, A., Baikenova, G.G., Aubakirov, Y.A., Brodskiy, A.R., Ma, F., & Makenov, D.K. (2021). Hydrogenation of polyaromatic compounds over NiCo/chrysotile catalyst. *Bulletin of the University of Karaganda — Chemistry, 103(3)*, 74–82. https://doi.org/10.31489/2021Ch3/74-82

14 Balpanova, N.Zh., Baikenov, M.I., Gyulmaliev, A.M., Absat, Z.B., Batkhan, Zh., Ma, F., Su, K., Kim, S.V., Baikeno-va, G.G., Aitbekova, D.E., & Tusipkhan, A. (2021). Thermokinetic parameters of the primary coal tars destruction in the presence of catalysts and polymeric materials. *Bulletin of the University of Karaganda — Chemistry, 102(2)*, 86–95. https://doi.org/10.31489/2021Ch2/86-95

15 Kim, S.V., Ibishev, K.S., Baikenov, M.I. *et al.* Catalytic Properties of Ultrafine Nickel Powder in the Hydrogenation of Anthracene and Phenanthrene. *Solid Fuel Chem.* **56,** 53–58 (2022). https://doi.org/10.3103/S0361521922010025

16 Vyazovkin, S., Burnham, A.K., Criado, J.M., Pérez-Maqueda, L.A., Popescu, C., & Sbirrazzuoli, N. (2011). ICTAC Kinetics Committee recommendations for performing kinetic computations on thermal analysis data. *Thermochimica Acta, 520,* 1–19. https://doi.org/10.1016/j.tca.2011.03.034

17 Loy, A., Gan, D., Yusup, S., Chin, B., Lam, M.K., Shahbaz, M., Unrean, P., Acda, M.N., & Rianawati, E. (2018). Thermogravimetric kinetic modelling of 1 in-situ catalytic pyrolytic conversion of rice husk to bioenergy using rice hull ash catalyst. *Bioresource Technology, 261,* 213–222. https://doi.org/10.1016/ j.biortech.2018.04.020

18 Heydari, M., Rahman, M., & Gupta, R. (2015). Kinetic Study and Thermal Decomposition Behavior of Lignite Coal. *International Journal of Chemical Engineering.* https://doi.org/10.1155/2015/481739

19 Yao, Z., Yu, S., Su, W., Wu, W., Tang, J., & Qi, W. (2019). Comparative study on the pyrolysis kinetics of polyurethane foam from waste refrigerators. *Waste Management & Research, 38(3),* 271–278. https://doi.org/10.1177/ 0734242X19877682

20 Balart, R., Garcia-Sanoguera, D., Quiles-Carrillo, L., Montanes, N., & Torres-Giner, G. (2019). Kinetic analysis of the thermal degradation of recycled acrylonitrile-butadiene-styrene by non-isothermal thermogravimetry. *Polymers, 11(2), 281*, 1–23. https://doi.org/10.3390/polym11020281

21 Kozlov, A.N., Svishchev, D.A., Khudiakova, G.I. *et al.* (2017) A kinetic analysis of the thermochemical conversion of solid fuels (A review). *Solid Fuel Chem.* **51,** 205–213. https://doi.org/10.3103/S0361521917040061

Information about authors[*]

Kim, Sergey Valerievich (corresponding author) — Doctoral student, Karagandy University of the name of academician E.A. Buketov, Universitetskaya street, 28, 100024, Karaganda, Kazakhstan; Research Engineer, Zh. Abishev Chemical-Metallurgical Institute, Karaganda, Ermekov street, 63, 100009, Kazakhstan; e-mail: vanquishV8@mail.ru; https://orcid.org/0000-0002-6044-9438;

Baikenov, Murzabek Ispolovich — Doctor of Chemical Sciences, Professor, Karagandy University of the name of academician E.A. Buketov, Universitetskaya street, 28, 100024, Karaganda, Kazakhstan; e-mail: murzabek_b@mail.ru; https://orcid.org/0000-0002-8703-0397;

Ibishev, Kanat Sansyzbaevich — Candidate of Chemical Sciences, Leading Researcher, Zh. Abishev Chemical-Metallurgical Institute, Karaganda, Ermekov street, 63, 100009, Kazakhstan; e-mail: ikan-at2014@mail.ru; https://orcid.org/0000-0001-7622-2791;

Meiramov, Mazhit Gabdullovich — Candidate of Chemical Sciences, Senior Researcher, Institute of Organic Synthesis and Coal Chemistry of the Republic of Kazakhstan, Karaganda, Alihanova street, 1, 100008, Kazakhstan; e-mail: majit_m@mail.ru; https://orcid.org/0000-0003-2498-6516;

Ma, Fengyun — PhD, Professor, Xinjiang University, Urumqi, Nan Min Lu street, 666, Xinjiang Uygur Autonomous Region (XUAR) People's Republic of China (PCR); e-mail: ma_fy@126.com;

Khamitova, Tolkyn Ondirisovna — PhD, Agronomic Faculty, S. Seifullin Kazakh Agro Technical University, Nur-Sultan, Zhenis avenue, 62, 010011, Kazakhstan; e-mail: khamitova.t@inbox.ru; https://orcid.org/0000-0002-4691-3732

_____

*The author's name is presented in the order: *Last Name, First and Middle Names*